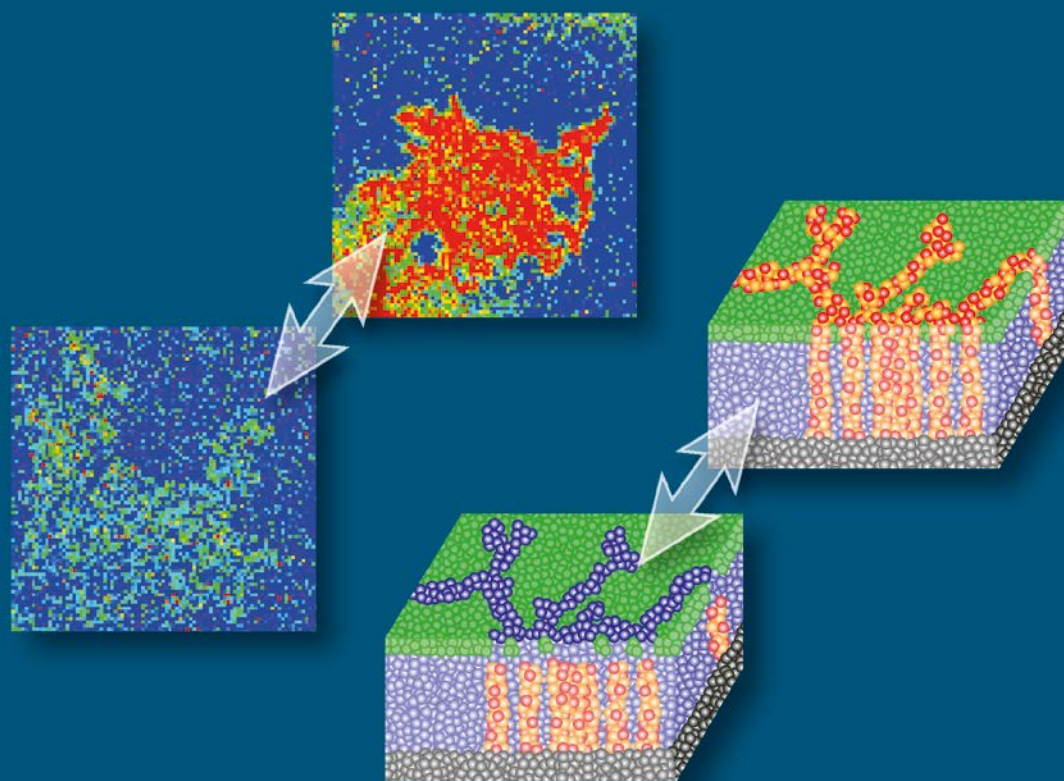


Redox processes and ionic transport in resistive switching binary metal oxides

Katharina Skaja



Information
Band/ Volume 49
ISBN 978-3-95806-236-8

Forschungszentrum Jülich GmbH
Peter Grünberg Institute (PGI)
Electronic Materials (PGI-7)

Redox processes and ionic transport in resistive switching binary metal oxides

Katharina Skaja

Schriften des Forschungszentrums Jülich
Reihe Information / Information

Band / Volume 49

ISSN 1866-1777

ISBN 978-3-95806-236-8

Bibliographic information published by the Deutsche Nationalbibliothek.
The Deutsche Nationalbibliothek lists this publication in the Deutsche
Nationalbibliografie; detailed bibliographic data are available in the
Internet at <http://dnb.d-nb.de>.

Publisher and
Distributor: Forschungszentrum Jülich GmbH
Zentralbibliothek
52425 Jülich
Tel: +49 2461 61-5368
Fax: +49 2461 61-6103
Email: zb-publikation@fz-juelich.de
www.fz-juelich.de/zb

Cover Design: Grafische Medien, Forschungszentrum Jülich GmbH

Printer: Grafische Medien, Forschungszentrum Jülich GmbH

Copyright: Forschungszentrum Jülich 2017

Schriften des Forschungszentrums Jülich
Reihe Information / Information, Band / Volume 49

D 82 (Diss. RWTH Aachen University, 2016)

ISSN 1866-1777
ISBN 978-3-95806-236-8

The complete volume is freely available on the Internet on the Jülicher Open Access Server (JuSER)
at www.fz-juelich.de/zb/openaccess.



This is an Open Access publication distributed under the terms of the [Creative Commons Attribution License 4.0](https://creativecommons.org/licenses/by/4.0/),
which permits unrestricted use, distribution, and reproduction in any medium, provided the original work is properly cited.

Abstract

The growing demand for non-volatile memories requires new concepts in data storage and mobile computing, as the existing flash technology runs into a physical scaling limit. One of the promising candidates for future non-volatile memories is Redox-based Resistive Random Access Memory (ReRAM). This memory technology is based on a non-volatile and reversible switching of device resistance with an external stimulus. The reversible resistance change in the memristive device can be attributed to an electro reduction, which takes place in the metal oxide and/or at the metal oxide electrode interface. The formation of ionic defects and their motion are involved in the electrically induced redox processes, which for most metal oxides is correlated to a valence change of metal ions. Within this thesis the microscopic processes in memristive devices are investigated in order to understand the defect configuration and defect motion in metal oxide thin films. Furthermore, the redox processes localized in nanoscale filaments induced by field-driven defect motion has been elucidated.

The resistive switching characteristic of $\text{Ta}_2\text{O}_{5-x}$ single layers as well as $\text{Nb}_2\text{O}_{5-x}/\text{Ta}_2\text{O}_{5-x}$ heterostructures has been investigated. It could be demonstrated that the forming voltage of the memristive devices can be modified by different reactive sputtering conditions. During electrical biasing a morphological change with a dendrite-like shape occurs at the top electrode. The formation of this dendrite-like structure at the metal oxide/metal interface, has been correlated to an avalanche discharge induced redox process in the metal oxide. The dendrite-like structure can be assigned to an oxygen deficient amorphous phase of the metal oxide. The predominant defects in TiO_{2-x} are determined by ionic charge compensation at intermediate oxygen partial pressure and dominated by electronic charge compensation at reducing conditions. For $\text{Ta}_2\text{O}_{5-x}$ ceramics as well as thin films the electrical conductivity is dominated by ionic charge compensation over the entire investigated oxygen partial pressure range. The formation energy for oxygen vacancies of single crystal/ceramics is comparable to the values of the thin films. At oxidizing conditions the thin films show an enhanced ionic conduction due to an increased concentration of defects at the grain boundaries and an accumulation of the space charges. The equilibration process in TiO_{2-x} single crystals as well as in thin films is dominated by a surface exchange process. The velocity of the equilibration process is influenced by the surface orientation of single crystals.

In TiO_{2-x} thin films a two-fold surface exchange process has been identified. As origin of this two fold process the incorporation or release of a second species such as water was discussed as well as the influence of the texturing of the thin film and the influence of the substrate.

Kurzfassung

Die wachsende Nachfrage nach nicht flüchtigen Speichern erfordert neue Konzepte in der Datenspeicherung, da die bestehende Flash-Technologie in eine physikalische Skalierungsgrenze läuft. Ein vielversprechendes Konzept für einen zukünftigen nicht flüchtigen Speicher ist der redox-basierte resistive RAM (ReRAM), dessen Widerstand durch einen äußeren Stimulus nicht flüchtig und reversibel verändert werden kann. Die reversible Widerstandsänderung in einem ReRAM kann auf eine Redoxreaktion zurückgeführt werden, die im Metalloxid und/oder an der Metalloxid Elektroden Grenzfläche stattfindet. Die Bildung von ionischen Defekten und deren Bewegung spielt hierbei eine wichtige Rolle. Für die meisten Metalloxide ist die Redoxreaktion mit einem Valenzwechsel korreliert. Im Rahmen dieser Arbeit wurden die mikroskopischen Prozesse in ReRAMs untersucht, um ein besseres Verständnis von der Defektchemie und dem Transport von Defekten in dünnen Metalloxidschichten zu erhalten. Darüber hinaus wurden die Redoxreaktionen in nanoskaligen Filamenten untersucht.

Die resistiven Schalteigenschaften von gesputterten $\text{Ta}_2\text{O}_{5-x}$ Dünnschichten sowie von $\text{Nb}_2\text{O}_{5-x}/\text{Ta}_2\text{O}_{5-x}$ Heterostrukturen wurden untersucht. Die Formierspannung kann durch die Depositionsparameter beeinflusst werden. Nach dem ersten Formierschritt wurde die Bildung einer dendritenähnlichen Struktur in der oberen Elektrode beobachtet. Die Bildung dieser dendritenähnlichen Struktur konnte auf eine Avalanche-Entladung an der Metalloxid/Metall-Grenzfläche zurückgeführt werden, die eine Redoxreaktion im Metalloxid auslöst. In der dendritenähnlichen Struktur konnte eine amorphe, reduzierte Metalloxidphase nachgewiesen werden. Als vorherrschende Defekte in TiO_{2-x} wurden für mittlere Sauerstoffpartialdrücke ionische Defekte identifiziert. Im reduzierenden Bereich wird die ionische Leitfähigkeit durch einen elektronischen Ladungsausgleich bestimmt. Für $\text{Ta}_2\text{O}_{5-x}$ Keramiken sowie für Dünnschichten ist die elektrische Leitfähigkeit durch einen ionischen Ladungsausgleich bestimmt. Die Bildungsenthalpie für Sauerstoffleerstellen in Einkristallen/Keramiken bzw. Dünnschichten wird nicht durch zusätzliche Korngrenzen beeinflusst. Für höhere Sauerstoffpartialdrücke ist die ionische Leitfähigkeit in den Dünnschichten aufgrund einer erhöhten Konzentration von Defekten an den Korngrenzen und einer Akkumulation der Raumladungszonen erhöht. Die Gleichgewichtskinetik in TiO_{2-x} Einkristallen sowie in dünnen Schichten ist durch

einen Oberflächenaustauschprozess dominiert. Die Geschwindigkeit des Gleichgewichtsprozesses wird durch die Oberflächenorientierung beeinflusst. In TiO_{2-x} Dünnschichten wurde ein doppelter Oberflächenaustauschprozess identifiziert. Als Ursprung dieser heterogenen Kinetik wurde der Einbau oder die Freisetzung einer zweiten Spezies wie Wasser diskutiert sowie der Einfluss der Dünnschichttexturierung und der Einfluss des Substrats.

Contents

1	Introduction	1
2	Fundamentals	5
2.1	Resistive switching	5
2.2	Structure of $\text{Ta}_2\text{O}_{5-x}$ and TiO_{2-x}	7
2.2.1	TiO_{2-x}	7
2.2.2	$\text{Ta}_2\text{O}_{5-x}$	8
2.3	Defect Chemistry	9
2.3.1	TiO_{2-x}	10
2.3.2	$\text{Ta}_2\text{O}_{5-x}$	16
2.4	Diffusion in solids	20
2.4.1	Ideal step response	20
2.4.2	Non ideal step response	24
2.4.3	Chemical diffusion in TiO_{2-x}	26
3	Experimental methods	31
3.1	DC magnetron sputter deposition	31
3.2	Atomic force microscopy (AFM)	32
3.3	X-ray photoelectron spectroscopy (XPS)	33
3.4	Photoemission electron microscopy (PEEM)	35
3.5	High temperature equilibrium conductance (HTEC) measurements	37
3.6	Electronic conductivity relaxation (ECR) measurements	39
4	Growth and characterization of thin oxide films	45
4.1	Surface morphology and structure of sputtered thin films	45
4.2	Spectroscopic characterization of thin films	48
4.2.1	Engineering the oxygen content in $\text{Ta}_2\text{O}_{5-x}$	48
4.2.2	Engineering the oxygen content in TiO_{2-x}	54
4.2.3	Spectroscopic characterization of $\text{Nb}_2\text{O}_{5-x}/\text{Ta}_2\text{O}_{5-x}$ heterosystems	57
4.3	Resistive switching in tantalum oxide based MIM structures	59
4.3.1	Sample preparation	59
4.3.2	Sample preparation for spectromicroscopy	59

4.3.3	Stoichiometry dependent switching characteristic in Pt/Ta ₂ O _{5-x} /Ta layer structures	60
4.3.4	Influence of different top electrodes on the resistive switching properties	63
4.3.5	Electrical characterization of Nb ₂ O _{5-x} /Ta ₂ O _{5-x} heterosystems	66
4.3.6	Comparison of resistive switching behavior	68
4.4	Summary	69
5	Surface sensitive investigation of the active interface in MIM structures	73
5.1	Morphological changes of the bottom electrode	74
5.1.1	Ta ₂ O _{5-x} MIM structures	74
5.1.2	Nb ₂ O _{5-x} /Ta ₂ O _{5-x} heterosystem	81
5.2	Studying the active MIM interface of Ta ₂ O _{5-x} based devices by spectromicroscopy	83
5.2.1	Dendrite-like structures investigated with a laboratory source	83
5.2.2	Electroforming process in Ta ₂ O _{5-x}	88
5.2.3	Dendrite-like structures investigated by synchrotron radiation	95
5.3	Investigation of the active interface of Nb ₂ O _{5-x} /Ta ₂ O _{5-x} heterosystems	98
5.3.1	Pt/5 nm Nb ₂ O _{5-x} /10 nm Ta ₂ O _{5-x} /Ta	99
5.3.2	Pt/10 nm Nb ₂ O _{5-x} /5 nm Ta ₂ O _{5-x} /Ta	108
5.3.3	Discussion	111
5.4	Summary	112
6	Point defects and ionic transport in TiO_{2-x}	115
6.1	High temperature conductivity in TiO _{2-x}	116
6.1.1	TiO _{2-x} single crystals	116
6.1.2	High temperature conductivity in TiO _{2-x} thin films	120
6.2	Chemical diffusion in TiO _{2-x}	128
6.2.1	TiO _{2-x} single crystals	128
6.2.2	Orientation dependent relaxation in TiO _{2-x} single crystals . .	136
6.2.3	TiO _{2-x} thin films	138
6.3	Summary	151
7	High temperature conductivity of Ta₂O_{5-x}	153
7.1	Sample preparation of polycrystalline Ta ₂ O _{5-x}	153
7.2	High temperature conductivity measurements of polycrystalline Ta ₂ O _{5-x}	155
7.3	High temperature conductivity of polycrystalline Ta ₂ O _{5-x} thin films	158
7.3.1	Sample preparation of Ta ₂ O _{5-x} thin films	159
7.3.2	High temperature conductivity measurements of Ta ₂ O _{5-x} thin films	161
7.4	Summary	164

8 Summary and Conclusion	167
A Appendix	171
A.1 Sputterdeposition parameters	171
List of abbreviations	173
Bibliography	175
Acknowledgement	201

1 Introduction

In many processes and procedures of everyday life consumer electronics e.g. computers, smartphones or cloud services play an important role. The growing demand for non-volatile memories, which are included in the consumer electronics, requires new concepts in data storage and mobile computing, as the existing flash technology runs into a physical scaling limit [1]. One of the promising candidates for future non-volatile memories is Resistive Random Access Memory (ReRAM) [1–4]. The scaling limit of ReRAM is in the nm range, which makes it suitable for future applications in the information technology. This memory technology is based on a non-volatile and reversible switching of device resistance with an external stimulus. The memory devices typically consist of a metal-insulator-metal (MIM) structure. The devices can usually be reversibly switched between low resistance state (LRS) and high resistance state (HRS). The reversible resistance change in the memristive device can be attributed to an electro-reduction, which is localized in the metal oxide and/or at the metal oxide electrode interface. The redox reaction can take place in the entire device region (area dependent switching) or in a nanoscale conductive filament (filamentary switching). The formation of ionic defects and their motion are involved in the electrically induced redox processes. In most metal oxides the local redox reaction is correlated to a valence change of metal ions. This process is called valence change mechanism (VCM).

In recent years, much effort has been expended in order to investigate the physical and chemical processes at the nanoscale. The non-volatile and reversible switching in the memristive device is enabled by a first quasi-static current voltage sweep with a higher voltage than the subsequent switching voltage in order to form a conductive filament the so called electroforming process. At a certain voltage during this sweep the current significantly increases and leads to a change of the resistance of the cell. Two microscopic effects have been identified for the formation of a conductive filament during the electroforming process. Ionic processes as well as electronic processes have been identified as origin for the formation process. Which of these processes is dominant in the formation of the conductive filament might vary strongly with the employed metal oxide. The ionic process is correlated to the generation of oxygen vacancies at the anode which goes along with a release of oxygen. Due to the applied electric field the oxygen vacancies drift towards the

anode. The increased oxygen vacancy concentration leads to an enhanced conductivity. This starts a self-accelerating process where the increased conductivity and Joule heating mutually reinforce. This process results in the formation of a conductive filament, which connects bottom and top electrode [5–7]. However, it has been also demonstrated for the first stage of electroforming that a purely electronic process initiates the forming process [8]. The electroforming in this model starts with reversible electronic processes. Due to electronic instabilities in the devices the initially homogeneous distributed current flow can be restricted reversibly to a localized current path. This process takes place before ionic motion occurs in the metal oxide layer. As soon as Joule heating is sufficient for ionic motion, the formation of a filament starts due to movement of mobile donor dopants, which results in a significant resistance change within the conductive filament. After the electroforming process morphological changes at the top electrode have been observed [5, 7, 9, 10]. The morphologic changes are correlated to the oxygen release at the upper interface due to local redox reactions. In a few reports within these morphological changes local valence changes were identified [11–14]. However, the localization of the switching event in the memristive devices is still not fully understood. Furthermore, there is still a lack of knowledge of the thermal activated ionic motion of oxygen vacancies in the metal oxides, which induces the non-linear switching kinetic [15]. Most studies in the last years, which investigated the point defect chemistry and also the transport properties of ionic defects, such as oxygen vacancies, focus on the properties of single crystals or ceramics. However, due to smaller grain size, stronger contribution from the surface and space charge layers within the thin metal oxide films the defect configuration, the ionic as well as the electronic transport and the oxygen exchange kinetic may differ from bulk properties.

Within this thesis, the influence of the thin film deposition parameters on the defect structure and switching properties will be studied. The local redox processes induced by the ionic movement will be monitored. As a filamentary mechanism is expected for the switching process in the investigated devices a spatially resolved technique is necessary for the investigation of the local induced electro redox reactions in operated devices. A suitable method to probe the different valence states in the operated devices with spatial resolution is X-ray photoelectron emission microscopy (X-PEEM). Additionally, the point defects, their transport properties and the oxygen exchange process in single crystals as well as thin films will be investigated and compared. For that purpose a conductivity relaxation setup had to be implemented. This thesis will focus on $\text{Ta}_2\text{O}_{5-x}$, $\text{Nb}_2\text{O}_{5-x}$ and TiO_{2-x} as possible candidates for ReRAM devices, due to their high scalability, fast switching speed and retention [16–20]. The thesis is organized as follows.

In chapter 2 of this thesis the resistive switching effect will be introduced and also a short overview of the current knowledge of resistive switching in tantalum

oxide based ReRAM cells is given. Furthermore, the basic material properties of titanium dioxide and tantalum oxide will be presented. Afterwards, a short overview of the defect chemistry of titanium dioxide and tantalum oxide will be given. At the end of this chapter the fundamentals of diffusion in solids will be presented.

In chapter 3 a brief description of the used experimental methods and setup is given. Afterwards, the properties of Ta_2O_5 , TiO_2 and $\text{Nb}_2\text{O}_5/\text{Ta}_2\text{O}_5$ pristine films are investigated in chapter 4. Especially the influence of deposition parameters on the oxygen vacancy concentration will be discussed and their influence on the electrical properties of the material. Then, the resistive switching characteristic of single layer $\text{Ta}_2\text{O}_{5-x}$ systems as well as $\text{Nb}_2\text{O}_{5-x}/\text{Ta}_2\text{O}_{5-x}$ heterosystems are presented. The influence of the oxygen content in the thin films on the resistive switching characteristic will be analyzed.

The morphologic changes, which occur during electroforming are presented in chapter 5. Afterwards, the active interface of $\text{Ta}_2\text{O}_{5-x}$ based ReRAM devices as well as $\text{Nb}_2\text{O}_{5-x}/\text{Ta}_2\text{O}_{5-x}$ heterostructures will be investigated. The local valence states of the operated states are investigated by spectromicroscopy and changes between the operating states, namely the low and high resistance state will be analyzed. Furthermore, the electronic structure of the different devices in terms of charge carrier concentration will be discussed.

Chapter 6 focuses on the investigation of defect chemistry in titanium dioxide as a model material. The high temperature conductivity in dependence on the oxygen partial pressure of single crystals with different orientations as well as thin films with varying thicknesses will be analyzed. Furthermore, the relaxation kinetics of rutile single crystals with different orientation and thin films will be investigated. The equilibration process after an abrupt change in oxygen partial pressure will be analyzed for a better understanding of relaxation processes in thin film. The influence of space charge zones and grain boundaries on the kinetic will be discussed.

In chapter 7 the defect chemistry of tantalum oxide ceramics and thin films is investigated by studying the high temperature conductivity.

At the end of this thesis a short summary of the presented results is given in chapter 8.

2 Fundamentals

In this chapter the resistive switching effect in metal insulator metal structures will be introduced. Afterwards, the fundamental properties of TiO_{2-x} and $\text{Ta}_2\text{O}_{5-x}$ will be presented. Also a brief overview of the defect chemistry in TiO_{2-x} and $\text{Ta}_2\text{O}_{5-x}$ will be given. At the end of this chapter the basic fundamentals of diffusion in solids will be introduced and a short overview of literature data for TiO_{2-x} will be given.

2.1 Resistive switching

Resistive switching in transition metal oxides has attracted considerable attention as a candidate for non-volatile memory in recent years, due to high scalability, fast switching speed and low power consumption [1–4]. A large variety of binary metal oxides [21–23] and also complex transition metal oxides [24–26] was reported as possible candidates for memristive memories. Recently, significant progress has been made in the device performance for amorphous $\text{Ta}_2\text{O}_{5-x}$ -based devices. High switching speed, long endurance (write cyclability) and low power consumption have been demonstrated [16–18].

The resistive switching effect describes the change of the electrical resistance of a material after an external voltage or current pulse is applied. Usually two states are defined, the first one is the high resistance state (HRS) and the second one the low resistance state (LRS). The resistance change in these structures is attributed to redox processes within the active layer [1]. A memory based on this principle is called Resistive Random Access Memory (ReRAM). The ReRAM cell consists of a metal insulator metal (MIM) structure. The insulator of the stack is the active film. The metal electrodes usually consist of two different materials. One of the electrodes has a high work function and a low oxygen affinity and the other has a low work function and a high oxygen affinity [1]. It is differentiated between two basic switching modes in resistive switching MIM structures. The first one is the unipolar switching mode (cf. figure 2.1 a)) where the cells can be set into LRS and HRS with the same voltage polarity. The second one is the bipolar switching

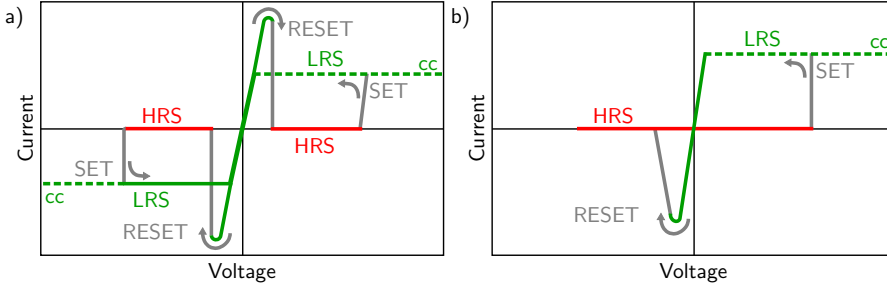


Figure 2.1: Basic operation modes of memristive devices: a) Unipolar switching mode where the cells can be set into LRS and HRS with the same voltage polarity. b) Bipolar switching mode where the device is set into LRS and HRS with opposite voltage polarities (adapted from [1]).

mode where the device is set into LRS and HRS with opposite voltage polarities (cf. figure 2.1 b)).

A common model for the resistive switching in metal oxides is the valence change mechanism (VCM), where the movement of native donor dopants such as oxygen vacancies (or cation interstitials) leads to an enrichment or depletion of electrons in the conduction band. It is widely accepted that a nanoscale conductive filament is responsible for the resistance change in these cells. It is usually reported that the filament consists of an accumulation of mobile native donors with a typical width between 10 nm to 500 nm [27–29]. The voltage-driven movement of mobile donors and the associated electrochemical redox process in the conductive filament promote the switching between the LRS and the HRS. A non-linear voltage acceleration of the kinetics in the valence change based ReRAM cells is caused by the temperature activated exponential increase of the oxygen vacancy mobility [15].

Typically, a first quasi-static I - V sweep with a voltage higher than the subsequent switching voltage is necessary to form this filament. At a certain voltage during the first sweep the current significantly increases and drives the change in the resistance of the cells. This process is called electroforming, which is commonly described as a self-accelerating process where increased conductivity and Joule heating mutually reinforce, leading to the formation of an oxygen deficient filament, which connects the bottom and top electrode [4, 6, 7]. It was observed that the filament preferentially nucleates at pre-existing defects of the MIM structures [30]. For the first stage of electroforming in $\text{Ta}_2\text{O}_{5-x}$, a purely electronic mechanism has been reported, which is initiated by the applied electric field and results in volatile changes of the device conductivity [8]. This first stage of forming

was described as formation of a current path in the oxide layer, which takes place before ionic motion occurs in the oxide layer. As soon as Joule heating is sufficient for ionic movement, the formation of a filament starts as a consequence of oxygen vacancy movement, which results in a significantly decreased resistance within a filament region. After the initial electroforming step the cells are in the LRS, where a n -conducting path connects bottom and top electrode, or HRS, depending on the forming polarity. It has been demonstrated that during the reset process an insulating gap arises at the Schottky-like diode due to axial movement of oxygen vacancies [31].

Recent reports show a radial movement of oxygen during resistive switching in Ta_2O_{5-x} based cells. Within this cell a highly conductive, oxygen deficient core has been observed with an oxygen rich, insulating shell. This phenomenon has been correlated to cluster of oxygen interstitials and vacancies [32,33].

2.2 Structure of Ta_2O_{5-x} and TiO_{2-x}

2.2.1 TiO_{2-x}

Titanium dioxide (TiO_{2-x}) is a semi-conducting material with a band gap reported to be 3.0–3.3 eV [34]. For titanium dioxide so far, the existence of three distinct phases was observed. They are known as rutile, anatase and brookite. Since the brookite phase has no relevance in this thesis, it will be therefore not further addressed. Rutile is the most stable phase of TiO_{2-x} [35]. It has a body-centered tetragonal unit cell. The lattice parameters are reported to be $a = b = 4.59 \text{ \AA}$ and $c = 2.96 \text{ \AA}$ [36]. Each of the titanium atoms is surrounded by six oxygen atoms forming an octahedral structure. Anatase is a metastable phase of TiO_{2-x} and transforms into rutile at $T = 600 \text{ K}$ [37]. It has a tetragonal structure with the following lattice parameters $a = b = 3.78 \text{ \AA}$ and $c = 9.51 \text{ \AA}$ [38]. Within the anatase structure the titanium atoms are also surrounded by six oxygen atoms forming octahedrons. The unit cells of rutile and anatase are presented in figure 2.2 a) and b).

The crystal structure of TiO_{2-x} consists of octahedrons where a titanium atom is surrounded by six oxygen atoms. The titanium atoms are arranged in rows parallel to the c -axis, resulting in open channels, which are not located perpendicular to the c -axis leading to an anisotropy in the crystal. This anisotropy of the rutile crystal influences the transport properties, such as electronic conductivity and diffusion. The diffusion properties of rutile will be discussed in a later section of this chapter (cf. section 2.4.3). For the electronic conductivity it has been demonstrated that

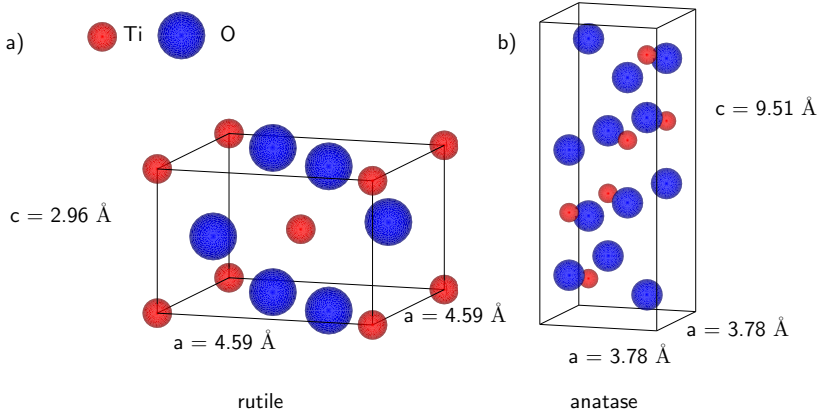


Figure 2.2: Crystal structure of TiO_2 in a) rutile and b) anatase form. The unit cells were created by *VESTA* [40] using the *ICSD database* [41].

there is a slight anisotropy. The electrical resistance measured parallel to the c -axis is higher than perpendicular to the c -axis [39].

The reduction of TiO_{2-x} , which corresponds to an increased oxygen vacancy concentration, results in the formation of crystallographic shear planes in TiO_{2-x} crystal structure. The new formed phases are called Magnéli-phases ($\text{Ti}_n\text{O}_{2n-1}$, $n \geq 2$) [42]. The Magnéli phases occur in rutile at an off-stoichiometry of $\text{TiO}_{1.999}$ [43,44]. All Magnéli phases are semi-conducting except Ti_4O_7 , which is reported to be metallic at room temperature [45,46].

2.2.2 $\text{Ta}_2\text{O}_{5-x}$

Tantalum oxide ($\text{Ta}_2\text{O}_{5-x}$) is a binary metal oxide with a band gap of 4.2 eV [47–49] and a high dielectric constant [50]. Two stable polymorphs have been reported for tantalum oxide. A low temperature phase named β - Ta_2O_5 with an orthorhombic structure [51] and a high temperature phase denoted as α - Ta_2O_5 with tetragonal crystal structure [52]. A variety of metastable phases have been observed in the past, an overview is given in the review by Garg et al. [53]. As a particularly frequently observed metastable phase TaO_2 should be mentioned here, which is formed as an interlayer between Ta_2O_5 and tantalum metal [54–56]. For thin films a third polymorph has been reported for tantalum oxide named δ - Ta_2O_5 with hexagonal symmetry [57,58], which undergoes a phase transition at 973 K to β - Ta_2O_5 [59]. For β - Ta_2O_5 a temperature of 1360 °C has been reported for the reversible phase

transition to δ -Ta₂O₅ [60,61]. Due to this reversible phase transition it is not possible to grow tantalum oxide single crystals with the standard procedures such like Verneuil or Czochralski method [51].

2.3 Defect Chemistry

As mentioned in the previous section 2.1, oxygen vacancies/defects play an important role for the switching in VCM cells. The control/manipulation of the defect concentration can enhance the electrical conductivity of a binary oxide or can lead to less conductivity depending on the defect concentration in the material. The defect structure of binary oxides depends on intrinsic defects as well as on the doping concentration (e.g. impurities, donor or acceptor doping). The formation and annihilation of defects can be described by chemical reactions

$$\sum_i x_i X_i \rightleftharpoons \sum_j y_j Y_j. \quad (2.1)$$

Here X_i describes the reactants and Y_j the products. The corresponding reaction coefficients are described by x_i and y_j . For all of these chemical reactions the mass and the charge of the system have to be conserved. The following equation describes the total charge of the system.

$$ep - en + \sum_i q_i [Q_i] = 0. \quad (2.2)$$

With e as the elementary electric charge, n the concentration of electrons, p the hole concentration and q_i the charge of the corresponding ion Q_i with respect to the lattice with the concentration $[Q_i]$.

Chemical reactions usually describe the formation of point defects, which are distributed over the entire samples. The formation of extended defects, which can also influence the electrical properties of the material [7,62], are neglected in the case of the defect chemistry model. The corresponding mass action law can be described as follows:

$$\prod_{i,j} [Y_i]^{y_i} [X_j]^{-x_j} = K(\Delta G, T) = \exp\left(-\frac{\Delta G}{k_B T}\right) = \exp\left(-\frac{\Delta H}{k_B T}\right) \exp\left(\frac{\Delta S}{k_B}\right) \quad (2.3)$$

where ΔG is the Gibbs free energy, ΔS is the entropy gain of the system, ΔH describes the enthalpy for the formation of defects and k_B is the Boltzmann constant.

The electrical conductivity of the binary oxide can be determined by

$$\sigma = \sigma_n + \sigma_p + \sigma_i \quad (2.4)$$

$$= e\mu_n n + e\mu_p p + \sum_i q_i \mu_i [Q_i] \quad (2.5)$$

where μ_i denotes the mobility of the corresponding charged particle. For the electrical charge carriers (electrons, holes) it was assumed that the electric charge is transported by a hopping mechanism, where the mobility can be expressed as

$$\mu_{n,p} = \mu_0 \exp\left(-\frac{\Delta H_m}{k_B T}\right). \quad (2.6)$$

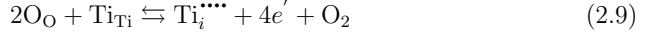
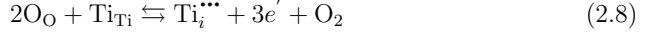
ΔH_m is the activation enthalpy of motion for the electronic charge carriers. Solving the above described equation of the conservation of charge and the mass action laws of all induced defect formation reactions, the electrical conductivity of the oxides can be described as a function of several external parameters, e.g. temperature T , oxygen partial pressure $p(\text{O}_2)$ and the dopant concentration.

This study will focus on the defect chemistry of two different binary oxides. The first one is TiO_{2-x} , which is a common material for photocatalytic applications [63, 64] and a well studied material for VCM cells. The other one is $\text{Ta}_2\text{O}_{5-x}$, which is a very promising candidate for VCM cells and is also used for electrolytic capacitors. In recent studies the defect chemistry of single crystalline and also polycrystalline TiO_{2-x} ceramics has been studied. Therefore, TiO_{2-x} acts in this study as a model binary oxide material. Whereas for $\text{Ta}_2\text{O}_{5-x}$ only little is known about the defect structure of the material. Only a few reports on polycrystalline material exist. In the following sections, the defect chemistry model for both system will be introduced briefly.

2.3.1 TiO_{2-x}

Titanium dioxide (TiO_{2-x}) is an n -type semiconductor, where the conduction is related to the existence of oxygen vacancies ($\text{V}_\text{O}^{\bullet\bullet}$) as the predominant defects and Ti interstitials ($\text{Ti}_i^{\bullet\bullet\bullet}$, $\text{Ti}_i^{\bullet\bullet\bullet\bullet}$) as minority defects [65, 66]. By oxygen release or incorporation into the TiO_{2-x} defects can be introduced to the material. Typi-

cally the formation of the defects in TiO_{2-x} is described by the following equations [65, 66].



If complete unit cells are removed, this will not be considered in the equations. The corresponding equilibrium constants can be expressed as follows.

$$K_1 = [\text{V}_\text{O}^{\bullet\bullet}] n^2 p (\text{O}_2)^{\frac{1}{2}} \quad (2.12)$$

$$K_2 = [\text{Ti}_\text{i}^{\bullet\bullet\bullet}] n^3 p (\text{O}_2) \quad (2.13)$$

$$K_3 = [\text{Ti}_\text{i}^{\bullet\bullet\bullet\bullet}] n^4 p (\text{O}_2) \quad (2.14)$$

$$K_4 = [\text{V}_\text{Ti}^{\bullet\bullet\bullet\bullet}] p^4 p (\text{O}_2)^{-1} \quad (2.15)$$

$$K_i = np \quad (2.16)$$

As has already been mentioned by equation (2.2), the charge of the system has to be conserved for the entire system. For TiO_{2-x} the neutrality conditions can be expressed as follows.

$$2[\text{V}_\text{O}^{\bullet\bullet}] + 3[\text{Ti}_\text{i}^{\bullet\bullet\bullet}] + 4[\text{Ti}_\text{i}^{\bullet\bullet\bullet\bullet}] + [\text{D}^\bullet] + p = n + 4[\text{V}_\text{Ti}^{\bullet\bullet\bullet\bullet}] + [\text{A}'] \quad (2.17)$$

The doping with donors D and acceptors A was taken into account. Usually, the defect chemistry model describes correlation between electrical conductivity and oxygen partial pressure. It is distinguished between three main oxygen partial pressure regions: the strongly reduced region, the reduced region and the oxidized region. Additionally between the two reduced regions there is a transition region, where the predominant mechanism is still under debate, it will be discussed separately in this section.

Extremely reduced region

Under extremely reducing conditions, the predominant defects are trivalent titanium interstitials $\text{Ti}_i^{\bullet\bullet\bullet}$, the charge neutrality condition (eq. 2.17) can be simplified to

$$3 [\text{Ti}_i^{\bullet\bullet\bullet}] = n. \quad (2.18)$$

With the corresponding reaction constant (eq. 2.12), the electron concentration can be calculated by

$$n = (3K_2)^{\frac{1}{4}} p (\text{O}_2)^{-1/4}. \quad (2.19)$$

Strongly reduced region

Under strongly reducing conditions the predominant defects are oxygen vacancies $\text{V}_\text{O}^{\bullet\bullet}$, the charge neutrality condition (eq. 2.17) can be simplified to:

$$2 [\text{V}_\text{O}^{\bullet\bullet}] = n. \quad (2.20)$$

With the corresponding reaction constant (eq. 2.12), the electron concentration can be calculated by

$$n = (2K_1)^{\frac{1}{3}} p (\text{O}_2)^{-1/6}. \quad (2.21)$$

Reduced region

The reduced region is dominated by the ionic charge compensation of oxygen vacancies and titanium vacancies. The charge neutrality condition for this region can be simplified to

$$[\text{V}_\text{O}^{\bullet\bullet}] = 2 [\text{V}_\text{Ti}^{\bullet\bullet\bullet}]. \quad (2.22)$$

Then the electron concentration can be calculated as a function of $p(\text{O}_2)$

$$n = \left(\frac{K_i^4 K_1}{2K_4} \right)^{\frac{1}{6}} p (\text{O}_2)^{-\frac{1}{4}}. \quad (2.23)$$

Oxidized region

Under oxidizing conditions the region is still dominated by the ionic charge compensation.

$$[V_O^{\bullet\bullet}] = 2 [V_{Ti}^{\bullet\bullet\bullet}] \quad (2.24)$$

However, with increasing oxygen partial pressure the concentration of electrons decreases. The predominant electronic defects in this regions are electron holes. The hole concentration p can be determined as a function of $p(O_2)$

$$p = \left(\frac{2K_4 K_i^2}{K_1} \right)^{\frac{1}{6}} p(O_2)^{\frac{1}{4}}. \quad (2.25)$$

If the mobility is independent of oxygen partial pressure, the electrical conductivity can be expressed by equation (2.5). The resulting relationship between conductivity and oxygen partial pressure is schematically shown in figure 2.3.

Transition region

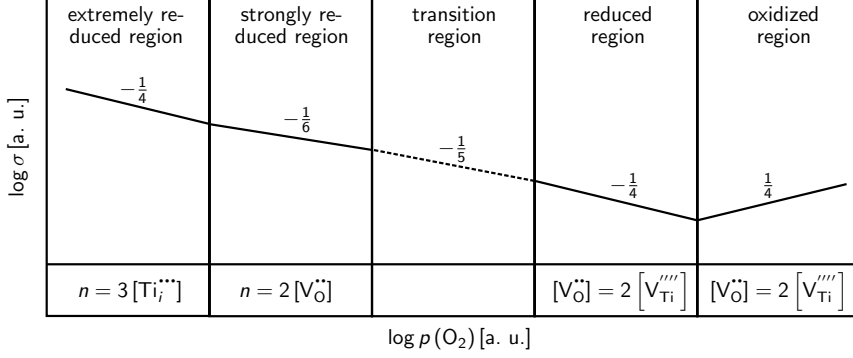
Studying the slope in the double logarithmic diagram of the electrical conductivity in dependence on the oxygen partial pressure can be an indication which of the presented models is dominant in the investigated oxygen partial pressure region. In some publications [67–69] a slope of $-\frac{1}{5}$ was reported for reducing oxygen conditions. This slope was associated with the formation of tetravalent titanium interstitials (cf. eq. 2.9) due to the relatively small ionization energies in TiO_{2-x} . The charge neutrality condition can be simplified to

$$n = 4 [Ti_i^{\bullet\bullet\bullet\bullet}]. \quad (2.26)$$

With equation (2.14) the electron concentration can be calculated as a function of $p(O_2)$

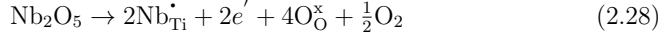
$$n = (4K_3)^{\frac{1}{5}} p(O_2)^{-\frac{1}{5}}. \quad (2.27)$$

Kofstad [70] reports that with decreasing oxygen partial pressure the concentration of tetravalent titanium interstitials increases, but these defects are not the predominant defects even at extremely reducing conditions. The group of Nowotny et al. [71, 72] interpret the slope as a transition region between the strongly reduced and reduced region.


 Figure 2.3: Schematic defect diagram of TiO_{2-x} .

Donor-doped TiO_{2-x}

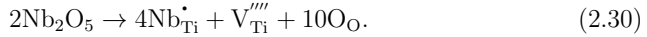
Donor doping e.g. with niobium [66, 73] changes the compensation mechanism in the TiO_{2-x} defect chemistry model. The strongly reduced regime is not affected by the donor doping of the system, it still has the same correlations as for the undoped case. However, the reduced region is influenced by the incorporated dopants. The incorporation of niobium into the TiO_{2-x} leads to the formation of electrons.



As a consequence this region is dominated by the electronic charge compensation of Nb.

$$n = [\text{Nb}_{\text{Ti}}^\bullet] \quad (2.29)$$

The concentration of electrons in this region strongly depends on the donor doping concentration. Consequently the electrical conductivity is independent of the oxygen partial pressure. With increasing oxygen partial pressure the niobium incorporation into the TiO_{2-x} can be described with the following reaction



The charge neutrality condition in this region can be simplified to

$$4 [\text{V}_{\text{Ti}}'''] = [\text{Nb}_{\text{Ti}}^\bullet] \quad (2.31)$$

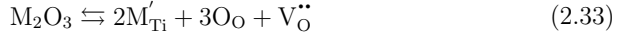
The resulting electronic concentration has the following correlation with the oxygen partial pressure

$$n = K_i \left(\frac{[\text{Nb}_{\text{Ti}}^\bullet]}{4K_4} \right)^{\frac{1}{4}} p(\text{O}_2)^{-\frac{1}{4}}. \quad (2.32)$$

With increasing oxygen partial pressure the dominant electronic charge carriers are electron holes p . The dependence of the hole concentration can be considered with the intrinsic equilibrium constant (eq. 2.16), which leads to an oxygen partial pressure dependency with a slope of $\frac{1}{4}$. In figure 2.4 b) a schematic diagram of the defect concentration for the different oxygen partial pressure regions is given.

Acceptor-doped TiO_{2-x}

The addition of M_2O_3 such like e.g. Al_2O_3 [73, 74], Cr_2O_3 [66, 75], Ga_2O_3 [76] leads to p-type doping in TiO_{2-x} . The incorporation of the M^{3+} cations into the lattice changes the defect chemistry in TiO_{2-x} . The major defect mechanism in the strongly reduced region is the same as in the case of undoped TiO_{2-x} . In the reduced regime the added cations causes the following reaction.



Taking this reaction into account, this region is dominated by the following ionic charge compensation.

$$[\text{M}'_{\text{Ti}}] = 2[\text{V}_{\text{O}}^{\bullet\bullet}] \quad (2.34)$$

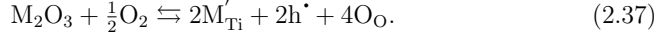
The electron concentration can be expressed as follows

$$n = \left(\frac{2K_1}{[\text{M}'_{\text{Ti}}]} \right)^{\frac{1}{2}} p(\text{O}_2)^{-\frac{1}{4}}. \quad (2.35)$$

With increasing oxygen partial pressure the major electronic defects are electron holes, the oxygen partial pressure dependence of p is given by

$$p = K_i \left(\frac{[\text{M}'_{\text{Ti}}]}{2K_1} \right)^{\frac{1}{2}} p(\text{O}_2)^{\frac{1}{4}}. \quad (2.36)$$

At very oxidizing conditions the addition of cations is compensated by holes instead of oxygen vacancies



The electronic charge compensation can be simplified to

$$p = \left[\text{M}'_{\text{Ti}} \right]. \quad (2.38)$$

In this region the hole concentration is independent of the oxygen partial pressure and only depends on the acceptor concentration.

In figure 2.4 the defect concentration in dependence on oxygen partial pressure for undoped, donor doped and acceptor doped TiO_{2-x} is shown. In the case of donor doping the electronic conductivity in the region of high oxygen partial pressure is in the reduced region (referred as reduced I region in figure 2.4 b)) constant in comparison to undoped TiO_{2-x} . For acceptor doped TiO_{2-x} the n - p -transition is shifted towards lower oxygen partial pressures.

2.3.2 $\text{Ta}_2\text{O}_{5-x}$

In this section a short overview of the existing defect chemistry model, which describes the formation of point defects in $\text{Ta}_2\text{O}_{5-x}$, is given. Previous publications investigated the defect chemistry of polycrystalline β - $\text{Ta}_2\text{O}_{5-x}$, which is almost over the entire oxygen partial pressure range an n -type conductor. At high temperatures and low oxygen concentration the defects have been consistently described by the formation of oxygen vacancies [77, 78]. In the case of high oxygen partial pressures the existence of oxygen interstitials has been discussed but up to now there was no experimental proof that oxygen interstitials exist in $\text{Ta}_2\text{O}_{5-x}$ [79, 80]. McHale et al. [80] calculated for 1100 °C that the oxygen interstitial concentration never exceeds 10^{15} 1/cm^3 and therefore can be neglected. For the intrinsic defect formation the following reactions are considered.



with the corresponding reaction constants

$$K_i = n \cdot p \quad (2.41)$$

$$K_2 = [\text{V}_\text{O}^{\bullet\bullet}] n^2 p (\text{O}_2)^{\frac{1}{2}}. \quad (2.42)$$

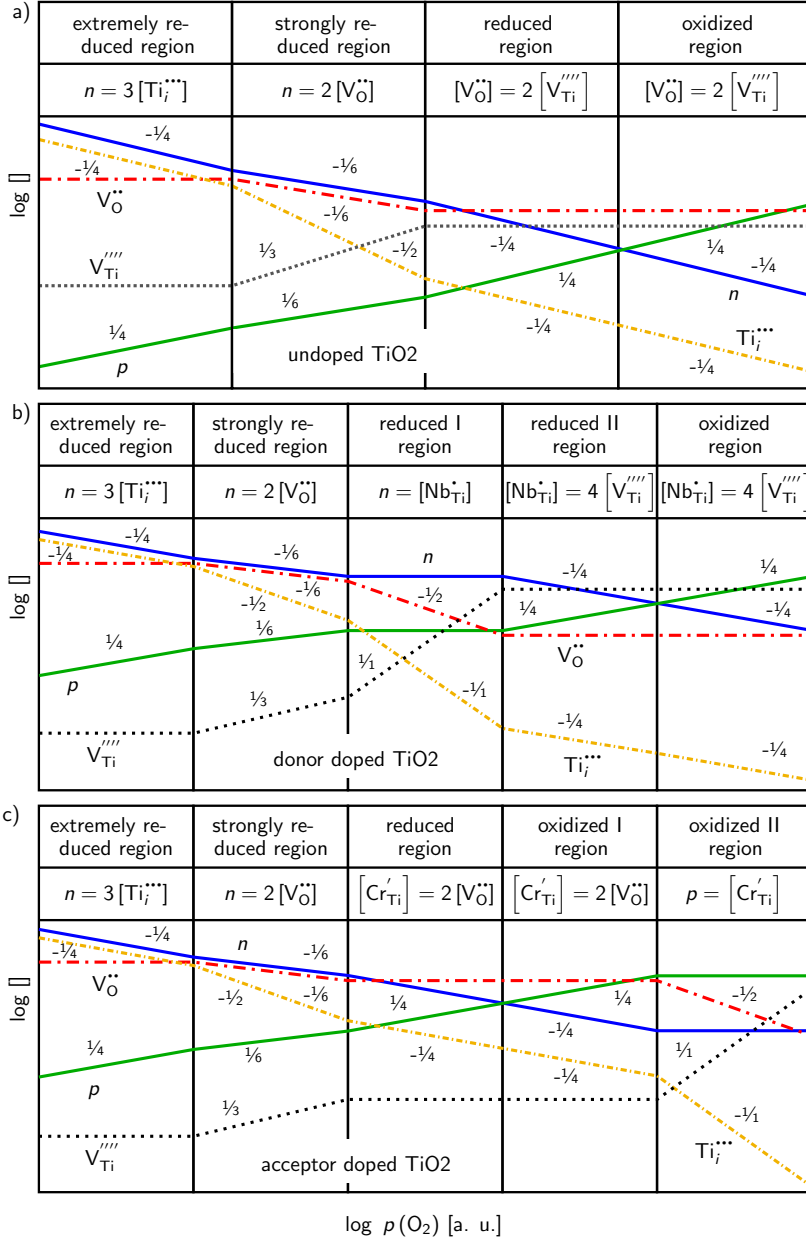


Figure 2.4: Brouwer-type diagrams for a) undoped TiO_{2-x} , b) donor doped TiO_{2-x} and c) acceptor doped TiO_{2-x} [66].

Nominally pure $\text{Ta}_2\text{O}_{5-x}$ contains always a small amount of trivalent impurities, which has to be taken into account in the defect chemistry model. These impurities act usually as acceptors and therefore, a doubly charged impurity M_{Ta}'' would be assumed. The corresponding charge neutrality condition is

$$n + 2 [\text{M}_{\text{Ta}}''] = 2 [\text{V}_{\text{O}}^{\bullet\bullet}] + p. \quad (2.43)$$

Intrinsic region

At reducing conditions oxygen vacancies are the predominant defect. The charge neutrality condition can be simplified to

$$n = 2 [\text{V}_{\text{O}}^{\bullet\bullet}]. \quad (2.44)$$

Taking the corresponding reaction constant (equation (2.42)) into account, the electron concentration n can be expressed as a function of oxygen partial pressure

$$n = (2K_2)^{\frac{1}{3}} p(\text{O}_2)^{-\frac{1}{6}}. \quad (2.45)$$

Extrinsic region

At higher oxygen partial pressure the concentration of vacancies is supposed to be fixed by the presence of the trivalent cations

$$[\text{V}_{\text{O}}^{\bullet\bullet}] = [\text{M}_{\text{Ta}}'']. \quad (2.46)$$

With equation (2.42) the electron concentration in the extrinsic defect dominated region can be expressed as follows

$$n = K_2^{\frac{1}{2}} [\text{M}_{\text{Ta}}'']^{-\frac{1}{2}} p(\text{O}_2)^{-\frac{1}{4}}. \quad (2.47)$$

At high oxygen partial pressures the conductivity is dominated by ionic conductivity, which is independent of the oxygen partial pressure (equation (2.46)). For more reducing conditions the conductivity has a characteristic slope of $-\frac{1}{4}$ in the double logarithmic oxygen partial pressure conductivity diagram. This simple model is not valid for all temperatures. McHale et al. [80] observe a change of the activation energy with increasing temperature for oxidizing conditions. In this report, two different explanations have been proposed, taking into account the relatively poor

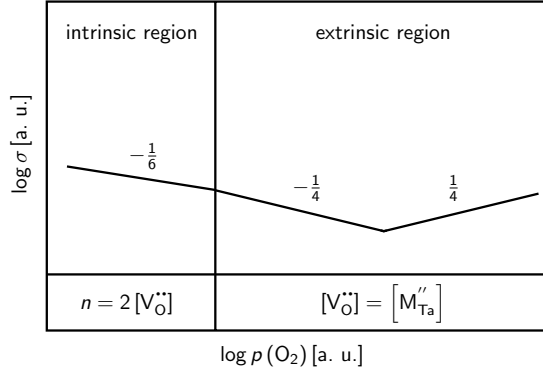
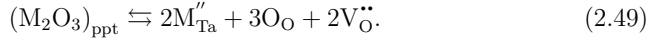


Figure 2.5: Schematic overview of the defect structure of Ta_2O_5 taking into account doping by impurities.

solubility of other oxides in $\text{Ta}_2\text{O}_{5-x}$ [51]. The first one is the dissociation, which was described by the following reaction



The second possible reaction of impurities with the $\text{Ta}_2\text{O}_{5-x}$ is the precipitation or dissolution, which can be described as follows.



It was shown by Dellis et al. [81] by impedance measurements that the concentration of impurities under certain temperature T_c is constant and above this temperature the concentration depends on the equilibrium of the precipitation-dissolution of impurities at grain boundaries. For T_c a temperature between 850° [80] and 860° [81] was reported. A schematic overview of the defect chemistry model in $\text{Ta}_2\text{O}_{5-x}$ is displayed in figure 2.5. The temperature dependence of the mobility of oxygen vacancies and electrons is given by [80]

$$\mu_{\text{V}_{\text{O}}^{\bullet\bullet}}(T) = \frac{6030}{T} \exp\left(-\frac{0.85 \text{ eV}}{k_B T}\right) \text{ cm}^2/\text{Vs} \quad (2.50)$$

$$\mu_e(T) = 0.075 \exp\left(-\frac{7.98 \cdot 10^{-2} \text{ eV}}{k_B T}\right) \text{ cm}^2/\text{Vs}. \quad (2.51)$$

In figure 2.6 the temperature dependence of electron and oxygen vacancy mobility is shown. The electron mobility slowly increases with rising temperature whereas the oxygen vacancy mobility strongly increased at higher temperatures.

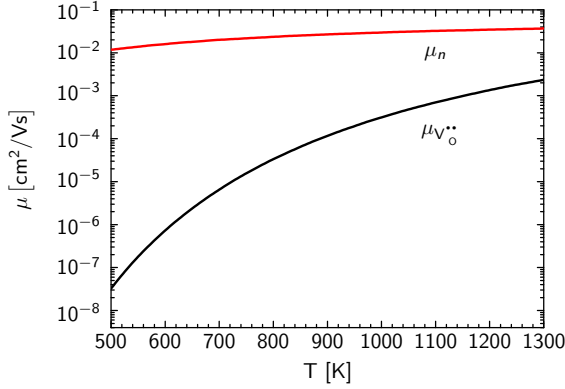


Figure 2.6: Temperature dependence of oxygen vacancy mobility and electrons in $\text{Ta}_2\text{O}_{5-x}$.

2.4 Diffusion in solids

As described in a previous chapter 2.1 for VCM cells the movement of oxygen vacancies plays an important role for the switching process in the filamentary region. It has been demonstrated that the non-linear voltage acceleration of the kinetics in the valence change based ReRAM cells is caused by the temperature activated exponential increase of the oxygen vacancy mobility [15]. Therefore, it is necessary to develop a better understanding of the diffusion process after the oxide has been set into a non-equilibrium state in order to verify simulation parameters. This process can be simulated with an abrupt change in the oxygen partial pressure in order to observe the diffusion processes during the equilibration of the surface.

2.4.1 Ideal step response

In an electronic conductivity relaxation (ECR) experiment the influence of the relation between stoichiometry and electrical conductivity is investigated. At the beginning of the experiment the sample is in equilibrium state in a defined atmosphere. If the oxygen activity changes the resistance of the sample relaxes to a new equilibrium state due to the release or incorporation of oxygen. The relaxation process is influenced by 1) the exchange process at the surface and 2) the diffusion

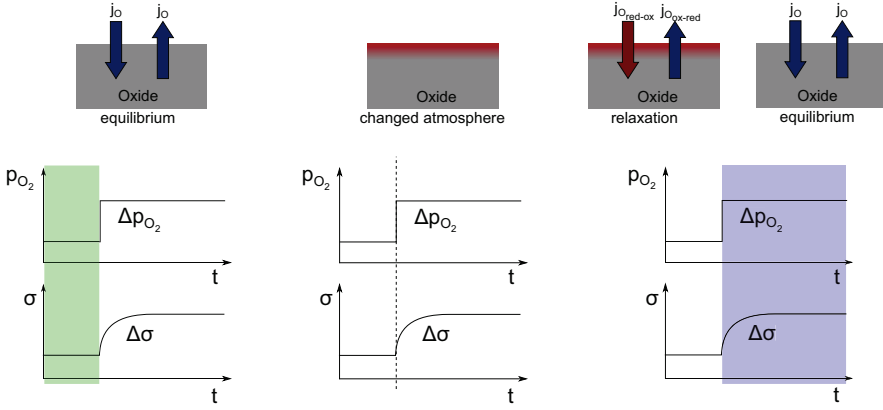


Figure 2.7: Schematic overview of the relaxation experiment.

through the solid. With Fick's first law the dependence of the particle flux to the local concentration gradient is described

$$j = -D_{\text{Chem}} \nabla c \quad (2.52)$$

where j is the particle flux density, D_{Chem} the chemical diffusion coefficient and c the concentration of oxygen. The continuity equation for the particle flux density leads to Fick's second law.

$$\frac{\partial c}{\partial t} = D_{\text{Chem}} \nabla^2 c \quad (2.53)$$

This equation can be solved in different ways, depending on the initial and boundary conditions. Here the solution for a sample with dimensions of $2l_x$, $2l_y$, $2l_z$ and the boundaries of $x = \pm l_x$, $y = \pm l_y$, $z = \pm l_z$ is presented. The change of oxygen concentration in the experiment is taken as instantaneous. It can be described by a Heaviside step function. The conditions for the flux density at the boundaries are the following:

$$-D_{\text{Chem}} \left. \frac{\partial c}{\partial x} \right|_{x=\pm l_x} = k_{\text{ex}} (c_{\infty} - c(t, x = \pm l_x, y, z)) \quad (2.54)$$

$$-D_{\text{Chem}} \left. \frac{\partial c}{\partial y} \right|_{y=\pm l_y} = k_{\text{ex}} (c_{\infty} - c(t, x, y = \pm l_y, z)) \quad (2.55)$$

$$-D_{\text{Chem}} \left. \frac{\partial c}{\partial z} \right|_{z=\pm l_z} = k_{\text{ex}} (c_{\infty} - c(t, x, y, z = \pm l_z)) \quad (2.56)$$

where k_{ex} is the surface transfer coefficient and c_∞ is the new concentration of oxygen after an infinite time in the new equilibrium state of the sample. The differential equation (2.53) can be solved with the Fourier method and the solution for the concentration, under the assumption that D_{Chem} is independent of c , is the following [82]:

$$\begin{aligned} \bar{c}(t) = \frac{c(x, t) - c_0}{c_\infty - c_0} = 1 - \sum_{i=1}^{\infty} \frac{2L_x \cos\left(\frac{\beta_i x}{l_x}\right)}{(\beta_i^2 + L_x^2 + L_x) \cos(\beta_i)} \exp\left(-\frac{t}{\tau_i}\right) \\ \cdot \sum_{j=1}^{\infty} \frac{2L_y \cos\left(\frac{\beta_j y}{l_y}\right)}{(\beta_j^2 + L_y^2 + L_y) \cos(\beta_j)} \exp\left(-\frac{t}{\tau_j}\right) \\ \cdot \sum_{k=1}^{\infty} \frac{2L_z \cos\left(\frac{\beta_k z}{l_z}\right)}{(\beta_k^2 + L_z^2 + L_z) \cos(\beta_k)} \exp\left(-\frac{t}{\tau_k}\right) \end{aligned} \quad (2.57)$$

with

$$\tau_i = \frac{l_x^2}{D_{\text{Chem}} \beta_i^2}; \tau_j = \frac{l_y^2}{D_{\text{Chem}} \beta_j^2}; \tau_k = \frac{l_z^2}{D_{\text{Chem}} \beta_k^2} \quad (2.58)$$

$$L_x = \frac{l_x k_{\text{ex}}}{D_{\text{Chem}}} = \beta_i \tan \beta_i; L_y = \frac{l_y k_{\text{ex}}}{D_{\text{Chem}}} = \beta_j \tan \beta_j; L_z = \frac{l_z k_{\text{ex}}}{D_{\text{Chem}}} = \beta_k \tan \beta_k. \quad (2.59)$$

The equations for the $\beta_{i,j,k}$ have to be solved numerically. The integration of equation (2.57) leads to the relative mass change during the relaxation process.

$$\bar{M} = \int_{-l_{x,y,z}}^{l_{x,y,z}} \bar{c}(\vec{x}, t) d\vec{x} = \frac{M(t) - M_0}{M_\infty - M_0} \quad (2.60)$$

$$\begin{aligned} = 1 - \sum_{i=1}^{\infty} \frac{2L_x^2}{\beta_i^2 (\beta_i^2 + L_x^2 + L_x)} \exp\left(-\frac{t}{\tau_i}\right) \\ \cdot \sum_{j=1}^{\infty} \frac{2L_y^2}{\beta_j^2 (\beta_j^2 + L_y^2 + L_y)} \exp\left(-\frac{t}{\tau_j}\right) \\ \cdot \sum_{k=1}^{\infty} \frac{2L_z^2}{\beta_k^2 (\beta_k^2 + L_z^2 + L_z)} \exp\left(-\frac{t}{\tau_k}\right) \end{aligned} \quad (2.61)$$

Due to the linear dependence between mass, particle number and conductivity the time dependent conductivity is given by [83]

$$\bar{M}(t) = \bar{N}(t) = \bar{\sigma}(t) = \frac{\sigma(t) - \sigma_0}{\sigma_\infty - \sigma_0}, \quad (2.62)$$

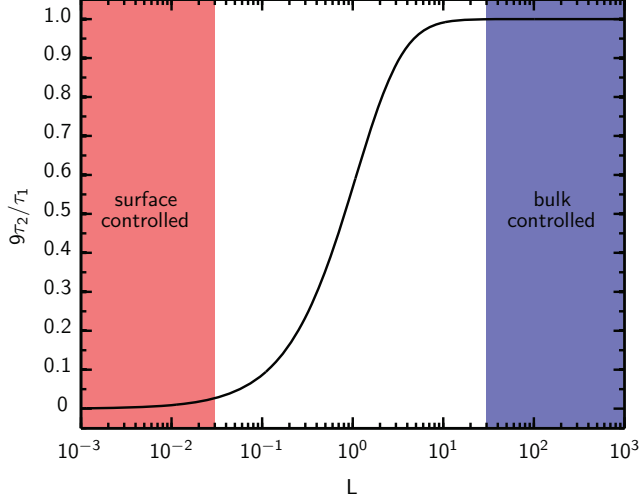


Figure 2.8: Ratio of time constants τ_1 and τ_2 in dependence of L .

where σ_0 is the equilibrium conductivity before the rapid oxygen partial pressure change and σ_∞ is the conductivity of the sample in the new equilibrium state. The diffusion process is usually defined by the three independent values k_{ex} , D_{Chem} and $l_{x,y,z}$. In one dimension it can be shown [84] that the diffusion parameters can be determined, taking equations 2.58 and 2.59 into account, with τ_1 , τ_2 and $l_{x,y,z}$. τ_1 and τ_2 are the first two solutions of equation 2.58.

In case that the chemical diffusion process is dominated by the surface exchange process ($D_{\text{Chem}} \gg k_{\text{ex}} l_{x,y,z}$), all terms of τ_i for $i \geq 2$ can be neglected. The time constants can be expressed as $\tau_1 = \frac{l_i}{k_{\text{ex}}}$ and $\tau_2 = 0$. In this case only one dimension (the shortest sample thickness) has to be taken into account, because the diffusion processes in the solid are very fast in comparison to the incorporation process. The solution for $\bar{\sigma}(t)$ and the conductivity can be simplified to:

$$\bar{\sigma}(t) = 1 - \exp\left(-\frac{k_{\text{ex}}}{l_x} t\right) \quad (2.63)$$

In opposite case where the bulk diffusion limits the diffusion process ($k_{\text{ex}} l_{x,y,z} \gg D_{\text{Chem}}$) the L diverges to infinity and the solution for the β_i is $((2i-1) \cdot \frac{\pi}{2})$, corresponding to $\tau_1 = \frac{4l_x^2}{\pi^2 D_{\text{Chem}}}$ and $\tau_2 = \frac{4l_x^2}{9\pi^2 D_{\text{Chem}}} = \frac{1}{9}\tau_1$. The solution for $\bar{\sigma}(t)$ and the conductivity can be simplified to:

$$\begin{aligned} \bar{\sigma}(t) = 1 - & \left(\frac{8}{\pi}\right)^3 \sum_{i=1}^{\infty} \frac{1}{(2i+1)^2} \exp\left(-\frac{(2i+1)^2 \pi^2 D_{\text{Chem}} t}{4l_x^2}\right) \\ & \cdot \sum_{j=1}^{\infty} \frac{1}{(2j+1)^2} \exp\left(-\frac{(2j+1)^2 \pi^2 D_{\text{Chem}} t}{4l_y^2}\right) \\ & \cdot \sum_{k=1}^{\infty} \frac{1}{(2k+1)^2} \exp\left(-\frac{(2k+1)^2 \pi^2 D_{\text{Chem}} t}{4l_z^2}\right) \end{aligned} \quad (2.64)$$

In figure 2.8 the dependence of the ratio $\frac{9\tau_2}{\tau_1}$ of L is displayed. It can be seen that for values smaller 0.03 the diffusion process is limited by the surface transfer reaction and above 30 only the bulk diffusion coefficient can be determined. In the intermediate regime both parameters D_{Chem} and k_{ex} influence the equilibration kinetic. It should be noted that this is a simplified contemplation, which takes only into account one dimension. In extreme cases of k_{ex} and similar lengths it would be difficult to evaluate the chemical diffusion coefficient D_{Chem} and the surface exchange coefficient k_{ex} simultaneously.

2.4.2 Non ideal step response

In the previous section the diffusion for an ideal oxygen partial pressure jump described by a step function was discussed. The solution of the differential equation gives the relation between surface exchange and bulk diffusion coefficient and the sample geometry. But this solution assumes that the surrounding gas ambient instantaneously changes from one oxygen activity to another one without a transition region. In this section the solution of Fick's equation for a non ideal oxygen jump is discussed. In the case of an ideal step response the dimensionless normalized pressure during gas exchange can be described by

$$\bar{p}_{\text{ideal}}(t) = \frac{p(t) - p_0}{p_{\infty} - p_0}. \quad (2.65)$$

The gas exchange in the measurement chamber takes a certain time. The cylindrical volume can be described as continuous ideally stirred-tank reactor (CISTR) [84], where the oxygen partial pressure change can be described as follows

$$\bar{p}_{\text{CISTR}}(t) = \frac{p(t) - p_{\infty}}{p_0 - p_{\infty}} = 1 - \frac{p(t) - p_0}{p_{\infty} - p_0} = \exp\left(-\frac{t}{\tau_f}\right). \quad (2.66)$$

A comparison with an ideal step is shown in figure 2.9 a) for a flushtime of six seconds. Hereby is τ_f the flushtime of the reactor volume, which characterizes the time, when a portion of $\frac{1}{e}$ of the gas in the reactor is exchanged. The flushtime can be expressed as

$$\tau_f = \frac{V_r}{\phi_V} \frac{T_{\text{STP}}}{T_r}. \quad (2.67)$$

V_r is the volume of the reactor, ϕ_V is the gas flux through the reactor, T_{STP} corresponds to the standard temperature (here $T_{\text{STP}} = 300$ K) and T_r is the reactor temperature. In the case of a non ideal step reaction the conductivity in the sample can be calculated by

$$\bar{\sigma}(t) = - \int_0^t \left[1 - \sum_{i,j,k=1}^{\infty} A_{i,j,k} \exp\left(-\frac{t}{\tau_{i,j,k}}\right) \right] \left[-\frac{t}{\tau_f} \exp\left(-\frac{t-\tau_f}{\tau_f}\right) \right] d\tau \quad (2.68)$$

with

$$A_{i,j,k} = \frac{2L_x^2}{\beta_i^2 (\beta_i^2 + L_x^2 + L_x)} \frac{2L_y^2}{\beta_j^2 (\beta_j^2 + L_y^2 + L_y)} \frac{2L_z^2}{\beta_k^2 (\beta_k^2 + L_z^2 + L_z)} \quad (2.69)$$

and

$$\tau_{i,j,k} = \frac{1}{D_{\text{Chem}}} \frac{1}{\left(\left(\frac{\beta_i}{l_x} \right)^2 + \left(\frac{\beta_j}{l_y} \right)^2 + \left(\frac{\beta_k}{l_z} \right)^2 \right)}. \quad (2.70)$$

Analytical integration leads to

$$\begin{aligned} \bar{\sigma}_{\text{CISTR}}(t) = & 1 - \exp\left(-\frac{t}{\tau_f}\right) \\ & - \sum_{i,j,k=1}^{\infty} A_{i,j,k} \frac{\tau_{i,j,k}}{\tau_{i,j,k} - \tau_f} \left[\exp\left(-\frac{t}{\tau_{i,j,k}}\right) - \exp\left(-\frac{t}{\tau_f}\right) \right]. \end{aligned} \quad (2.71)$$

In figure 2.9 b) the relaxation curves are shown for different values of L and τ_f . For small values of the flushtime the resulting curve is only affected a little bit. But as can be seen already with a flushtime of 10 s the conductivity relaxation behavior is significantly affected. Therefore it is important to note that the flushtime should be considered during the calculation of diffusion coefficients.

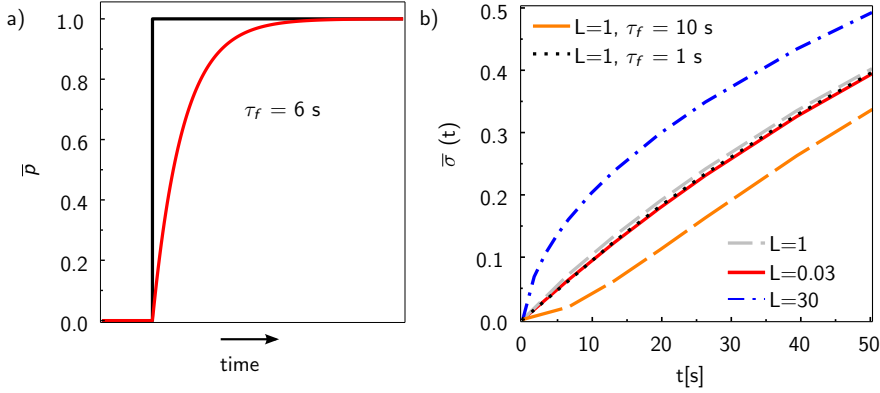


Figure 2.9: a) Time development of an ideal oxygen partial pressure jump (black) and with a reactor flushtime of six seconds (blue). b) Theoretical relaxation curves for different L and flushtimes.

2.4.3 Chemical diffusion in TiO_{2-x}

As mentioned in the HTEC section during this work the defect chemistry of TiO_{2-x} will be studied and in addition also the kinetics of this material will be investigated. This work will focus on the chemical diffusion in TiO_{2-x} . During chemical diffusion a change in the oxygen partial pressure induces a chemical potential gradient to the system. And the solid reacts with a relaxation reaction, where depending on the direction of the pressure jump usually oxygen is incorporated or released from the solid. At the beginning it is necessary that the oxygen diffuses from the ambient gas phase to the solid surface. This process is very fast and can be neglected in comparison to the other processes [85]. Afterwards the oxygen absorbs on the surface and the chemisorption process starts [86], where the following processes takes place



It is still under debate whether incorporation process of oxygen into the bulk is with the assistance of oxygen vacancies or titanium interstitials. As already mentioned in the defect chemistry section the point defects, which occur in TiO_{2-x} strongly depend on temperature and oxygen partial pressure. In the case that oxygen is

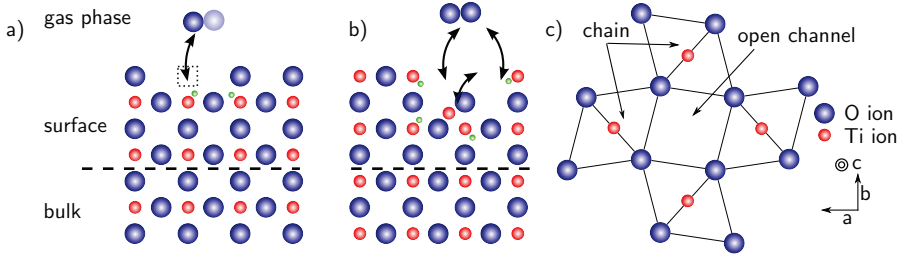
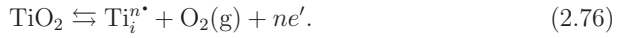


Figure 2.10: Scheme of chemisorption at the rutile surface with assistance of surface a) oxygen vacancies (blue) or b) titanium interstitials (red) after creation of electrons (green). c) Top view of rutile, where it is shown that perpendicular to the *c*-axis there is an open channel, which acts as diffusion path, whereas the diffusion parallel to *c* is slower for oxygen vacancies and titanium interstitials.

incorporated into the solid via an oxygen vacancy the following reactions takes place [87–89]



A schematic scheme of this process is shown in figure 2.10 a). Some reports in literature also observe incorporation/release via titanium interstitial (possible are trivalent or a tetravalent interstitials (cf. figure 2.10 b)), which is described by



The localization of the electrons arising during the reduction process is still under debate. Calculations have predicted that they are completely free in the conduction band, while more recent work finds localized states associated with the five fold surface-coordinate titanium and defect site [90–92].

The self-diffusion in TiO_{2-x} has been studied extensively in the past [93–96]. It was reported for tracer diffusion experiments that titanium diffuses via the interstitialcy mechanism [97]. Additionally an anisotropy for the self diffusion process was reported, which becomes more pronounced with decreasing temperature. The diffusion perpendicular to the *c*-axis is faster than parallel to the *c*-axis [96] due to open channels in the rutile structure (cf. figure 2.10 c)). Moreover, a decrease of oxygen activity leads to an increased titanium self-diffusion. The self-diffusion of oxygen takes place via the vacancy mechanism due to the large size of the oxygen vacancies [98]. The diffusion was enhanced perpendicular to the *c*-axis and

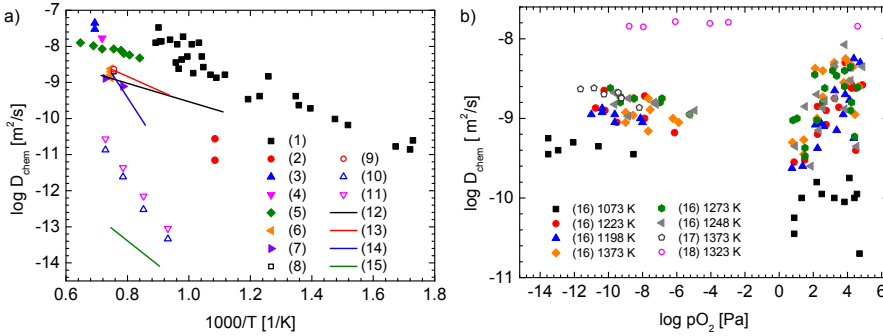


Figure 2.11: a) Temperature and b) oxygen partial pressure dependence of the chemical diffusion coefficient reported in literature. ((1) Barbanell et al. [104], (2) Moser et al. [105], (3) Crosbie [106], (4) Morin [107], (5) Baumard [99], (6) Ait-Younes et al. [100], (7) Lee et al. [69], (8) Millot [108] ($\parallel c$ -axis), (9) Millot [108] ($\perp c$ -axis), (10) Iguchi et al. [98] ($\perp c$ -axis), (11) Iguchi et al. [98] ($\parallel c$ -axis), (12) Radecka et al. [109], (13) Nowotny et al. [102] (rutile sc, 10^{-9} Pa), (14) Nowotny et al. [110] (polycrystalline, 10^{-9} Pa), (15) Nowotny et al. [102] (rutile sc, 75 kPa), (16) Nowotny et al. [102], (17) Ait-Younes et al. [100], (18) Morin [107]).

slower for parallel motion to c -axis. Bagshaw et al. [94] demonstrate for rutile Magnéli ($\text{Ti}_n\text{O}_{2n-1}$) phases that the diffusion coefficients are lower in comparison to nearly stoichiometric rutile. The transport of titanium interstitials in rutile is two orders of magnitude faster than for oxygen due to the different diffusion mechanisms [97, 98].

After a small change of oxygen activity the fast defects (oxygen vacancies/titanium interstitials) are predominant in the relaxation process in TiO_{2-x} [66, 99, 100], resulting in a new equilibrium state. The bulk diffusion coefficient D_{Chem} depends on the oxygen partial pressure. A maximum of the chemical diffusion coefficient D_{Chem} has been reported for the n - p -transition [101, 102] (cf. figure 2.11 a)). For reducing oxygen partial pressure conditions D_{Chem} seems to increase. In the case of high oxygen activities a slow relaxation process was reported via titanium vacancies [102]. Lee et al. [69] reported for reducing oxygen activity that the equilibration is dominated by a surface exchange process and bulk diffusion. For higher oxygen partial pressures they reported a heterogeneous process, where the diffusion in anion and cation sub-lattice is governed by different bulk diffusion coefficients. An overview of literature values of D_{Chem} in dependence on temperature is given in figure 2.11 b). For thin layers a surface exchange dominated equilibration kinetic was reported [103].

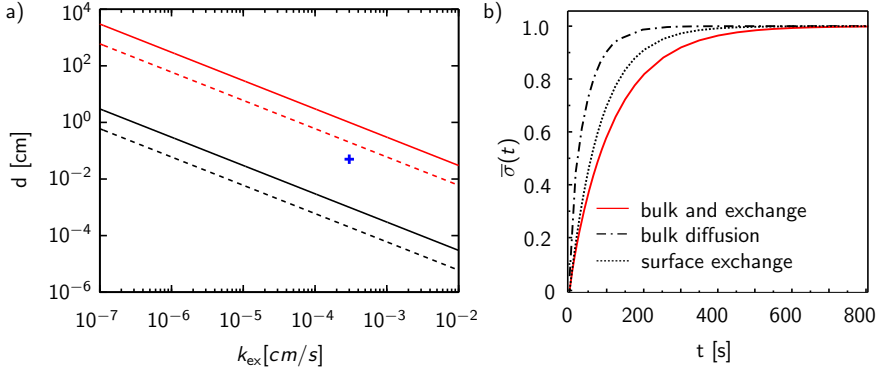


Figure 2.12: a) Critical film thickness in dependence on surface exchange coefficient assuming a fixed value for the chemical diffusion coefficient. For low oxygen activity a value of $D_{\text{chem,red}} \approx 5 \cdot 10^{-5} \text{ cm}^2/\text{s}$ (solid lines) and for high oxygen activity a $D_{\text{chem,ox}} \approx 5 \cdot 10^{-6} \text{ cm}^2/\text{s}$ (dashed lines) is used. The red curve marks the region, where the chemical diffusion dominates the relaxation process and the black line marks the region of surface exchange process domination. The chemical diffusion coefficients are measured at a temperature of approximately 1000 K [66]. The blue cross marks the position of a sample with 0.05 cm thickness and a surface exchange coefficient of $k_{\text{ex}} = 3 \cdot 10^{-4} \text{ cm/s}$, where the relaxation process is dominated by the surface exchange process and chemical diffusion. b) Theoretical relaxation curves for a sample with sizes $0.05 \times 0.5 \times 1.0 \text{ cm}^3$ and a chemical diffusion coefficient $D_{\text{Chem}} \approx 5 \cdot 10^{-6} \text{ cm}^2/\text{s}$ and surface exchange coefficient $k_{\text{ex}} \approx 3 \cdot 10^{-4} \text{ cm/s}$.

Finally the critical film thickness for pure bulk limited or surface limited process as rate limiting step is estimated based on the published literature values. The equilibration process is defined by the three independent parameters D_{Chem} , k_{ex} and $l = \frac{d}{2}$ (cf. section 2.4.1). It was shown that for $0.03 \leq L \leq 30$ the equilibration is influenced by both processes and D_{Chem} and k_{ex} can be determined simultaneously. Given the known value of D_{Chem} for oxidation and reduction of TiO_{2-x} , one can estimate with equation (2.59) the film thickness for which $0.03 \leq L \leq 30$ is fulfilled, assuming different values for k_{ex} . In figure 2.12 a) the critical film thickness for chemical diffusion coefficients $D_{\text{chem,red}} \approx 5 \cdot 10^{-5} \text{ cm}^2/\text{s}$ and $D_{\text{chem,ox}} \approx 5 \cdot 10^{-6} \text{ cm}^2/\text{s}$ was determined for different surface exchange coefficients. The chemical diffusions coefficients are extracted from a previous report [66] at a temperature of 1000 K. Above the red line the process is purely dominated by bulk diffusion and below the black line the process is only dominated by the surface exchange process. For

a sample with a thickness of 0.05 cm the relaxation process is dominated by bulk diffusion and the surface exchange process if the surface exchange coefficient is in the range of $k_{\text{ex}} \approx 3 \cdot 10^{-4} \text{ cm/s}$.

In figure 2.12 b) the theoretical relaxation curves for pure bulk diffusion, surface exchange and the transition regime are shown for a sample with dimensions $0.05 \times 0.5 \times 1.0 \text{ cm}^3$ (these are the sample dimensions used in this study). Here, fixed values for $D_{\text{Chem}} \approx 5 \cdot 10^{-6} \text{ cm}^2/\text{s}$ and $k_{\text{ex}} \approx 3 \cdot 10^{-4} \text{ cm/s}$ were used. There is a clear difference visible between the three different curves and neither the bulk nor surface curves overlap with the theoretical curve containing both processes. The relaxation process in the transition region is the slowest, whereas the other processes equilibrate faster. In the transition regime none of the processes have a negligible speed, therefore during the incorporation or release of oxygen the surface exchange process and the bulk diffusion are connected in series. This results in a longer relaxation time than for each individual single process. Therefore, for the later analysis the full equation (2.71) was used for the determination of the diffusion coefficients, since it is not clear in which regime the diffusion takes place.

3 Experimental methods

3.1 DC magnetron sputter deposition

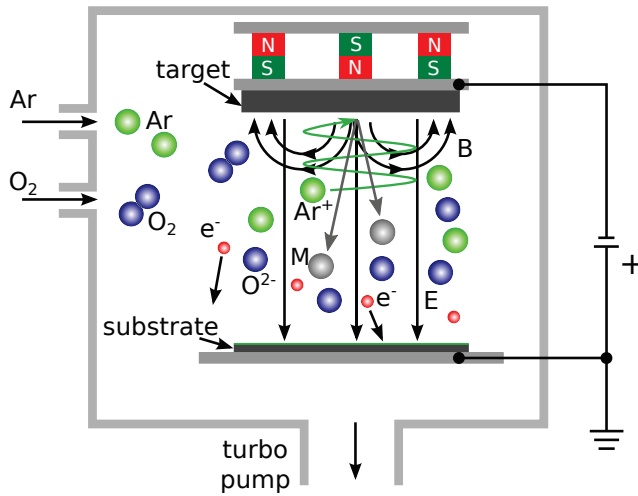


Figure 3.1: Principle scheme of a magnetron.

DC magnetron sputter deposition is a physical vapor deposition method. A principle scheme of a magnetron sputter tool is shown in figure 3.1. It consists of a sputter target, usually a metallic target, and a substrate mounted on the opposite position. During the deposition process argon gas is let in into the chamber and a high voltage is applied between substrate and target, which ignites a charge neutral plasma. Due to the electrical field the argon ions are accelerated to the target and collide with the target atoms. The released atoms move towards the substrate and can adsorb on the surface. If the process gas is pure argon a metallic film is deposited on the sample surface. A magnetic field which is caused by a permanent magnet on the backside of the target increases the sputtering rate. The use of reactive gases such like oxygen or nitrogen during reactive sputtering leads to the formation of metal oxide or nitrides during sputtering.

In this work a UHV sputter tool was used with four magnetrons. The base pressure of the chamber is $5 \cdot 10^{-9}$ mbar. As process gases argon and oxygen were used. The oxygen to argon flow ratio in the system is set by mass flow controllers. The flow of the two gases is adjusted by a proportional-integral-derivative (PID) controller. During deposition a constant process pressure is present in the sputtering chamber. The deposition parameters are listed in the appendix A.1.

3.2 Atomic force microscopy (AFM)

The surface morphology of a sample can be studied with atomic force microscopy (AFM), which typically consists of a cantilever with a tip. The tip is moved across the sample in order to get a microscopic image of the sample surface. The microscopic image is obtained from the topographic information of the individual measured points. Two operation modes were used in this work, namely the tapping mode and the contact mode. The topography of the pristine sample is measured under ambient conditions with the tapping mode. During this measurement mode the cantilever is excited with a fixed frequency near the resonance frequency of the cantilever. The forces between the tip of the cantilever and the sample surface change the resonance frequency of the system, which results in a phase change of the exciting amplitude. The oscillation amplitude is used as a control signal during the measurement of the sample surface. With a control loop the oscillation amplitude is kept constant by adjusting the distance of cantilever tip and sample surface. This results in a change in force interaction between tip and sample surface. For each scanned position the control loop signal is stored which gives microscopic information about the surface morphology. The other operating mode, which is used in this thesis, is the contact mode. The tip has in this measurement mode a direct mechanical contact with the sample surface. This creates a strong electrostatic repulsion between the electron shells of the sample surface and the probing tip, respectively. Analogous to the tapping mode a control loop keeps the deflection of the cantilever constant. From the feed back signal information about the surface morphology can be generated. In this operation mode it is also possible to measure the local conductivity of the sample by using a conductive tip. The local conductivity is measured by applying a constant voltage to the tip. During scanning across the sample the current is monitored and the resulting image gives information about the local conductivity.

The topography measurements were conducted with a *Cypher Atomic Force Microscope* from *Asylum Research* operated in tapping mode. The combined AFM/LC-AFM measurements were performed using an *Omicron VT-SPM* system by *Omicron Nano Technology GmbH* operating at room temperature under UHV condi-

tions. The detection of the local surface conductance was achieved by the use of silicon cantilevers with a boron doped polycrystalline diamond coating.

3.3 X-ray photoelectron spectroscopy (XPS)

X-ray photoelectron spectroscopy (XPS) is based on the photoelectric effect and is a surface sensitive measurement tool [111, 112]. A depiction of the basic working principle is given in figure 3.2 a). The sample is irradiated with monochromatic photons which excite electrons in the sample. The binding energy of the excited electrons can be calculated by

$$E_{bin} = h\nu - E_{kin} - \phi \quad (3.1)$$

with E_{bin} as binding energy, $h\nu$ the photon energy, E_{kin} the kinetic energy and ϕ the work function of the material. The binding energy is an element specific parameter, which makes XPS to an element sensitive analysis tool. In figure 3.2 b) the density of states of the electrons is schematically shown as a function of energy. It can be distinguished between two states in the solid. The first ones are the core levels with a discrete energy and the second one is the valence band. The valence electrons have a continuous energy distribution. The upper limit of the valence band is the Fermi energy E_F . The core level electrons have a higher binding energy than those in the valence band. For the photoelectron emission spectrum the number of the emitted electrons are measured as a function of their kinetic energy E_{kin} . The resulting spectrum is also displayed in figure 3.2 b). The core level states at low kinetic energy and the valence band at a high kinetic energy can be identified. The Fermi-edge as the upper limit of the valence band is not sharply defined in the spectrum due to the limited resolution of the measurement setup and due to thermal excitations in the solid.

The kinetic energy of the emitted electrons depends not only on the element specific binding energy of the electron in the atom, it is also influenced by the chemical bonds with the neighboring atoms [113]. The binding energy of a cation excited from a metal oxide has a higher binding/lower kinetic energy compared to the metal compound due to a stronger bound of the cations in the metal oxide. In figure 3.3 a) a Ti 2p spectra from a metallic titanium and a titanium oxide film are shown. It is clearly visible that the binding energy for the electrons excited in the metallic film is lower than for those who are excited from the oxide film. This makes photoelectron spectroscopy to a valence state sensitive measurement tool.

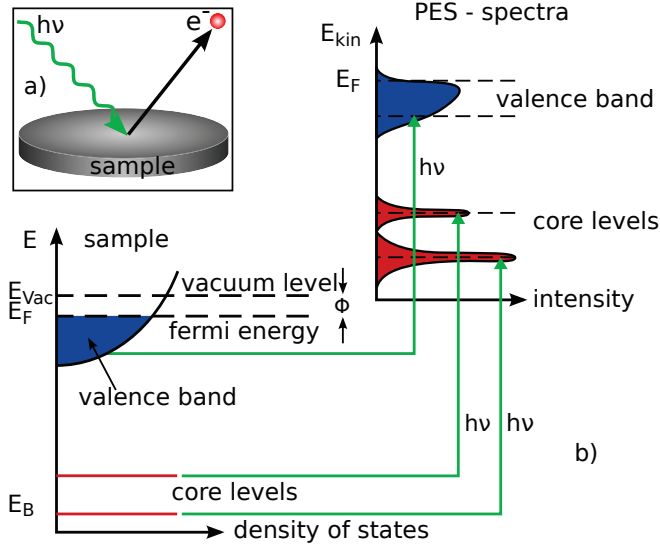


Figure 3.2: Principle scheme of photoelectron spectroscopy a) X-ray irradiates the sample's surface and photoelectrons exit the sample's surface. b) Overview of density of states in a solid and the resulting photoelectron spectroscopy.

Another important factor in photoelectron spectroscopy is the inelastic mean free path λ of the electrons [114], which is defined as the distance over which the numbers of non-scattered electrons is reduced to $\frac{1}{e}$. The escape depth of the electrons is limited by inelastic scattering processes. The escape depth depends strongly on the kinetic energy of the electrons. This determines from which sample depth electrons can escape into vacuum. An overview of the electron mean free path in dependence of the kinetic energy is given in figure 3.3 b). The inelastic mean free path is usually in the range of a few nanometer, which makes XPS a surface sensitive method. Measurements with a detection angle of $\theta = 90^\circ$ (normal emission) have the maximum intensity from the bulk, whereas lower detection angles enhances the measurement of the surface layer.

If the XPS measurement is carried out with an X-ray source having a constant flux, it is also possible to determine the stoichiometry. The stoichiometry of the material can be calculated by the integration of the peak area. As the photoionization cross-sections is different for the elements and core levels, it is necessary to take this into account with the so-called relative sensitivity factors (RSF). Furthermore, knowledge of the sample geometry and the transmission function of the spectrometer is

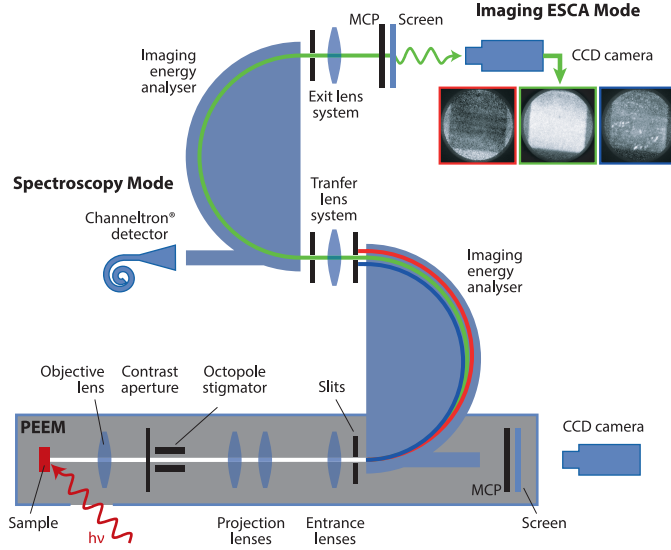


Figure 3.4: Schematic overview of a photoemission electron microscope used in this work (*NanoEsca*, from *Omicron NanoTechnology GmbH*) [117]. In the lower part of the tool the electrons are mapped by electrostatic lenses. The two hemispherical analyzers enables recording of aberration corrected photoemission spectra.

intensity in dependence of the kinetic energy. In a photoemission electron microscope the core level spectra are taken by measuring the lateral intensity distribution of the photoelectrons for a certain energy. In order to determine core level spectra an image stack over a range of kinetic energies is taken. The core level spectra can be extracted from this image stack by integration over the photoelectron intensity at a certain position/pixel of the image.

In addition to the core level spectra it is also possible to measure the work function of the sample surface. The work function is defined as secondary electron cut-off of the threshold spectra in relation to the Fermi level (E_F). The total intensity of the secondary electrons is high, which enables measurements with low integration times and higher lateral resolution. The work function can be therefore used for identification of morphological changes and navigation on the surface due to the low integration times.

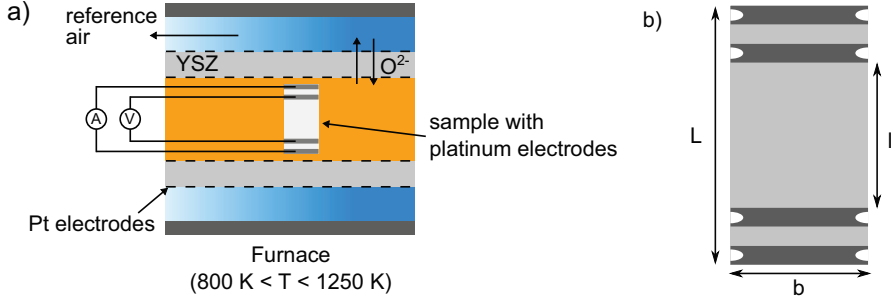


Figure 3.5: a) Scheme of a HTEC setup. b) Depiction of the sample dimension for HTEC measurements.

3.5 High temperature equilibrium conductance (HTEC) measurements

In this thesis the high temperature equilibrium conductivity (HTEC) of TiO_{2-x} and $\text{Ta}_2\text{O}_{5-x}$ will be investigated in dependence on the oxygen partial pressure. With this measurement setup the dominant point defects in the material can be determined in dependence on oxygen partial pressure and temperature. Furthermore, the activation energy which is necessary for the formation of a point defect such like oxygen vacancies can be determined. A schematic illustration of the measurement setup is shown in figure 3.5 a). A detailed description of the measurement setup is given in reference [122]. The HTEC setup consists of a furnace, which provides temperatures in the range of 800 K to 1250 K. Inside the furnace an yttrium stabilized zirconium oxide (YSZ) tube is located, which acts as an oxygen pump. The sample and the electrical contacts are located inside this tube. By using a YSZ oxygen pump it is possible to continuously adjust the oxygen partial pressure in a range of 1 bar to 10^{-23} bar. The working principle of the YSZ oxygen pump will be explained in the following.

The YSZ oxygen pump system

In a temperature regime above 700 K YSZ is an oxygen ion conductor. If the oxygen partial pressure at the outside ($p_{\text{O}_2}^{\text{out}}$) differs from the one in the inside ($p_{\text{O}_2}^{\text{in}}$) of the tube oxygen is moving through the YSZ in order to reach a new equilibrium. Due to the ionic current between inside and outside of the YSZ tube

a voltage gradient arises. The voltage can be calculated by the Nernst equation

$$U_N = \frac{k_B T}{4e} \ln \left(\frac{p_{\text{O}_2}^{\text{out}}}{p_{\text{O}_2}^{\text{in}}} \right), \quad (3.2)$$

where e is the elementary charge, k_B is the Boltzmann constant and T is the temperature. In the measurement setup at the outside of the YSZ tube a constant air flow is provided ($p_{\text{O}_2}^{\text{out}} = 0.2064$ bar) and thus the oxygen partial pressure inside the tube can be calculated by

$$p_{\text{O}_2}^{\text{in}} = 0.2064 \text{ bar} \cdot \exp \left(-46.42 \text{ K/mV} \cdot \frac{U_N}{T} \right). \quad (3.3)$$

With this the actual oxygen partial pressure inside the tube can be determined. Furthermore, it is also possible to control the oxygen partial pressure by the above described principle. For this purpose, two additional electrodes are attached to the YSZ tube. By applying a certain voltage to this electrodes oxygen can be pumped in or out from the system. With a second pair of electrodes (the sense electrodes) the actual oxygen partial pressure can be measured. A control loop regulates the voltage at the pump electrode so that there is a constant voltage drop at the sensor electrodes. This allows the continuous adjustment of the oxygen partial pressure in the measurement setup.

Sample design

Rectangular shaped samples with four contact geometry with a contact width of $800 \mu\text{m}$ were used for the measurements (cf. figure 3.5 b)). A current was applied to the outer contacts and the voltage was measured at the inner contacts. The specific electrical resistance ρ for a resistor with a uniform cross-section is defined as

$$\rho = R \cdot \frac{bd}{l} \quad (3.4)$$

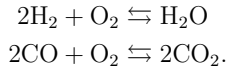
where R is the measured electrical resistance, b the width of the sample, l the distance between the inner contacts (in this study 5 mm) and d the sample thickness. The corresponding conductivity can be determined as follows

$$G \equiv \frac{1}{R_S} = \frac{1}{\rho} \frac{bd}{l} = \sigma \frac{bd}{l}. \quad (3.5)$$

The electrical contact was provided by sputtered platinum electrodes with a thickness of 250 nm and wound platinum wires around the contacts. In order to fix these wires small slits were cut into the site of the contacts.

Titration effects

Due to unavoidable oxygen leakage and residual gases in the measurement setup an oxygen partial pressure gradient arises in the intermediate oxygen partial pressure regime 10^{-6} – 10^{-12} bar and at temperatures lower than approximately 950 K [123, 124]. The oxygen gradient is attributed to the following residual gas reaction



The sense electrodes of the measurement setup have a slightly different position compared to the sample, therefore the actual oxygen partial pressure at the sample may be different in comparison to the measured value at the sense electrode. In reference [124] it has been demonstrated with a reference λ sensor at the same position as the sample that the oxygen partial pressure differs in the intermediate oxygen partial pressure regime and for low temperatures from the sense electrode values. For the high temperature equilibrium conductance characteristics the oxygen partial pressure values measured at the sample position will be used instead of the sense electrode value.

3.6 Electronic conductivity relaxation (ECR) measurements

After a sudden change of the oxygen ambient, an initially equilibrated metal oxide sample changes the conductivity until a new equilibrium state is reached. With this kind of experiment it can be analyzed whether the relaxation is dominated by the surface exchange process or by bulk diffusion. Furthermore, the activation energy for the dominating relaxation process can be determined. For the bulk diffusion the activation energy is correlated to the energy barrier for the defect motion. The activation energy for the surface exchange process is the sum of all processes involved in the incorporation or release of oxygen. The relaxation process is schematically illustrated in figure 3.6. This kinetic process can be studied by a so called ECR experiment where the conductance of the metal oxide is studied in dependence on the time after a rapid change of the oxygen partial pressure. The oxygen ambient exchange within the chamber should be as fast as possible.

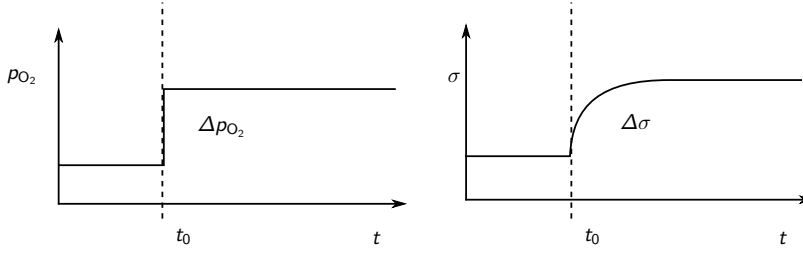


Figure 3.6: A rapid change of the oxygen partial pressure in the surrounding atmosphere leads to a change in electrical conductivity in a metal oxide, which is initially in equilibrium.

Therefore, a YSZ oxygen pump is unsuitable for this experiment, since the time required for the adjustment of the oxygen partial pressure is too large. A good way to adjust the oxygen partial pressure and to switch between two different atmospheres, is the use of gas mixtures. In the oxidizing atmosphere it can be realized by argon/oxygen mixtures and the reducing oxygen partial pressure can be adjusted by a hydrogen/argon mixture. The gases are saturated with water vapor. An overview of the oxygen partial pressure regime, which can be achieved by these gas mixtures is given in figure 3.7. As can be seen, the oxygen atmosphere can not be adjusted continuously by gas mixtures. The gap between oxidizing and reducing regime shrinks with increasing temperature.

A schematic illustration of the measurement setup is given in figure 3.8. The ECR setup consists of a furnace which provides temperatures up to 1473 K. Inside the furnace there is an alumina tube, in which the sample holder is located. The construction of the holder is based on the HTEC experiment. The sample is located in the front part of the sample holder, which is a separated volume with cylindrical shape. The gas flows from the entrance of this small volume to the outer part. The electrical conductance is measured with a four probe setup. At the outer electrodes a constant current is applied and at the inner electrodes the voltage is measured in dependence on time. The electrical probes are shielded by platinized alumina tubes. The actual temperature of the probe volume is measured by a thermocouple.

The gas for the adjustment of the different oxygen partial pressures is provided by two gas pipelines. The gas mixture is controlled by two mass flow controllers for each pipeline. The gas mixture can be chosen with a valve by switching back or forth. In this thesis argon/hydrogen mixtures are used for the reducing atmosphere. The gases are saturated with water by gas flowing through washing bottles. The water has a temperature of 273 K, which is achieved by the use of ice water. The

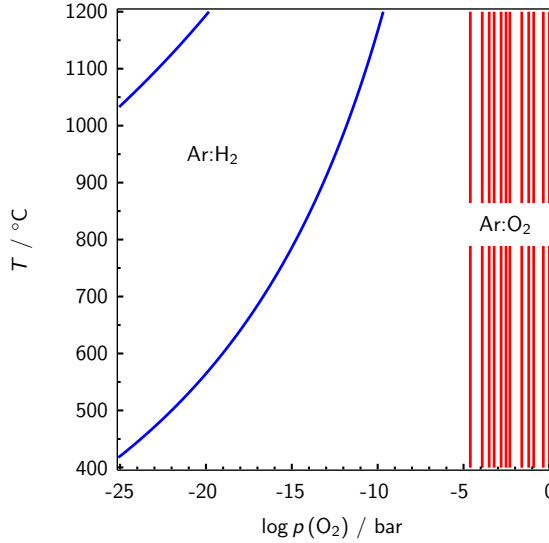
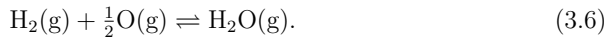


Figure 3.7: Feasible pressures for different gas mixtures. In the reducing regime the pressures are determined by the law of mass action for reaction (3.6) and in the oxidizing regime the pressures are calculated for different argon to oxygen flow ratios.

gases are flowing from the sample volume in the front to the exhaust, where the oxygen partial pressure is measured by a λ sensor. The sensor has an operation temperature of 1023 K. The oxygen ambient in this partial pressure region is dominated by the following reaction



The reaction equilibrium depends on temperature, so that the measured oxygen partial pressure in the sensor does not correspond to the oxygen partial pressure in the probe volume, which may have a different temperature. With the law of mass action and the oxygen partial pressure of the sensor, the oxygen pressure in the chamber can be calculated. The law of mass action for the gas reaction can be described by

$$K_{\text{H}_2\text{O}}(T) = \frac{p_{\text{H}_2\text{O}}(T)}{p_{\text{H}_2}(T)\sqrt{p_{\text{O}_2}}(T)} = K_{\text{H}_2\text{O}} \exp\left(-\frac{\Delta G_{\text{H}_2\text{O}}}{RT}\right). \quad (3.7)$$

The equilibrium constant for the reaction between hydrogen, oxygen and gaseous water is temperature dependent. $\Delta G_{\text{H}_2\text{O}}$ is the standard Gibb's free energy for

the formation of water and R is the ideal gas constant. In reference [125] some values for the reaction constants at certain temperatures are listed. The values for a temperature range of 700–1400 K are given in table 3.1. For temperatures

T [K]	log $K_{\text{H}_2\text{O}}$
700	15.588
800	13.293
900	11.503
1000	10.066
1100	8.888
1200	7.904
1300	7.069
1400	6.325

Table 3.1: Literature data for reaction constant log $K_{\text{H}_2\text{O}}$ [125].

which are not listed in the table the data were interpolated with a third-degree polynomial, which will be used for the calculation of the oxygen partial pressure in the sample volume.

$$\log K_{\text{H}_2\text{O}}(T) = (49.922 - 0.079 \cdot T + 5.208 \cdot 10^{-5} \cdot T^2 - 1.261 \cdot 10^{-8} \cdot T^3) \cdot \text{bar}^{-\frac{1}{2}} \quad (3.8)$$

The oxygen partial pressure in the λ sensor for a temperature of 750 °C is calculated by

$$p_{\text{O}_2}^{\text{in}} = 0.2064 \text{ bar} \cdot \exp \left(-46.42 \text{ K/mV} \cdot \frac{U_N}{T} \right). \quad (3.9)$$

The impurity concentration of hydrogen is neglected for the calculation, because the amount is small in comparison to the hydrogen generated by reaction 3.6. The partial pressure of hydrogen at $T = 750$ °C is set equal to Δx .

$$p_{\text{H}_2}(T_{\text{sensor}}) = \Delta x \quad (3.10)$$

The partial pressure of water can thus be expressed as follows

$$p_{\text{H}_2\text{O}}(T_{\text{sensor}}) = p_{\text{H}_2\text{O}}(T_{\text{waterbath}}) - \Delta x, \quad (3.11)$$

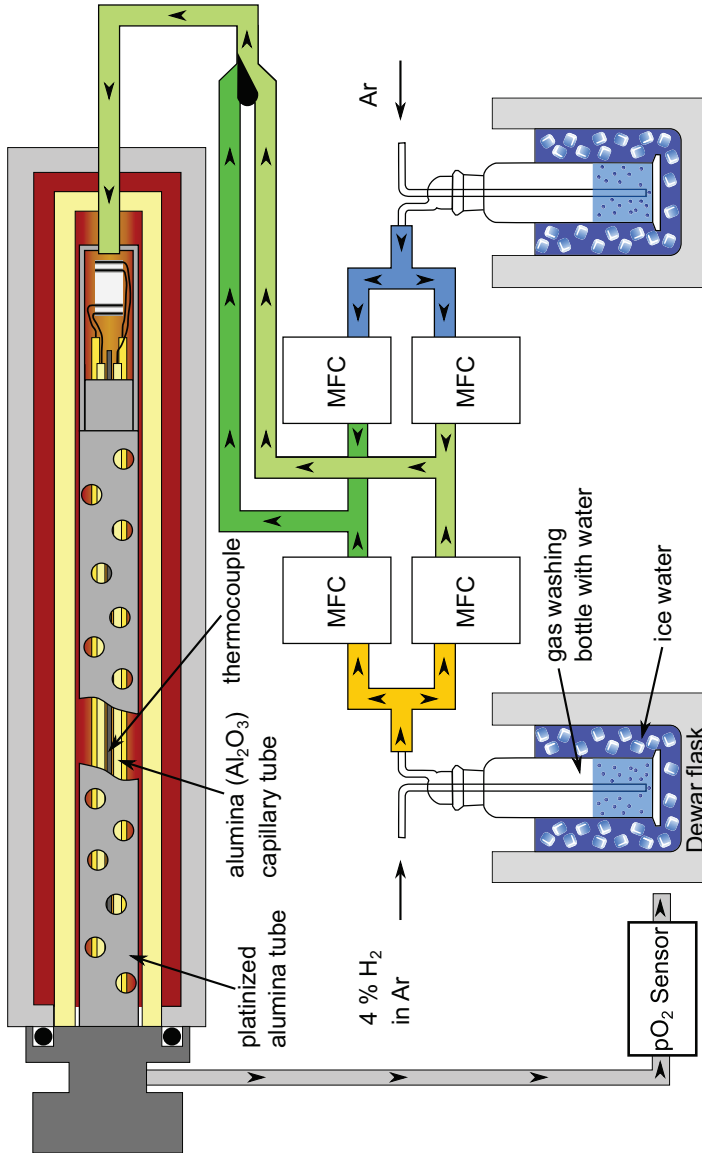


Figure 3.8: Scheme of electrical conductance relaxation setup.

3 Experimental methods

where $p_{\text{H}_2\text{O}}(T_{\text{waterbath}})$ is the water vapor pressure for the temperature of the water bath. The water gas equilibrium constant for the sensor temperature can be calculated by

$$K_{\text{H}_2\text{O}}(T_{\text{sensor}}) = \frac{p_{\text{H}_2\text{O}}(T_{\text{sensor}})}{p_{\text{H}_2}(T_{\text{sensor}})\sqrt{p_{\text{O}_2}(T_{\text{sensor}})}} \quad (3.12)$$

$$= \frac{p_{\text{H}_2\text{O}}(T_{\text{waterbath}}) - \Delta x}{\Delta x \sqrt{p_{\text{O}_2}(T_{\text{sensor}})}}. \quad (3.13)$$

By solving equation (3.13), the partial pressure of hydrogen at the sensor temperature can be determined. Since the temperature in the furnace is not equal to that of the sensor, a new reaction equilibrium must be considered here. The partial pressures at temperature T can be expressed as a function of the determined values for $T = 750$ °C.

$$p_{\text{H}_2\text{O}}(T) = p_{\text{H}_2\text{O}}(T_{\text{sensor}}) - \Delta y \quad (3.14)$$

$$p_{\text{H}_2}(T) = p_{\text{H}_2}(T_{\text{sensor}}) + \Delta y \quad (3.15)$$

$$p_{\text{O}_2}(T) = p_{\text{O}_2}(T_{\text{sensor}}) + \frac{1}{2}\Delta y \quad (3.16)$$

Δy describes the portion by which the reaction equilibrium is shifted in relation to the one at $T = 750$ °C. The equilibrium constant can be expressed by

$$K_{\text{H}_2\text{O}}(T) = \frac{p_{\text{H}_2\text{O}}(T)}{p_{\text{H}_2}(T)\sqrt{p_{\text{O}_2}(T)}} \quad (3.17)$$

$$= \frac{p_{\text{H}_2\text{O}}(T_{\text{sensor}}) - \Delta y}{(p_{\text{H}_2}(T_{\text{sensor}}) + \Delta y) \sqrt{p_{\text{O}_2}(T_{\text{sensor}}) + \frac{1}{2}\Delta y}}. \quad (3.18)$$

By solving this cubic equation Δy can be determined by using the calculated values of Δx , $p_{\text{H}_2}(T_{\text{sensor}})$, $p_{\text{O}_2}(T_{\text{sensor}})$ and $p_{\text{H}_2\text{O}}(T_{\text{sensor}})$. An increase of temperature in comparison to the sensor temperature leads to a shift of the reaction equilibrium to oxygen and hydrogen, since equation (3.6) describes an exothermic reaction. The oxygen partial pressure in the sample volume is increased in comparison to the pressure determined in the oxygen sensor. For lower temperatures, the reaction is shifted to the right side of equation (3.6), which results in lower oxygen partial pressure than the values measured with the oxygen sensor.

4 Growth and characterization of thin oxide films

Later on in this study the memristive devices will be studied by spectromicroscopy in order to find out where the switching-induced redox reaction is located. Therefore, knowledge of elemental composition and electronic structure in the pristine films is helpful for the understanding of processes taking place during resistive switching. The stoichiometry in sputter deposited thin films can be controlled by the oxygen partial pressure during deposition [126] and also by the deposition rate [127]. First, the sample preparation will be described. Then the surface morphology and structure of the prepared thin films will be presented. Afterwards, the influence of oxygen content in deposition atmosphere and sputtering power on the stoichiometry of $\text{Ta}_2\text{O}_{5-x}$ and TiO_{2-x} will be analyzed by means of XPS¹ and their influence of the electrical properties will be discussed. Furthermore, the $\text{Nb}_2\text{O}_{5-x}/\text{Ta}_2\text{O}_{5-x}$ bilayer structure will be investigated by XPS and the results will be compared to the ones from the single layer. Then the switching characteristics will be analyzed for single layer $\text{Ta}_2\text{O}_{5-x}$ structures and also for $\text{Nb}_2\text{O}_{5-x}/\text{Ta}_2\text{O}_{5-x}$ heterosystems. The influence of the stoichiometry on the switching properties will be discussed as well as the influence of the preparation method of the top electrode on the resistive switching parameters. Also the difference between single layer and heterosystem will be analyzed.

4.1 Surface morphology and structure of sputtered thin films

All thin films presented here were prepared by DC magnetron sputtering from metallic targets with a diameter of 46 mm. Metallic films were sputtered in pure argon (99.9999% purity) and oxide films were prepared in an argon/oxygen (99.999% purity) gas mixture at room temperature. All samples were prepared on $1 \times 1 \text{ cm}^2$ silicon pieces with (001) orientation covered by 430 nm SiO_2 . Before deposition

¹Part of the XPS measurements for oxygen content series were performed by Michael Andrä, Peter Grünberg Institute, Forschungszentrum Jülich GmbH, Jülich, Germany.

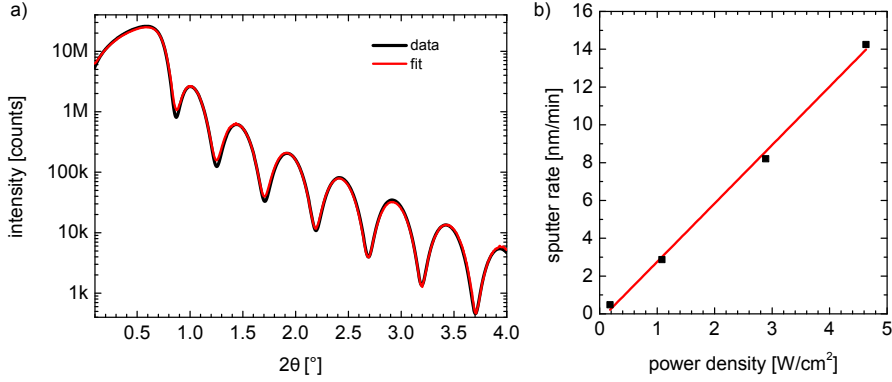


Figure 4.1: a) XRR data for a $\text{Ta}_2\text{O}_{5-x}$ film deposited with 1.20 W/cm^2 , $3.5 \cdot 10^{-2} \text{ mbar}$ and 10% oxygen in argon. b) Power density dependence of sputtering rate.

the substrates were cleaned with acetone and isopropanol in an ultrasonic bath and plasma ashed to remove residual protective coating. The different parameters for the variation of the argon to oxygen flow ratio and the sputtering power density are listed in table 4.1. The deposition pressure was set to $3.5 \cdot 10^{-2} \text{ mbar}$ (a detailed overview of all used parameters is given in appendix A.1). The deposition rates were determined by X-ray reflectometry (XRR). A representative XRR curve is displayed in figure 4.1 a). The data show clear thickness fringes. Fitting of this XRR curve with *GenX* [128] reveals a film thickness of 17 nm. An overview of the different deposition rates in dependence of the power density is given in figure 4.1 b). The deposition rate linearly increases with rising power, which is in good agreement with previous reports [129, 130]. The deposition rate does not change significantly with the used oxygen to argon flow ratios. Therefore, an insulator to metal transition

power variation		variation of O_2 content	
power density	O_2/Ar flow ratio	power density	O_2/Ar flow ratio
0.30 W/cm^2	25.0%	1.20 W/cm^2	25.0%
1.20 W/cm^2	25.0%	1.20 W/cm^2	14.3%
3.00 W/cm^2	25.0%	1.20 W/cm^2	10.0%
4.81 W/cm^2	25.0%		

Table 4.1: Sputtering parameter for the $\text{Ta}_2\text{O}_{5-x}$ thin films for a deposition pressure of $3.5 \cdot 10^{-2} \text{ mbar}$.

can be excluded as one expects a clear increase in the sputter rate if the reactive sputtered film is more metallic-like [131].

The surface morphology of the samples was investigated with AFM. The surface of the prepared $\text{Ta}_2\text{O}_{5-x}$, $\text{Nb}_2\text{O}_{5-x}$ and TiO_{2-x} (cf. figure 4.2 a),b),c)) is rather smooth and the root mean squared roughness is below 1 nm for all films. Finally, the structure of all films was investigated by X-ray diffraction (XRD) under grazing incident (cf. figure 4.2 d) and e)). For the $\text{Nb}_2\text{O}_{5-x}$ and $\text{Ta}_2\text{O}_{5-x}$ films no significant signal can be observed within the measured angular range, which allows the conclusion that the $\text{Ta}_2\text{O}_{5-x}$ as well as the $\text{Nb}_2\text{O}_{5-x}$ films are amorphous in the range of XRD measurement accuracy. This observation fits well to the previous reported results for reactively sputtered $\text{Ta}_2\text{O}_{5-x}$ and $\text{Nb}_2\text{O}_{5-x}$ where a transition to crystalline structures was only observed for temperatures above 600 °C [132, 133] and 550 °C [134], respectively. In the XRD scan of the TiO_{2-x} film weak signals are visible, which can be assigned to the anatase phase. The signal at $2\theta = 55^\circ$ could also be a (211) rutile reflex [135, 136].

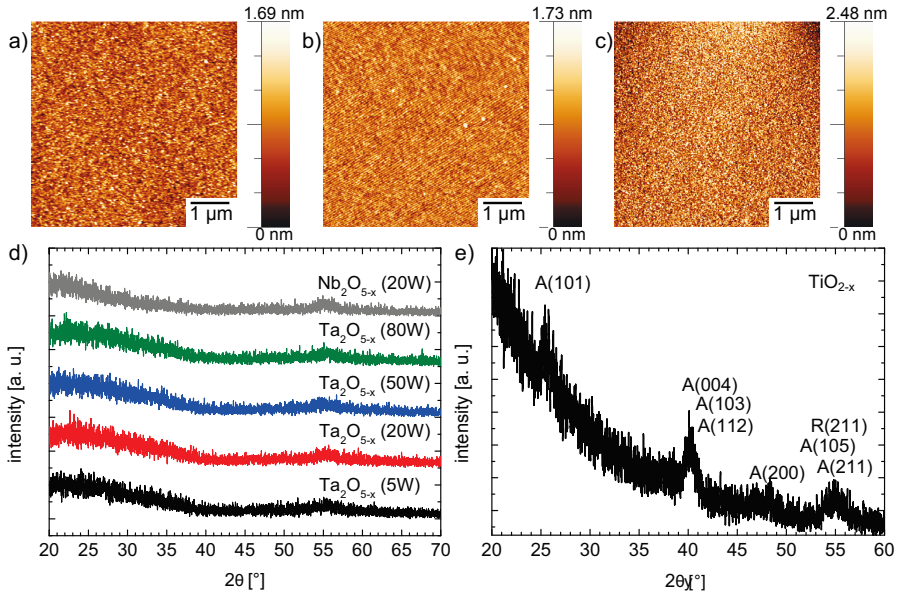


Figure 4.2: AFM scans of a) $\text{Ta}_2\text{O}_{5-x}$, b) $\text{Nb}_2\text{O}_{5-x}$ and c) TiO_{2-x} thin films deposited on a silicon substrate with 430 nm SiO_2 on top. XRD scans for d) thin films $\text{Nb}_2\text{O}_{5-x}$ and $\text{Ta}_2\text{O}_{5-x}$ prepared with different parameters e) and a TiO_{2-x} film taken under grazing incident.

4.2 Spectroscopic characterization of thin films

All investigated films in this section were transferred *in-situ* from the sputtering chamber to the XPS setup under UHV conditions in order to prevent oxidation and contamination due to adsorbates. For all films a survey scan and single core level spectra were taken with electron neutralization in order to compensate charging effects on the surface. The presented spectra were all recorded at normal emission to the surface. For all films no significant carbon signal can be detected, which confirms the presence of good preparation and measurement conditions. Moreover, no other contaminations are visible in the survey scans.

4.2.1 Engineering the oxygen content in $\text{Ta}_2\text{O}_{5-x}$

First the influence of the oxygen to argon flow ratio on the film stoichiometry is studied. The DC sputtering power density was set to 1.20 W/cm^2 . The elemental composition of the thin films is determined by the integral intensity of the core level spectra (cf. 3.3). The sensitivity factors (RSF) are calibrated to stoichiometric tantalum oxide powder. The results for the different oxygen contents are presented in figure 4.3 b). All three prepared films have an oxygen to tantalum ratio smaller than 2.5, which corresponds to stoichiometric tantalum oxide. The Ta 4f core level spectra show only slight differences with decreasing oxygen fraction in deposition atmosphere (cf. figure 4.3 a)). For the sample prepared with an oxygen to argon flow ratio of 10 % the intensity drop between the two core levels is less pronounced than for the other samples, which could be a hint for an additional component. The allowed off-stoichiometry in $\text{Ta}_2\text{O}_{5-x}$ ceramics was reported to be larger than $x = 0.1$ [137] before reduced components arises in tantalum oxide. However, in thin films the oxygen deficiency, before a significant amount of reduced tantalum oxide is visible, might be larger. In order to extract the differences in the spectra, a peak model with two components is employed. The Ta $4f_{7/2}$ for Ta_2O_5 is located at a binding energy of $26.8 \pm 0.4 \text{ eV}$ [138] and the O 2s level at 23 eV [115]. Therefore, an additional peak pair was added to the fitting model. The first component in the tantalum spectra is assigned to the Ta_2O_5 and the second one is shifted 0.6 eV towards lower binding energies, which represents the reduced species TaO_2 . The area ratio between the two Ta 4f are fixed to 0.75 and the energy distance due to spin orbit splitting is 1.87 eV , which fits well to previously reported literature values [138, 139]. This energy shift of the two tantalum oxide components (Ta_2O_5 and TaO_2) is in good agreement with literature [139–141]. The results for the samples prepared with an oxygen to argon flow ratios of 10% and 25% are shown in figure 4.3 a). For the lower oxygen content a small contribution of TaO_2 is visible,

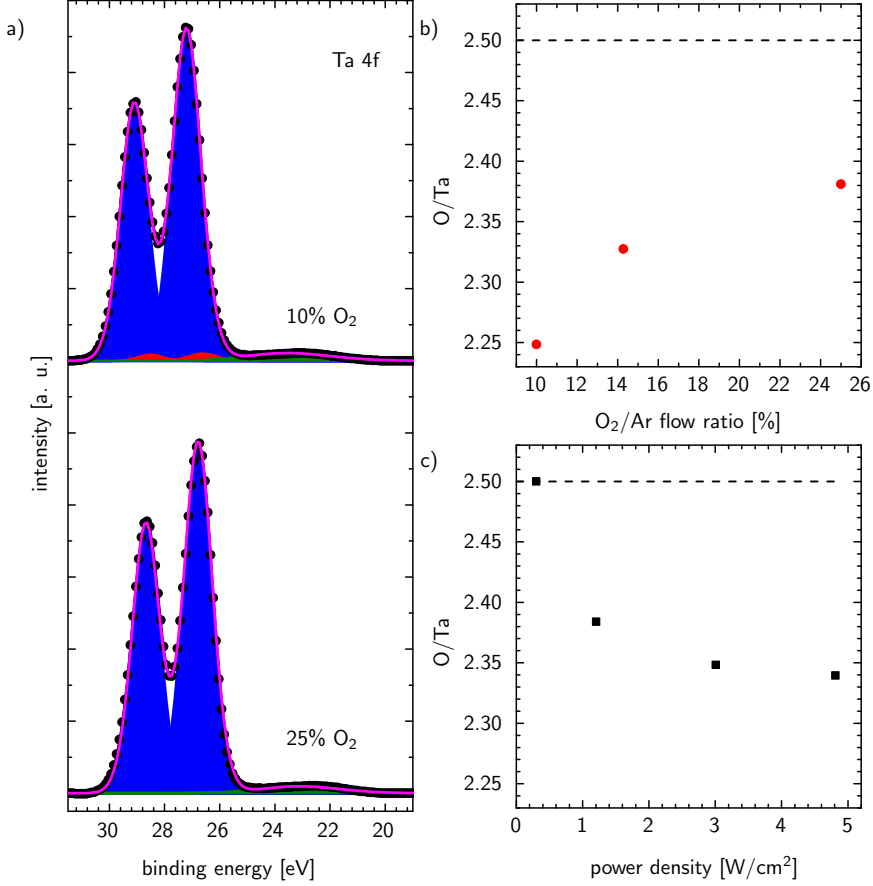


Figure 4.3: a) Ta 4f core level spectra for oxygen to argon flow ratios of 10% and 2%. In the case of lower oxygen content a small contribution of TaO₂ (red) is visible. Oxygen to tantalum ratio in dependence of b) oxygen content in deposition atmosphere and c) power density.

whereas for the highest used amount of oxygen no additional component is visible. For the other sample it is below the detection limit.

Additional to the variation of oxygen concentration during deposition the influence of DC sputtering power density on the stoichiometry is investigated. For all films no significant difference is visible between the different Ta 4f core level spectra. Again, the stoichiometry of the films was determined by the integral intensity of the core levels. The results are shown in figure 4.3 c). The sample prepared with a power density of 0.30 W/cm^2 has an oxygen to tantalum ratio which corresponds to stoichiometric Ta_2O_5 . With increasing power density the oxygen content in the films decreases. This phenomenon can be correlated to the deposition rate, which increases with rising power density and therefore the total time in which the cells stay in the deposition atmosphere is shorter. This was also reported previously for TiO_{2-x} films [127].

In figure 4.4 a) an overview of the different single spectra for the samples prepared with an oxygen to argon flow ratio of 10% and 25% is given. The energy scale is referred to the Fermi level E_F of metallic tantalum (cf. figure 4.4 b)), which is indicated by the dotted line. The valence band of tantalum oxide is formed by the hybridization of O 2p, Ta 5d and 6 sp orbitals [142]. For oxygen deficient tantalum oxide a decrease of the hybridized states of O 2p, Ta 5d and 6 sp orbitals in energy range of 4–10 eV and an increase of the Ta 5d states in the band gap region has been observed [143]. However, in the valence spectra in figure 4.4 b) there are no indications for a strong increased oxygen vacancy concentration as there is no signal in the energy range of 4 eV to the Fermi level visible [143, 144]. In all core levels (O 1s, Ta 4f) and the valence band spectra, a clear shift towards lower binding energy is visible for the sample prepared with an oxygen to argon flow ratio of 10%. This can be explained by relative shift of the conduction band towards the Fermi level. A similar energy shift was also observed in the case of oxygen deficient $\text{Ta}_2\text{O}_{5-x}$ [145]. It is also correlated with an increased donor dopant concentration [146].

In order to quantify the shift and the resulting carrier concentration differences, the energy shifts for the different thin films was measured through the position of the valence band maximum (VBM), which can be extracted from a linear regression fit [147]. As an example, the determination of the VBM for the sample prepared with an oxygen to argon flow ratio of 10% is shown in figure 4.4 c). An overview of all VBM fitting results is shown in figure 4.5 a). The lowest binding energy is given for the stoichiometric sample. With decreasing oxygen content the VBM shifts towards lower energies.

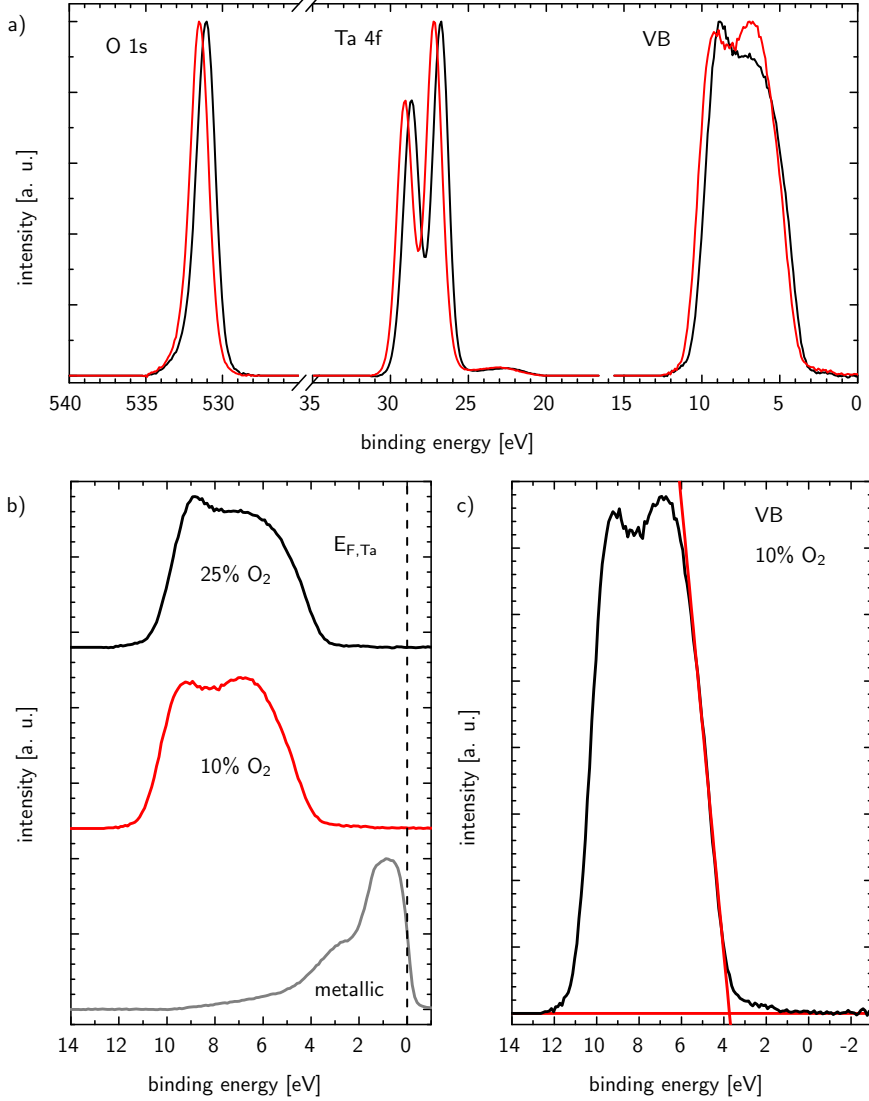


Figure 4.4: a) Ta 4f, O 1s and VB spectra for oxygen to argon flow ratios of 10% (red) and 25% (black). b) Valence band spectra for metallic (grey) Ta and Ta_2O_{5-x} films deposited with oxygen to argon flow ratios of 10% (red) and 25% (black) in deposition atmosphere. c) Determination of valence band maximum for the sample prepared with an oxygen to argon flow ratio of 10%.

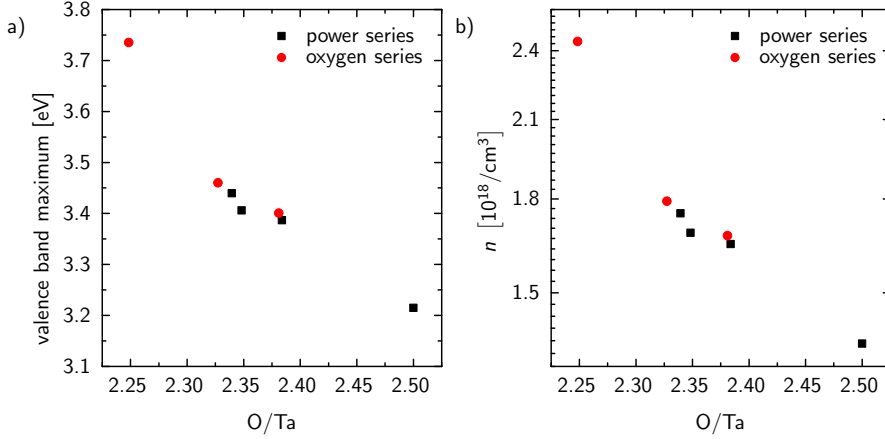


Figure 4.5: a) Valence band maximum position for the different stoichiometries and b) charge carrier concentration of the different films.

If the relative position of the Fermi level is known (in this study the tantalum Fermi edge E_F) the position of the conduction band E_C can be determined by

$$E_C - E_F = E_{\text{VBM}} - E_F + E_g. \quad (4.1)$$

Here, E_g is the energy of the band gap, which was reported to be 4.2 eV [47–49] for amorphous tantalum oxide. The charge carrier concentration in a semiconductor can be expressed as follows [148]

$$n = N_C \exp\left(-\frac{E_C - E_F}{k_B T}\right) \quad (4.2)$$

with the effective density of states N_C

$$N_C = 2 \left(\frac{2\pi m_n^* k_B T}{h^2} \right)^{\frac{3}{2}}. \quad (4.3)$$

The effective mass m_n^* was reported to be $0.3 \cdot m_e$ for $\text{Ta}_2\text{O}_{5-x}$ [149]. The calculated charge carrier concentrations are shown in figure 4.5 in dependence of the oxygen to tantalum ratio. With decreasing oxygen content in the oxide layer, the charge carrier concentration rises. It can be concluded that the stoichiometry of the thin films can be either influenced by the oxygen content in deposition atmosphere or the sputtering power density. This results in different amounts of n -type doping.

In addition to the previously shown argon to oxygen flow ratio variations thin $\text{Ta}_2\text{O}_{5-x}$ films with a gas mixture of 3% oxygen in argon are studied. Two different layers were deposited with a sputtering power density of 1.20 W/cm^2 and a deposition pressure of $3.0 \cdot 10^{-2} \text{ mbar}$. The films have thicknesses of 9 nm and 15 nm, respectively. In the Ta 4f core level spectra no suboxide is visible. The fitted spectra of the 9 nm thin film is shown in figure 4.6 a). The oxygen to tantalum ratio is determined to 2.3 and 2.4 for the 9 nm and 15 nm. Therefore, the deposition with these parameters is not homogeneous. With increasing layer thickness the oxygen content increases. This may be caused by the different residence time in the deposition atmosphere or the target may be oxidized during the deposition. In figure 4.6 b) the magnetron voltage and current in dependence of the deposition time is shown. The magnetron is operated in constant power mode. As can be seen the voltage increases over time and consequently the current decreases, which means that the target is oxidized during the deposition. This means that the different stoichiometry is most likely caused by poisoning of the target.

It has been demonstrated in this thesis that the stoichiometry in thin films is influenced by the sputtering power density and therefore also a film with a sputtering power of 2.11 W/cm^2 is investigated. The magnetron voltage (244 V) for this sputtering power was stable over the entire deposition time, which indicates that there is no poisoning of the target during deposition. The Ta 4f core level spectra show clearly sub-stoichiometric tantalum oxide. The Ta 4f core level spectra with the corresponding fit are shown in figure 4.6 c). The peak at a binding energy of 22.1 eV can be assigned to metallic tantalum and the other peaks which have relative shifts of 1.6 eV and 4.4 eV to the metallic tantalum corresponds to TaO and Ta_2O_5 . The values are in good agreement with the literature [138, 140, 141]. The oxygen to tantalum ratio is determined to 1.00, which means a strong oxygen deficiency. This is also clearly visible in the valence band spectra, which is shown in figure 4.6 d). In the energy range of 4 eV to the Fermi level an additional signal is visible, which can be assigned to 5d states due to an increased oxygen vacancy concentration and the presence of metallic tantalum [143, 144].

Additionally, a thin film with a sputtering pressure of $2.00 \cdot 10^{-2} \text{ mbar}$ was prepared. The sputtering power density was the same as for the thin film prepared with 3% oxygen in argon, where no suboxides has been observed. The magnetron sputter voltage is stable over the entire deposition time, which means that the metallic target is not significantly poisoned with oxygen. The oxygen to tantalum ratio is determined to 0.95, which is comparable to the film deposited with an increased sputtering power. The Ta 4f and valence band spectra are similar to the recently presented spectra for the increased sputtering power (cf. figure 4.6 c) and d)), which show clearly the presence of sub-stoichiometry. Thus it can be concluded that the sputtering power, the total gas volume and also the argon to oxygen flow ratio influences the stoichiometry of the reactive sputtered film.

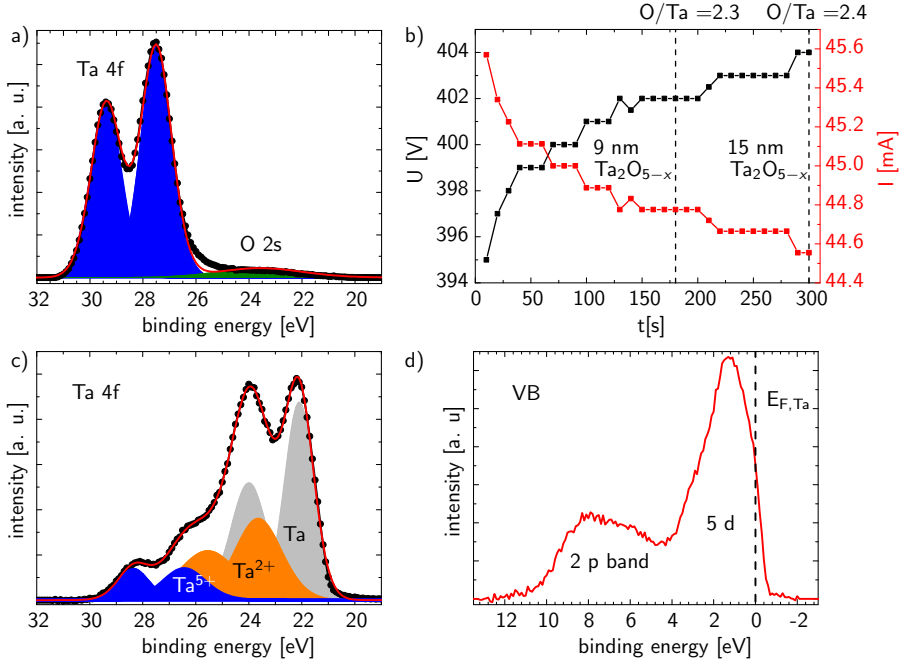


Figure 4.6: a) Ta 4f and O 2s core level spectra for a Ta₂O_{5-x} film deposited with a sputtering power density of 1.20 W/cm² and a gas mixture of 3% oxygen in argon. b) Magnetron voltage and current in dependence of sputtering time. c) Ta 4f d) and valence band spectra of a sub-stoichiometric Ta₂O_{5-x} film deposited with a power density of 2.11 W/cm².

4.2.2 Engineering the oxygen content in TiO_{2-x}

In the following section the influence of the oxygen to argon flow ratio on the oxygen deficiency in TiO_{2-x} will be studied. The used sputtering power density and flow ratios are listed in table 4.2. All films were studied with *in-situ* XPS. The stoichiometry of the thin films is determined by the Ti 2p and O 1s core level spectra. The peak shape of the Ti 2p core level spectra does not change for the different oxygen to argon flow ratio. The Ti 2p core level spectra can be fitted with a doublet, which can be assigned to TiO₂. In figure 4.7 a) the Ti 2p core level spectrum for the film prepared with an oxygen to argon flow ratio of 8.3% is shown. The binding energy of Ti 2p_{3/2} was determined to 458.5 eV. The spin orbit splitting is 5.7 eV. There is no indication for a reduced titanium valence state, since there is no signal visible at binding energies of 456.7 eV (Ti³⁺) and 455.9 eV

power density	O ₂ /Ar flow ratio
4.51 W/cm ²	25.0%
4.51 W/cm ²	14.3%
4.51 W/cm ²	10.0%
4.51 W/cm ²	8.3%

Table 4.2: Sputtering parameter for the TiO_{2-x} thin films for a deposition pressure of $3.5 \cdot 10^{-2}$ mbar.

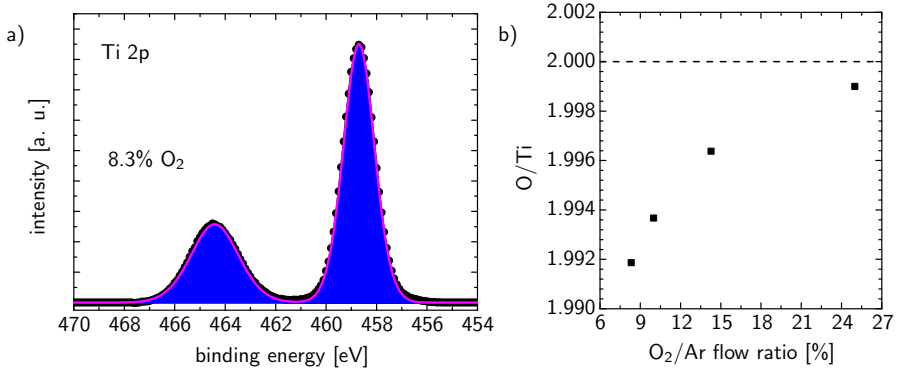


Figure 4.7: a) Ti 2p core level spectrum for a TiO_{2-x} film prepared with an oxygen to argon flow ratio of 8.3%. b) Oxygen to titanium ratio in dependence of the oxygen content in the deposition atmosphere.

(Ti²⁺) [150, 151]. The elemental composition of the TiO_{2-x} films is determined by the integral intensity of the Ti 2p and O 1s core level spectra. The element specific sensitivity factors were calibrated by polycrystalline TiO_{2-x} powder. The results are shown in figure 4.7 b). The oxygen deficiency decreases with increasing oxygen to argon flow ratios. The oxygen off-stoichiometry in TiO_{2-x} varies from $x = 0.001$ – 0.009 . These values are below the resolution limit of XPS, nonetheless, there is a clear trend visible. The concentration of oxygen vacancies in TiO_{2-x} is thus significantly lower than in the Ta₂O_{5-x} films. The titanium ions may soak more oxygen from the sputtering ambient in comparison to the tantalum ions due to the lower free energy of the formation of the titanium oxygen phase [152] and therefore the TiO_{2-x} layers are less oxygen deficient in comparison to the Ta₂O_{5-x} layers.

Based on the previously studied Ta₂O_{5-x} films also the absolute energy positions of the Ti 2p, O 1s and valence spectra are compared. In figure 4.8 the spectra for oxygen to argon flow ratios of 8.3% and 25% are shown. A slight shift towards

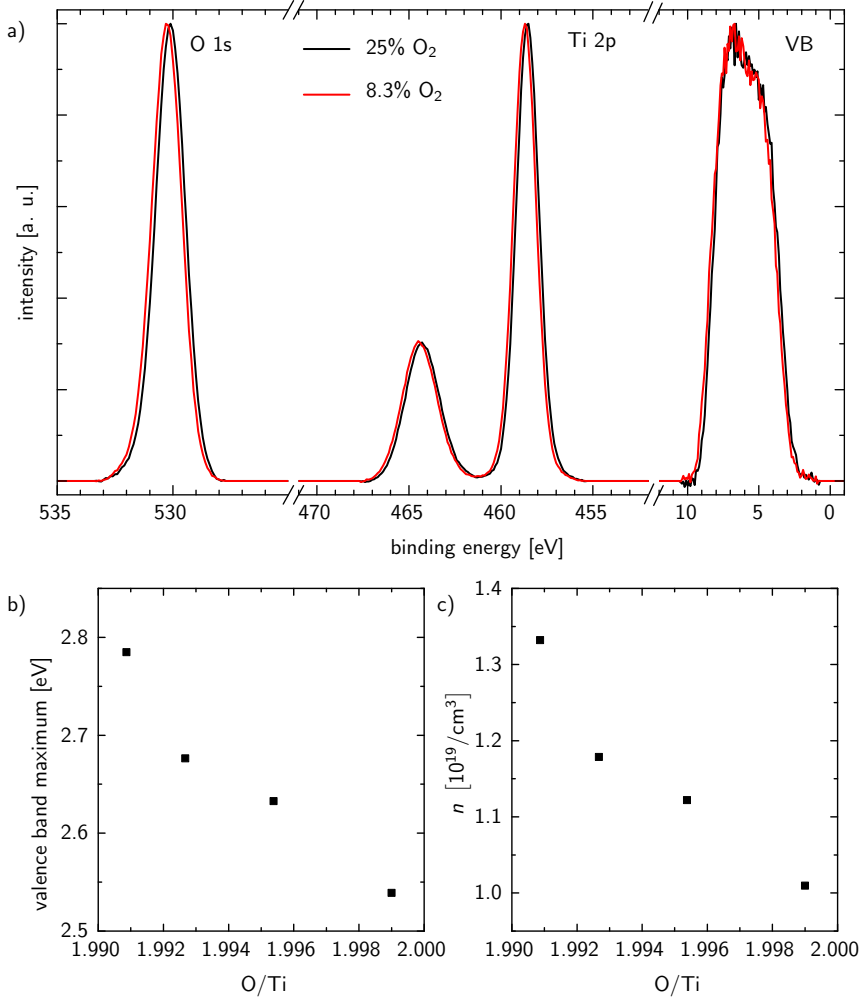


Figure 4.8: a) Ti 2p, O 1s and VB spectra for oxygen to argon flow ratios of 8.3% (red) and 25% (black). b) Valence band maximum position for the different stoichiometries and c) charge carrier concentration of the different films.

lower binding energies is visible for the sample prepared with an oxygen to argon flow ratio of 8.3%, which indicates a relative shift of the conduction band towards the Fermi level. Analogous to the $\text{Ta}_2\text{O}_{5-x}$ films the positions of the VBM positions is determined. The results are shown in figure 4.8 b). The VBM shifts to higher binding energy with decreasing oxygen content, which fits well to the observed shifts in the core level spectra. In accordance to the charge carrier concentration determination of $\text{Ta}_2\text{O}_{5-x}$ thin films, the charge carrier concentration of the TiO_{2-x} is calculated with equations (4.2) and (4.3). The effective mass m_n^* was reported to be $0.8 \cdot m_e$ [153] and a band gap energy of 3.05 eV was employed [34]. The calculated charge carrier concentrations in dependence of the TiO_{2-x} stoichiometry are shown in figure 4.8 c). The n -type doping in the TiO_{2-x} films increases with a decrease in the oxygen to titanium ratio.

As the stoichiometry of the TiO_{2-x} layers differs only slightly, in the following only the resistive switching characteristics of the $\text{Ta}_2\text{O}_{5-x}$ layers will be studied. Due to the higher variation in the oxygen vacancy concentration a greater effect on the switching characteristic is expected.

4.2.3 Spectroscopic characterization of $\text{Nb}_2\text{O}_{5-x}/\text{Ta}_2\text{O}_{5-x}$ heterosystems

In addition to the single layer systems also the heterogeneous system consisting of $\text{Nb}_2\text{O}_{5-x}$ and $\text{Ta}_2\text{O}_{5-x}$ is analyzed in terms of resistive switching characteristic and afterwards the spectromicroscopic information of the operated cells. For the XPS analysis stacks with 5 nm and 10 nm thick $\text{Nb}_2\text{O}_{5-x}$ films are prepared on top of tantalum oxide films. The thickness of the $\text{Ta}_2\text{O}_{5-x}$ layer is selected so that the total thickness of the stack is 15 nm in all cases. A depiction of the different layer stacks is shown in figure 4.9 a). In order to prevent contamination due to adsorbates at the surface the samples are transferred *in-situ* to the XPS setup. All photoemission spectra are recorded under normal emission to sample surface. The core level spectra of O 1s, Nb 3d, Ta 4f and the valence band (VB) are investigated. For all film arrangements the Ta 4f signal is still visible. Therefore, the information depth of the heterosystem is estimated to 10 nm. All prepared films show no significant carbon signal, which proves the good preparation and measurement conditions.

In figure 4.9 c)-d) the Nb 3d, Ta 4f and valence band spectra for the heterosystems are shown. The intensity of the Ta 4f signal decreases in relation to O 2s, which contains signals of $\text{Nb}_2\text{O}_{5-x}$ and $\text{Ta}_2\text{O}_{5-x}$ layers, with increasing $\text{Nb}_2\text{O}_{5-x}$ thickness. There is no indication in the Nb 3d and Ta 4f core level spectra for an oxygen deficient component. Likewise, the shape of the valence band spectra looks similar for

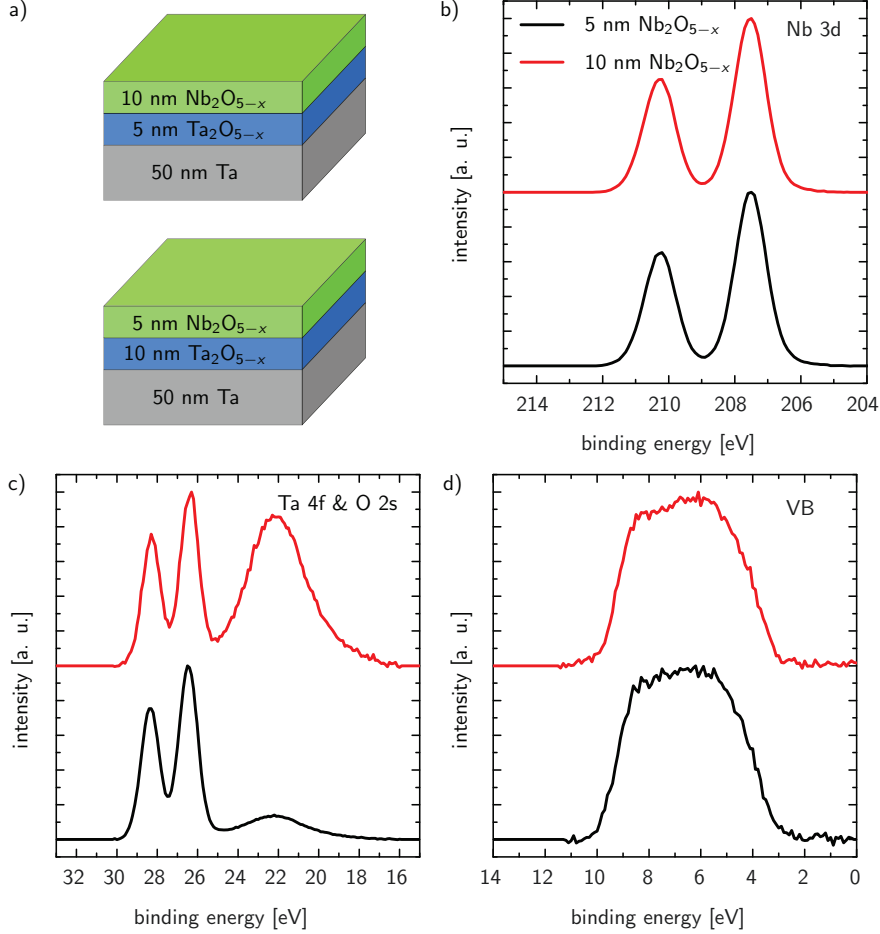


Figure 4.9: a) Depiction of the investigated Nb₂O_{5-x}/Ta₂O_{5-x} systems. b) Nb 3d, c) Ta 4f and O 2s and d) valence band (VB) spectra of 5 nm Nb₂O_{5-x}/10 nm Ta₂O_{5-x} (black curve) and 10 nm Nb₂O_{5-x}/5 nm Ta₂O_{5-x} (red curve) heterosystems.

both samples and no shift in the valence band maximum is apparent. The core levels are also not shifted. The VBM of the heterosystem can be determined to 3.4 eV. Although the recorded valence band spectrum is a convolution of electrons excited from the $\text{Nb}_2\text{O}_{5-x}$ and $\text{Ta}_2\text{O}_{5-x}$ layers, the main distribution is originating from the $\text{Nb}_2\text{O}_{5-x}$ layer. Considering equation (4.2) one can conclude that with the decreased band gap of amorphous $\text{Nb}_2\text{O}_{5-x}$ ($E_g(\text{Nb}_2\text{O}_5) = 3.2 \text{ eV}$ [154,155]) the charge carrier concentration in the heterosystem is increased in comparison to the single $\text{Ta}_2\text{O}_{5-x}$ layer. Hereby an effective electron mass of $0.4 \cdot m_e$ for $\text{Nb}_2\text{O}_{5-x}$ is assumed [156]. The $\text{Nb}_2\text{O}_{5-x}$ layers are also slightly *n*-doped.

4.3 Resistive switching in tantalum oxide based MIM structures

4.3.1 Sample preparation

All samples with MIM structures were prepared on a $1 \times 1 \text{ cm}^2$ silicon piece with (001) orientation covered by 430 nm SiO_2 . For all layer structures a 50 nm metallic tantalum layer acts as bottom electrode. The film was prepared by DC sputtering in a pure argon atmosphere, a deposition pressure of $7 \cdot 10^{-3} \text{ mbar}$ and a DC power density of 1.80 W/cm^2 . Afterwards for the single layer $\text{Ta}_2\text{O}_{5-x}$ or for the heterosystem $\text{Ta}_2\text{O}_{5-x}$ and $\text{Nb}_2\text{O}_{5-x}$ were deposited *in-situ* by reactive sputtering (cf. chapter 4). The total oxide thickness was 15 nm for all prepared MIM structures. On all films 70 nm platinum was deposited *ex-situ* on top of the layer stacks. Depending on the later analysis, there have been used two ways for patterning the top electrode. For the cells which were only characterized electrically, the platinum layer was evaporated on the whole surface and afterwards the structures were etched with ion beam etching after a standard photolithography process. The structures have a size of $50 \times 50 \mu\text{m}^2$. In figure 4.10 a microscope picture of the prepared structures is shown.

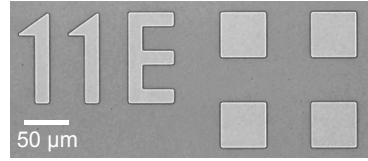


Figure 4.10: Top electrodes prepared with lithography

4.3.2 Sample preparation for spectromicroscopy

For the cells which will be characterized by spectromicroscopy it is necessary to remove the top electrode after they were switched (cf. chapter 3.4). It has been previously shown that one possibility is to use evaporated platinum as top electrode

because of the low adhesion of this material on oxides [117,157]. Platinum top electrodes structured with photolithography cannot be removed by this method. This may be explained by the redeposition effect at the edges during reactive ion beam etching, which leads to an adhesion of the electrode to the oxide. For this purpose, the platinum was evaporated through a shadow mask, the thickness of this layer is 70 nm. An illustration of the different process steps is displayed in figure 4.11. The mask is made from Nickel and can be mounted on the sample surface using a magnet on the backside. For this study pads with a size of $50 \times 50 \mu\text{m}^2$ were used. After the samples were characterized electrically, the top electrode has to be removed for the spectromicroscopic analysis. Therefore a 70 nm homogeneous platinum layer is evaporated on the structures and the top electrodes are removed with an adhesive copper tape. Due to the high oxidation potential of $\text{Ta}_2\text{O}_{5-x}$ and $\text{Nb}_2\text{O}_{5-x}$ [152] this step has to be done in a vacuum environment, otherwise potentially reduced states can be oxidized before spectromicroscopic analysis. A description of this step can be found in reference [117]. Approximately 80–90% of the top electrodes can be removed by this method, only some platinum at the edges is left. Due to evaporation through a shadow mask the top electrodes have no steep edges, which corresponds to smaller thicknesses at the edge. For this areas with thinner platinum the adhesion is increased and this parts of the top electrode are not removed by the delamination procedure. This does not affect the measurements, since there is no platinum within the active switching area. At the end of this chapter the influence of the top electrode preparation will be discussed and therefore also cells with a 70 nm sputtered platinum electrode will be discussed.

4.3.3 Stoichiometry dependent switching characteristic in Pt/ $\text{Ta}_2\text{O}_{5-x}$ /Ta layer structures

In this section the resistive switching characteristics of $\text{Ta}_2\text{O}_{5-x}$ based cells are analyzed. The switching behavior of cells in dependence of the sputtering power density will be investigated in terms of initial resistance, forming voltage, reset current and set current. For electrical characterization, the top electrodes are contacted with tungsten whisker probes. The contact to the bottom electrode was enabled with wire bonding for all samples. As voltage source a *Keithley 2611* is used, which also measured the actual current flow through the cells simultaneously. Before the MIM structures are resistively switched, the initial resistance of the cells was measured with an I - V -sweep from -0.5 V to 0.5 V. These voltage values are chosen in order to ensure that the samples are not changed electrically. All samples are highly insulating and have an initial resistance in the range of several G Ω (cf. figure 4.13 a)). The initial resistances were read out at a voltage of 60 mV. The ini-

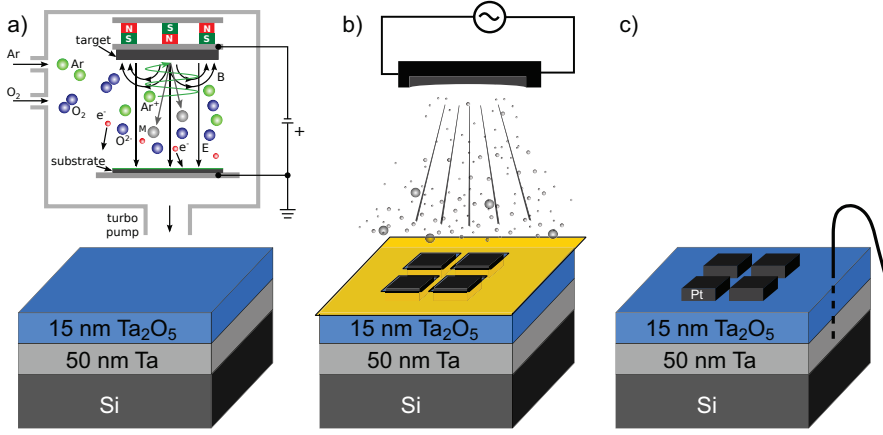


Figure 4.11: Scheme of sample preparation starting with a) deposition of 50 nm tantalum and 15 nm $\text{Ta}_2\text{O}_{5-x}$ by reactive sputtering and b) deposition and structuring of the platinum top electrode by evaporation through a shadow mask and finally c) contacting the bottom electrode with wire bonding.

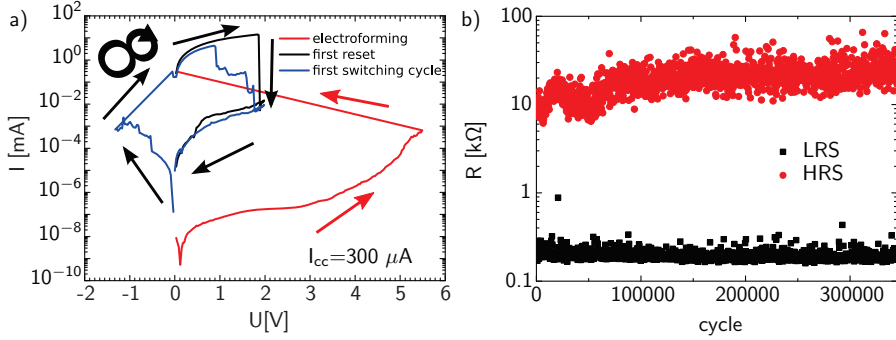


Figure 4.12: a) I - V characteristic for a $\text{Ta}_2\text{O}_{5-x}$ cell prepared with a power density of 4.81 W/cm^2 (O/Ta: 2.34). b) Endurance measurement. The set voltage was -2.25 V ($300 \mu\text{A cc}$), reset voltage 2 V (no cc), every 250th data point is shown.

tial resistances are all in the detection limit of the measurement setup except for the devices with a $\text{Ta}_2\text{O}_{5-x}$ layer with an oxygen to argon ratio of 1.00. These devices have an initial resistance in the range of $\text{k}\Omega$ and it was not possible to switch these cells, therefore they are not further discussed in this section. The samples prepared with $1.20 \text{ W}/\text{cm}^2$, $3.00 \text{ W}/\text{cm}^2$ and $4.81 \text{ W}/\text{cm}^2$ have a slightly lower initial resistance than the one prepared with a sputtering power density of $0.30 \text{ W}/\text{cm}^2$. In order to switch the initially highly insulating cells, an electroforming step is necessary as mentioned in 2.1. Therefore all cells were formed with a first voltage sweep into the LRS with positive voltage at the platinum top electrode. In order to prevent a hard breakdown it is necessary to limit the current in the devices with a current compliance of $300 \mu\text{A}$ (cf. chapter 2.1). Afterwards the cells can be switched in counter-eightwise polarity [158, 159]. In figure 4.12 a) the I - V -characteristic for a cell prepared with $4.81 \text{ W}/\text{cm}^2$ is shown. The other samples show similar I - V -characteristics, only the absolute values of the reset currents and set voltages differ. For the other cells prepared with a different sputtering power, a similar forming step is necessary. The current compliance was set for all samples to $300 \mu\text{A}$, but the forming voltage U_{FORMING} varies with sputtering power density. The forming voltage represents the voltage, where a high insulating sample is set into LRS. An overview of the evaluated forming voltages U_{FORMING} is given in figure 4.13 b). The highest forming voltage is necessary for the nearly stoichiometric cells and the forming voltage decreases with rising oxygen deficiency. This behavior was recently shown for hafnium oxide films with different oxygen vacancy concentrations. With increasing oxygen vacancy concentration the forming voltage decreases [160, 161]. The same effect was observed for different metal oxide stacks, where an increase of the oxidizable metallic layer thickness increases the oxygen vacancy concentration in the metal oxide [162, 163]. This leads also to an decrease of the forming voltage. The increased oxygen vacancy concentration leads to a higher electronic conductivity. Therefore, the Joule heating and the temperature activated ionic motion is significant already at lower temperatures.

The cells were subsequently switched and the maximum reset current and the set voltage were determined for at least 20 cells per sample type. The results are shown in figure 4.13 c) and d). The reset current rises from stoichiometric to off-stoichiometric films, which can be correlated to increased charge carriers leading to higher leakage currents. The set voltage for the sample with the highest oxygen deficiency is increased in comparison to the other film stoichiometries. Additionally, the endurance of all samples was checked. As an example, the endurance analysis for the 80 W sample is shown in figure 4.12 c). The endurance of the sample with a O/Ta ratio of 2.34 was determined by pulse measurement with a pulse width of $200 \mu\text{s}$. The set voltage was set to -2.25 V with a current compliance of $300 \mu\text{A}$ and a reset voltage of 2.00 V . The voltages for the other samples are in the same range. In comparison to quasi-static measurements the voltages are increased, which is

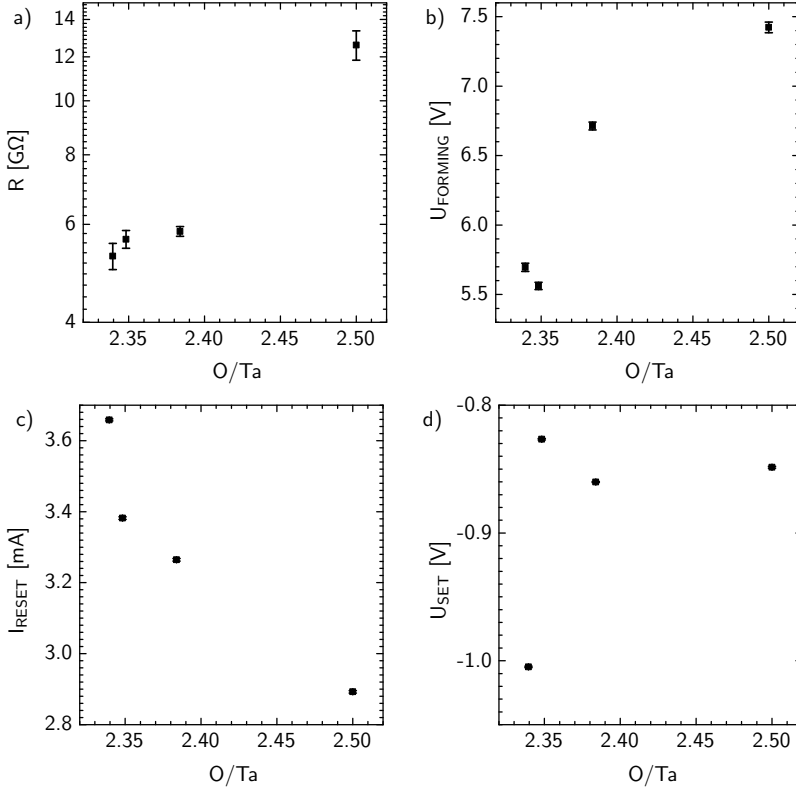


Figure 4.13: Stoichiometry dependence of electrical parameters.

caused by the strong non-linearity of the switching process [15]. For all samples, an endurance of at least more than $3 \cdot 10^5$ cycles is observed. In the range of the investigated cycles no dependence of the stoichiometry on the endurance was visible.

4.3.4 Influence of different top electrodes on the resistive switching properties

In this section the switching characteristic of identical layer stacks (Pt/15 nm Ta₂O₅/Ta) but differently prepared top electrodes is presented. The Ta₂O_{5-x} layer was sputtered with a power density of 1.20 W/cm². First the resistive switching behavior

of MIM structures prepared by evaporation through a shadow mask are investigated. In order to enable resistive switching in these cells an initial electroforming step is necessary. The voltage is averaged to be 7.6 V. After forming the cells are set into LRS with a resistance of 2 k Ω . The hard breakdown of the cells is prevented by a current compliance, which is set to 300 μ A. The cells are switched back into the HRS by applying a positive voltage to top electrode and setting no current compliance. The MIM structures can be switched subsequently in counter-eightwise polarity. The averaged set voltage is $U_{\text{SET}} = 1.91$ V and the reset current $I_{\text{RESET}} = 20.86$ mA. An endurance of at least more than $3 \cdot 10^5$ cycles is observed (cf. figure 4.14 b)). In the range of the investigated cycles no dependence of the stoichiometry on the endurance was visible. For spectromicroscopic analysis it is important that the switched cells have a good retention since the measurement time for the core level spectra is in the range of one week with a laboratory X-ray source. Therefore, the retention of the devices is checked at room temperature and LRS and HRS are stable over more than three weeks, which is sufficient for the spectromicroscopic measurements.

In previous section 4.3.3 results for evaporated electrodes prepared with photolithography are presented. The forming voltage for the lithography samples is averaged to 6.7 V and for the shadow mask sample 7.6 V. The electrode preparation thus seems to have an impact on the forming voltage. In order to examine this effect in more detail, additionally cells with sputtered electrodes structured with lithography are also analyzed with quasi-static I - V -sweeps. The Ta₂O_{5-x} is prepared with the same parameters, which are used for the other two samples. The initial resistance is also in the range of several G Ω and does not differ from the other two types of samples in the range of measurement accuracy. The switching is enabled with an initial forming step with an averaged forming voltage of 6 V (cf. figures 4.14 a) and 4.15 a)).

The forming polarity is the same as for the other samples. The forming voltage is further decreased in comparison to the other samples. It seems that the ion bombardment during reactive ion beam etching as well as the argon ion bombardment of the sputtering process has an influence on the forming process. Due to *ex-situ* preparation, the Ta₂O_{5-x}/Pt interface consists of hydrocarbons and water. This interfacial layer is effected by the argon ion bombardment during sputtering. The more pronounced interface adsorbate layer in the cell with evaporated electrodes leads to an additional capacitance at the interface, which can be correlated to an increased forming voltage. The etching of the top electrodes can additionally lower the forming voltage.

In addition to the forming behavior, also the subsequent switching characteristic of the cells with sputtered electrodes is analyzed. The cells are set into HRS by applying positive voltage to the top electrode. Then the cells are subsequently

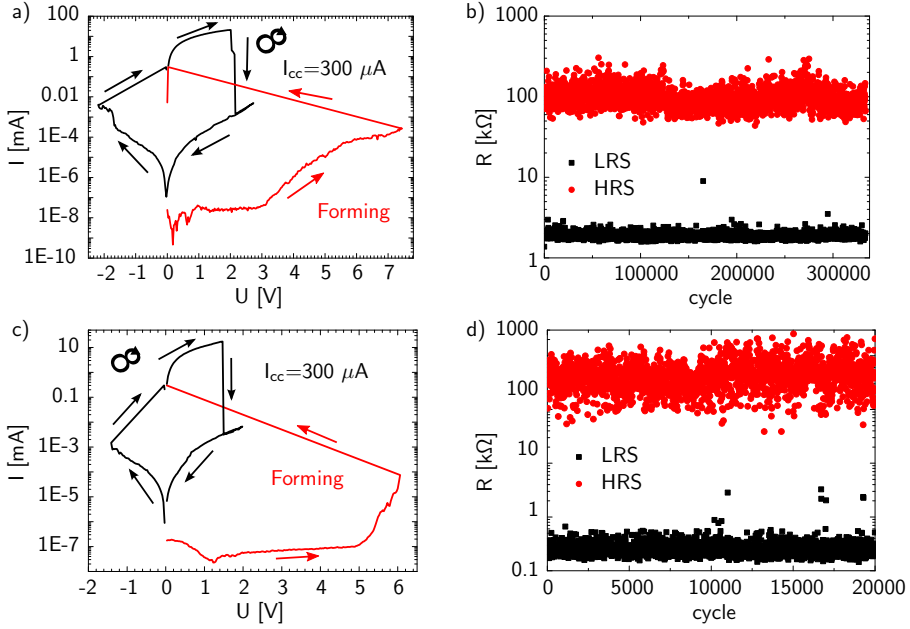


Figure 4.14: a) Switching curve for a 15 nm $\text{Ta}_2\text{O}_{5-x}$ film with evaporated electrodes patterned with a shadow mask. The current compliance was set to $300 \mu\text{A}$. Counter-Eightwise switching is observed. b) Endurance measurement for this stack [164], every 125th data point is displayed. c) Switching curve for a 15 nm $\text{Ta}_2\text{O}_{5-x}$ film stack with sputtered and etched top electrodes. The current compliance was set to $300 \mu\text{A}$. d) Endurance measurement of the MIM structure with sputtered electrodes, every 10th data point is shown.

switched in counter-eightwise polarity. Figure 4.14 c) shows an exemplary I - V -curve for $\text{Ta}_2\text{O}_{5-x}$ cells with sputtered electrodes. The reset current is averaged to 3.26 mA and the set voltage to 0.86 V. An overview of the averaged reset currents and set voltages for the different prepared cells is given in figure 4.15 b). The set voltage and the reset current are highest for the evaporated cells and for the lithography structured cells they are similar, also the forming voltage was different. A possible explanation for the high reset current is that the evaporated cells have a slightly higher LRS and therefore more current is needed in order to set the cells into HRS. Due to the relatively deep reset in the next step there is also a higher voltage necessary for the set process. Additionally the endurance of the layer stack is also investigated. A stable switching behavior over at least $2 \cdot 10^4$ cycles is

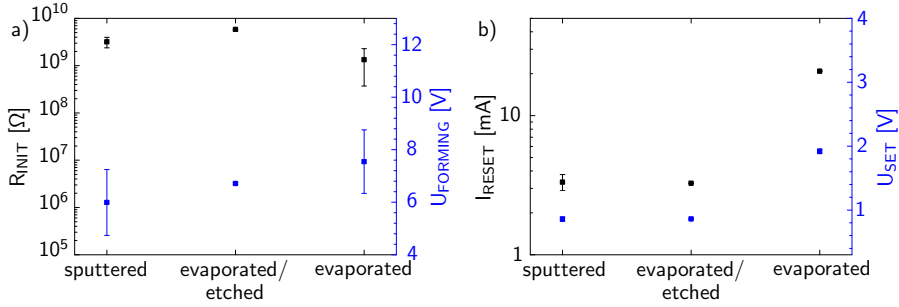


Figure 4.15: a) Initial current and forming voltage of Ta₂O_{5-x} MIM structures with Pt top electrodes prepared by evaporation through a shadow mask, evaporation and reactive ion beam etching and sputter deposition and reactive ion beam etching. b) Reset current and set voltage for the same samples.

observed (cf. figure 4.14 d)). A greater number of cycles has not been tested.

The fabrication method used for the platinum electrodes seems to influence the switching procedure. The interface properties as well as some reduced channels at the edges might lead to different forming voltages, which also influences the switching parameters for the subsequent switching. A preparation-method-dependent switching performance has also been reported for Nb doped SrTiO₃ [165].

4.3.5 Electrical characterization of Nb₂O_{5-x}/Ta₂O_{5-x} heterosystems

In addition to the Ta₂O_{5-x} based single layer structures the resistive switching in a bilayer system consisting of Nb₂O_{5-x} and Ta₂O_{5-x} is also investigated. The electrical structure of the heterosystem was already discussed in chapter 4.2.3 and the preparation of the structures was presented in section 4.3.2. In this section the influence of the Nb₂O_{5-x} layer thickness on the switching characteristics is analyzed and also the differences to the single layer Ta₂O_{5-x} system are discussed.

Resistive switching in 5 nm Nb₂O_{5-x}/10 nm Ta₂O_{5-x} bilayer structures

The quasi-static I - V -characteristic of the Pt/5 nm Nb₂O_{5-x}/10 nm Ta₂O_{5-x}/Ta cells is presented in figure 4.16 a). Resistive switching in these cells was initiated

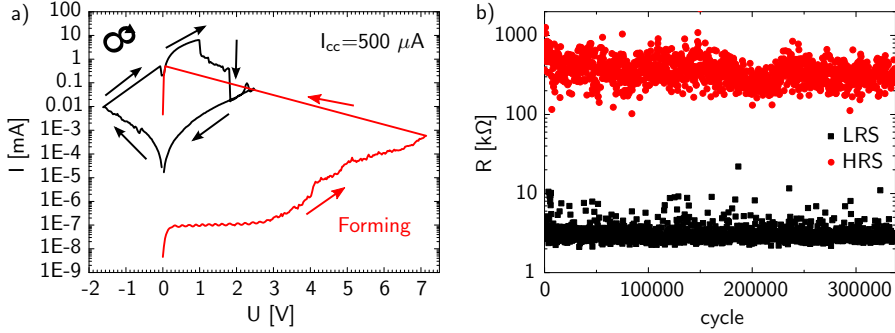


Figure 4.16: a) Switching curve for a 5 nm $\text{Nb}_2\text{O}_{5-x}$ /10 nm $\text{Ta}_2\text{O}_{5-x}$ film stack. The current compliance was set to $500 \mu\text{A}$. The cells can be switched in counter-eightwise polarity. b) Endurance measurement on this stack, every 250th data point is shown.

by an electrical forming step from the pristine state ($\sim \text{G}\Omega$) into the LRS. Stable counter-eightwise switching behavior was found for current compliances of $300 \mu\text{A}$ and $500 \mu\text{A}$ with averaged forming voltages of 6.7 V and 6.9 V , respectively. The formed cells in the LRS are switched into HRS with a voltage of 2.0 V . For the reset no current compliance was necessary. The resistance was changed over four orders of magnitude. Subsequently the device can be switched back into the LRS by applying a negative voltage to the device. The averaged voltage required for the set process was -1.7 V . The retention of the sample is in the range of several weeks at room temperature, so long enough for the later spectromicroscopic analysis. Furthermore the endurance of the device was investigated by pulse measurements. For the set process a voltage of 2.0 V with a current compliance of $500 \mu\text{A}$ was applied and the sample was turned into the LRS with a voltage of -2.0 V and no current compliance. The resistance states are read out with a voltage of 100 mV . All pulses have a width of $200 \mu\text{s}$. In figure 4.16 b) the endurance measurement is presented. The measured cell shows stable switching behavior in the range of $3 \cdot 10^5$ switching cycles.

Resistive switching in 10 nm $\text{Nb}_2\text{O}_{5-x}$ /5 nm $\text{Ta}_2\text{O}_{5-x}$ bilayer structures

The initial resistance of the Pt/5 nm $\text{Nb}_2\text{O}_{5-x}$ /10 nm $\text{Ta}_2\text{O}_{5-x}$ /Ta bilayer structures is also in the range of $\text{G}\Omega$. The resistive switching is only possible with an initial forming step at an averaged forming voltage of 6.40 V . The same forming polarity was chosen as for the previous presented cells. The current compliance was set to $500 \mu\text{A}$. The usage of lower current compliances leads to unstable resistive

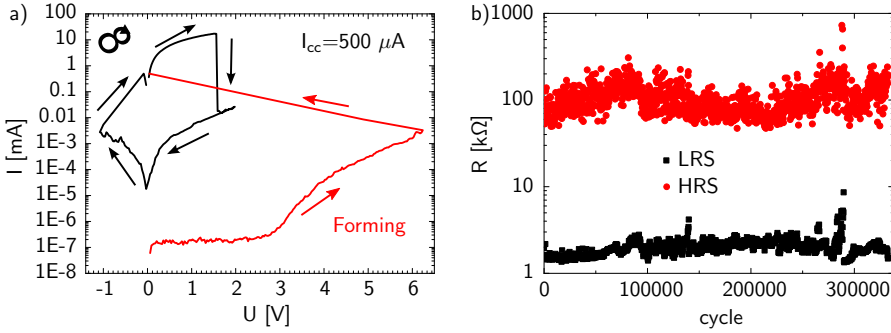


Figure 4.17: a) Switching curve for a 10 nm $\text{Nb}_2\text{O}_{5-x}/5$ nm $\text{Ta}_2\text{O}_{5-x}$ film stack. The current compliance was set to $500 \mu\text{A}$. The cells can be switched in counter-eightwise polarity. b) Endurance measurement on this stack, every 250th data point is shown.

switching characteristics and bad reproducibility from pad to pad. The cells can be switched reversible with counter-eightwise polarity. A representative I - V -curve of one of the cells is shown in figure 4.17 a). The devices were subsequently cycled with voltages from 2.0 V to -2.0 V. For the set voltage a current compliance is also necessary, which was set to $500 \mu\text{A}$. The resistance increases from LRS to HRS by three order of magnitude. The cells can be switched back into the LRS at an averaged set voltage of -1.2 V. The resistance states of the cells are stable over several weeks. Furthermore, the endurance of this layer stack was checked (cf. figure 4.17 b)). A set voltage of -2.0 V and a reset voltage of 1.5 V with a length/width of $200 \mu\text{s}$ were applied to the samples. The actual resistance was read out with a voltage pulse of 100 mV. A stable switching behavior in the range of $3 \cdot 10^5$ switching cycles is observed.

4.3.6 Comparison of resistive switching behavior

The switching characteristic of a single layer $\text{Ta}_2\text{O}_{5-x}$ and heterosystem $\text{Nb}_2\text{O}_{5-x}/\text{Ta}_2\text{O}_{5-x}$ was presented. All devices can be reversible switched in counter-eightwise polarity after an electrical forming step. All layer structures have good endurance and a reliable retention. However, the current compliance for the electrical forming and the set process has to be increased to enable stable and reproducible switching behavior for increasing $\text{Nb}_2\text{O}_{5-x}$ layer thickness. This indicates that the $\text{Nb}_2\text{O}_{5-x}$ layer leads to higher leakage currents in the devices, which is caused by an increased charge carrier concentration already in the pristine state. Due to higher leakage currents the resistance of the cells is smaller leading to an increased current flow

through the sample. In order to produce a sufficient amount of heat in the resistive switching cell it is necessary to increase the total amount of current flowing through the cells during set process. The increased amount of charge carriers has also been shown by the measurement of the VBM position in chapter 4.2.3. The forming voltage is reduced by increasing thickness of the $\text{Nb}_2\text{O}_{5-x}$ layer (cf. figure 4.18 a)). This can be interpreted in terms of a higher oxygen deficiency and it has been shown that it is easier to reduce $\text{Nb}_2\text{O}_{5-x}$ in comparison to $\text{Ta}_2\text{O}_{5-x}$ [166, 167]. Furthermore the reset current and set voltage (cf. figure 4.18 b) and c)) were reduced with increasing layer thickness of the $\text{Nb}_2\text{O}_{5-x}$ layer. The smaller reset currents and set voltage can be correlated to lower HRS for the $\text{Nb}_2\text{O}_{5-x}/\text{Ta}_2\text{O}_{5-x}$ bilayer systems, because the cells cannot be switched off with the same amount of voltage as the $\text{Ta}_2\text{O}_{5-x}$ cells. Higher voltages would lead to an irreversible short-circuit of the cell. Therefore, the total amount of mobile donors, which has to be moved to switch the cell back in the HRS is lower. Moreover, the $R_{\text{HRS}}/R_{\text{LRS}}$ ratio is decreased with increasing $\text{Nb}_2\text{O}_{5-x}$ layer thickness (cf. figure 4.18 d)), which is correlated to the lower reset voltages used for the resistive switching. However, the combination of $\text{Nb}_2\text{O}_{5-x}$ and $\text{Ta}_2\text{O}_{5-x}$ layers is a possibility to control the forming voltage, reset current and also the LRS to HRS ratio.

4.4 Summary

The preparation of different films of $\text{Ta}_2\text{O}_{5-x}$, $\text{Nb}_2\text{O}_{5-x}$ and TiO_{2-x} prepared by reactive sputtering was presented. The influence of the oxygen content in the deposition atmosphere and sputtering power density is studied. The surface morphology of the thin films is not influenced by the preparation parameters. All films show a smooth surface with a low roughness. The stoichiometry of the $\text{Ta}_2\text{O}_{5-x}$ and TiO_{2-x} films was determined by *in-situ* XPS analysis. The elemental oxygen content can be influenced by sputtering power density or the oxygen to argon ratio in the deposition atmosphere. With increasing sputtering power density or decreasing oxygen content the films are increasingly oxygen deficient. The off-stoichiometry in the $\text{Ta}_2\text{O}_{5-x}$ films was significantly higher in comparison to the TiO_{2-x} films. In the Ta 4f core level spectra a small contribution of reduced tantalum was found, whereas in TiO_{2-x} only the stoichiometric phase is present. A shift of the VBM towards higher binding energies is observed for $\text{Ta}_2\text{O}_{5-x}$ and TiO_{2-x} , which is correlated to an increased *n*-type doping and therefore an elevated charge carrier concentration. In addition to the single $\text{Ta}_2\text{O}_{5-x}$ layer the chemical composition of $\text{Nb}_2\text{O}_{5-x}/\text{Ta}_2\text{O}_{5-x}$ heterosystems is investigated by photoemission spectroscopy. No evidence for reduced components is found and the core level and valence band maximum positions do not depend on the $\text{Nb}_2\text{O}_{5-x}$ layer thickness, which means that there is no indication for an increase in charge carrier concentration. However,

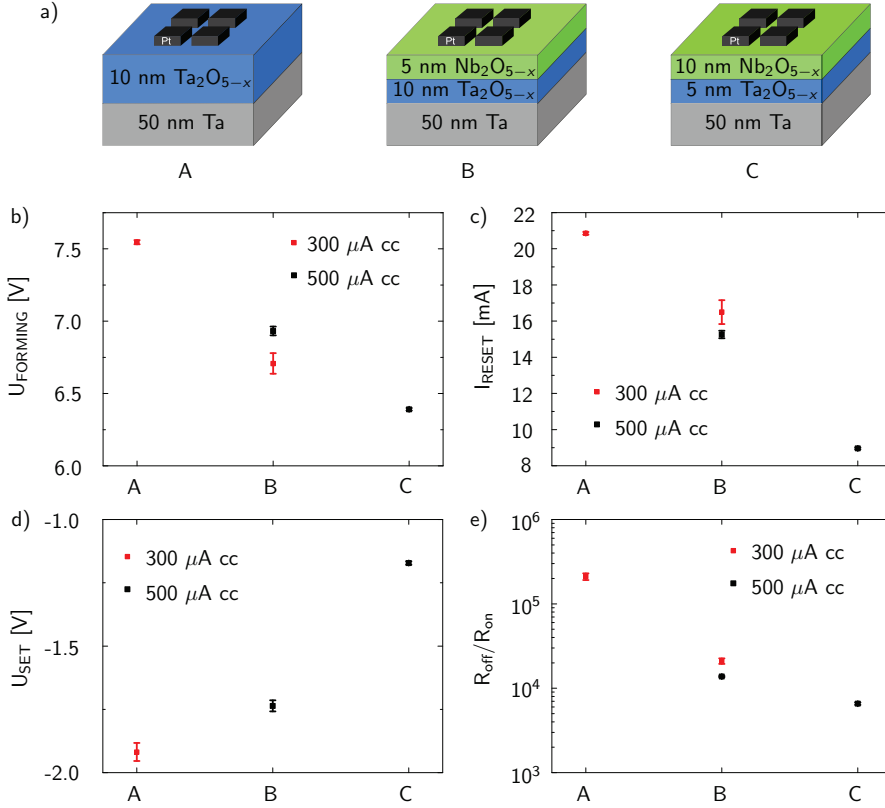


Figure 4.18: Comparison of switching parameters for the different MIM structures. The red dots display data switched with a current compliance of 300 μA and the black dots with 500 μA . a) Overview of measured MIM structures, b) forming voltage, c) reset current, d) set voltage and e) $R_{\text{on}}/R_{\text{off}}$.

due to a lower band gap energy in amorphous $\text{Nb}_2\text{O}_{5-x}$ and similar values of effective electron mass and valence band maximum position it is concluded that the charge carrier concentration in the heterosystem is increased in comparison to the single layer system.

Afterwards the stoichiometry dependent switching of $\text{Ta}_2\text{O}_{5-x}$ based MIM structures has been investigated. A correlation between charge carrier concentration in pristine films and forming voltage has been demonstrated. For high charge carrier concentrations, the forming voltage was the lowest. In addition it has been shown that the other parameters such as reset current and set voltage show the same trend as the forming voltage. Furthermore, an influence of the top electrode preparation has been observed. It has been assumed that in the case of evaporated platinum through a shadow mask a pronounced interface adsorbate layer affects the forming process significantly. This assumption is discussed in more detail in the following chapters. Moreover, it has been shown that the forming voltage is lowered in the $\text{Nb}_2\text{O}_{5-x}/\text{Ta}_2\text{O}_{5-x}$ heterosystem due to an increased charge carrier concentration in the $\text{Nb}_2\text{O}_{5-x}$. Also the reset current and the set voltage is lowered.

5 Surface sensitive investigation of the active interface in MIM structures

In the previous chapter 4 memristive devices with $\text{Ta}_2\text{O}_{5-x}$ single- and $\text{Nb}_2\text{O}_{5-x}/\text{Ta}_2\text{O}_{5-x}$ bilayers were electrically characterized. The switching in memristive devices is correlated to a conductive filament formed during an initial electroforming step with higher voltages than for the subsequent switching [4, 6, 7]. During the electroforming process morphological changes at the top electrode have been observed [9, 10]. The morphologic changes have been correlated to the oxygen release at the upper interface due to redox reactions during forming, which leads to the conductive filament. In $\text{Ta}_2\text{O}_{5-x}$ devices it has been shown that in LRS the amount of TaO_{2-x} is increased in comparison to HRS, but spatially resolved information about the localization of the switching event in the operated cell are still elusive [11]. Moreover, the formation of a single oxygen deficient filament in $\text{Ta}_2\text{O}_{5-x}$ has been shown, but a difference between LRS and HRS has not been reported [12, 13]. Most of the studies report a filamentary process for the operation of $\text{Ta}_2\text{O}_{5-x}$ based MIM structures. However there are also some works which show switching in spatially extended conductive regions. Especially Yang et al. [14] reported a homogeneous interface switching. Furthermore Park et al. [18] demonstrated multi-filamentary switching, in which redox processes occur during resistive switching. So there is still a lack of the detailed understanding of switching in $\text{Ta}_2\text{O}_{5-x}$ and the subsequent redox processes during switching.

Since it is assumed that the conductive filament in memristive devices is located at the same place as the morphologic changes, the appearance of the top electrode after electroforming is of great interest. Therefore, the morphology of the investigated devices will be analyzed for all electrical characterized MIM structures of this work. The results for pure $\text{Ta}_2\text{O}_{5-x}$ based MIM structures will be presented first. The elementary composition of the former $\text{Pt}/\text{Ta}_2\text{O}_{5-x}$ interface of LRS and HRS is studied by energy filtered PEEM, which provides a spatial and chemical

information at the same time (part of this chapter has been published in reference [164]).¹

In the last section of this chapter the spectromicroscopy investigations of the $\text{Nb}_2\text{O}_{5-x}/\text{Ta}_2\text{O}_{5-x}$ heterosystem, which has already been electrical characterized in section 4.3.5, will be presented. Previous studies investigated the resistive switching for different bilayer structures, e.g. TaO_x/WO_x [169], $\text{Ta}_2\text{O}_{5-x}/\text{TaO}_{2-x}$ [18,170] and $\text{Ta}_2\text{O}_{5-x}/\text{TiO}_2$ [14]. The studies investigated the changed resistive switching behavior under the influence of different oxygen deficiencies or oxidation potentials. In this thesis the resistive switching behavior of $\text{Nb}_2\text{O}_{5-x}/\text{Ta}_2\text{O}_{5-x}$ bilayer stacks is investigated by spectromicroscopy and the chemical and structural changes in comparison to the single layer system are analyzed.²

5.1 Morphological changes of the bottom electrode

5.1.1 $\text{Ta}_2\text{O}_{5-x}$ MIM structures

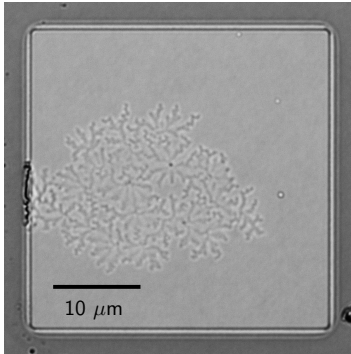


Figure 5.1: Dendrite-like structure at platinum top electrode.

The $\text{Ta}_2\text{O}_{5-x}$ cells are formed with a positive bias at top electrode and therefore it can be expected that oxygen is exorporated at the upper interface as it was reported in literature [5, 171]. The oxygen gas is released from the metal oxide layer due to electro-reduction. This can result in morphological changes of the top electrode, such as the evolution of bubbles. However, during the electroforming process in this study the development of a structure occurs at the platinum top electrode, which looks like Lichtenberg structures [172]. This morphological change will be referred as dendrite-like structures. In figure 5.1 an exemplary microscope image of a platinum top electrode after electroforming is shown. The dendrite-like structure has a size of $27 \times 20 \mu\text{m}^2$, which is relatively large in comparison to observations of filamentary switching in previous reports [12, 13, 18]. They have reported morphological changes taking place within a small area of a few hundred nm. Within the dendrite-like structures, certain points are visible of which apparently dendrite-like arms are growing outwards.

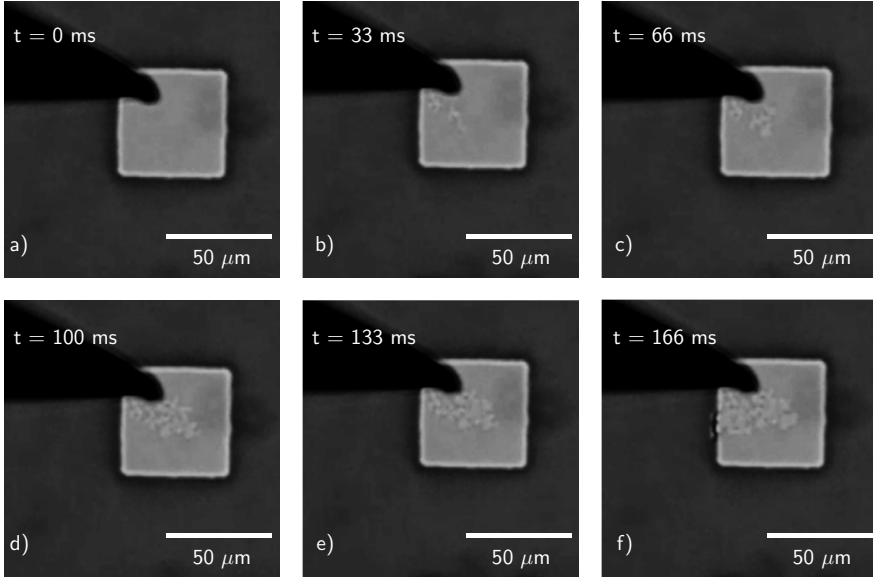


Figure 5.2: Time development of dendrite-like structure during the forming process for a $\text{Ta}_2\text{O}_{5-x}$ MIM structure with platinum electrode, which was evaporated through a shadow mask [164].

The dendrite-like structure seems to be randomly distributed over the platinum electrode.

It is assumed that the development of rather large morphological changes within the top electrode takes a certain time. Therefore, the time evolution of these structures was investigated with an optical microscope with a magnification of forty. To track the temporal evolution of the morphological change, a video sequence of the forming process was taken. Single frames of such a movie are shown in figures 5.2 a)-f). In the vicinity of the contact probe the dendrite-like structure starts to grow and spreads perpendicular to the electrical field until the current compliance is reached. Although it seems that the needle point is the starting point for this structure, for other cells it is observed that the starting point is randomly distributed over the cell and not correlated to the needle positions. Defects and impurities in the pristine films might be the preferred points in which the dendrite-like structure starts to grow, which has also been demonstrated for SrTiO_3 based MIM structures [30]. The duration of the growth is in the range of approximately 200 ms or lower. The perpendicular growth to the electrical field of the dendrite-like structure cannot be explained in terms of an electroforming process due to an enhanced Joule heat-

¹Part of the data was collected as part of the master's thesis of Oliver Peters, Peter Grünberg Institute, Forschungszentrum Jülich GmbH, Jülich, Germany [168].

²The PEEM measurements were taken with the help of Christoph Bäumer, Peter Grünberg Institute, Forschungszentrum Jülich GmbH, Jülich, Germany.

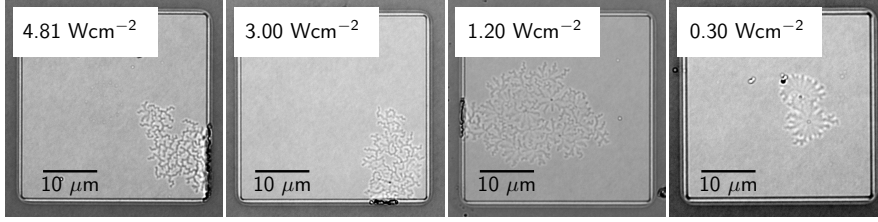


Figure 5.3: Microscope images of $\text{Ta}_2\text{O}_{5-x}$ MIM structures formed with positive voltage prepared with different DC sputtering power densities.

ing [4, 6, 7] and/or an electrical breakdown [8]. Before possible explanations will be discussed, first the morphological structures in dependence of stoichiometry and also the preparation of the top electrode are analyzed.

In chapter 4.3.3 the stoichiometry dependent switching characteristic of $\text{Ta}_2\text{O}_{5-x}$ based MIM has been discussed. For all devices with platinum electrodes fabricated with electron beam evaporation a dendrite-like structure occurs within the top electrode during the electrical forming with positive voltage at the top electrode. figure 5.3 shows a representative top electrode after the forming procedure for each used DC sputtering power density. For all sputtering power densities a dendrite-like structure is clearly visible. For sputtering power densities of 4.81 Wcm^{-2} , 3.00 Wcm^{-2} and 1.20 Wcm^{-2} the shape of the dendrite-like structures looks very similar. The total size of the dendrite-like structure cannot be correlated to stoichiometry or elemental composition of the pristine film. In the case of $\text{Ta}_2\text{O}_{5-x}$ cells prepared with a sputtering power density of 0.30 Wcm^{-2} a differently shaped dendrite-like structure arises during forming. In the cells shown here there are two circular spots visible. Each of them has a spot in the middle from which the dendrite-like arms appear to have grown in the lateral direction. The number of these central spots is not fixed, as there were cells with only one spot, but there were also cells with three spots. The size of these spots has a diameter in the range of $10 \mu\text{m}$ or less.

In chapter 4.3.3 it has been shown that the forming voltage increases with rising oxygen content. Therefore, a critical field at which size and shape of dendrite-like structure change might explain why the size and shape of the dendrite-like structure is different for the nearly stoichiometric film grown with a sputtering power density of 0.30 Wcm^{-2} . Also the charge carrier concentration of the thin films might have an impact on the propagation of the dendrite-like structure (cf. chapter 4.2.1). Similar observations have been made by Klein [173] in metal-oxide-silicon capacitor systems, where he demonstrated that the type of dielectric breakdown depends on

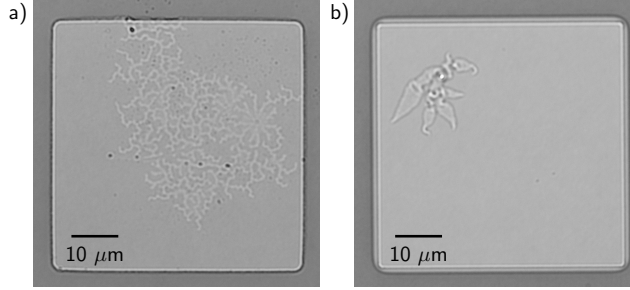


Figure 5.4: Comparison of a) evaporated and b) sputtered platinum electrode after electrical forming [164].

the magnitude of the electric field and he showed an impact of the sample resistance on size and shape of the breakdown channel.

In 4.3.4 the switching parameters of a $\text{Ta}_2\text{O}_{5-x}$ film sputtered with 1.20 Wcm^{-2} for differently prepared platinum electrodes was presented. It has been shown that the deposition technique and also the type of structuring of the top electrode have an influence on the averaged switching parameters. The cells with top electrodes prepared by evaporation through a shadow mask have higher forming voltages than those prepared by sputtering and lithography. Dendrite-like structures occur at the platinum top electrodes prepared by evaporation through a shadow mask as well as on those structured by lithography. For these cells no difference in size and shape of the dendrite-like structures are visible, although the forming voltages differ. This leads to the assumption that the ion etching of the top electrodes influences the forming voltage due to some reduction at the edges of the sample. However, the interface should not be changed during lithography as there is still the same dendrite-like structure visible than for the devices structured with a shadow mask. Additionally, also sputtered electrodes were studied. The morphologic change in the cells with sputtered electrode differs in comparison to the evaporated ones. The morphological changes of platinum electrodes prepared by evaporation through a shadow mask and sputtering are shown in figure 5.4 a) and b). The devices with evaporated platinum electrodes and structured by lithography are already presented in figure 5.3.

The morphological change of the sputtered top electrode is smaller in comparison to the one for the evaporated cells. There also seems to be a central point at which the structure starts to grow. It is important to note that in contrast to the evaporated top electrodes some of the sputtered ones show no morphology change in the range of measurement accuracy of an optical microscope. The smaller size of the morphologic change might be correlated to the smaller electric field during

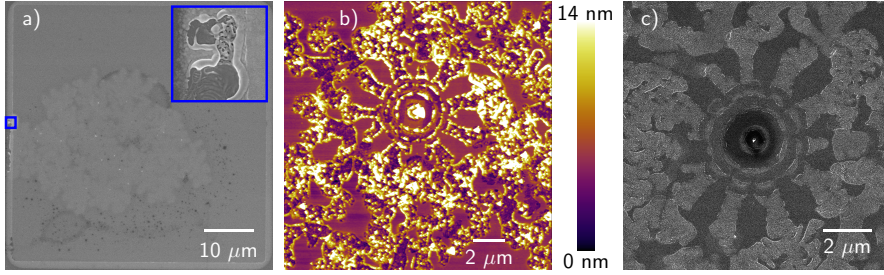


Figure 5.5: a) SEM image of an undelaminated cell. b) AFM scan of a center point of the dendrite-like structure after delamination of the top electrode and c) SEM image of the same position [164].

the electroforming process. However, the magnitude of the electric field should not be the only influencing factor of structure and size of morphological changes. This can be seen by a comparison of the samples prepared by sputtering power density of 1.20 Wcm^{-2} with platinum electrodes evaporated through a shadow mask and those devices prepared with a sputtering power density of 0.30 Wcm^{-2} (stoichiometric) and evaporated electrodes structured by lithography. These devices have a comparable average forming voltage, but the dendrite-like structures are different. For the 1.20 Wcm^{-2} sample the dendrite-like structure is widely spread over the top electrode and the morphologic changes have a meander type shape. In contrast the 0.30 Wcm^{-2} sample shows punctual breakdowns, which are limited to a smaller areas. The interface of both samples should contain some adsorbate due to *ex-situ* preparation, so there should be no difference between the cells. However, for the formation of dendrite-like structures not only an increased electric field is necessary, also the stoichiometry of the cells seems to influence the propagation of the dendrite-like structure.

The dendrite-like structure of the cells prepared for spectroscopic investigation (cf. chapter 4.3.4) are now studied in more detail. In figure 5.5 a) a scanning electron microscope (SEM) picture of a switched electrode is shown. Despite some altered platinum at the edge, which has been melted due to some Joule heat during forming, the electrode remains continuous. The morphology of the former interface is analyzed by AFM after delamination of the top electrode [117, 157]. The dendrite-like structure is clearly visible in the $\text{Ta}_2\text{O}_{5-x}$ layer (cf. figure 5.5 b)). Within this dendrite-like structure, there is a center with circular fronts of which dendrite-like arms extend to the outer regions. The dendrite-like structure has a grainy morphology and is in some regions deeper than the unaltered surrounding. In figure 5.5 c) an SEM image is shown from the same region where the AFM scan is taken. The dendrite-like structure is also visible in the contrast, which

might be correlated to some local variation in the work function [174] as will be discussed in the chapter where the spectromicroscopic results will be presented (cf. chapter 5.2).

The AFM has shown that the morphology within the dendrite-like structure is changed in comparison to the unaltered surrounding. One might presume that the former amorphous $\text{Ta}_2\text{O}_{5-x}$ within this region has been crystallized. In order to prove this assumption nano-diffraction measurements in a scanning transmission electron microscopy (STEM) on a *FEI Titan STEM 80-300* are performed.³ In figure 5.6 a) an SEM image of the investigated structure is shown. The white rectangle marks the region in which the lamella for the cross-section measurement is cut out.⁴ In the cross-section image of the lamella (cf. figure 5.6 b)) the single layers are clearly visible. Due to thickness variation between unaltered surrounding and dendrite-like structure it can be clearly distinguished between the two regions. The black dotted line in figure 5.6 b) indicates the edge of the unaltered surrounding on the left hand side and the dendrite-like structure on the right. A possible explanation for the thickness variation is that the bonding length of $\text{Ta}_2\text{O}_{5-x}$ in the dendrite-like structure is lower than in the unaltered surrounding. The orange rectangle in figure 5.6 b) marks the region where the nano-diffraction measurements are performed. For the $\text{Ta}_2\text{O}_{5-x}$ layer and the tantalum layer two representative diffraction patterns are extracted and shown in figure 5.6 c) and d). The positions where the spectra are taken are marked with a green and red cross respectively. In the pattern from the $\text{Ta}_2\text{O}_{5-x}$ layer no signal of crystallization is visible. It can be concluded that the dendrite-like structure has not crystallized during the electroforming step. Only the metallic tantalum layer shows diffraction patterns. The crystallite size in the tantalum bottom electrode is estimated to be 2 nm.

In order to verify which part of the dendrite-like structure is conductive, LC-AFM measurements are performed at the former $\text{Pt}/\text{Ta}_2\text{O}_{5-x}$ interface. For the measurements it is necessary that the delamination is carried out under UHV conditions in order to prevent oxidation of the investigated material. The detailed description of the UHV delamination is reported in [117]. For the purpose of orientation on the sample after the platinum removal it is necessary to have some markers on the surface for orientation in the LC-AFM measurement tool, which is equipped with an optical microscope. The marker structures in this work are evaporated titanium metal structures with a good adhesion on the $\text{Ta}_2\text{O}_{5-x}$ layer. The former

³Measurements are provided by Manuel Bornhöfft and Dr. Hongchu Du, Ernst Ruska-Centre for Microscopy and Spectroscopy with Electrons, Forschungszentrum Jülich GmbH, Jülich, Germany.

⁴The TEM lamella is prepared by Maximilian Kruth, Ernst Ruska-Centre for Microscopy and Spectroscopy with Electrons, Forschungszentrum Jülich GmbH, Jülich, Germany.

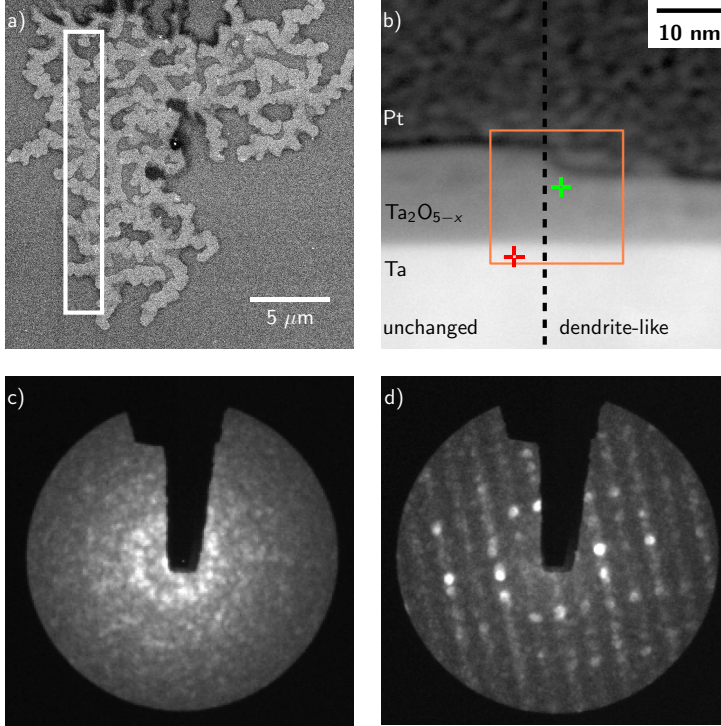


Figure 5.6: a) SEM image of the dendrite-like structure after delamination. The white rectangle marks the region from which the lamella is prepared. b) Cross-section image from a part of the prepared lamella. At the top of the lamella there is platinum from the lamella preparation, then the $\text{Ta}_2\text{O}_{5-x}$ layer and at the bottom the metallic tantalum layer. The orange rectangle marks the region in which the nano-diffraction patterns were taken. The green and red crosses mark the regions, where the diffraction patterns of the dendrite-like c) and the metallic regions d) are extracted [164].

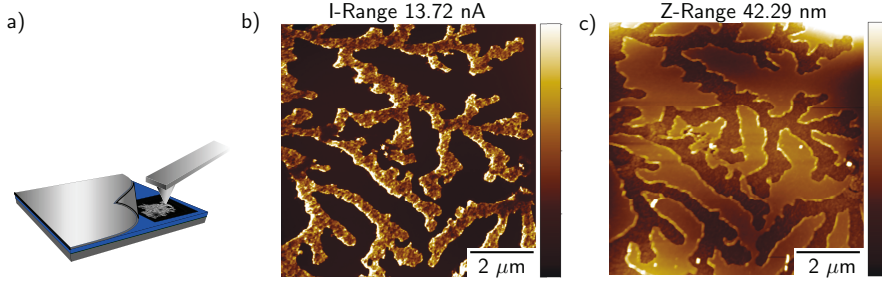


Figure 5.7: a) Depiction of platinum delamination and LC-AFM measurements. b) Current map of dendrite-like structure and c) the corresponding morphology. For the LC-AFM scans a tip voltage of + 10 V is applied [164].

Pt/Ta₂O_{5-x} interface is investigated with a conductive tip.⁵ During the measurements a bias of 10 V is applied to the tip. This relatively large tip voltage is necessary due to adsorbates on the surface or bad conductivity of the tip. The resulting current scan is shown in figure 5.7 c). Regions of enhanced conductivity are visible, which can be correlated to the deeper laying dendrite-like structures of morphology (cf. figure 5.7 c)). The unaltered surrounding is still insulating. Thus it is demonstrated that instead of a small tiny filament the entire dendrite-like structure, which emerges within an insulating matrix during forming, is conductive.

5.1.2 Nb₂O_{5-x}/Ta₂O_{5-x} heterosystem

In addition to the single layer Ta₂O_{5-x} MIM structures also the heterosystem Nb₂O_{5-x}/Ta₂O_{5-x} was electrically characterized in previous chapter (cf. chapter 4.3.5). The dendrite-like structures in Ta₂O_{5-x} based MIM cells have a size of several μm and they are visible within the platinum electrode. In microscopic measurements the appearance of similar dendrite-like structures after the electrical forming of the Nb₂O_{5-x}/Ta₂O_{5-x} cells can be observed. In figure 5.8 a) and b) two cells, one of the 5 nm Nb₂O_{5-x}/10 nm Ta₂O_{5-x} and the other of the 10 nm Nb₂O_{5-x}/5 nm Ta₂O_{5-x}, are shown. For both cell types the dendrite-like structure is clearly visible in the platinum pad. In comparison to the previously studied Ta₂O_{5-x} devices the size of the dendrite-like structure is smaller. The size decreases with increasing thickness of the Nb₂O_{5-x} layer.

⁵The measurements were carried out by Dr. Marco Moors, Peter Grünberg Institute, Forschungszentrum Jülich GmbH, Jülich, Germany.

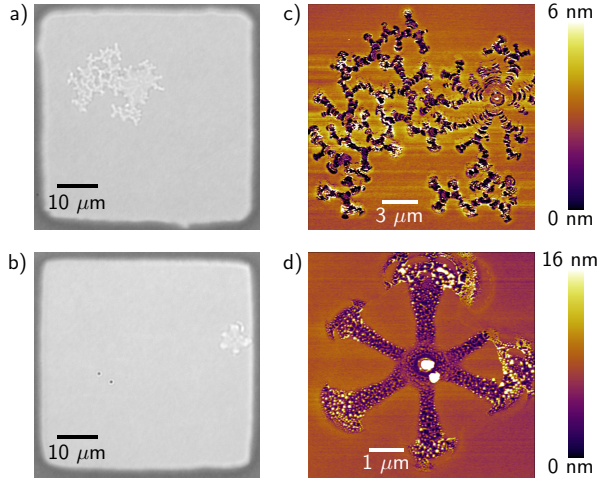


Figure 5.8: a) and b) microscopic images of Pt/5 nm Nb₂O_{5-x}/10 nm Ta₂O_{5-x}/Ta and Pt/10 nm Nb₂O_{5-x}/5 nm Ta₂O_{5-x}/Ta switched cells before the platinum electrode was delaminated. c) and d) AFM scans after delamination of the platinum electrode.

In addition AFM measurements of the dendrite-like areas were performed, after the cells were delaminated. The results are presented in figure 5.8 c) and d). Within these dendrite-like structures, there are centers of which dendrite-like arms extend to the outer regions similar to the case of the Ta₂O_{5-x} cells. The dendrite-like region of the 5 nm Nb₂O_{5-x}/10 nm Ta₂O_{5-x} cell develops with circular shaped fronts in the middle. The dendrite-like structure of the 10 nm Nb₂O_{5-x}/5 nm Ta₂O_{5-x} cell has also a center of which dendrite-like arms extend to the outer regions, but without circular fronts around this center. It is limited to a region of around 1–2 μm and dendrite-like arms extend from this point to the outer region and have a length of approximately 3–4 μm. The structure within in the dendrite-like arms has an increased roughness comparable to the structures presented for the Ta₂O_{5-x} cells. The surface of these structures exhibits little globules, which suggest that the Nb₂O_{5-x} layer was temporary melted and afterwards rapidly cooled down. The lowered thickness within the dendrite-like region might be correlated to a changed atomic bonding in the Nb₂O_{5-x} and Ta₂O_{5-x} layers. The smaller structures occurring in the heterosystem during forming might be correlated to the decreased breakdown voltages and also the increased carrier concentration in the thin films might play an important role for the propagation of the dendrite-like structure.

5.2 Studying the active MIM interface of $\text{Ta}_2\text{O}_{5-x}$ based devices by spectromicroscopy

5.2.1 Dendrite-like structures investigated with a laboratory source

The LRS and HRS of $\text{Ta}_2\text{O}_{5-x}$ based MIM structure are studied by spectromicroscopy. Therefore, cells which are randomly distributed over the entire sample are switched into LRS or HRS. All cells were electroformed with a positive bias at the top electrode. The platinum electrodes are removed under UHV conditions and the sample is transferred *in-situ* to the measurement setup.

Work function of the active interface of $\text{Pt}/\text{Ta}_2\text{O}_{5-x}/\text{Ta}$

First the secondary electrons, which are excited by a mercury lamp ($h\nu = 5.2$ eV), from the dendrite-like structures are studied. Representative PEEM images of the dendrite-like structures are shown in figure 5.9 a) and b) for LRS and HRS. The dendrite-like structures are clearly visible in the secondary electron contrast. In order to quantify energy shifts in the work function, spectral information was extracted for both states from regions of interest (ROI) in the dendrite-like structures as well as in the unaltered surrounding. From the ROI the averaged spectral intensity is extracted. The spectra were extracted and image stacks were investigated using the *IGOR Pro* software. The resulting spectra are shown in figure 5.9 c) and d) for LRS and HRS, where $E - E_F$ indicates the photoelectron energy above the Fermi level (E_F). The work function is defined as secondary electron cut-off of the threshold spectra in relation to the Fermi level (E_F). The determination of the work function is done by fitting the spectra with a convolution of Gauss and Heaviside function [175]. The determined work function values are indicated by the black dotted lines in figure 5.9 c) and d). As the work function is strongly influenced by surface adsorbates, only the relative shifts are discussed and not the absolute values of the work function [176]. For both resistive states the work function of the dendrite-like structure is shifted towards lower kinetic energies compared to the unaltered surrounding, the relative shifts are determined to 0.4 eV and 0.1 eV for LRS and HRS, respectively. This values are representative for the entire dendrite-like structure.

In figure 5.9 e) the composition of the work function is shown, which is the sum of electrochemical potential μ (for example band alignment) and surface dipole Δ [177]. The electrochemical potential μ describes hereby the energetic distance of the Fermi level E_F to the vacuum level $E_{vac,\infty}$, and the surface potential Δ

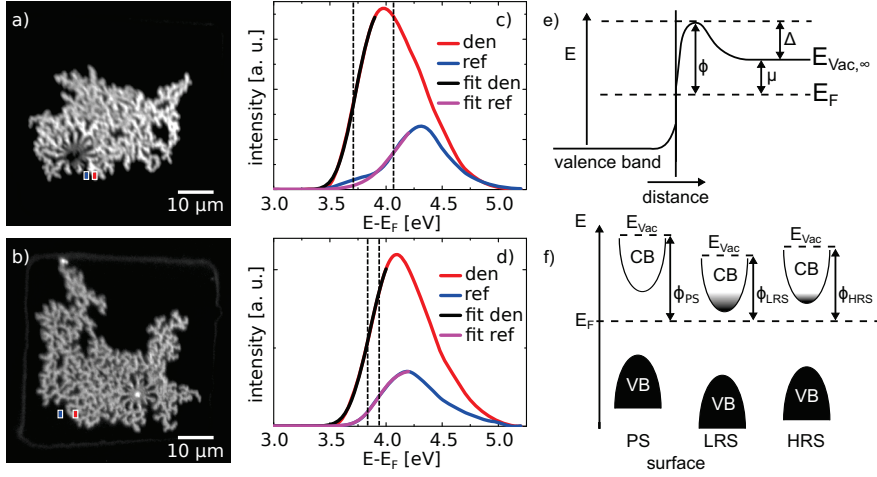


Figure 5.9: Secondary electron image taken at an energy of 4 eV for a) LRS and b) HRS cell. From the regions of interest for the dendrite-like structure (red rectangle) and the unaltered surrounding (blue rectangle) photoemission spectra are extracted for c) LRS and d) HRS. e) Illustration of the relative position of conduction band (CB) and valence band (VB) in relation to the Fermi level (E_F) for the pristine state (PS), LRS and HRS. The work function ϕ is shown for each cell condition. f) Depiction of the energy levels in a semiconductor showing that the work function (ϕ) is composed of surface dipole (Δ) and chemical potential (μ) [164].

is the additional energy barrier, which an electron has to overcome in order to leave the solid. The surface dipoles can be caused by adsorbents and electron density spilling at the solid surface [178]. A variety of material properties can influence the energy barrier height of the surface dipole such as crystallographic orientation [175,179], surface roughness [180] and also surface adsorbents [176]. The electrochemical potential is affected by the internal state of solid e.g. impurities and doping concentration [181]. With increased oxygen vacancy concentration in some transition metal oxides, e.g. TiO_2 , Ta_2O_5 and V_2O_5 [182], the chemical potential is lowered, which means that the energetic distance between vacuum level and Fermi level is smaller than in stoichiometric metal oxides. If the surface potential is not changed significantly the work function for an oxygen deficient oxide is lower in comparison to a stoichiometric oxide. This is correlated with a relative energy shift of the conduction band towards the Fermi level.

The observed energy shifts in the dendrite-like structure can be explained by a relative shift of the conduction band towards the Fermi level (cf. figure 5.9 f)). In case of LRS the distance of the conduction band is the lowest. Similar energetic shifts are also reported for oxygen deficient amorphous $\text{Ta}_2\text{O}_{5-x}$ [145] and an increased donor dopant concentration [146]. An increased donor dopant concentration within the dendrite-like structure indicates an increased charge carrier concentration, which leads to an enhanced conductivity within the dendrite-like structure. This observation is also supported by the previously presented LC-AFM results (cf. chapter 5), where it has been demonstrated that the entire dendrite-like structure at the former $\text{Pt}/\text{Ta}_2\text{O}_{5-x}$ interface is conductive.

Identification of the localization of the switching event by spectromicroscopy

Since the surface roughness of the dendrite-like structure is increased and could change the surface dipoles, the work function shift is not a sufficient spectroscopic evidence for enhanced n -doping. For an explicit proof of increased n -doping within the entire dendrite-like structure it has to be demonstrated that the core level spectra are also shifted towards lower binding energies as it has been recently shown for reduced metal oxides [182]. Therefore, Ta 4f core level spectra are recorded from the same cells as for the work function measurements (cf. figure 5.9).

The photoelectron intensity images of the Ta 4f core level obtained at a binding energy of 26.2 eV are shown in figure 5.10 a) and b) for LRS and HRS. For both resistance states an intensity contrast can be observed, which has a similar shape as the dendrite-like structures also visible in the work function contrast. Because of the intensity contrast Ta 4f spectra of the dendrite-like structure and unaltered surrounding can be extracted from image stacks. The results are presented in figure 5.11 a) and b) for LRS and HRS, respectively. In case of the LRS the Ta 4f core level spectrum is shifted towards lower kinetic binding energy in comparison to the insulating surrounding. For the LRS the shift is less pronounced in comparison to the HRS. The core level shifts can be determined to 0.4 eV and 0.1 eV towards lower kinetic energies. This results clearly proves the previous suspicion that the observed decreased work function is correlated to donor doping in the dendrite-like structure instead of morphological change.

Closer inspection of the extracted spectra leads to the impression that for the LRS cell the dendrite-like region has a broader peak shape than the unaltered surrounding. The drop between the two core levels is less pronounced. In order to get a detailed insight into the differences in chemical composition between LRS and HRS the core level spectra are quantitatively analyzed. Due to the limited photon flux of a laboratory X-ray source, the signal to noise ratio of the measured

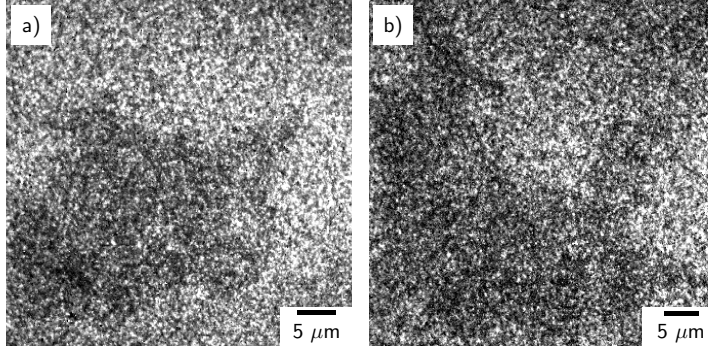


Figure 5.10: PEEM image for a) LRS and b) HRS extracted at a binding energy of 26.2 eV [164].

spectra is low despite a very long integration time (the entire measurement takes several days). A well known procedure for noise reduction in PEEM data is the principal component analysis (PCA) [183,184]. For this analysis, *CasaXPS* version 2.3.16 was used after binning of 4×4 pixel² in order to reduce the noise level. For the spectrum analysis the same fitting model is used as already presented in chapter 4.2.1, where the stoichiometry of different $\text{Ta}_2\text{O}_{5-x}$ layers was investigated by XPS. The results for LRS and HRS are shown in figure 5.11 e) and f). For both cells two components are present in the dendrite-like structure, which can be assigned to $\text{Ta}_2\text{O}_{5-x}$ (blue) and TaO_2 (red), which are absent in the unaltered surrounding. For the cell with lower resistance the quantity of reduced tantalum is significantly increased in comparison to the HRS cell. A map of the spatial distribution of Ta^{4+} and Ta^{5+} is displayed for LRS and HRS in figure 5.11 c) and d). The red colored regions correspond to an increased concentration of Ta^{4+} and the blue regions are associated with the absence of such a component. In case of LRS the entire dendrite-like structure shows a homogeneous increased concentration of TaO_2 . Whereas the HRS dendrite-like region only has a weak contribution of TaO_2 . This is also clearly visible in the representative core level spectra of the dendrite-like region for LRS and HRS, shown in figure 5.11 e) and f). The fraction of TaO_2 in the Ta 4f core level spectra for the LRS is considerably increased in comparison to the HRS, which means that the entire dendrite-like structure undergoes a valence change during switching from LRS to HRS.

The LC-AFM measurements, which show that the entire dendrite-like structure is conductive, confirms the observation that in the dendrite-like structure an additional phase occur, which can be assigned to the conductive TaO_2 [18]. The entire dendrite-like structure in a LRS cell is conductive and connects bottom and top

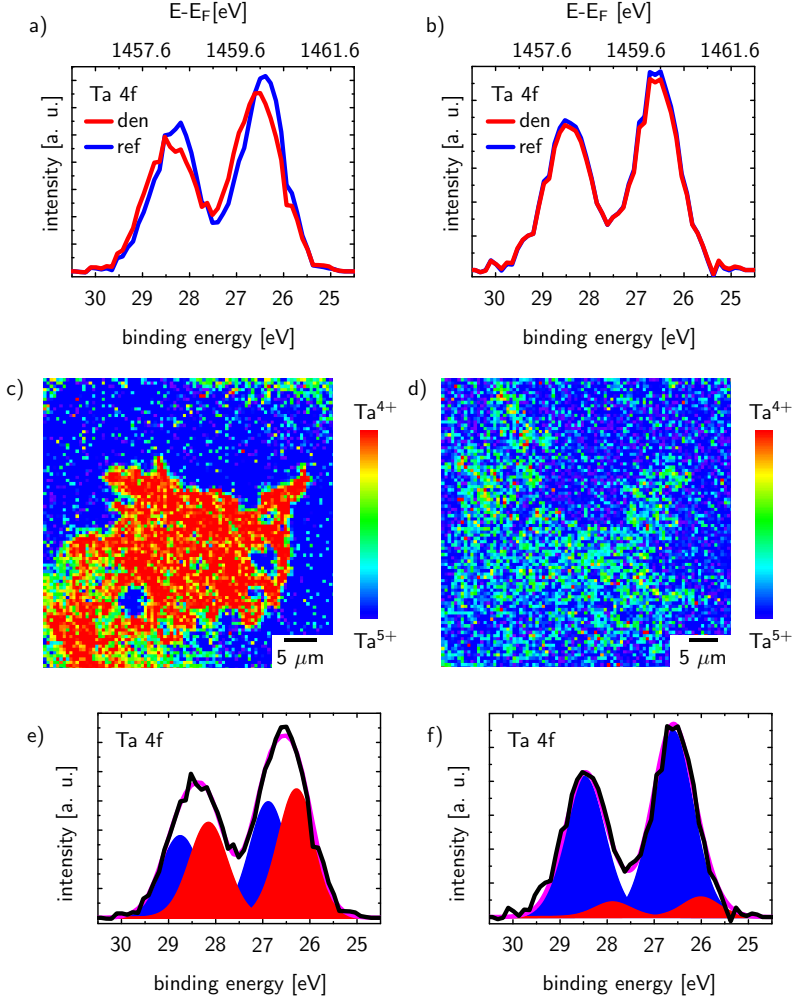


Figure 5.11: Extracted Ta 4f core level spectra for the dendrite-like region (red) and the unaltered surrounding (blue) for a) LRS and b) HRS. False color maps of valence state distribution in the operated cells. The red colored region represents an increased concentration of Ta^{4+} and the blue of Ta^{5+} for c) LRS and d) HRS. The results of the fitting analysis in dendrite-like regions for e) LRS and f) HRS. The red component is correlated to TaO_2 , the blue to Ta_2O_5 and the pink curve represents the total fit for the measured data (black).

electrode (cf. figure 5.12). With subsequently I - V -sweeps the cells can be reversible switched between LRS and HRS. The resistance change in the HRS cells can be attributed to a significant decrease of TaO_2 concentration in the entire dendrite-like region, resulting in a reoxidized layer of $\text{Ta}_2\text{O}_{5-x}$ at the former $\text{Pt}/\text{Ta}_2\text{O}_{5-x}$ interface (cf. figure 5.12). For the reset process it is assumed that oxygen vacancies are moved downward to the tantalum bottom electrode due to the external field. This oxygen vacancy migration is responsible for the observed redox reaction within the top few nanometers of the dendrite-like structure, which results in a Ta_2O_5 layer. This can be regarded as an insulating gap in the cells leading to a cell resistance of several $\text{M}\Omega$.

Due to the limited escape depth of photoelectrons, the thickness of the insulating layer can be estimated. For electrons excited in $\text{Ta}_2\text{O}_{5-x}$ with an Al-K_α source an inelastic mean free path of 2.3 nm at a kinetic energy of 1460 eV is reported [185]. Therefore, it can be concluded that the insulating gap between platinum top electrode and conductive regions in $\text{Ta}_2\text{O}_{5-x}$ is equal to or greater than 2.5 nm.

It is explicitly shown that a valence change occurs during switching at the $\text{Pt}/\text{Ta}_2\text{O}_{5-x}$ interface in $\text{Ta}_2\text{O}_{5-x}$ based MIM structures. The occurrence or the absence of enhanced conductivity in the dendrite-like structure can be correlated with the reduction to TaO_2 or the reoxidation to $\text{Ta}_2\text{O}_{5-x}$. In comparison to previous reports [12,13,18] the reduction and reoxidation takes place not within a small area of a few 100 nm, but over the entire former $\text{Pt}/\text{Ta}_2\text{O}_{5-x}$ interface of the dendrite-like region with a size of several micrometers, which is a consequence of the preparation-induced pronounced interface adsorbate layer. As mentioned at the beginning of this chapter, so far only the formation of a reduced phase after electroforming was shown in several reports [11–14,18]. However, the localization of the insulating gap has never been identified in these reports. The demonstrated valence change at the active interface is a clear proof of the valence change mechanism in $\text{Ta}_2\text{O}_{5-x}$ based memristive devices.

5.2.2 Electroforming process in $\text{Ta}_2\text{O}_{5-x}$

In the last chapters results from a variety of measurements have been presented for $\text{Ta}_2\text{O}_{5-x}$ based MIM structures. Now the results will be discussed and a model for the forming process in the cells will be introduced. The cells are formed with a positive bias at top electrode, which leads to oxygen release at the $\text{Pt}/\text{Ta}_2\text{O}_{5-x}$ interface and the occurrence of a dendrite-like structure at the interface. The resistive switching effect is enabled by a first quasi-static current voltage sweep with a higher forming voltage than the subsequent switching voltage in order to form a conductive filament. At a certain voltage during this sweep the current significantly

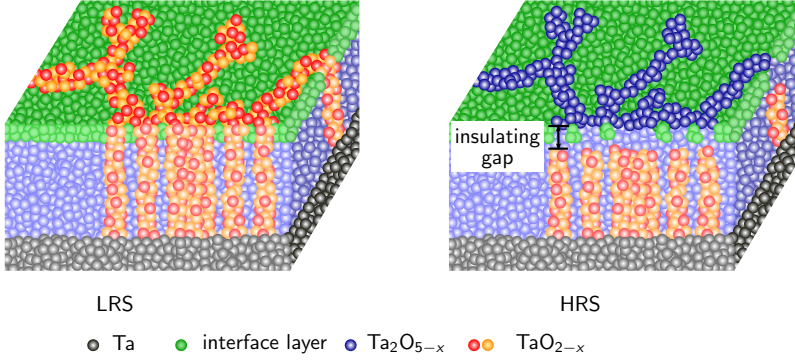


Figure 5.12: A side view of the dendrite-like structure beneath the platinum top electrode with a pronounced interface adsorbate layer (green circles), $\text{Ta}_2\text{O}_{5-x}$ (blue circles), Ta bottom electrode (gray circles), and the conductive channel (orange/yellow circles), which has an increased concentration of TaO_2 . In the LRS cell a conductive path from top to bottom electrode is present. During reset process the entire dendrite-like structure undergoes a valence change between Ta^{4+} and Ta^{5+} . The insulating gap is estimated due to measurement limitations to be equal to or greater than 2.5 nm

increases and leads to a change of the resistance of the cell. For the so-called electroforming process two different approaches exist in literature. The first one is based on ionic processes and the second on electronic processes within the metal oxide. The electroforming step, which is driven by ionic processes, is correlated to the generation of oxygen vacancies at the anode. Due to the applied electric field the oxygen vacancies drift towards the anode. The increased oxygen vacancy concentration leads to an enhanced conductivity. This starts a self-accelerating process where the increased conductivity and Joule heating mutually reinforce. This process results in the formation of a conductive filament, which connects bottom and top electrode [5–7]. However, it has been also demonstrated for the first stage of electroforming that a purely electronic process initiates the forming process [8]. The electroforming in this model starts with reversible electronic processes. Due to electronic instabilities in the devices the initially homogeneous distributed current flow can be restricted reversibly to a localized current path. This process takes place before ionic motion occurs in the metal oxide layer. As soon as Joule heating is sufficient for ionic motion, the formation of a filament starts due to movement of oxygen vacancies, which results in a significant resistance change within the conductive filament.

In both electroforming processes Joule heating plays a significant role in the formation of a conductive filament. In the following it will be discussed if an ionic process or an electronic process driven forming initiates the formation of the dendrite-like structure at the interface. Moreover, it will be considered whether the perpendicular propagation of the dendrite-like structure can be explained by ionic or electronic processes. The nano-diffraction measurements performed on our cells show that the amorphous $\text{Ta}_2\text{O}_{5-x}$ did not crystallize during the electroforming. For the crystallization by post-deposition annealing of thin amorphous $\text{Ta}_2\text{O}_{5-x}$ films a temperature above 873 K was reported in literature [132, 133]. Therefore, it is assumed that the temperature, reached during the electroforming process, is below or equal to 873 K.

To substantiate this assumption, the temperature development during the formation of a conductive filament caused by an electric field between top and bottom electrode and Joule heating with an axial symmetrical model (cf. figure 5.13 a)) were simulated.⁶ The dendrite-like structures typically have a size of several μm and the central part with circular fronts has a diameter of approximately 300 nm. As can be seen in figure 5.13 b) the maximum temperature within the simulated model is less than or equal to 900 K for 100 nm-sized filaments and a current compliance of 300 μA . The temperature rapidly decreases with increasing radius of the filament. For a filament diameter of 300 nm the reached temperature decrease to approximately 500 K. In a filament with a diameter in the μm as it was observed in the dendrite-like structures the temperature, which occurs during the forming process, is even lower. Therefore, it is unlikely that an electric field and Joule heating as reported in literature [6–8] result in these spacious dendrite-like structures. Nevertheless, changes in the tantalum oxygen bonds are observed in amorphous materials for annealing at lower temperatures [186], which is in good agreement with the observation of a new amorphous, conducting phase in the dendrite-like region [12, 13].

Since the models based on ionic and electronic processes can not explain the formation of the dendrite-like structure with a lateral expansion of several μm , other effects included in the forming process will be considered. The electroforming process is comparable with a dielectric breakdown. The difference between these processes is that after a dielectric breakdown the devices are irreversibly switched into a low resistance state whereas in the memristive devices this is prevented by a current compliance. However, the processes that take place before set into LRS should be similar. In the past, numerous analysis were performed to dielectric breakdown in $\text{Ta}_2\text{O}_{5-x}$ prepared by anodization [187–189]. During the oxidation of metallic tantalum prepared by anodization in an aqueous electrolyte morphological changes

⁶The simulations were performed by Dr. Stephan Menzel, Peter Grünberg Institute, Forschungszentrum Jülich GmbH, Jülich, Germany. Detailed information is reported in [164].

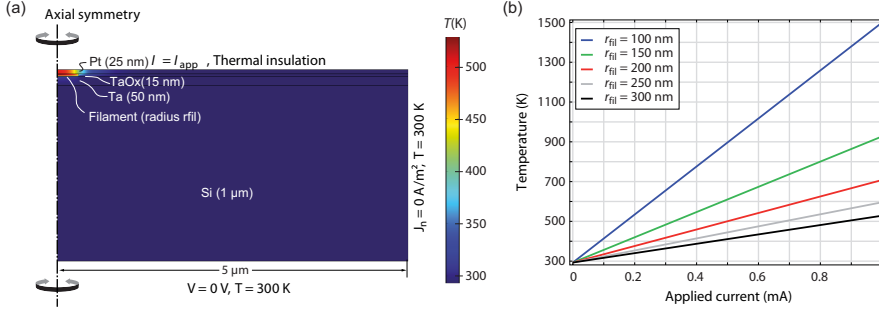


Figure 5.13: a) Depiction of the simulated cell structure with a filament diameter and a current of 1 mA and the boundary conditions. The color scale is correlated to the reached temperature during forming process. b) Temperature development in the simulated cell in dependence of filament diameter and applied current [164].

are reported after breakdown processes. The changed structures are denoted as micro-fissures and cracks [190,191]. The presented structures in these reports have a similar shape compared to the observed dendrite-like structure in this thesis. It is widely accepted in the literature that the breakdown process in this experimental configuration is correlated to an avalanche mechanism [188,192]. The process begins with the formation of free electrons at the upper metal oxide/electrolyte interface. The applied voltage generates an electric field in the range of MV/cm and accelerates the electrons. Due to collision processes in the metal oxide additional electrons are generated. Consecutive chain reactions initiate an electron avalanche. Consequently, an electron avalanche is initialized, which leads to an electrical breakdown after a critical current is reached. During this process sparking and scintillation were observed at the electrolyte/oxide interface, where the discharge paths develop perpendicular to the electric field [192,193].

The avalanche induced breakdown process in a metal oxide/electrolyte system can be adapted to the here presented development of the dendrite-like structure. It is assumed that the MIM structure has an additional interfacial adsorbate layer. The assumed layer structure of the investigated memristive device is shown in figure 5.14 a). The MIM stack consist of the tantalum bottom electrode (gray), Ta_2O_{5-x} layer (light blue), an interface adsorbate layer (blue) and a platinum top electrode (dark gray). The elevation in the Ta_2O_{5-x} layer represents defects/impurities within the thin film. The adsorbate layer leads to an additional capacitance in the memristive device. At the beginning of the forming process, the electric field is homogeneously distributed over the entire cell. At a critical voltage an avalanche discharge is initiated in the adsorbate layer. This discharge

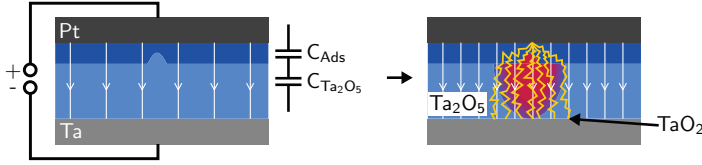


Figure 5.14: Scheme for an additional adsorbate layer which introduces an additional capacitance to the stack [164].

propagates perpendicularly to the applied electric field leading to the dendrite-like structures, which are visible in the top electrode. Due to sparking during avalanche discharge heat is introduced to Ta₂O_{5-x}. In combination with the high electric field this heat leads to a reduction of the Ta₂O_{5-x} layer. This redox process takes place everywhere where sparking occurs (cf. figure 5.14). At the end of the forming process the entire dendrite-like structure is conductive and reduced and the cell is in the LRS.

The starting point of the soft-breakdown event seems to be randomly distributed over the cells. It is assumed that impurities and/or pre-existing defects are the preferred starting points due to their elevated position and electrical field enhancement at these points (cf. figure 5.14). In figure 5.15 the time evolution of the dendrite-like structure is schematically illustrated. The spread of dendrite-like structures in the top electrode and the development of the conductive TaO₂ channels are shown. At the beginning of the formation of a dendrite-like structure at the elevated position a first conductive channel is created. Since the overshoot of the current compliance is relatively large, the avalanche discharge spreads at the Ta₂O_{5-x} surface further. This leads to additional conductive channels in the MIM structure. In contrast to the purely electronic and ionic effects, the origin of dendrite-like filament formation is localized in the additional adsorbate layer on the upper electrode/metal oxide interface and not in the metal oxide layer.

Still the question of whether there is an experimental evidence for the existence of an additional adsorbate layer at the interface remains. In section 4.3 the switching characteristics of Ta₂O_{5-x} cells with different elemental composition and differently prepared top electrodes have been discussed. It has also been shown at the beginning of this chapter that size and shape of the dendrite-like structure depend on the magnitude of the electrical field and the stoichiometry of the thin film. It has been also demonstrated that the preparation of the top electrode has an influence on the morphological changes, which arise after electroforming. The dendrite-like structures in the sputtered films are significantly smaller and there are also some cells where no morphological changes can be obtained. A possible explanation is a difference at the Pt/Ta₂O_{5-x} interface. Due to the *ex-situ* preparation of the elec-

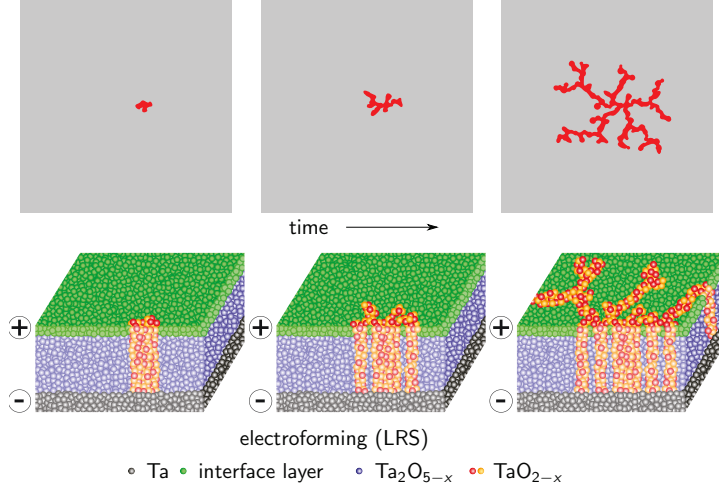


Figure 5.15: Time evolution of a dendrite-like structure during electroforming with positive bias. The growth starts randomly distributed at an initial point and develops perpendicular to the applied electrical field. A side view of the dendrite-like structure beneath the platinum top electrode with a pronounced interface adsorbate layer (green circles), $\text{Ta}_2\text{O}_{5-x}$ (blue circles), Ta bottom electrode (gray circles), and the conductive channel (orange/yellow circles), which has an increased concentration of TaO_2 .

trode adsorbates, such as water or hydrocarbons, are present on the $\text{Ta}_2\text{O}_{5-x}$ surface before electrode deposition. The Ta 4f and C 1s core level spectra of 15 nm thick $\text{Ta}_2\text{O}_{5-x}$ film deposited on a silicon substrate are first analyzed *ex-situ* by XPS. Afterwards the sample is *in-situ* transferred to the evaporation chamber and 2 nm of platinum are deposited on top of the film. After evaporation the sample is transferred back under UHV conditions to the XPS measurement setup and the same core level spectra are recorded again. The recorded spectra are shown in figure 5.16. The red curves represents the core level spectra before deposition of platinum and the black curves are taken with platinum on top. For both films a significant carbon signal is visible, which supports the statement of the pronounced adsorbate layer at the interface for evaporated cells. In a sputtering process this layer should be reduced due to argon ion bombardment during deposition, which partially removes the adsorbate layer. The adsorbate layer of the evaporated electrode in comparison to the sputtered electrodes should be more pronounced due to the lower impact of heat, leading to desorption during evaporation. The existence of such an adsorbate layer for *ex-situ* prepared cells is demonstrated by XPS measurements shown

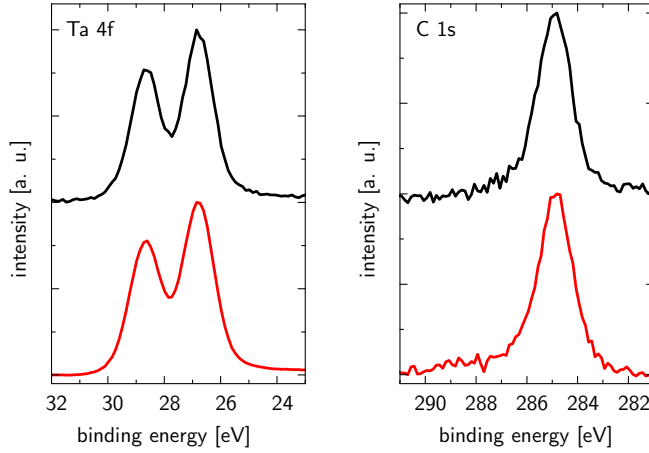


Figure 5.16: Normalized Ta 4f and C 1s spectra measured *ex-situ* of a sputtered $\text{Ta}_2\text{O}_{5-x}$ film (red line) and after *in-situ* deposition of 2 nm Pt and *in-situ* transfer (black line). The interfacial layer is still present at the interface [164].

in figure 5.16. The adsorbate layer introduces an additional capacitance to the layer stack resulting in an increased forming voltage. Since the previous models for electroforming based on ionic and electronic processes localized in the metal oxide layer cannot explain the formation of such large morphological changes and the perpendicular propagation of the dendrite-like structures, an avalanche discharge within the adsorbate layer is the most likely explanation for the formation of the dendrite-like structure.

Finally, the influence of the current compliance on the formation of the dendrite-like structure will be discussed. The response time of the current compliance is estimated to approximately $1 \mu\text{s}$ leading to an overshoot in the switched cells, which is correlated to parasitic capacitance [194,195]. But the current compliance of the voltage source only limits the current between top and bottom electrode. The current overshoot in the here presented cells is higher due to perpendicular propagation of the avalanche discharge. Therefore, the reduced area in the here presented cells is larger, which leads to higher reset currents due to an increased amount of donors in the conductive region.

5.2.3 Dendrite-like structures investigated by synchrotron radiation

A good way to improve the signal to noise ratio of the core level spectra, which also enables a better spatial resolution, is the use of synchrotron radiation, which has a higher flux compared to a laboratory X-ray source. Therefore, the measurements presented in the last section were also performed at the NanoEsca endstation at Elettra synchrotron in Trieste [196]. For the measurements an identical device structure as presented in the last section is used. The platinum top electrode is removed under UHV conditions and the sample is transferred afterwards *in-situ* to the measurement setup. The Ta 4f core level spectra are recorded at a photon energy of 200 eV. Figures 5.17 a) and b) show threshold images of a part of the dendrite-like structure in a switched cell in the LRS. The images are extracted from two different sweeps of the Ta 4f core level measurement. In the first image the dendrite-like structure is clearly visible whereas in the second scan the contrast is almost faded. Under the influence of the synchrotron beam, the material seems to change. In order to quantify the changes under synchrotron radiation spectra of the dendrite-like region (black rectangle) and the unaltered surrounding (red rectangle) are extracted for both sweeps (cf. figures 5.17 c) and d)).

In the first sweep (black curve) there is no indication for a reduced component in the spectrum of the unaltered surrounding. Only for the dendrite-like region a small shoulder at lower binding energies is visible. After the second sweep (red curve) both spectra show an increased low binding energy component, which can be correlated to a reduction of the $\text{Ta}_2\text{O}_{5-x}$ layer or with the formation of carbides (TaC_x) at the surface (for which a binding energy of 23.3 eV has been reported [197–199]) due to highly intense synchrotron radiation. A reduction of the $\text{Ta}_2\text{O}_{5-x}$ layer should not only cause a shoulder at the lower binding energy side, but also cause a shift towards higher binding energy, which is correlated to a shift of the conduction band towards the Fermi level, as was shown in section 5.2. However, the shift of the spectrum in the reference region is in the direction of lower binding energy. This is correlated to a bigger distance of Fermi level and conduction band, which leads to a decrease of charge carriers. Similar shifts have been observed in nitrogen doped $\text{Ta}_2\text{O}_{5-x}$, where the majority carrier type changes from *n*-type to *p*-type due to nitrogen doping [200]. Moreover, it has been reported for carbon doped $\text{Ta}_2\text{O}_{5-x}$ that the leakage current is reduced [201], which is also correlated with a shift of the conduction band away from the Fermi level. This leads to the conclusion that the formation of carbides at the surface is more likely than a reduction of the $\text{Ta}_2\text{O}_{5-x}$ surface.

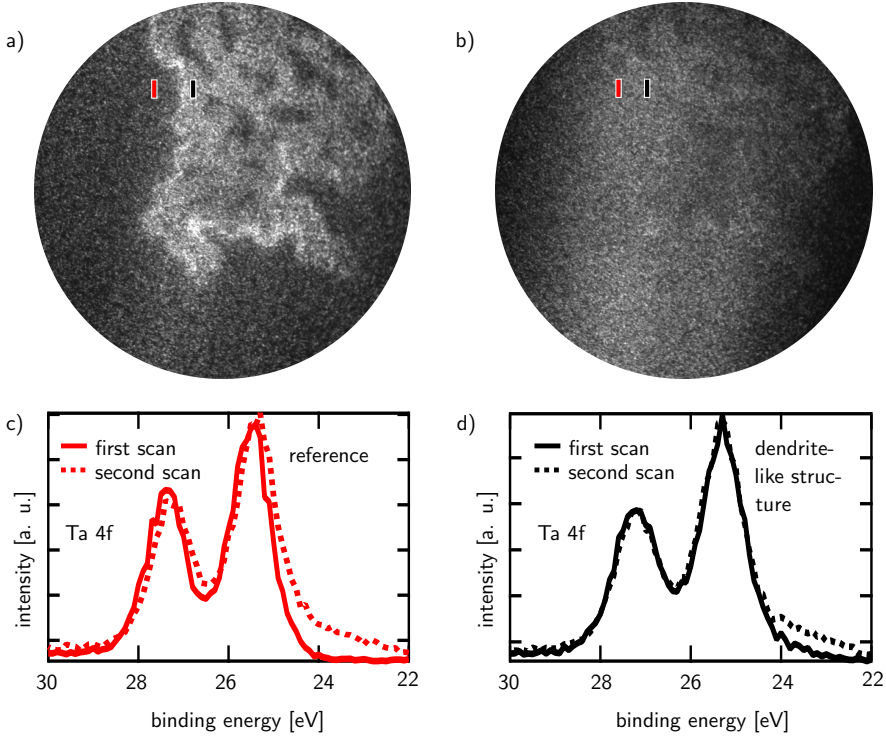


Figure 5.17: Beam reduction a) first scan at a binding energy of 24.5 eV b) second scan at the same energy. c) Extracted spectra of the unaltered region for reference d) extracted spectra from the dendrite-like region.

Due to the rapid formation of carbides it is not possible to record a reliable spectrum from the former $\text{Pt}/\text{Ta}_2\text{O}_{5-x}$ interface. In order to reduce the influence of synchrotron beam radiation on the sample surface the total beam intensity was reduced and Ta 4f core level spectra at different LRS and HRS cells were taken. The temporal stability of the spectra is examined and for the decreased beam intensity no changes in dependence on time can be observed in the core level spectra. At a binding energy of 23.3 eV, which is the TaC_x component [197–199], no signal can be observed and also no other changes are visible for different sweeps. In figure 5.18 a) and b) the core level images for LRS and HRS are shown.

The dendrite-like structure is clearly visible. The edges of dendrite-like structures have a brighter contrast than the dendrite-like structure itself and the unaltered

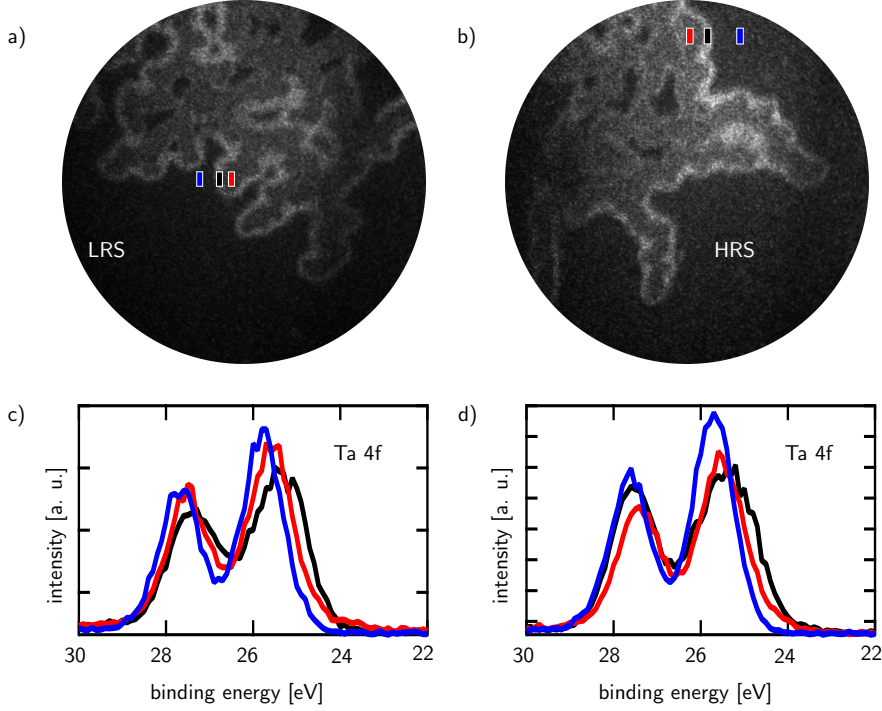


Figure 5.18: Core level images of dendrite-like structures for cells in a) LRS and b) HRS extracted at a binding energy of 25 eV. Extracted Ta 4f spectra from the edge of the dendrite-like structure (black rectangle), unaltered surrounding (blue rectangle) and the dendrite-like structure (red rectangle) for c) LRS and d) HRS.

surrounding. Core level spectra are extracted from the different regions of interest. The resulting spectra are shown in figure 5.18 c) and d) for LRS and HRS. In contrast to the measurement with the Al- K_{α} source there is no clear difference between LRS and HRS visible. The spectra of the dendrite-like structure and the edge of the dendrite-like structure are shifted towards lower binding energy and for both resistance states the core levels are broadened. The shift towards lower binding energies indicates p -type doping or a decrease of n -type doping of the material, which is in contrast to the previous observation in section 5.2. Also the rather large peak broadening is not observed during measurements with the laboratory X-ray source, which means that although the beam intensity is decreased there is still a great influence onto the measured structure.

The VBM (cf. chapter 4.2.1) of these dendrite-like structures are also shifted towards lower binding energy, which supports the interpretation of p -type doping at the upper surface of the $\text{Ta}_2\text{O}_{5-x}$ layer. A possible explanation can be a reaction of the hydrocarbons and water at the surface with the $\text{Ta}_2\text{O}_{5-x}$ layer under assistance of the synchrotron beam leading to a p -type layer at the upper surface. In contrast to higher beam intensities no carbides are formed, but the energy of the beam might still be high enough to create some bonds between $\text{Ta}_2\text{O}_{5-x}$ and the adsorbate at the surface.

This is also supported by the observation that the secondary electron contrast changes during measurements, which can be correlated to a change of the surface potential due to adsorbates. Before synchrotron measurements a work function contrast image of a dendrite-like cell is taken using a Hg source as described in section 5.2 (cf. figure 5.19 a)). The dendrite-like structure is clearly visible and also the edge of the switched cell. After synchrotron measurements a work function contrast image at the same energy is recorded and now a black cross is visible, which corresponds to the beam profile (cf. figure 5.19 b)). At higher kinetic energies the dendrite-like structure is visible again in the secondary electron contrast (cf. figure 5.19 c)), which means that the work function in the dendrite-like region and at the edges is increased. This supports the previous observation from the core level shifts that the upper layer gets p -doped due to synchrotron radiation.

Although measurements at a synchrotron enables higher spatial resolution and a better signal-to-noise-ratio it is demonstrated that under a highly intense beam the upper layer of oxides can be changed. It is assumed that these changes are correlated to hydrocarbons and water at the upper layer. Moreover the information depth of the synchrotron measurements is more surface sensitive in comparison to the laboratory X-ray source. The influence of X-rays of a laboratory source is significantly smaller due to the much lower intensity, which enables the investigation of the valence states of the switched memristive devices.

5.3 Investigation of the active interface of $\text{Nb}_2\text{O}_{5-x}/\text{Ta}_2\text{O}_{5-x}$ heterosystems

The $\text{Nb}_2\text{O}_{5-x}/\text{Ta}_2\text{O}_{5-x}$ bilayer devices, which are characterized here, have the same tantalum bottom electrode as the single layer system. The devices of the studied sample are kept in LRS or HRS and they are randomly distributed over the entire sample. All cells were electroformed with a positive voltage at top electrode. In this section the spectromicroscopic results of the investigated $\text{Nb}_2\text{O}_{5-x}/\text{Ta}_2\text{O}_{5-x}$ bilayer

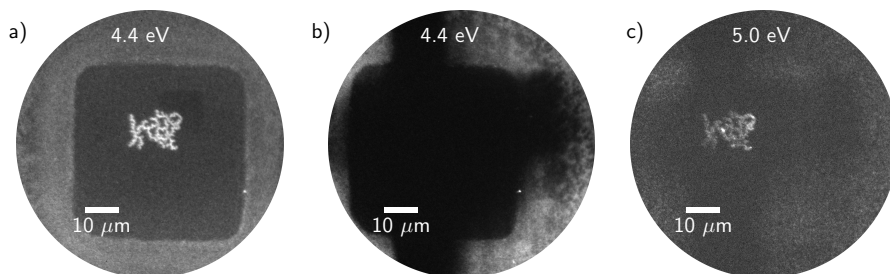


Figure 5.19: Work function images before a) and after XPS measurements with synchrotron beam b) and c). The photoelectrons are excited with a mercury lamp.

devices will be presented. As the used method is surface sensitive it is necessary to remove the top electrode from the analyzed devices. Therefore, the top electrodes are removed with the same method described previously for the $\text{Ta}_2\text{O}_{5-x}$ cells in chapter 4.3.2. First the results of the 5 nm $\text{Nb}_2\text{O}_{5-x}/10$ nm $\text{Ta}_2\text{O}_{5-x}$ devices will be presented and afterwards the results for the 10 nm $\text{Nb}_2\text{O}_{5-x}/5$ nm $\text{Ta}_2\text{O}_{5-x}$ devices. The chemical changes due to electrical forming will be discussed and compared with the previous results from the $\text{Ta}_2\text{O}_{5-x}$ devices.

5.3.1 Pt/5 nm $\text{Nb}_2\text{O}_{5-x}/10$ nm $\text{Ta}_2\text{O}_{5-x}/\text{Ta}$

Work function of former Pt/5 nm $\text{Nb}_2\text{O}_{5-x}/10$ nm $\text{Ta}_2\text{O}_{5-x}$ interface

First the work function contrast of switched cells in LRS and HRS is studied. The results of these measurements are presented in figure 5.20 a) and c). For both cells dendrite-like structures are visible in the work function contrast. This is comparable to the measurements performed on the $\text{Ta}_2\text{O}_{5-x}$ cells. Spectra are extracted from regions of interest, which are defined within the dendrite-like structure and the unaltered surrounding. The extracted spectra are presented in figure 5.20 b) and d). The work function is determined analogues to chapter 5.2.1. The work function in the dendrite-like structures is shifted towards lower energies, which indicates a relative shift of the conduction band towards the Fermi edge. This effect was induced by donor doping in the dendrite-like structure. The work function is shifted by 0.7 eV and 0.4 eV for LRS and HRS towards lower energies. The shift for LRS is higher than for HRS, which is the same trend as observed for the single layer $\text{Ta}_2\text{O}_{5-x}$ MIM structures. In order to verify the increased donor doping within dendrite-like structure, it is necessary to demonstrate also an energy shift of the core level spectra.

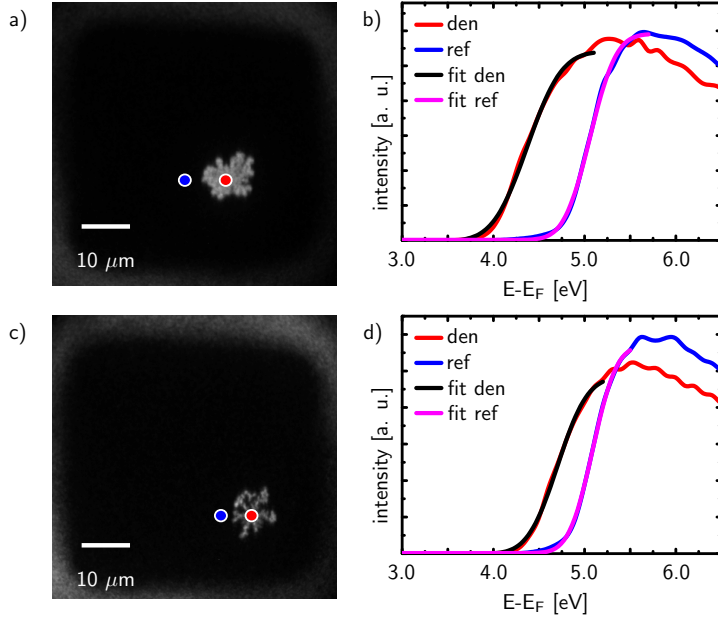


Figure 5.20: Work function images of a) LRS and c) HRS cell extracted at an energy of 4.5 eV. The photoelectrons are excited with an Al- K_α source. Corresponding extracted threshold photoemission spectra for b) LRS and d) HRS.

Nb 3d core level spectra of former Pt/5 nm Nb₂O_{5-x}/10 nm Ta₂O_{5-x} interface

In addition to the work function also the Nb 3d core level of the switched cells are studied by spectromicroscopy. Comparable to the Ta 4f core level spectra for the Ta₂O_{5-x} cells a contrast between the dendrite-like structure and the surrounding is visible in the PEEM images of Nb 3d spectra for LRS and HRS (cf. figure 5.21 a) and b)). Core level spectra are extracted from regions of interest in the dendrite-like structure and the unaltered surrounding. Here, the blue curves are extracted from the surrounding and the red curves represent the spectra within the dendrite-like structure (cf. figure 5.21 c) and d)). The spectra of the dendrite-like structures for the HRS and LRS cells reveal a clear deviation from the surrounding. In comparison to the previously presented results in Ta₂O_{5-x} based MIM structures (cf. chapter 5.2) the signal-to-noise-ratio is lower. The total density of the Nb 3d spectra for the dendrite-like structure is reduced in comparison to the unaltered surrounding. This observation will be discussed in more detail later. The drop between the

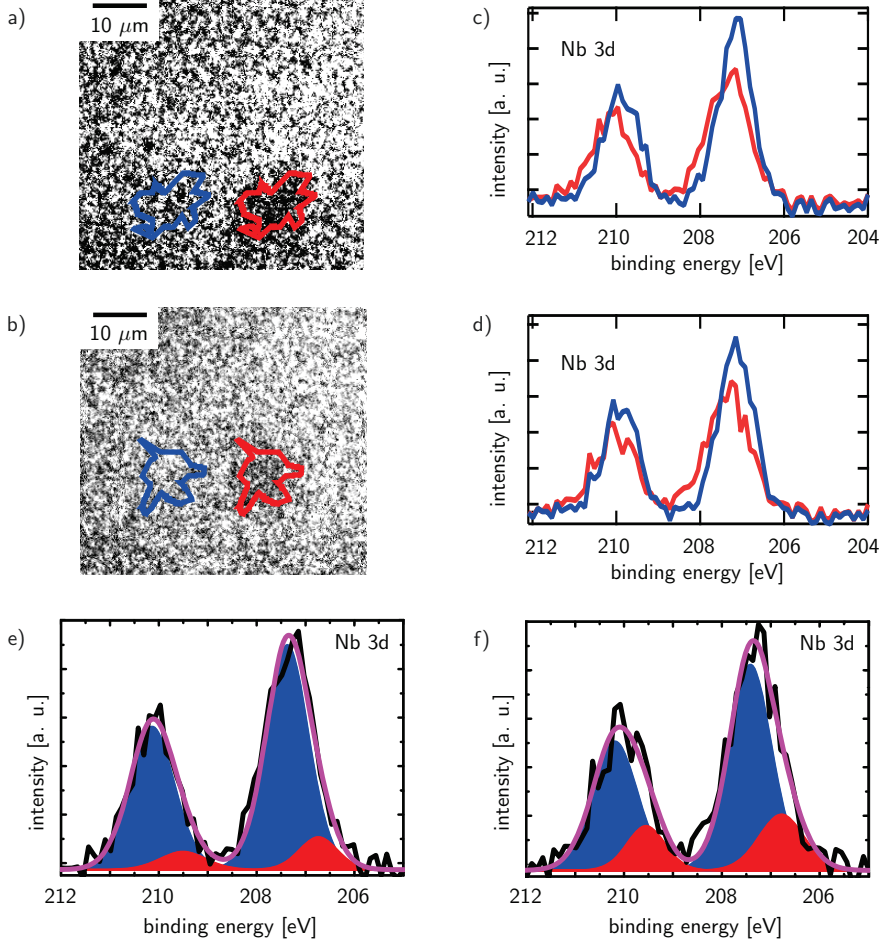


Figure 5.21: PEEM image for a) LRS and b) HRS extracted at a binding energy of 206.8 eV and 207.9 eV. Extracted photoemission spectra of dendrite-like structure (red) and unaltered surrounding (blue) for c) LRS and d) HRS. Fitted Nb 3d spectra for e) LRS and f) HRS. The oxygen deficient niobium oxide is represented by the red component and the stoichiometric niobium oxide by the blue curve.

two core levels is less pronounced and a slight shoulder to lower binding energies is present. The reference spectrum can be described by a doublet for $\text{Nb}_2\text{O}_{5-x}$, whereas for the dendrite-like structure an additional component is necessary for peak fitting analysis. The second component is shifted 0.6 eV towards lower binding energies and can be correlated to a slightly reduced $\text{Nb}_2\text{O}_{5-x}$ [202], which will be referred to as $\text{Nb}_2\text{O}_{5-\delta}$ in the following. This shows that also in the heterosystem a valence change occurs after electroforming. However, the energy shift is not large enough to be assigned to NbO_2 . Typically shifts of 1.3–1.6 eV are reported in literature for NbO_2 [203–205]. Therefore it is assumed that the $\text{Nb}_2\text{O}_{5-x}$ within the dendrite-like structure is reduced, but the oxygen release was not sufficient to create a pure NbO_2 phase.

For both resistance states the dendrite-like structure contains reduced $\text{Nb}_2\text{O}_{5-\delta}$. In contrast to the previously shown $\text{Ta}_2\text{O}_{5-x}$ dendrite-like structure the difference between LRS and HRS is less pronounced, and due to the poor signal-to-noise-ratio it cannot be quantified clearly. The results of the peak fitting for the LRS and HRS cells are shown in figure 5.21 e) and f) for the spectra from the dendrite-like structures. The red peaks represents the oxygen deficient $\text{Nb}_2\text{O}_{5-\delta}$ phase in the dendrite-like structure and the blue ones the stoichiometric Nb_2O_5 .

The energy positions of the $\text{Nb}_2\text{O}_{5-x}$ core levels are shifted about 0.3 eV towards higher binding energies in comparison to the surrounding unaltered $\text{Nb}_2\text{O}_{5-x}$ reference material for both resistance states. In accordance with the discussion of the energy shift of the Ta 4f core level, the shift to higher binding energies in the Nb 3d core levels can be correlated to an increased *n*-type conductivity. The conduction band is shifted towards the Fermi level due to the enrichment of oxygen vacancies in the dendrite-like structure. In contrast to work function measurements, however, the energy shifts are identical for both resistance states. This might be caused by the large regions of interests in comparison to the ones defined for the $\text{Ta}_2\text{O}_{5-x}$ dendrite-like structures, where a PCA analysis was performed and the core level spectra of 3 pixel \times 3 pixel are averaged. The large regions of interests, which are defined for the dendrite-like structure in the $\text{Nb}_2\text{O}_{5-x}$ layer, lead to a more significant averaging of the data. However, it is not possible to define a region of interest for a PCA analysis on the intensity contrast which reproduces the shape of the dendrite-like structure in $\text{Nb}_2\text{O}_{5-x}$ because of the poor signal-to-noise-ratio.

Ta 4f core level spectra

In addition to the Nb 3d core level spectra the Ta 4f core level spectra were measured for the same cells. The inelastic mean free path λ of the photoelectrons within the layers is around 2–3 nm [185], but as already shown in chapter 4.2.3 the

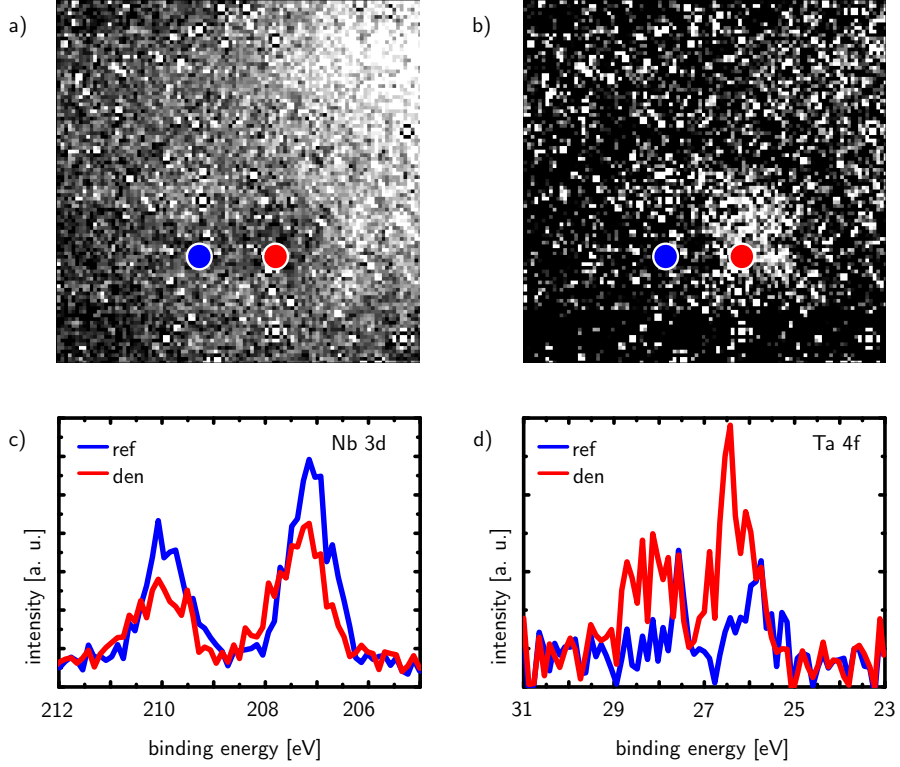


Figure 5.22: PEEM images for a LRS cell of a) Nb 3d and b) Ta 4f core level spectra and the extracted c) Nb 3d and d) Ta 4f spectra from the dendrite-like structure (red) and reference region (blue).

information depth of the system is higher in comparison to the inelastic mean free path. The information depth is defined as the thickness of a layer where 95% of the signal originates from, which is typically in the range of 3λ [206]. The information depth in the heterosystem is estimated to be in the range of 5–8 nm, which is in good agreement to literature. Therefore, we are able to probe the $\text{Nb}_2\text{O}_{5-x}/\text{Ta}_2\text{O}_{5-x}$ interface. The recorded PEEM images for a representative cell are displayed in figure 5.22 a) and b) for the Nb 3d and Ta 4f core levels. Within the dendrite-like structure, a difference in the intensity is visible in comparison to the unaltered surrounding. Core level spectra in defined regions of interest from the dendrite-like structure and unaltered surrounding region are extracted. The spectra are presented in figure 5.22 c) and d). The intensity of the Nb 4f signal is decreased within the dendrite-like structure whereas the intensity of the Ta 4f signal is in-

creased for the same region. Because of the poor signal-to-noise-ratio, the Ta 4f core level spectra are not analyzed with a peak fitting model. However, a shift towards lower binding energies is also obtained in these spectra, which is in good agreement with the previous results of work function spectra and Nb 3d core level scans. Therefore, it might be assumed that also the Ta₂O_{5-x} layer within the dendrite-like structure is oxygen deficient, which has also been observed for the dendrite-like structures in single layer Ta₂O_{5-x} memristive devices.

For quantification the peak areas of the different Nb 3d and Ta 4f core levels are calculated for the considered regions. The ratio $\frac{I_{\text{Ta 4f,den}}}{I_{\text{Nb 3d,den}}} / \frac{I_{\text{Ta 4f,ref}}}{I_{\text{Nb 3d,ref}}}$ is determined to 1.5. This means that the Ta 4f/Nb 3d signal is increased in the dendrite-like structure. The ratios for the HRS and LRS cells are similar. The rise of the intensity within the dendrite-like structure can have different reasons. One possibility is that due to the inhomogeneities in the Nb₂O_{5-x} layer thickness caused by surface roughening the ratio was increased. Another possibility is that an accumulation of tantalum at the upper interface caused by Ta diffusion to the uppermost layer leads to an increase of the Ta 4f core level intensity. To figure out, which of these scenarios is the more likely explanation, some theoretical considerations about the photoelectron intensity in a multi-layer system are presented in the following.

The photoelectron intensity of a homogeneous sample is described by the following equation [207]

$$I = \phi s \int_0^t \exp\left(-\frac{z}{\lambda \sin \theta}\right) dz \quad (5.1)$$

where ϕ is the X-ray flux density in the analysis position, s is an element specific sensitivity factor, z is the distance from the sample surface, t the thickness of the analyzed material, θ the detection angle and λ is the inelastic mean free path of the photoelectrons. The photoemission angle of a photoelectron under normal emission is defined as $\theta = 90^\circ$.

The photoelectron intensities of a sample system consisting of four different layers will be discussed. A depiction of such a sample is shown in figure 5.24. The sample consists of four different layers A, B, C and D with layer thicknesses t_A, t_B, t_C and t_D , while i, j, k, l describes the element, selected independently for the different layers. The summed thicknesses on the left side of the depiction in figure 5.24 show which way an emitted electron has to go through from the respective layer

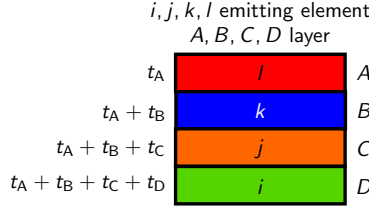


Figure 5.23: Depiction of a stack with four different layers (i, j, k, l) with thicknesses $t_{A,B,C,D}$.

to the surface. The intensity for the single layers of the multilayer system can be calculated by

$$I_l^A = \phi_{sA} \lambda_l^A \sin \theta \left(1 - \exp \left(-\frac{t_A}{\lambda_l^A \sin \theta} \right) \right) \quad (5.2)$$

$$I_k^B = \phi_{sB} \lambda_k^B \sin \theta \exp \left(-\frac{t_A}{\lambda_k^A \sin \theta} \right) \left(1 - \exp \left(-\frac{t_B}{\lambda_k^B \sin \theta} \right) \right) \quad (5.3)$$

$$I_j^C = \phi_{sC} \lambda_j^C \sin \theta \exp \left(-\frac{t_A}{\lambda_j^A \sin \theta} \right) \exp \left(-\frac{t_B}{\lambda_j^B \sin \theta} \right) \left(1 - \exp \left(-\frac{t_C}{\lambda_j^C \sin \theta} \right) \right) \quad (5.4)$$

$$I_i^D = \phi_{sD} \lambda_i^D \sin \theta \exp \left(-\frac{t_A}{\lambda_i^A \sin \theta} \right) \exp \left(-\frac{t_B}{\lambda_i^B \sin \theta} \right) \cdot \exp \left(-\frac{t_C}{\lambda_i^C \sin \theta} \right) \left(1 - \exp \left(-\frac{t_D}{\lambda_i^D \sin \theta} \right) \right). \quad (5.5)$$

For the sample in the pristine state and for the unaltered surrounding area the layer system is the following: layer A is 5 nm $\text{Nb}_2\text{O}_{5-x}$, layer B 10 nm $\text{Ta}_2\text{O}_{5-x}$ and layer C 50 nm Ta (cf. figure 5.24 a)). In the case of the dendrite-like structure, where the AFM scans (cf. chapter 5.1.2) show some roughening of the surface, five different cases will be discussed and how they influence the intensity ratio of Ta 4f/Nb 3d for the dendrite-like structure and the unaltered surrounding area. In all cases the assumption is made that 50% of the dendrite-like surface have an increased layer thickness where the material of the layers agglomerates. For the deeper regions in the dendrite-like structure a decreased thickness of 2 nm is assumed and for the parts with increased height a thickness of 8 nm is assumed. The averaged thickness of the layer is 5 nm, which corresponds to the $\text{Nb}_2\text{O}_{5-x}$ layer thickness of the pristine region. This is roughly justified by the AFM analysis.

Several cases for the dendrite-like structure of the studied multilayer system ($\text{Nb}_2\text{O}_{5-x}/\text{Ta}_2\text{O}_{5-x}/\text{Ta}$) will be discussed. An overview of the different layer structures in the dendrite-like structure for all considered cases is shown in figure 5.24. The illustrated layers are not to scale. Five different cases which are depicted in figure 5.24 are described shortly in the following

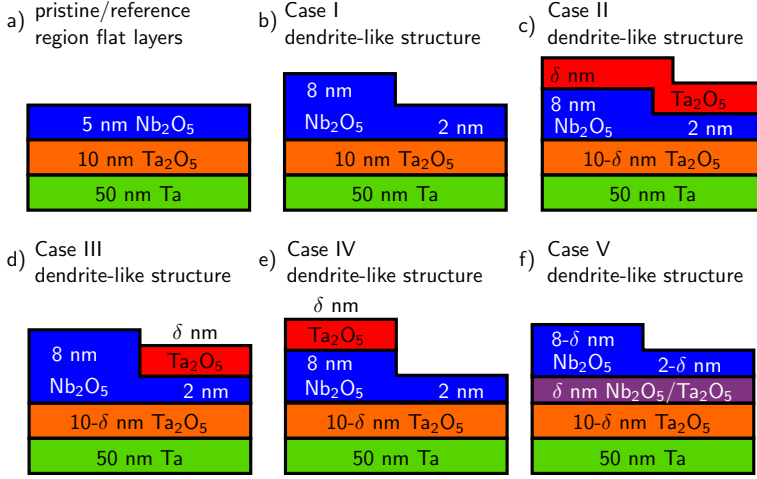


Figure 5.24: Layer models for the consideration of Ta 4f signal increase for the $\text{Nb}_2\text{O}_{5-x}/\text{Ta}_2\text{O}_{5-x}$ heterosystem. δ is here the thickness of the top layer/the intermediate layer. Thicknesses of 0.1 nm and 0.5 nm are used for the calculation.

- (I) only the $\text{Nb}_2\text{O}_{5-x}$ agglomerates, for the thinner parts a thickness of 2 nm is assumed and the remaining structure then has a layer thickness of 8 nm (cf. figure 5.24 b)).
- (II) $\text{Ta}_2\text{O}_{5-x}$ or Ta agglomerates at the surface layer over the entire dendrite-like structure (cf. figure 5.24 c)).
- (III) $\text{Ta}_2\text{O}_{5-x}$ or Ta agglomerates at the surface layer at the thinner dendrite-like structure (cf. figure 5.24 d)).
- (IV) $\text{Ta}_2\text{O}_{5-x}$ or Ta agglomerates at the surface layer at the thicker dendrite-like structure (cf. figure 5.24 e)).
- (V) The $\text{Nb}_2\text{O}_{5-x}$ layer agglomerates as already described in case I. However, there is an additional intermixing layer at the $\text{Nb}_2\text{O}_{5-x}/\text{Ta}_2\text{O}_{5-x}$ consisting of a mixture of $\text{Nb}_2\text{O}_{5-x}$ and $\text{Ta}_2\text{O}_{5-x}$. A mixing ratio for $\text{Nb}_2\text{O}_{5-x}/\text{Ta}_2\text{O}_{5-x}$ of 1:1 is assumed for this layer (cf. figure 5.24 f)).

In figure 5.24 the thickness of the uppermost $\text{Ta}_2\text{O}_{5-x}$ layer and the $\text{Nb}_2\text{O}_{5-x}/\text{Ta}_2\text{O}_{5-x}$ intermixing layer is denoted as δ . For the intensity calculation thicknesses of $\delta = 0.1$ nm and 0.5 nm are considered in the intensity ratio calculation.

emitting element	layer	$\lambda[\text{nm}]$
Ta	$\text{Ta}_2\text{O}_{5-x}$	2.3
Ta	$\text{Nb}_2\text{O}_{5-x}$	2.7
Ta	Ta	2.0
Ta	$\text{Nb}_2\text{O}_{5-x}$	2.7
Ta	$\text{Nb}_2\text{O}_{5-x}/\text{Ta}_2\text{O}_{5-x}$	2.5
Nb	$\text{Nb}_2\text{O}_{5-x}$	2.4
Nb	$\text{Ta}_2\text{O}_{5-x}$	2.0
Nb	$\text{Nb}_2\text{O}_{5-x}/\text{Ta}_2\text{O}_{5-x}$	2.3

Table 5.1: List of all used inelastic mean free paths for the calculation of $\frac{I_{\text{Ta } 4f, \text{den}}}{I_{\text{Nb } 3d, \text{den}}} / \frac{I_{\text{Ta } 4f, \text{ref}}}{I_{\text{Nb } 3d, \text{ref}}}$.

In order to evaluate the intensity ratios for the different considered cases the inelastic mean free path λ values are required for the different materials and emitters (here Ta and Nb). The values are taken from the *NIST Electron Inelastic-Mean-Free-Path Database-Version 1.2* for the corresponding kinetic energy of the emitter [185]. An overview of all used inelastic mean free paths is given in Table 5.1. The layer thicknesses for the different cases can be taken from the particular pictures in figure 5.24. An overview of all calculated $\frac{I_{\text{Ta } 4f, \text{den}}}{I_{\text{Nb } 3d, \text{den}}} / \frac{I_{\text{Ta } 4f, \text{ref}}}{I_{\text{Nb } 3d, \text{ref}}}$ intensity ratio is given in Table 5.2.

The $\frac{I_{\text{Ta } 4f, \text{den}}}{I_{\text{Nb } 3d, \text{den}}} / \frac{I_{\text{Ta } 4f, \text{ref}}}{I_{\text{Nb } 3d, \text{ref}}}$ ratio for the $\text{Nb}_2\text{O}_{5-x}/\text{Ta}_2\text{O}_{5-x}$ intermixing layer (case V) seems to be unchanged due to the value of 0.9 and 1.1 for the assumed values of δ , respectively. However, when the intermixing layer has a thickness of 1 nm the ratio is calculated to 1.5, which fits quite well to the intensity ratio for the representative cell shown in figure 5.22. When only $\text{Nb}_2\text{O}_{5-x}$ agglomerates at the surface (case I) the intensity ratio is increased by 1.9, which is higher than the measured value in this thesis. However, for $\text{Nb}_2\text{O}_{5-x}$ layer thicknesses of 7.3 nm and 2.7 nm the intensity ratio is also 1.5. In this case the morphological structure, which was obtained in the AFM scans, should also be visible in the Ta 4f core level image of the dendrite-like structure. Due to the inhomogeneities of the layer thickness within the dendrite-like structure the total intensity should be increased in the lower areas and decreased in the thicker areas. Due to the poor signal-to-noise ratio and the spatial resolution limit it is not possible to figure this out. It should be noted here, that all considered cases are greatly simplified and the assumed layer thicknesses may differ from the arrangement in the studied dendrite-like structure. Therefore, it should only be estimated which of the scenarios is most likely. For all other considered cases the intensity ratio is higher in comparison to the studied cells. An increase of the thickness of the upper most layer would lead to a significant increase of the intensity ratio, which is correlated to a higher concentration of tantalum at

Case	Layer				$\frac{I_{\text{Ta 4f,den}}}{I_{\text{Nb 3d,den}}} / \frac{I_{\text{Ta 4f,ref}}}{I_{\text{Nb 3d,ref}}}$		
	A	B	C	D	0 nm	0.1 nm	0.5 nm
I	-	Nb ₂ O _{5-x}	Ta ₂ O _{5-x}	Ta	1.9	-	-
II	Ta ₂ O _{5-x}	Nb ₂ O _{5-x}	Ta ₂ O _{5-x}	Ta	-	2.3	3.8
III	Ta ₂ O _{5-x}	Nb ₂ O _{5-x}	Ta ₂ O _{5-x}	Ta	-	2.1	2.5
IV	Ta ₂ O _{5-x}	Nb ₂ O _{5-x}	Ta ₂ O _{5-x}	Ta	-	2.1	3.0
V	Nb ₂ O _{5-x}	Nb ₂ O _{5-x} /Ta ₂ O _{5-x}	Ta ₂ O _{5-x}	Ta	-	0.9	1.1

Table 5.2: Overview of different layer arrangements and the resulting intensity ratios.

the surface. Thus it is unlikely that the cases II, III and IV are in accordance with the morphology in the investigated dendrite-like structure. Because of the limited local resolution a diffusion of tantalum through the surface cannot be completely excluded. However, a stronger increase of the intensity ratio is expected due to a larger contribution of a tantalum layer at top of the dendrite-like structure, which leads to a significant increase of the total Ta 4f intensity. Therefore, it is assumed that the most likely cases for the here studied MIM structure is that an accumulation of the uppermost Nb₂O_{5-x} layer or the formation of an Nb₂O_{5-x}/Ta₂O_{5-x} intermixing layer at the Nb₂O_{5-x}/Ta₂O_{5-x} interface leads to the increase of the Ta 4f/Nb 3d intensity ratio.

5.3.2 Pt/10 nm Nb₂O_{5-x}/5 nm Ta₂O_{5-x}/Ta

After switching and subsequent *in-situ* delamination, the 10 nm Nb₂O_{5-x}/5 nm Ta₂O_{5-x} MIM structures were also investigated by spectromicroscopy. Therefore, the cells were kept in different resistance states. Based on the previous studies on switched cells, first the work function contrast will be discussed. Afterwards the Nb 3d core levels are analyzed for the same cells.

Work function of former Pt/10 nm Nb₂O_{5-x}/5 nm Ta₂O_{5-x} interface

The work function measurements were performed with an Al-K_α source on an LRS and HRS cell. Images of the work function contrast at an energy E-E_F of 4 eV are presented in figure 5.25 a) and c) for LRS and HRS. For quantitative analysis spectra are extracted from the dendrite-like structure and unaltered surrounding. The spectra are displayed in figure 5.25 c) and d). In accordance to the previous analyzed work function measurements the work function for the dendrite-like

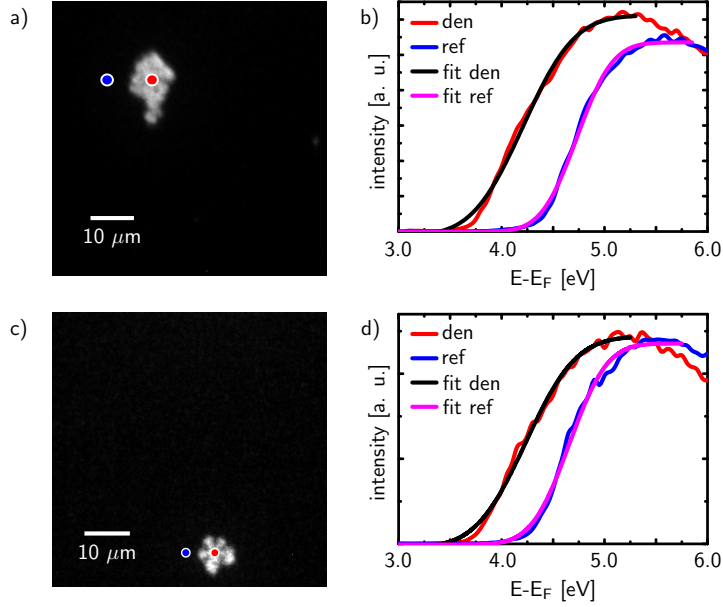


Figure 5.25: Work function scans of an a) LRS and c) HRS cell extracted at an energy of 4 eV. The work function scans are recorded with an Al-K_α source. b) and d) extracted work function scans from the dendrite-like structure (red) and the unaltered surrounding (blue) with corresponding fitting curves.

structure is shifted to lower energies, which can be interpreted as a shift of the conduction band towards the Fermi level. This is correlated to n -type doping within the switching structure. The energy shifts are determined to 0.5 eV and 0.4 eV for LRS and HRS, respectively. In contrast to the previously investigated $\text{Ta}_2\text{O}_{5-x}$ structures and the 5 nm $\text{Nb}_2\text{O}_{5-x}$ heterosystem the energy gap of LRS and HRS is smaller, but still present. In order to verify the increased donor dopant concentration in the dendrite-like structures also the Nb 3d core level spectra will be analyzed.

Nb 3d core level spectra of former Pt/10 nm $\text{Nb}_2\text{O}_{5-x}$ /5 nm $\text{Ta}_2\text{O}_{5-x}$ interface

The Nb 3d core level spectra are measured for LRS and HRS. The PEEM images are shown in figure 5.26 a) and b) for a binding energy of 207.2 eV. The dendrite-like structure is barely visible, but still it is possible to distinguish between dendrite-

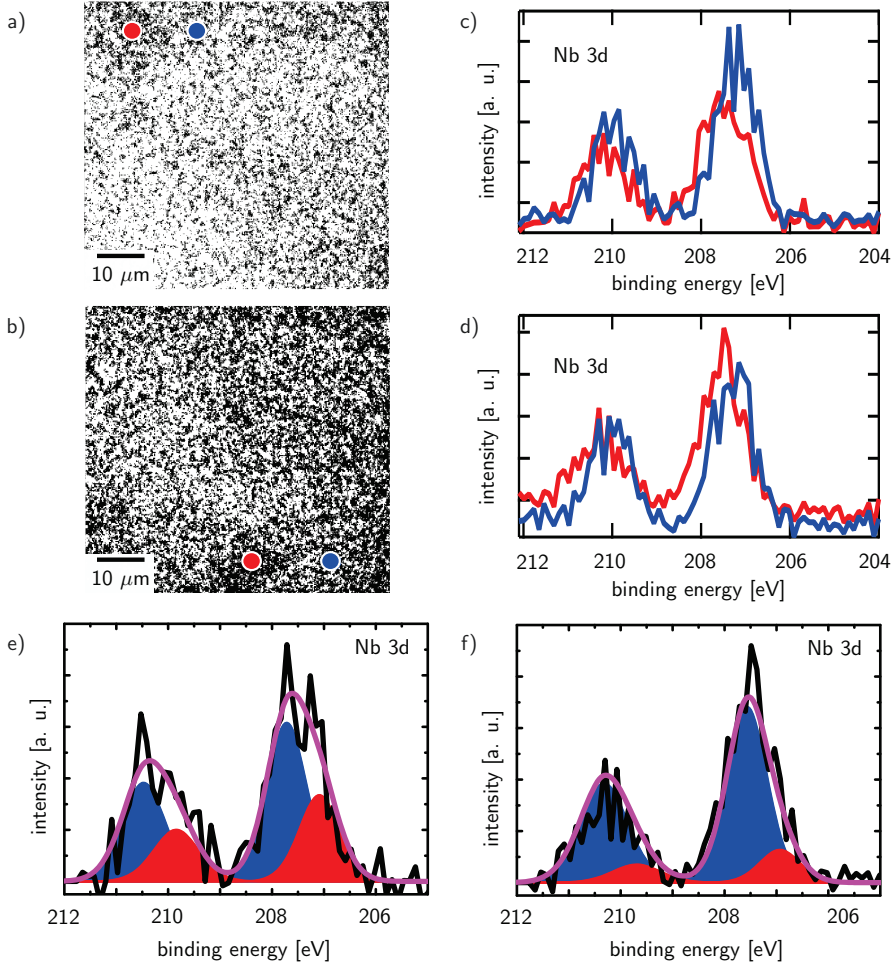


Figure 5.26: PEEM images for a) LRS and b) HRS extracted at a binding energy of 207.2 eV. Corresponding Nb 3d core level spectra from dendrite-like structure (red) and unaltered surrounding (blue) for c) LRS and d) HRS. Fitted Nb 3d spectra for e) LRS and f) HRS. The oxygen deficient niobium oxide is represented by the red component and the stoichiometry one by the blue curve.

like structure and unaltered surrounding. The corresponding extracted spectra are displayed in figure 5.26 c) and d). As can be seen the core level of the dendrite-like structure are also shifted towards higher binding energies and the two core level peaks are broadened towards lower binding energies. This is in accordance with the previously investigated $\text{Nb}_2\text{O}_{5-x}/\text{Ta}_2\text{O}_{5-x}$ heterosystem (cf. section 5.3.1). The spectra are fitted with the same model used in section 5.3.1. Within the dendrite-like structure, a reduced $\text{Nb}_2\text{O}_{5-\delta}$ component is visible similar to the previous discussed 5 nm $\text{Nb}_2\text{O}_{5-x}/10$ nm $\text{Ta}_2\text{O}_{5-x}$, while in the unaltered surrounding this component is absent (cf. figure 5.26 e) and f)). Based on the previous discussion on the binding energy shifts of the oxide core levels, the energy positions of the Nb^{5+} core level for the LRS and HRS cells in relation to the reference spectra are determined. The core level for the dendrite-like structure is shifted 0.4 eV and 0.3 eV for the LRS and HRS towards higher binding energies. That means that both regions have an increased n -conductivity in comparison to the pristine state due to the reduction of the $\text{Nb}_2\text{O}_{5-x}$. The energy gap between LRS and HRS is 0.1 eV, which corresponds well to the already determined value of the work function.

In the previous section 5.3.1 an intensity increase of the Ta 4f core level has been observed within the dendrite-like structure. It is assumed that this difference might be mainly caused by the roughening of the upper $\text{Nb}_2\text{O}_{5-x}$ layer or the formation of a $\text{Nb}_2\text{O}_{5-x}/\text{Ta}_2\text{O}_{5-x}$ intermixing layer. For the structures studied in this section, the Ta 4f core level spectra were also recorded. In the core level image stack no intensity contrast can be observed, only background noise is visible. This indicates that there is no significant amount of Ta diffused towards the interface or to the uppermost oxide layer on top. This observation supports the previous interpretation of the increase of the Ta 4f signal in the 5 nm $\text{Nb}_2\text{O}_{5-x}/10$ nm $\text{Ta}_2\text{O}_{5-x}$ cells.

5.3.3 Discussion

The presence of a region with increased n -type doping after electroforming has been shown for the $\text{Nb}_2\text{O}_{5-x}/\text{Ta}_2\text{O}_{5-x}$ heterosystem with different layer thicknesses. It is assumed that the forming process based on the discussion for $\text{Ta}_2\text{O}_{5-x}$ MIM structures is caused by an avalanche discharge due to a pronounced interface adsorbate layer. As the charge carrier concentration in the pristine layers of the heterosystem is increased in dependence of the $\text{Nb}_2\text{O}_{5-x}$ layer thickness the averaged forming voltages are decreased. This results in smaller dendrite-like structures in comparison to the single $\text{Ta}_2\text{O}_{5-x}$ layer. The dendrite-like structure of the heterosystems can be correlated with the presence of reduced $\text{Nb}_2\text{O}_{5-\delta}$. The energy gap determined by work function scans between the two resistance states (LRS and

HRS) is 0.1 eV for the 10 nm $\text{Nb}_2\text{O}_{5-x}$ sample and 0.3 eV for the 5 nm $\text{Nb}_2\text{O}_{5-x}$ and the $\text{Ta}_2\text{O}_{5-x}$ cells. This might be correlated to a relatively increased donor dopant concentration within the dendrite-like structure of the 10 nm $\text{Nb}_2\text{O}_{5-x}$ cell. However, it would also be possible that due to the limited spatial resolution the averaging over the different pixels leads to the different determined values. It has been demonstrated for $\text{Ta}_2\text{O}_{5-x}$ that the insulating gap arises directly at the former $\text{Pt}/\text{Ta}_2\text{O}_{5-x}$ interface during subsequent switching. The concentration of Ta^{4+} has been significantly increased within the dendrite-like structure for LRS and decreased for HRS. However, due to the poor signal-to-noise ratio of the Nb 3d core level spectra it cannot be judged whether the concentration of the oxygen deficient niobium oxide in the dendrite-like structure of LRS in comparison to HRS one is increased or not.

The missing proof of the valence change in the heterosystem can also be explained by an insulating gap, which does not occur at the upper $\text{Pt}/\text{Nb}_2\text{O}_{5-x}$ interface, but somewhere in between. Due to the limited information depth it is not possible to prove this assumption. The shift of the insulating gap towards the bottom electrode might be caused by the difference of thermal heat capacities of $\text{Ta}_2\text{O}_{5-x}$ [208] and $\text{Nb}_2\text{O}_{5-x}$ layers [209] in the MIM stacks. An altered distribution of heat capacity can induce that the maximum Joule heat does not drop at the active electrode, which is in this thesis the platinum electrode. The place in the layer stack, where then highest Joule heat is localized, might be shifted away from the platinum electrode resulting in an insulating gap within the $\text{Nb}_2\text{O}_{5-x}/\text{Ta}_2\text{O}_{5-x}$ layer stack. This has been reported also for $\text{Ta}_2\text{O}_{5-x}$ based MIM structures with different top electrodes. It has been demonstrated with a physical electro-thermal model of the resistive switching cell that the insulating gap of the memristive devices does not necessarily arise at the active electrode. With decreasing heat capacity the insulating gap is moving towards the oxide layer [210].

5.4 Summary

In this chapter the morphology changes in the top electrode, which arise during the forming process, are investigated. The $\text{Ta}_2\text{O}_{5-x}$ based MIM cells as well as the $\text{Nb}_2\text{O}_{5-x}/\text{Ta}_2\text{O}_{5-x}$ heterosystem show dendrite-like structures, which are spread over the platinum electrode. The growth has a duration of approximately 200 ms or lower. The starting point of the change is randomly distributed and might be correlated to impurities or imperfections in the pristine film. The extent of the propagation is correlated to the forming voltage. Moreover, the properties of the top electrode influence shape and size of the dendrite-like structure, which is caused by different interface and contact properties. In STEM measurements it

is shown that the $\text{Ta}_2\text{O}_{5-x}$ dendrite-like structures are still amorphous, although the total thickness in these structures is decreased. Nevertheless, the most plausible explanation is a change in the tantalum oxygen bonds leading to a decreased layer thickness. With *in-situ* LC-AFM measurements it is demonstrated that the entire dendrite-like structure, which is embedded in an unaltered matrix, is conductive.

The former $\text{Pt}/\text{Ta}_2\text{O}_{5-x}$ interface of dendrite-like structures of $\text{Ta}_2\text{O}_{5-x}$ based MIM structures has been studied by spectromicroscopy with a laboratory source and synchrotron radiation. The dendrite-like structure is caused by an additional adsorbate layer at the former interface layer leading to an avalanche discharge during the electroforming process. In contrast to the electroforming models based on ionic and electronic processes the dendrite-like structures induced by an avalanche discharge are propagated perpendicular to the electric field. The induced heat in this process results in the reduction of the entire dendrite-like structure. The reduced phase is assigned to conductive TaO_2 . This is also supported by previous LC-AFM and work function measurements, which show an increased donor dopant concentration in the entire structure. An explicit proof of the valence change from Ta^{4+} to Ta^{5+} for the subsequent switching is shown within the entire dendrite-like structure.

During measurements with synchrotron radiation changes at the surface occur, which lead to a shift of the conduction band away from the Fermi level. This corresponds to a *p*-type doping of the upper layer. Even with decreased beam intensity still a massive influence of the beam is obtained. The measurements carried out with a standard laboratory X-ray source are stable over the measurement time due to significant lower beam intensities. Therefore, it is concluded that it is not possible to study the switched cells with a highly intense beam.

Additionally, the dendrite-like structure of the $\text{Nb}_2\text{O}_{5-x}/\text{Ta}_2\text{O}_{5-x}$ heterosystem has been investigated by spectromicroscopy. The structures have a lower forming voltage in comparison to single layer $\text{Ta}_2\text{O}_{5-x}$, which results in smaller dendrite-like structures during the electroforming process. The dendrite-like structures are clearly visible in work function contrast and also in the PEEM images of the core levels. The presence of an *n*-type doped region is correlated with dendrite-like structures. Comparable to the results for $\text{Ta}_2\text{O}_{5-x}$ the work function shift for LRS is higher than for HRS. Therefore, it can be concluded that the charge carrier concentration within the dendrite-like structure for LRS is decreased in comparison to HRS for both investigated heterosystems. In the Nb 3d core level spectra a second oxygen deficient component $\text{Nb}_2\text{O}_{5-\delta}$ in addition to the stoichiometric niobium oxide can be identified. This is in good agreement to the results for the $\text{Ta}_2\text{O}_{5-x}$ devices. The oxygen deficient $\text{Nb}_2\text{O}_{5-\delta}$ cannot be assigned to pure NbO_2 or Nb_2O_5 . For the sample with a 5 nm $\text{Nb}_2\text{O}_{5-x}$ layer an increased Ta intensity is observed, which

might be explained by surface roughening of the $\text{Nb}_2\text{O}_{5-x}$ layer occurring during the local heat due to avalanche discharge at the upper interface. Also the formation of an $\text{Nb}_2\text{O}_{5-x}/\text{Ta}_2\text{O}_{5-x}$ intermixing layer at the $\text{Nb}_2\text{O}_{5-x}/\text{Ta}_2\text{O}_{5-x}$ interface would be a possible explanation. In contrast to single layer $\text{Ta}_2\text{O}_{5-x}$ structures there is no direct proof for a valence change at the upper interface during subsequent switching between LRS and HRS. With the recorded Nb 3d core level spectra it cannot be judged whether the proportion of the reduced niobium oxide in the dendrite-like structure is decreased for the HRS compared to LRS. The absence of an insulating gap at the upper interface might also be correlated to the shift of the gap towards the bottom electrode.

6 Point defects and ionic transport in TiO_{2-x}

The electroforming process in memristive devices is based on ionic and electronic processes. The formation and motion of ionic defects as well as the release of oxygen play a major role during electroforming and the subsequent switching. In recent years, especially the ionic defects and their transport properties in single crystals and ceramics were investigated. However, the thin films used for memristive devices are often nano-crystalline, which leads to an increase of the total grain boundary area. This may result in the dilution of impurities within the material and a space charge accumulation. Up to now there is still a lack of knowledge of the formation of ionic defects and their motion in thin films. Therefore, the point defect chemistry and the ionic transport in TiO_{2-x} single crystals and thin films will be investigated in this chapter. The high temperature conductivity of differently oriented rutile (TiO_2) single crystals will be characterized, which were investigated first as reference material. Furthermore, the influence of the crystal orientation on the electric properties and the defect formation within the single crystals were analyzed. Afterwards, the sample preparation of the TiO_{2-x} thin films by reactive sputter deposition onto r-plane sapphire single crystals will be described and their HTEC characteristics for different thicknesses will be presented. The thin film results will be discussed with respect to the single crystal. Furthermore, the equilibration kinetics in TiO_{2-x} as a model material will be investigated. By changing rapidly the surrounding oxygen atmosphere an oxygen concentration gradient is introduced to the surface of the studied sample. The change of defect concentration is correlated to the electric conductivity and therefore the relaxation process can be monitored by measuring the electrical conductivity of the sample as a function of time. In a first step the relaxation processes in bulk TiO_{2-x} for (001) and (110) orientation will be analyzed and the results will be compared under consideration of geometry and previously published results. Afterwards the diffusion in a 300 nm thin TiO_{2-x} film will be investigated and compared to the results of the single crystals.

6.1 High temperature conductivity in TiO_{2-x}

Single crystalline TiO_2 substrates with a size of $10 \times 5 \text{ mm}^2$ and a thickness of 0.5 mm in (001) and (110) orientation were supplied by Crystec GmbH, Berlin, Germany. The substrates were polished on one side and the electrical platinum contacts were deposited by sputter deposition onto the single crystals. The geometry of the electrical contacts was described in 3.5. The electrical conductivity was investigated in the temperature range of 850 K to 1100 K and an oxygen partial pressure range of 10^{-2} – 10^{-23} bar.

6.1.1 TiO_{2-x} single crystals

TiO_{2-x} (001)

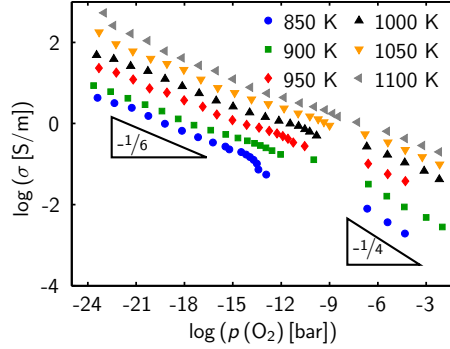


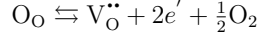
Figure 6.1: HTEC characteristics of a $\text{TiO}_2(001)$ single crystal.

In a first step the HTEC characteristics of a rutile single crystal in (001) orientation is studied. The results are presented in figure 6.1. The conductivity was determined by equation (3.5). The HTEC characteristics show n -type conductivity over the measured $p(\text{O}_2)$ range. At higher oxygen activities (10^{-2} – 10^{-6} bar) and lower temperatures in the range of 850–900 K the region is governed by ionic charge compensation (cf. section 2.3.1).

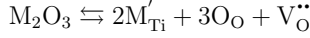
$$2 \left[\text{V}_{\text{Ti}}^{\prime\prime\prime} \right] = \left[\text{V}_{\text{O}}^{\bullet\bullet} \right]$$

The conductivity of a rutile single crystal in this region decreases with a slope of $-\frac{1}{4}$ in the double logarithmic plot. For lower oxygen activities/more reducing conditions the conductivity of the rutile single crystal is determined by the generation

of oxygen vacancies due to oxygen loss. This can be described by the following reaction.



As already mentioned in 2.3.1 the defect chemistry in TiO_{2-x} can be influenced by the trivalent impurities in the single crystals.



Therefore the equilibrium conductivity behavior can also be described by the following charge neutrality equation,

$$[\text{M}'_{\text{Ti}}] = [\text{V}_\text{O}^{\bullet\bullet}]$$

which leads to an oxygen partial pressure dependence on $-\frac{1}{4}$. It is important to note that it is not possible to distinguish between the two compensation mechanisms in the intermediate oxygen partial pressure range by conductivity measurements as both lead to the same oxygen partial pressure dependence.

For lower oxygen partial pressures the conductivity decreases in a double logarithmic plot with a slope of $-\frac{1}{6}$, which is correlated to the following charge neutrality condition

$$n = 2[\text{V}_\text{O}^{\bullet\bullet}].$$

The conductivity oxygen partial pressure characteristics at higher temperatures can be described over the whole measured oxygen partial pressure range with this slope. Therefore, the charge compensation plays a minor role at higher temperatures. The presented conductivity oxygen partial pressure characteristic is in good agreement with the predicted defect chemistry model of TiO_2 .

The enthalpy for the defect formation in the rutile single crystals can be determined from the temperature dependency of the conductivity, which can be described by an Arrhenius-type activated behavior

$$\sigma = \sigma_0 \exp\left(-\frac{E_A}{k_B T}\right). \quad (6.1)$$

The activation energy for $p(\text{O}_2) = 10^{-4}$ bar and $p(\text{O}_2) = 10^{-18}$ bar were determined by an Arrhenius plot (cf. figure 6.2). By fitting the conductivity at a constant oxygen partial pressure the activation energy can be determined to 1.76 eV and 1.37 eV, respectively. The activation energy is a function of the defect formation enthalpy ΔH_f of oxygen vacancies and the migration enthalpy

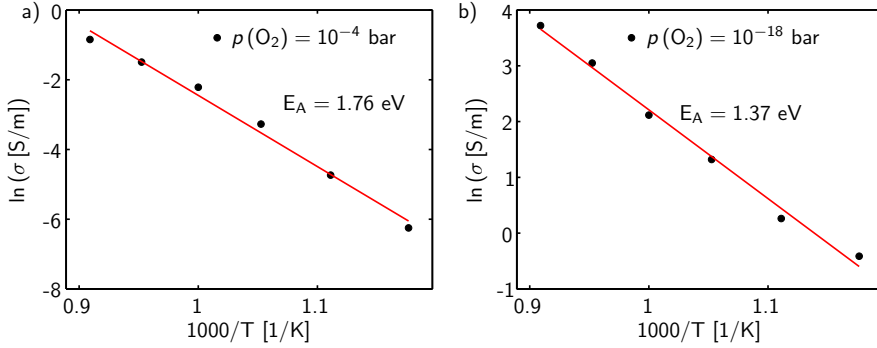


Figure 6.2: Arrhenius plots at a) $p(\text{O}_2) = 10^{-4} \text{ bar}$ and b) 10^{-18} bar for a TiO_2 (001) single crystal.

ΔH_m for electronic defects [211]. Depending on the law of mass action and the defect formation reaction the activation energy can be expressed as follows for 10^{-4} bar

$$E_A = \frac{\Delta H_f}{2} + \Delta H_m \quad (6.2)$$

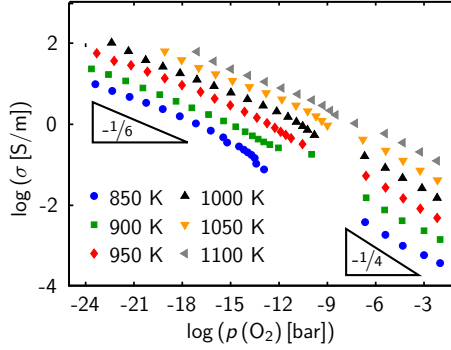
In literature a value of $\Delta H_m = 4 \frac{\text{kJ}}{\text{mol}} = 0.04 \text{ eV}$ [212] is reported for the migration enthalpy of electronic defects. Thus, a formation energy of 3.44 eV was determined. In the reducing oxygen ambient the defect chemistry in the rutile single crystal is dominated by oxygen vacancies compensated by electrons leading to the following dependence on activation energy and formation enthalpy

$$E_A = \frac{\Delta H_f}{3} + \Delta H_m. \quad (6.3)$$

leading to a formation enthalpy for oxygen vacancies of 3.99 eV, which is slightly larger than the previous determined value for the region with a slope of $-\frac{1}{4}$ in the double logarithmic plot. The results will be compared with literature values in the following section 6.1.1, after the presentation of the TiO_2 (110) results.

TiO_{2-x} (110)

In addition to the rutile single crystal in (001) orientation the HTEC for rutile in (110) orientation was also studied. The measured data are presented in figure 6.3. Over the entire oxygen partial pressure regime the rutile (110) single crystal shows

Figure 6.3: HTEC characteristics of a $\text{TiO}_2(110)$ single crystal

n-type conductivity. The conductivity is slightly enhanced in comparison to the previously studied rutile single crystal in (001) orientation, which might be caused by different impurity concentration within the single crystals. The conductivity to oxygen partial pressure dependency is similar to the behavior of the rutile single crystal in (001) orientation. A slope of $-\frac{1}{4}$ at slightly reduced conditions and one of $-\frac{1}{6}$ for reducing conditions can be identified in the double logarithmic conductivity-oxygen-partial-pressure-diagram, which is in good agreement with the previously presented results. The activation energies were determined to be 1.88 eV and 1.22 eV by Arrhenius plots for oxygen partial pressures of $p(\text{O}_2) = 10^{-4}$ bar and $p(\text{O}_2) = 10^{-18}$ bar (cf. figure 6.4 a) and b)). According to the previous calculations, these activation energies result in enthalpies of 3.68 eV and 3.52 eV for the formation of oxygen vacancies, respectively. These results are similar to those determined for the rutile single crystal in (001) orientation.

Comparison of activation energies to literature values

The determined activation energies can be correlated to point defects and the related semi-conducting properties of TiO_2 [66]. The activation energy of the studied TiO_2 single crystals is affected by the oxygen partial pressure, which can be seen in figure 6.5 a). The activation energies in the oxidizing regime ($p(\text{O}_2) = 10^{-2}$ – 10^{-4} bar) are higher than the energies obtained for the reduced regime for both studied rutile single crystals. Under reducing conditions, the activation energy within the measurement accuracy appears to be constant.

In figure 6.5 b) literature values for rutile single crystals and polycrystalline material are displayed for different oxygen partial pressures. The activation energy

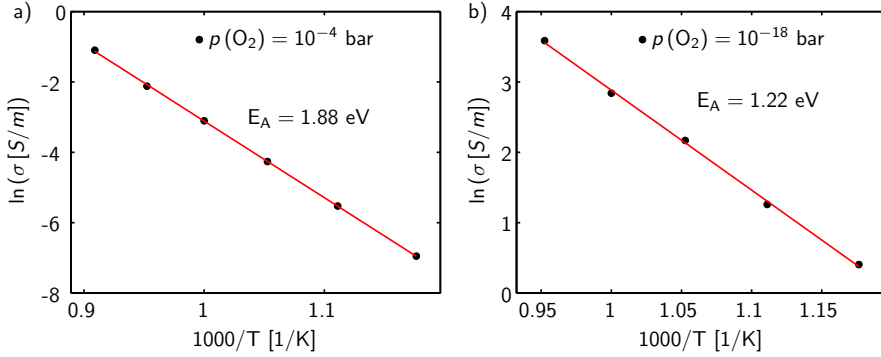


Figure 6.4: Arrhenius plots at a) $p(\text{O}_2) = 10^{-4} \text{ bar}$ and b) 10^{-18} bar for a $\text{TiO}_2(110)$ single crystal.

increases up to a maximum at an oxygen partial pressure range of $p(\text{O}_2) = 10^{-4}$ – 10^{-11} bar and decreases at lower and higher oxygen partial pressures. This is in good agreement with the oxygen partial pressure dependence on the activation energy observed in this study. Also the studied temperatures can influence the activation energy as the temperature is correlated to the predominant point defects. Most of these values were determined at higher temperatures ($\geq 1100 \text{ K}$) than the ones in this study.

6.1.2 High temperature conductivity in TiO_{2-x} thin films

After studying rutile single crystals the HTEC characteristics of thin TiO_{2-x} films were studied. At first the preparation of the thin films will be described. Afterwards the electrical conductivity in dependence on the oxygen partial pressure will be discussed in terms of the TiO_{2-x} defect chemistry model.

Preparation of TiO_{2-x} thin films for HTEC measurements

For the HTEC measurements of a TiO_{2-x} thin film a substrate is required, which is a poorly conductive material and has a low oxygen partial pressure dependence. A material which fulfills the requirements is sapphire. Due to its large band-gap it has highly insulating properties. It was reported for sapphire single crystals that up to 1473 K the conductivity of sapphire does not change significantly with decreasing oxygen partial pressure [218,219]. In this study sapphire with a r-plane orientation

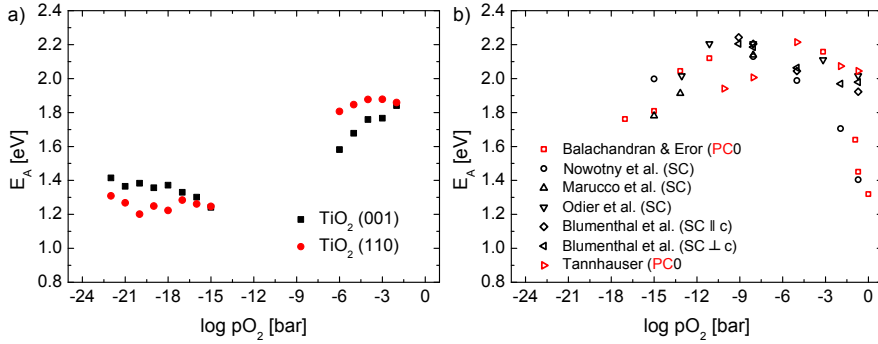


Figure 6.5: Activation energies determined from Arrhenius plots of rutile single crystals in (001) and (110) orientation a) from this study and b) values published in literature for rutile. (Balachandran et al. [68], Nowotny et al. 1997 [213], Marucco et al. [214], Odier et al. [215], Blumenthal et al. [216], Tanhauser et al. [217])

with double-sided polishing was used. In order to create a smooth surface the as-received substrates were annealed for 4 hours at 1000 °C in air. Then the TiO_{2-x} films were deposited by reactive sputter deposition with a power of 75 W at a pressure of $3.5 \cdot 10^{-2}$ mbar and an argon to oxygen mixture with a 3:1 ratio. Films with thicknesses of 100 nm, 200 nm and 300 nm were prepared. A SEM cross-section image of an exemplary as-deposited sample is displayed in figure 6.6 a). For this purpose the sample was scratched at the back with a diamond cutter and then cracked. In the SEM image it can be seen that the TiO_{2-x} grows in orientated columns on the sapphire.

In order to eliminate crystallization effects during the HTEC measurements the samples were annealed for 2 hours at 950 °C in air. A cross-section image of a sample after this preparation step is presented in figure 6.6 b). The surface of the thin film is roughened due to the crystallization and the fine columnar structure of the pristine film is not visible anymore, which might be caused by fusion of the columns during the annealing procedure. The as-deposited and crystallized layer were additionally analyzed with grazing incidence XRD (cf. figure 6.6 c) and d)). In the as-deposited film the anatase phase is predominant. Only the signal at $2\theta = 55^\circ$ can also be assigned to the (211) rutile reflex. After crystallization only rutile signals are detected and additionally the platinum signals of the electrical contacts. All details for the measurement of the HTEC characteristic are described in 3.5.

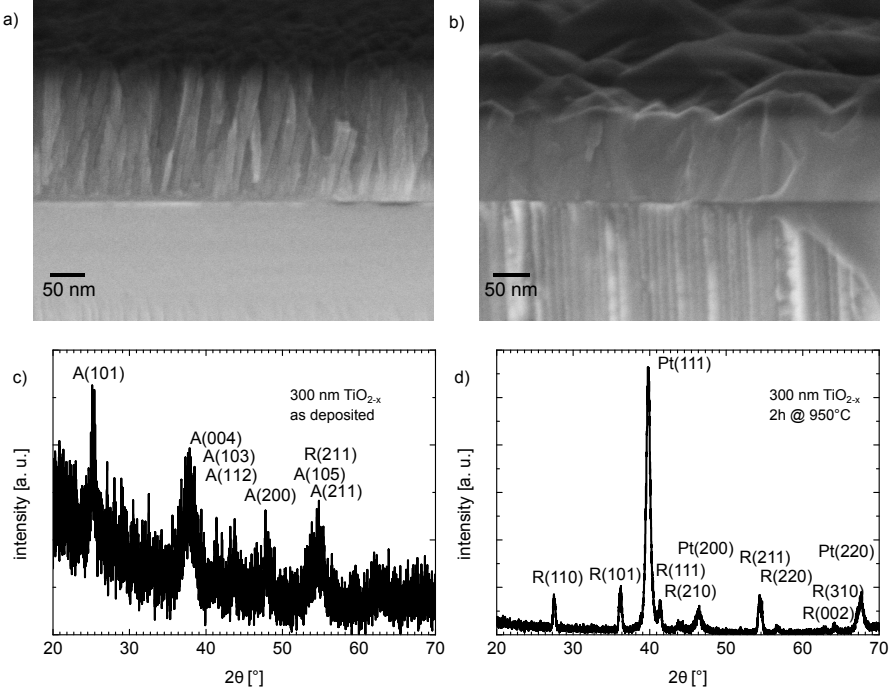


Figure 6.6: a) SEM cross-section image of the as deposited TiO_{2-x} film and b) after post deposition annealing for two hours at 950 °C. XRD measurements of a 300 nm thick TiO_{2-x} thin film c) after deposition and d) after annealing at 950 °C for two hours.

HTEC characteristic of TiO_{2-x} thin films

In this section the HTEC characteristic of a TiO_{2-x} thin film will be presented. The resistance of the thin film was measured parallel to the substrate. First the HTEC characteristic of a r-plane sapphire single crystal was studied in a temperature range of 850–1100 K. In order to improve the electrical contact between the platinum wire and the sputtered platinum contacts additionally platinum paste was used for the contacts. The substrate has a thickness of 0.5 mm, a length of 10 mm and a width of 5 mm. The resulting HTEC characteristic for a r-plane sapphire single crystal is presented in figure 6.7 a). The conductivity of the sapphire substrate changes marginally with decreasing oxygen partial pressure. Moreover, up to a temperature of 900 K there are no significant changes in the conductivity visible. At 1100 K the resistance was decreased by one order of magnitude. In summary,

we demonstrate that a variation of the oxygen partial pressure and temperature leads to no significant changes in the electrical conductivity. Therefore, it can be concluded that sapphire is a suitable substrate for the HTEC measurement of binary oxide thin films e.g. TiO_{2-x} .

As already mentioned, the resistance of the thin films were measured in parallel to the substrate (cf. inset in figure 6.7). Therefore, the measured conductance G_{meas} can be determined as follows

$$G_{\text{meas}} = G_{\text{film}} + G_{\text{substrate}}. \quad (6.4)$$

Taking into account equation (3.5), the conductivity of the film can be calculated.

$$\sigma_{\text{film}} = \frac{l}{bd} \cdot \left(\frac{1}{R_{\text{meas}}} - \frac{1}{R_{\text{substrate}}} \right) \quad (6.5)$$

In the range of $p(\text{O}_2) = 10^{-2}$ – 10^{-6} bar and temperatures lower than 950 K the measured conductance is similar to the sapphire substrate conductance. At lower oxygen partial pressure the conductance of the TiO_{2-x} thin films increases over orders of magnitude, therefore at this oxygen partial pressures the resistance of the substrate can be neglected. The HTEC characteristics of a 100 nm, 200 nm and 300 nm thick TiO_{2-x} film is presented in figure 6.7 b)-d). The conductivity of the thin film was calculated by equation (6.5). For all films n -type conduction is observed. Only at higher oxygen activities ($\geq 10^{-6}$ bar) a slight n - p -transition is visible. At oxidizing conditions (10^{-2} – 10^{-6} bar) the ionic conduction is predominant, which can be seen at the missing slope in the double logarithmic plot of the conductivity versus the oxygen partial pressure. In the entire oxygen partial pressure range the conductivity is dominated by ionic charge compensation. Due to the unavoidable background impurities in the thin films the point defects in this region are dominated by the extrinsic defects, which are described by the following charge neutrality condition (cf. 2.3.1).

$$[M'_{\text{Ti}}] = 2[V_{\text{O}}^{\bullet\bullet}]$$

This defect mechanism corresponds to a characteristic slope of $-\frac{1}{4}$, which can be determined for the measured conductivity data in this study. Slight differences in comparison to the theoretical value can be caused by local variations of defects and their interaction with the grain boundaries [211]. In comparison to the single crystals, which were also studied in the previous section (cf. 6.1), the slope of the HTEC characteristic does not change with reducing characteristic. This observations are in good agreement with previous reported data from Ko et al. [103], where the HTEC characteristic of a 450 nm TiO_{2-x} thick film was reported for temper-

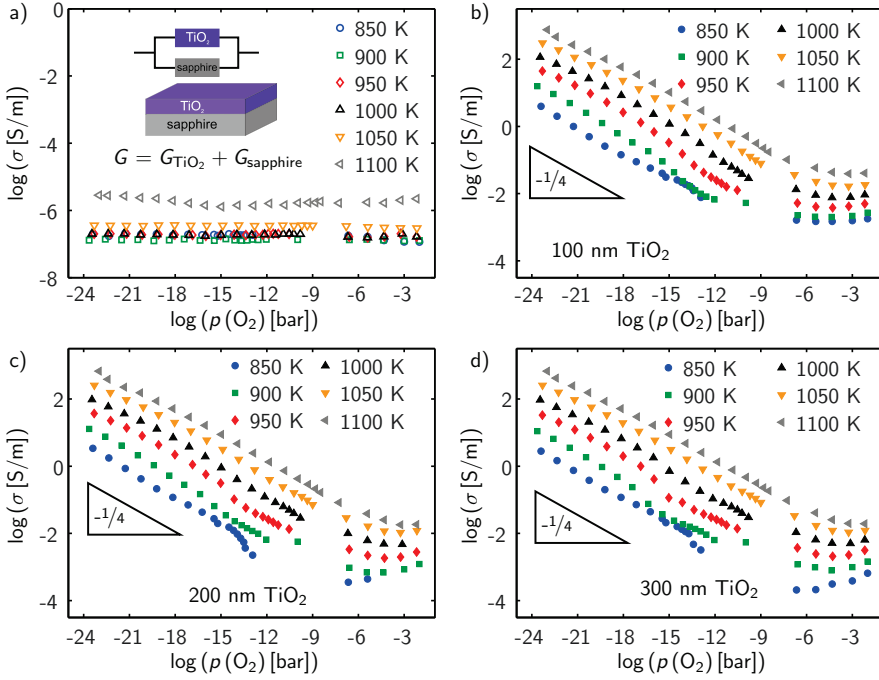
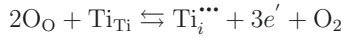


Figure 6.7: a) HTEC characteristic of a r-plane sapphire single crystal. The inset illustrates a simple model for conductance calculations for thin film coatings, where it can be described by a parallel circuit. HTEC characteristic of TiO_{2-x} thin films with b) 100 nm, c) 200 nm and d) 300 nm thickness.

atures of 973 K to 1223 K. In contrast to this study they assigned the slope to the formation of trivalent titanium interstitials ($\text{Ti}_i^{\bullet\bullet\bullet}$), which is also correlated to a slope of $-\frac{1}{4}$.



Due to the lack of data in this report at higher oxygen partial pressure in a temperature range of 973–1123 K, it is hard to figure out whether the region at higher oxygen partial pressure is governed by intrinsic defects ($n=2[\text{V}_\text{O}^{\bullet\bullet}]$). Then a transition of the slope between $-\frac{1}{6}$ to $-\frac{1}{4}$ should be visible at higher oxygen partial pressures and lower temperatures. For polycrystalline material a transition of the slope between $-\frac{1}{4}$ to $-\frac{1}{6}$ was reported for reducing atmospheres [68,211]. Therefore

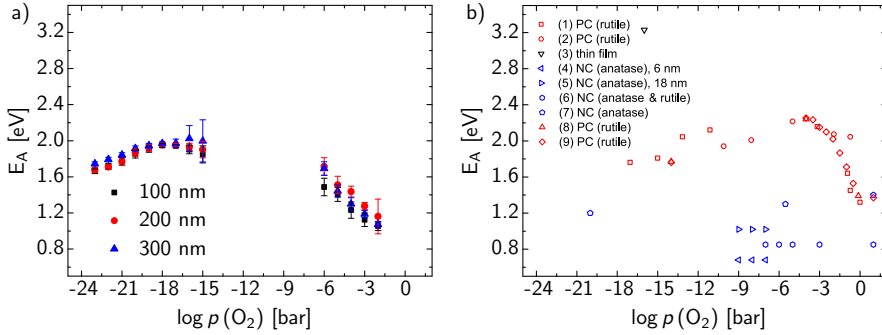


Figure 6.8: a) Activation energy of the studied thin TiO_{2-x} films with different thicknesses. b) Literature values of activation energies for polycrystalline (PC), nanocrystalline (NC) and thin film TiO_{2-x} . ((1) Balachandran and Eror [68], (2) Tannhauser et al. [217], (3) Ko et al. [103], (4) and (5) Huber et al. [220], (6) Dittrich et al. [221], (7) Weibel et al. [222], (8) Nowotny et al. [71], (9) Bak et al. [211].)

it can be concluded that the structure and the grain size of the material influences the defect chemistry in the TiO_{2-x} thin films.

In accordance to the rutile single crystals the activation energy of the TiO_{2-x} thin films were determined by Arrhenius plots. The effect of oxygen partial pressure onto the activation energy is shown in figure 6.8 a). The activation energy increases at high oxygen activities and decreases at reducing conditions. This behavior is valid for all investigated film thicknesses.

For $p(\text{O}_2) = 10^{-18}$ bar and a film thickness of 200 nm the activation energy can be determined to 1.96 eV (cf. figure 6.9 a)), which corresponds to an oxygen vacancy formation enthalpy of 3.84 eV. This result is in good agreement with the previously determined values for single crystalline rutile. Thus the defect formation energy seems not be influenced by the sample size. In comparison to the data published for nanocrystalline materials [220–222] the activation energy is higher in the studied films than in the nanocrystalline material. The difference might be explained by the different phases as most of this data were determined for pure anatase. The activation energy of 3.23 eV reported by Ko et al. [103] has the highest discrepancy to activation energies in this study, which might be explained by different preparation method and investigated temperature ranges. The defect formation energy for oxygen vacancies might also be influenced by space charge zones at grain boundaries and surfaces as it has been recently reported for SrTiO_3 [223, 224]. The space charges are associated with an electrical potential and a defect concentration gradient. The formation energy of oxygen vacancies in the surface layer is lower than in

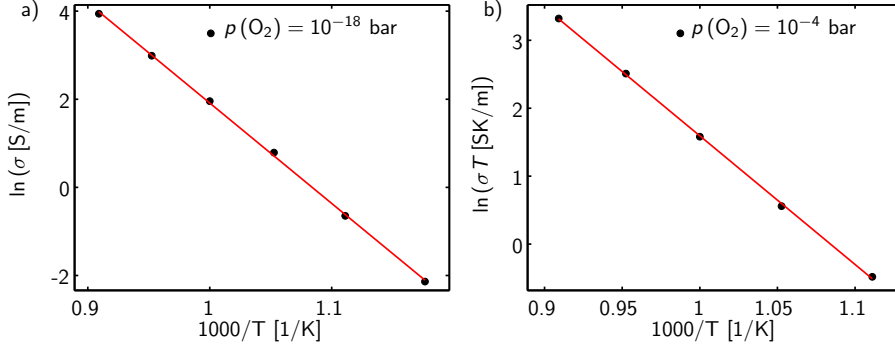


Figure 6.9: a) Arrhenius plot for an oxygen partial pressure of $p(\text{O}_2) = 10^{-18}$ bar for a 200 nm thick TiO_{2-x} film. b) Arrhenius plot for the determination of thermal activation energy of oxygen vacancy diffusion at an oxygen partial pressure of $p(\text{O}_2) = 10^{-4}$ bar.

the bulk. A summary of the literature values for the activation energy is displayed in figure 6.8 b).

In the case of high oxygen activities the conductivity is dominated by ionic conduction. The concentration of oxygen vacancies is pinned by the concentration of acceptor dopants.

$$[M'_{\text{Ti}}] = 2[V_{\text{O}}^{\bullet\bullet}] = \text{const.}$$

With this the conductivity in the oxygen rich partial pressure region can be expressed by

$$\sigma = 2e\mu_{V_{\text{O}}^{\bullet\bullet}}[V_{\text{O}}^{\bullet\bullet}] = e\mu_{V_{\text{O}}^{\bullet\bullet}}[M'_{\text{Ti}}]. \quad (6.6)$$

The oxygen vacancy mobility in the ionic conduction region can be calculated with the Nernst-Einstein-equation [225]

$$\mu_{V_{\text{O}}^{\bullet\bullet}} = \frac{q}{k_B T} D^\sigma \exp\left(-\frac{E_A}{k_B T}\right) \quad (6.7)$$

where q denotes the charge of the species, D^σ is the diffusion coefficient and E_A is the thermal activation energy. With equation (6.6) the ionic conductivity can be described by

$$\sigma_{\text{V}_\text{O}^{\bullet\bullet}} = \frac{2e^2}{k_B T} \left[M'_{\text{Ti}} \right] D^\sigma \exp \left(-\frac{E_A}{k_B T} \right). \quad (6.8)$$

The thermal activation energy of oxygen vacancy diffusion is determined for an oxygen partial pressure of $p(\text{O}_2) = 10^{-4}$ bar by an Arrhenius plot to 1.63 eV (cf. figure 6.9 b)). In literature, values for oxygen vacancy diffusion in thin films are not available, only a few reports for polycrystalline ceramics exist. Burg [226] reports for a temperature range of 1123–1323 K an activation energy of 2.146 eV for an oxygen partial pressure range of $p(\text{O}_2) = 8 \cdot 10^{-5}$ – $4.5 \cdot 10^{-4}$ bar. For higher oxygen activities ($p(\text{O}_2) = 0.60$ – 0.75 bar) an activation energy of 1.53 eV was observed. The activation energy seems to increase for more reducing conditions. The value for higher oxygen activities is in good agreement with the determined value of this work, whereas the value for the comparable oxygen partial pressure range is lower than in the polycrystalline material. Adepalli et al. [227] investigated spark plasma sintered TiO_{2-x} ceramics with dislocations and determined a thermal activation energy for oxygen vacancy diffusion of 1.57 eV at 0.1 bar. In this report the negatively charged dislocations are correlated to space charge zones leading to an enhanced conductivity and at high oxygen activity to ionic conduction. The value determined here fits well to the previously reported results at high oxygen activities.

In contrast to the rutile single crystal, the polycrystalline films have an enhanced ionic conduction in the high oxygen partial pressure regime. The enhanced ionic conductivity for high oxygen activities in TiO_{2-x} has been also reported previously in literature for nano-crystalline material [106, 228–231]. The change from predominant electronic to ionic conduction was explained by dilution of impurities due to an increased size of the grain boundary area. Furthermore, an increase of the space charge regions is discussed as origin for the ionic conduction. In polycrystalline ceramics with grain sizes of several μm no ionic conduction has been observed for high oxygen partial pressures [68, 232, 233]. Therefore, it can be concluded that the ionic conductivity is correlated to the grain boundary size. At a certain grain boundary size the conduction mechanism switches from electronic to ionic. Adepalli et al. [227] show that in polycrystalline ceramics with grain sizes in the μm range conduction changes from electronic to ionic after the creation of line defects by spark plasma sintering. The enhanced ionic conduction was interpreted in terms of an increased titanium vacancy concentration in the dislocations (created by spark plasma sintering) and adjacent space charge accumulation.

For the single crystals a change from ionic charge compensation to intrinsic electronic conduction has been observed for reducing oxygen partial pressure conditions. However, for the thin films only ionic charge compensation has been observed. A

change of the predominant defects has been also reported for an increased acceptor concentration in rutile single crystals [75, 234]. It has been also demonstrated in literature that at temperatures below 1000 K the influence of the background impurities is significant in contrast to higher temperatures [235]. Therefore, it can be concluded that the conduction in the thin films is strongly influenced by the impurities.

6.2 Chemical diffusion in TiO_{2-x}

6.2.1 TiO_{2-x} single crystals

First, the reaction of rutile single crystals to a sudden change in chemical potential is studied. Therefore, ECR measurements were performed (detailed description in section 3.6). The same four point sample geometry is used as for the HTEC measurements (cf. section 3.5). The samples have the same dimensions as the ones used in section 6.1. The relaxation was studied in the reduced regime at an oxygen partial pressure range of 10^{-16} bar to 10^{-20} bar and temperature range of 1000 K to 1100 K. The reducing atmosphere was created with a gas mixture of 4% H_2/Ar and pure argon. All gases were saturated with water before they flow into the measurement setup. The water had a temperature of 0 °C, which corresponds to a vapor pressure of $6.112 \cdot 10^{-3}$ bar [236]. The current pressure is measured at the exhaust of the measurement setup. The corresponding oxygen partial pressure at the sample can be calculated by the procedure described in section 3.6. The total gas flow rate was kept constant during the whole measurement. The pressure in the chamber is adjusted by switching between different gas mixtures. The gas pipes of the setup are permanently flushed with gas to minimize impurities in the gas mixture, which can significantly influence the oxygen partial pressure. In figure 6.10 an exemplary oxygen partial pressure profile for a sample temperature of 1050 K is shown. The oxygen partial pressure at the exhaust is displayed in a logarithmic plot in dependence on the time. The oxygen partial pressure is increased stepwise up to a certain oxygen partial pressure and afterwards decreased. Each of this oxygen partial pressure jumps correspond to a fixed ratio of 4% H_2/Ar to argon. In order to ensure that the diffusion is ambipolar and no other driving forces are present the oxygen jumps are smaller than one order of magnitude. The current resistance of the sample is measured with a four probe setup (cf. chapter 3.5). A constant current is applied to the outer platinum contacts and the voltage is measured at the inner ones. The measurement range of the voltmeter is fixed. The voltage is read out every 750 ms.

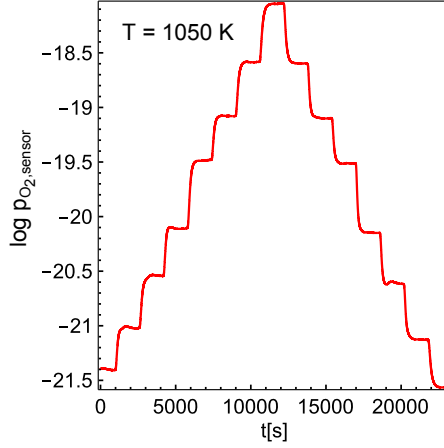


Figure 6.10: Overview of all oxygen partial pressure jumps at a sample temperature of $T_{\text{sample}} = 1050$ K.

TiO_{2-x} (001)

The reaction of a (001) rutile single crystal to changes of oxygen partial pressure is studied first. Within the investigated oxygen partial pressure range, the defect chemistry in the single crystal is dominated by intrinsic defects, such as oxygen vacancies and electrons (cf. section 6.1). The sample was first equilibrated at a certain oxygen partial pressure. Then, a rapid gas exchange was performed. The voltage at constant applied current was measured over time. After some time the voltage converged against a constant value. Since the total number of charge carriers is not known, only the relative changes in conductivity will be considered. Therefore the normalized conductivity is calculated by

$$\bar{\sigma}(t) = \frac{\sigma(t) - \sigma_0}{\sigma_{\infty} - \sigma_0}. \quad (6.9)$$

In figure 6.11 a) three representative relaxation curves for temperatures of 1025 K, 1075 K and 1100 K are shown. The oxygen partial pressure was changed from $1.2 \cdot 10^{-17}$ bar to $3.5 \cdot 10^{-17}$ bar. As can be seen the relaxation process is temperature activated. At a temperature of 1025 K the conductivity converges after approximately 1000 s, whereas at a temperature of 1100 K the conductivity equilibrates already after 700 s.

Before the relaxation curves will be analyzed quantitatively, the values of the conductivity in equilibrium will be determined by averaging over the first and the last

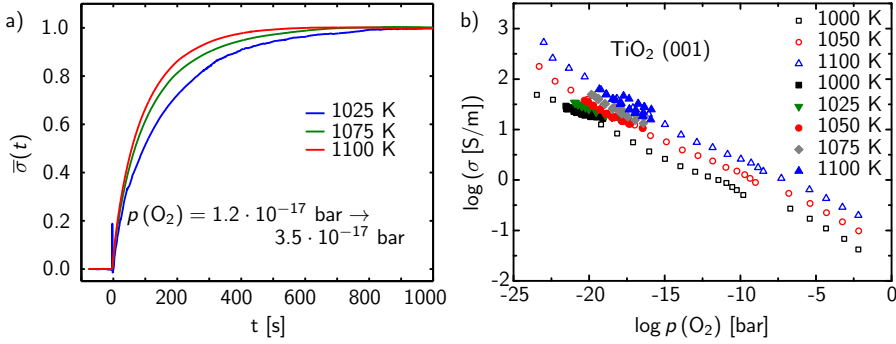


Figure 6.11: a) Normalized electronic conductivity relaxation curves of a $\text{TiO}_2 (001)$ single crystal for oxygen jumps in a temperature range of 1025–1100 K. b) Comparison of HTEC characteristics for $\text{TiO}_2 (001)$. The solid dots represents the data from the ECR measurements and the open circles are from HTEC measurements (cf. section 6.1).

fifty measurement points. All received values are displayed in figure 6.11 b) in dependence on the oxygen partial pressure with solid dots. The conductivity values determined by equilibrium measurements (cf. section 6.1) for $\text{TiO}_2 (001)$ are also shown in figure 6.11 b). The HTEC measurements were not performed at the same sample as the one used for the ECR experiment. However, it can be clearly shown that the high temperature electric characterization of the samples yields very consistent results in both experimental setups (cf. figure 6.11 b)).

In a next step the surface exchange and/or chemical diffusion coefficients will be determined from the relaxation curve. In previous reports bulk dominated diffusion was observed in single crystalline rutile (cf. chapter 2.4.3) and the relaxation curves were fitted with an approximation formula (cf. equation (2.64)). The temperature in these reports starts at 1050 K or was even higher. As the investigated temperature range is lower than in the previous reports, the surface exchange process and the bulk diffusion will be considered both for the equilibration process. All conductivity relaxation curves are analyzed by equations

$$\bar{\sigma}(t) = 1 - \exp\left(-\frac{t}{\tau_f}\right) - \sum_{i,j,k=1}^{\infty} A_{i,j,k} \frac{\tau_{i,j,k}}{\tau_{i,j,k} - \tau_f} \cdot \left[\exp\left(-\frac{t}{\tau_{i,j,k=1}}\right) - \exp\left(-\frac{t}{\tau_f}\right) \right] \quad (6.10)$$

with

$$A_{i,j,k} = \frac{2L_x^2}{\beta_i^2 (\beta_i^2 + L_x^2 + L_x)} \frac{2L_y^2}{\beta_j^2 (\beta_j^2 + L_y^2 + L_y)} \frac{2L_z^2}{\beta_k^2 (\beta_k^2 + L_z^2 + L_z)} \quad (6.11)$$

and

$$\tau_{i,j,k} = \frac{1}{D_{\text{Chem}}} \frac{1}{\left(\left(\frac{\beta_i}{l_x} \right)^2 + \left(\frac{\beta_j}{l_y} \right)^2 + \left(\frac{\beta_k}{l_z} \right)^2 \right)} \quad (6.12)$$

taking all three sample dimension into account. This equation considers both surface exchange and bulk diffusion during the relaxation process. Additionally, it takes a non ideal change of the oxygen partial pressure into account (cf. section 2.4.2). The flushtime for the different temperatures of the cylindrical shaped probe volumes was calculated by

$$\tau_f = \frac{V_r}{\phi_V} \frac{T_{\text{STP}}}{T_r}. \quad (6.13)$$

V_r is the volume of the reactor, ϕ_V is the gas flux through the reactor, T_{STP} corresponds to the standard temperature (here $T_{\text{STP}} = 300 \text{ K}$) and T_r is the reactor temperature. The reactor flushtime for the probe volume lies in the range of approximately 4–6 s. The flushtime is not treated as a fitting parameter, because it has been demonstrated in a previous report that the use of fixed values for the flushtime improves the fitting results for D_{Chem} and k_{ex} [237].

Equation (2.71) cannot be solved analytically due to equation (2.59), which describes the dependence on the surface exchange coefficient k_{ex} , chemical diffusion coefficient D_{Chem} and the respective width of the sample. For each pair of k_{ex} and D_{Chem} equation (2.59) has an infinite number of solutions for $\beta_{i,j,k}$. However, only the first solutions have a significant contribution to the theoretical conductivity relaxation curve. In this thesis the first ten values of $\beta_{i,j,k}$ were considered for the determination of k_{ex} and D_{Chem} . In figure 6.12 a) the best fits determined for the same relaxation curves which were already presented in figure 6.11 a) are shown. The calculated curves fit well with the measured data for all of three presented curves. The best fit was determined by the calculation of the squared error $\chi = \left| \vec{\sigma}_{\text{theoretical}}(t) - \vec{\sigma}_{\text{meas}}(t) \right|^2$. An overview of the different determined squared errors for different values of k_{ex} and D_{Chem} is given with the logarithmic false color map in figure 6.12 b) for the 1100 K conductivity curve. The red color is correlated to high values of the squared error and the dark blue color corresponds to the minimum of the determined squared errors for the analyzed ranges of k_{ex} and D_{Chem} .

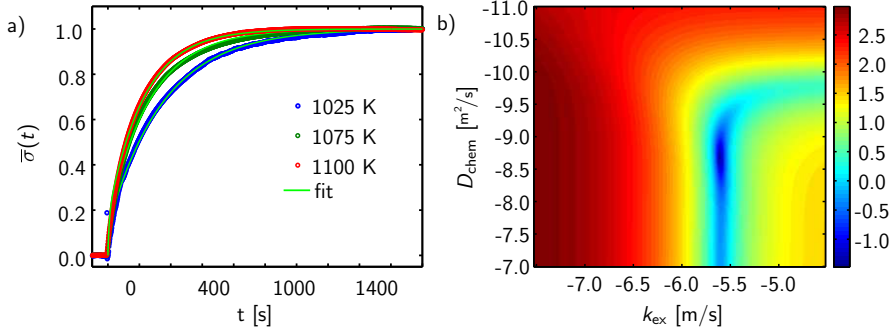


Figure 6.12: a) Electronic conductivity relaxation curves for a (001) orientated rutile single crystal for a temperature range of 1025–1100 K. b) False color map of the logarithm of the squared error matrix for the evaluation of chemical diffusion parameters at $T = 1100$ K.

It is clearly visible in the false color map that the relaxation within the rutile single crystal with (001) orientation is dominated by the surface exchange process, since there is a clear minimum for $\log(k_{\text{ex}} [\text{m/s}]) \approx -5.7$. However, the values for the bulk diffusion coefficient are not reliable due to the broad minimum within the squared error (a variation of D_{Chem} over about two/three orders of magnitude results in similarly well data fits). Therefore, it is not possible to determine in this temperature range the values for k_{ex} and D_{Chem} at the same time. Only the determination of the surface exchange coefficient is possible. However, a lower limit for the chemical diffusion coefficient can be estimated from the false color map, it is about $3 \cdot 10^{-10} \text{ m}^2/\text{s}$ for (001) TiO_2 at 1100 K. An overview of the determined values for k_{ex} is given in figure 6.13 a) for all measured temperatures and oxygen partial pressures.

In contrast to previous results [69] the surface exchange coefficient does not show a convex behavior in dependence on the oxygen partial pressure. No oxygen partial pressure dependence is visible.

The relaxation process is a thermally activated process. The temperature dependence of the exchange coefficient can be expressed by

$$k_{\text{ex}}(T) = k_0 \exp\left(-\frac{E_A}{k_B T}\right). \quad (6.14)$$

Hence, the activation energy for the surface exchange reaction can be determined to 1.17 eV from the Arrhenius plot (cf. figure 6.13 b)) for an oxygen partial pressure

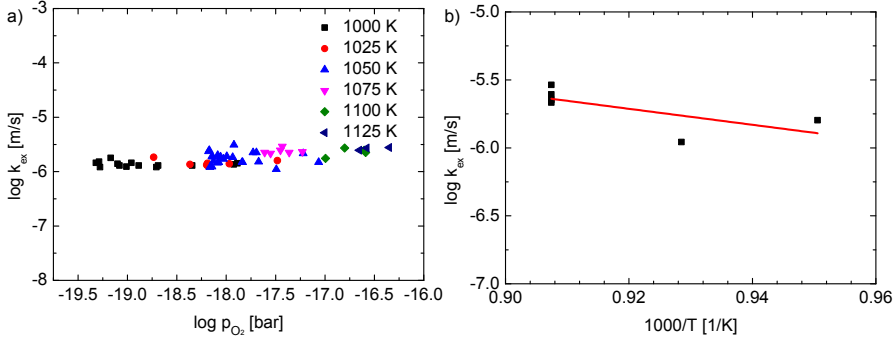


Figure 6.13: a) Surface exchange coefficients for (001) rutile for different reducing atmospheres and b) Arrhenius plot for an oxygen partial pressure of $p(O_2) = 2.5 \cdot 10^{-17}$ bar.

of $2.5 \cdot 10^{-18}$ bar. The temperature dependence of the surface exchange coefficient can be expressed as

$$k_{ex,(001)}(T) = 0.492 \exp\left(-\frac{1.17 \text{ eV}}{k_B T}\right) \text{ m/s.}$$

The results of this section will be discussed in more detail after the electronic conductivity relaxation characteristics of TiO_2 (110) have been analyzed. The results for TiO_2 (110) will be presented in the next section.

TiO_{2-x} (110)

The dominant charge compensation mechanism in (110) rutile single crystals are oxygen vacancies compensated by electrons in the investigated oxygen partial pressure regime. Representative curves for an oxygen jump of $2.4 \cdot 10^{-17}$ bar to $5.8 \cdot 10^{-17}$ bar are shown in figure 6.14 a) for temperatures of 1050 K, 1075 K and 1100 K. The conductivity is normalized by equation (6.9). The relaxation process of the (110) rutile single crystal is also thermally activated. In comparison to the (001) orientation the relaxation process is significantly slower (cf. figure 6.11 a)).

The equilibrium conductivity values at the beginning σ_0 and after equilibration σ_∞ are determined by averaging the first and the last fifty measurement points. All received values are displayed in figure 6.14 b) in dependence on the oxygen partial pressure with solid dots. The conductivity values determined by equilibrium

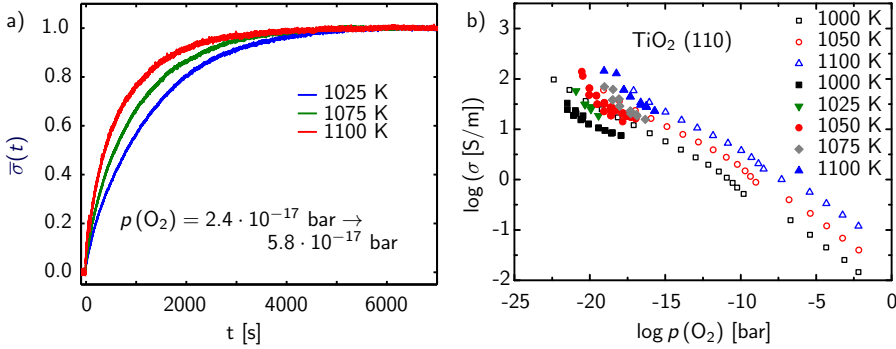


Figure 6.14: a) Normalized relaxation curves for oxygen jumps in a temperature range of 1050–1100 K. b) Comparison of HTEC characteristics for $\text{TiO}_2 (110)$. The solid dots represents the data from the ECR measurements and the open circles are from HTEC measurements (cf. section 6.1).

measurements (cf. section 6.1) for $\text{TiO}_2 (110)$ are also shown in figure 6.14 b). The HTEC measurements were not performed at the same sample as the one used for the ECR experiment. The conductivity values determined by the ECR measurement for (110) TiO_2 are slightly lower in comparison to the values of the HTEC measurement. This might be caused by slightly different temperatures in the measurement setups. The samples which were used for the ECR and HTEC measurements are not the same. Therefore, the impurity concentration of the samples might differ. This might lead to a shift of the transition regime from extrinsic to intrinsic dominated defects towards lower oxygen partial pressures.

In a next step, the relaxation curves will be quantitatively analyzed. The procedure for the quantitative analysis for the determination of chemical diffusion coefficient D_{Chem} and surface exchange coefficient k_{ex} is analogous to the previous section, where the relaxation in $\text{TiO}_2 (001)$ was studied. The resulting best fitting curves are displayed in figure 6.15 a). The determined conductivity curves represent nicely the data for the different temperatures. In figure 6.15 b) the false color map of the squared error matrix for the conductivity at 1100 K is shown. In the false color map it is clearly visible that the diffusion process is dominated by the surface exchange process and the bulk diffusion coefficient has no clear global minimum. The false color maps of the other temperatures also show a clear minimum for the surface exchange coefficient, but no clear results for the diffusion coefficient. Therefore, it is only possible to determine the surface exchange coefficient in this experiment for the different obtained temperatures and oxygen partial pressures. It can be concluded that for the investigated (110) orientated rutile single crystal the relaxation process is dominated by the surface exchange process and the bulk

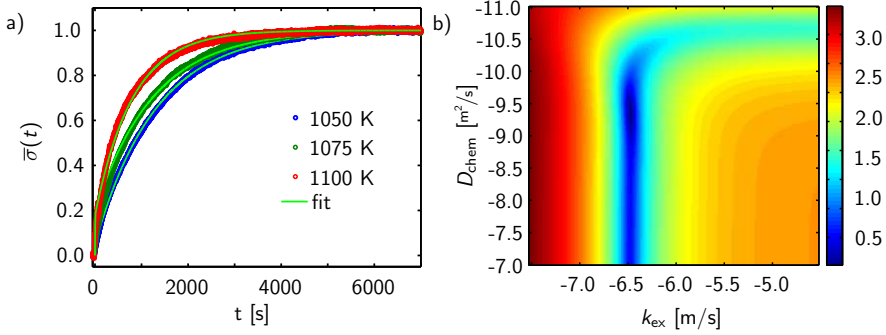


Figure 6.15: a) Electronic conductivity relaxation curves for (110) orientated rutile single crystal for a temperature range of 1050–1100 K. b) False color map of the logarithm of the squared error matrix for the evaluation of chemical diffusion parameters at $T = 1100$ K.

diffusion does not limit the relaxation process. The lower limit of the chemical diffusion is estimated to $6 \cdot 10^{-11} \text{ m}^2/\text{s}$ from the false color map for (110) TiO_2 at 1100 K.

An overview of all determined surface exchange coefficients is displayed in figure 6.16 a) for the different oxygen partial pressures and temperatures. The data show some scattering which might be explained by fitting and measurement inaccuracies. For the fitting analysis the flushtime has been calculated by equation (2.67) for a continuous ideally stirred-tank reactor. The actual flushtime in the probe volume could however differ from this, which can lead to inaccuracies in the determination of k_{ex} and D_{Chem} [84]. Moreover, the measurements in the reduced oxygen partial pressure regime can be influenced by background impurities such as water and hydrocarbons in the probe volume leading to slight different oxygen partial pressures. This slight difference in the oxygen partial pressure might also lead to some scattering of the determined k_{ex} values. Nevertheless, there is no indication for an oxygen partial pressure dependence on the surface exchange coefficient as it seems to be almost constant over the entire investigated oxygen partial pressure regime.

The relaxation process is temperature activated and therefore the temperature dependence of the surface coefficient was determined with the Arrhenius equation resulting in an activation energy of 2.57 eV. The temperature dependence of k_{ex} is given by

$$k_{\text{ex},(110)}(T) = 1.3 \cdot 10^5 \exp\left(-\frac{2.57 \text{ eV}}{k_B T}\right) \text{ m/s}.$$

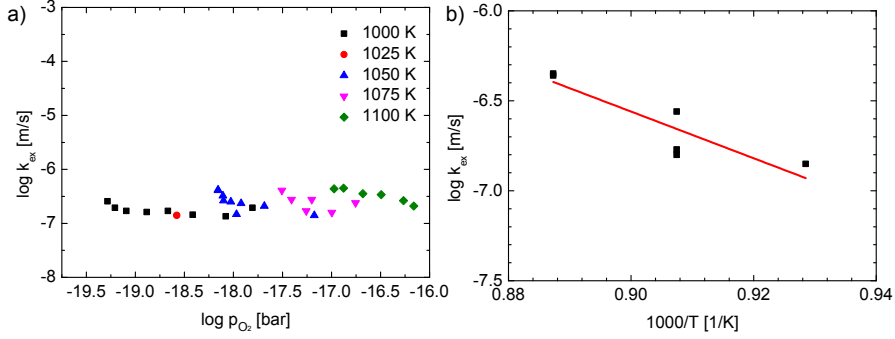


Figure 6.16: a) All determined surface exchange coefficients for all temperature and oxygen partial pressures. b) Arrhenius plot in order to determine the activation energy of the surface exchange process for an oxygen partial pressure of $p(\text{O}_2) = 10^{-17}$ bar.

The corresponding Arrhenius plot for an oxygen partial pressure of 10^{-17} bar is displayed in figure 6.16 b).

6.2.2 Orientation dependent relaxation in TiO_{2-x} single crystals

The chemical diffusion in (001) and (110) orientated rutile was studied for different temperatures and oxygen partial pressures. The relaxation process for both single crystal orientations was found to be limited by the surface exchange process at 1000–1100 K. The observed surface exchange coefficient for the (001) orientation was approximately one order of magnitude higher than for the (110) rutile single crystal. The activation energies were determined to 2.57 eV and 1.17 eV, respectively. In figure 6.17 the temperature dependence of the surface exchange coefficients for (001) and (110) are shown.

It has been previously reported that the redox reaction on rutile surface strongly depends on the crystal orientation [238, 239]. It has been demonstrated that the surface energy (formation energy of the particular surface) of the (110) surface is the lowest and that the (001) surface has the highest energy [240–242]. However, the oxygen vacancy formation energy of the (001) orientation is lower in comparison to (110) orientation [242]. The surface reaction consists of multiple steps. Since the details of surface exchange reactions are still under debate, it is not possible to determine the activation energy, which is necessary for the formation of oxygen vacancies at the surface of the studied single crystals. However, it seems to be a plausible

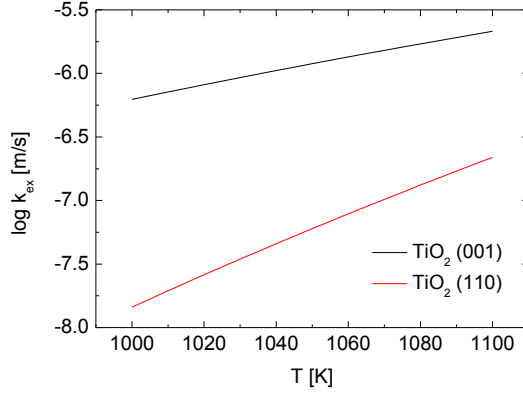
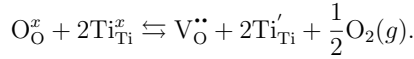


Figure 6.17: Temperature dependence of surface exchange coefficients determined in a reducing atmosphere for (001) (black) and (110) (red) TiO_2 for 1000–1100 K.

explanation that the formation of the oxygen vacancies at the surface plays an important role during the relaxation process, which can explain the difference in the relaxation times. The lower formation energy at the (001) surface might be caused by a different geometry of the reactive titanium sites, where the electrons required for surface exchange reaction are provided [242].



The rate limitation of the relaxation process by the surface reaction is in contrast to the previously published works [98–100, 107–109, 243], which all report that the relaxation process in TiO_2 is mainly dominated by bulk diffusion in reducing oxygen partial pressure conditions. Millot [108] and Iguchi et al. [98] report an anisotropy in the chemical diffusion process. They report on a faster diffusion perpendicular to the c -axis and a slower one parallel to c , which fits quite well to self-diffusion experiments published for rutile [96]. This effect was explained by open channels in the rutile crystal structure (cf. section 2.4.3). The surface exchange process in all these reports is neglected due to the assumption that it plays a minor role in the relaxation process. The studied temperature range in these reports was 900–1400 K. In this thesis a temperature range of 1000–1100 K was investigated, which is included in the already reported investigated temperature range. However, the results in this thesis clearly show a strong impact of the surface exchange process on the relaxation in contrast to the previously published works. Due to the highly

temperature activated process at the surface the surface exchange reaction might be neglected for the higher temperature regime, but this cannot explain the differences in the rate limiting processes (chemical diffusion vs. surface exchange process) for lower temperatures. Morin [107] already discussed the inaccuracies that may arise due to the use of an approximation formula for chemical diffusion, which does not take all processes during relaxation into account. Another possible explanation might be that at lower temperatures, differences might be caused by different surface treatments/properties. It has been demonstrated e.g. for SrTiO_3 [244] that the surface properties have a strong influence on the surface reaction. Lee et al. [69] have demonstrated for low oxygen activity in a rutile single crystal with (001) orientation a combination of chemical diffusion and surface exchange dominated equilibration process, where the diffusion coefficient was approximately $10^{-9} \text{ m}^2/\text{s}$ and the exchange coefficient in the range of 10^{-6} – 10^{-7} m/s at $T = 1273$ – 1373 K . The values for the surface exchange coefficient are in the same order of magnitude as the values determined in this thesis. The estimated values for the lower limit of the chemical diffusion coefficient from the false color maps ($3 \cdot 10^{-10} \text{ m}^2/\text{s}$ for (001) TiO_2 and $6 \cdot 10^{-11} \text{ m}^2/\text{s}$ for (110) TiO_2 at 1100 K) are also within the range of previously reported values.

A dependence of the surface exchange process on the crystal orientation as it has been observed in this thesis has not yet been reported. Similar observation was reported for different orientated SrTiO_3 single crystals [245]. In contrast to this work the fastest diffusion was observed for the most stable surface of SrTiO_3 (100). Here the surface exchange coefficient for (001) is higher in comparison to (110). The (110) orientation has a more stable surface, but a higher formation energy for oxygen vacancies at the surface. So it can be concluded that not only the surface stability influences the kinetics of the relaxation process, but also the formation energy for the defects which are involved during the surface exchange process should be considered. Also the formation of different space charge zones [223] at the surface can have a non negligible effect on the surface exchange kinetics.

6.2.3 TiO_{2-x} thin films

In the previous section the chemical diffusion in single crystalline rutile with different orientations was studied. Now the relaxation behavior in TiO_{2-x} thin films will be investigated and it will be discussed how the diffusion is changed due to additional grain boundaries. The relaxation coefficients of a 300 nm polycrystalline film will be analyzed. As the conductance of the studied polycrystalline film was in the same order of magnitude as the sapphire substrate at high oxygen activity (cf. chapter 6.1.2), the relaxation process will be investigated for low oxygen partial pressures. The reducing atmosphere in the probe volume is adjusted by a mixture

of 4% H_2/Ar and argon (cf. figure 6.18), with a constant gas flow over the entire measurement time. The electronic relaxation behavior was studied for different reducing oxygen atmospheres and it was switched back and forth between higher and lower oxygen partial pressures. The sample design for the measurement is already described in section 6.1.2 and the details of the measurement setup are described in section 3.6.

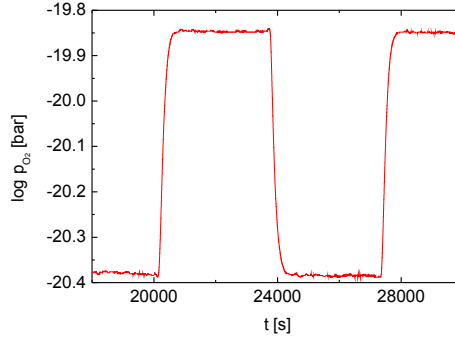


Figure 6.18: Overview of oxygen partial pressure jumps at a sample temperature of $T_{\text{sample}} = 1050$ K.

The conductivity of TiO_{2-x} in the reduced oxygen partial pressure range is orders of magnitudes higher than for the sapphire substrate. Therefore, the contribution of the sapphire substrate can be neglected in this regime. As shown by the HTEC measurements the point defect chemistry is dominated by the oxygen vacancy concentration being compensated by aliovalent impurities. This is in contrast to the bulk material where the intrinsic defects are dominating. However, it has been shown by Grzesik et al. [101] that the change in oxygen vacancy concentration in the extrinsic regime induces a change in the concentration of electrons and holes and therefore the relaxation process of the oxygen sublattice within this regime can be studied by measuring the electronic conductance in dependence on time. Based on the bulk measurements the chemical diffusion behavior was studied in a temperature range of 1000–1100 K and oxygen partial pressures in the range of 10^{-17} bar to 10^{-20} bar.

Two typical normalized relaxation curves for the studied thin film are shown in figure 6.19 a) for 1000 K and 1100 K. The sample equilibrates faster for a temperature of 1100 K which indicates a thermally activated process. The relaxation time can be estimated to 300 s. In order to show that the equilibrium values

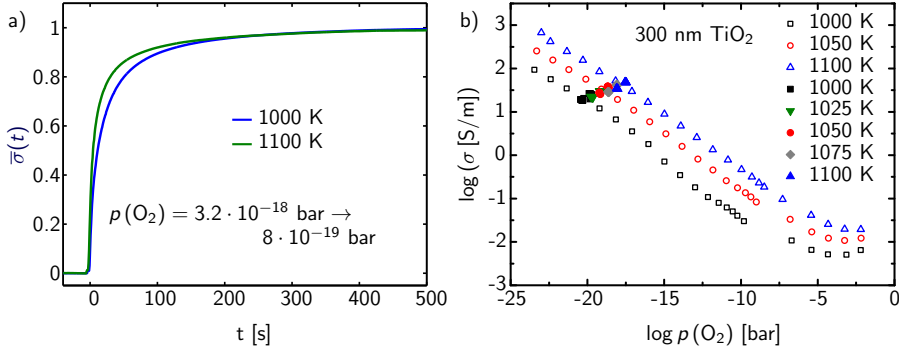


Figure 6.19: a) Normalized relaxation curves for oxygen jumps at temperatures of 1000 K and 1100 K. b) Comparison of HTEC characteristics for a 300 nm thin film of TiO_2 on sapphire. The solid dots represent the data from the ECR measurements and the open circles are from HTEC measurements (cf. chapter 6.1.2).

match those of the previously determined by HTEC measurement, the equilibrium values of the ECR measurements are determined. For this the first and the last fifty measured values are averaged. All values are displayed in figure 6.19 b) in dependence on the oxygen partial pressure with solid dots. The conductivity values determined by equilibrium measurements (cf. chapter 6.1.2) for the 300 nm TiO_{2-x} film are also shown in figure 6.19 b) (open dots). The measured equilibrium values of the ECR measurements fit well to those from the HTEC characteristic. The small deviations can be explained due to slightly different temperatures in the furnaces.

In a next step the kinetics of the relaxation process will be studied. The same fitting routine as for the single crystalline rutile (cf. section 6.2.1) leads to the fit displayed in figure 6.20 a) at $T = 1100 \text{ K}$, which only reproduces poorly the measured normalized data. The best fit with the standard model, which considered both the bulk diffusion and surface exchange coefficient, is dominated by the surface exchange process as can be seen in the false color map (cf. figure 6.20 b)) of the logarithm of the squared error matrix for the evaluation of different relaxation parameters. There is no pronounced minimum for the chemical diffusion D_{Chem} . For the surface exchange coefficient a slight minimum is visible. However, the minimum is not as pronounced as for the single crystals. Therefore, it is necessary to consider other processes during the relaxation and to adjust the theoretical conductivity equation.

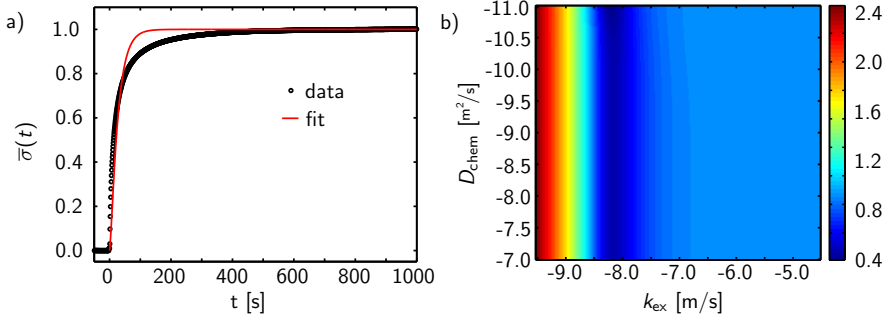


Figure 6.20: a) Normalized conductivity curve for an oxygen jump from $3.2 \cdot 10^{-18}$ bar to $8.0 \cdot 10^{-19}$ bar at 1100 K. b) False color map of the logarithm of the squared error matrix for the evaluation of relaxation parameters at 1100 K.

There are two approaches to explain this behavior. The first one would be a stronger influence of the flushtime on the relaxation behavior. The second one is that there are two distinct processes, which are taking place at the surface [69, 103, 245, 246]. It has been previously reported that in the case of two surface processes this should be visible in a semilogarithmic plot of the relaxation curve [103, 245]. In order to test these two scenarios first, the equations for the different cases will be introduced and afterwards the appearance in the semi-logarithmic plot will be discussed. Equation (2.71), which considers the additional flushtime contribution, can be simplified in the case of a surface exchange limited process ($L \rightarrow 0$) to

$$\sigma_{\text{CISTR, surface}} = 1 - \exp\left(-\frac{t}{\tau_f}\right) - \frac{1}{1 - \frac{k_{\text{ex}}}{l}\tau_f} \left[\exp\left(-\frac{k_{\text{ex}}}{l}t\right) - \exp\left(-\frac{t}{\tau_f}\right) \right]. \quad (6.15)$$

In the case of two processes at the surface, the total conductivity is the weighted sum of two of these terms, where each exchange process has its own surface exchange coefficient $k_{\text{ex},1}$ and $k_{\text{ex},2}$. The weighting of each process to the total normalized conductivity are expressed by the pre-exponential factors A_1 and A_2

$$\sigma = A_1 \cdot \sigma_1 + A_2 \cdot \sigma_2 \quad (6.16)$$

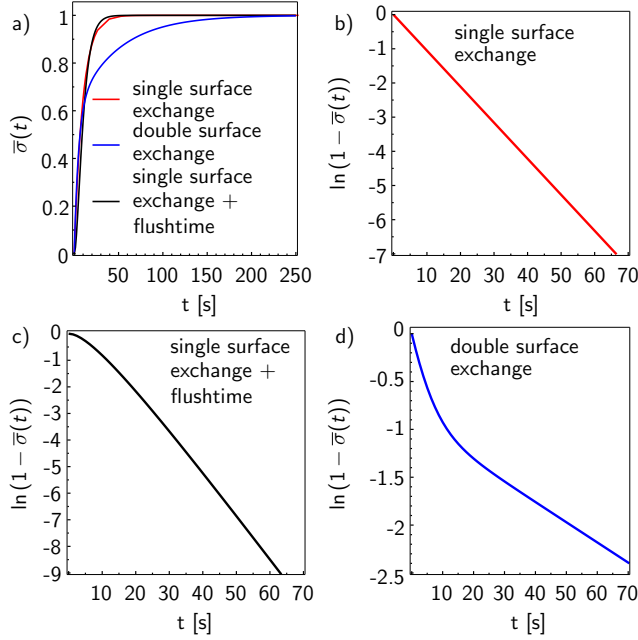


Figure 6.21: a) Theoretical relaxation curves for an equilibration kinetic with a simple surface reaction (red), a simple surface reaction with flush-time (blue) and a two fold surface exchange process (blue). Semi-logarithmic plot for a b) single surface exchange, c) single surface plus flushtime and d) double surface process.

with $A_1 + A_2 = 1$ and equation (2.63)

$$\sigma = 1 - A_1 \exp\left(-\frac{k_{\text{ex},1}}{l_x}t\right) - A_2 \exp\left(-\frac{k_{\text{ex},2}}{l_x}t\right). \quad (6.17)$$

In this case, the two processes are treated as statistically independent, which means that there is no measurable interaction or coupling of the two kinetic processes. An overview of the different relaxation processes and the theoretical normalized conductivity relaxation curves are displayed in figure 6.21 a). The equation for a single surface exchange process can be linearized to $\ln(1 - \sigma) = -\frac{k_{\text{ex}}}{l_x}t$. In the resulting semilogarithmic plot the normalized conductivity is a straight line (cf. figure 6.21 b)). In the case of a flushtime influenced surface exchange the curve has at the beginning a concave curvature. Thereafter, the curve passes in a straight line (cf. figure 6.21 c)). In the case of a double folded relaxation process there is

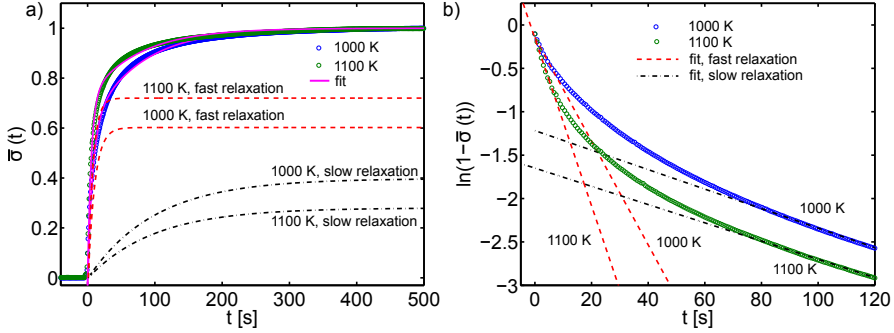


Figure 6.22: a) Relaxation curve at 1000 K fitted with a slow and a fast relaxation process. b) Semi-logarithmic plot of the same curve, which clearly indicates that there are two processes present during the relaxation.

a convex curvature in the semilogarithmic plot, where two areas are visible with different slopes corresponding to a slow and a fast surface exchange process (cf. figure 6.21 d)).

Now the data obtained experimentally in this study will be analyzed in a semilogarithmic plot. Clearly there are two areas with different slopes visible in the semilogarithmic plot of the experimental data (cf. figure 6.22 b)). Therefore, the best representation of the data is given by a scenario of two simultaneous relaxation processes at the surface. The best fitting result is shown in figure 6.22 a), where the fast surface exchange process has a surface exchange coefficient in the range of $3 \cdot 10^{-8}$ m/s and the slower surface exchange process is in the range of $3 \cdot 10^{-9}$ m/s at $T = 1100$ K. This values fit quite well to the values determined by Ko et al. [103], who observed also these two different surface coefficients for a 450 nm thin titania film. They obtained surface exchange coefficients of $3.2 \cdot 10^{-8}$ m/s and $3.2 \cdot 10^{-9}$ m/s at a temperature of 1123 K, respectively. An overview of all determined values for the two surface exchange coefficients are shown in figure 6.23 a). The activation energy of the thermally activated exchange process can be determined by an Arrhenius plot to be 1.98 eV and 0.72 eV for the fast and slow relaxation processes at an oxygen partial pressure of approximately 10^{-17} – 10^{-18} bar, respectively (cf. figure 6.23 b)). These values are lower than previously reported ones by Ko et al. [103] for a thin titania film. They obtained an activation energy of 2.79 eV and 1.82 eV for slow and fast diffusion relaxation process. The temperature dependence of the surface exchange coefficients in this study can be expressed as follows

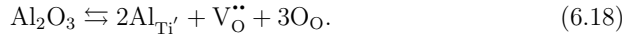
$$k_{\text{ex},1}(T) = 51.57 \exp\left(-\frac{1.98 \text{ eV}}{k_B T}\right) \text{ m/s}$$

$$k_{\text{ex},2}(T) = 4.89 \cdot 10^{-6} \exp\left(-\frac{0.72 \text{ eV}}{k_B T}\right) \text{ m/s}.$$

The two different activation energies indicate that two processes are present during the surface exchange process. As already mentioned the two processes have to be independent from each other in the frame work of the applied model. Now different possibilities for the origin of this double relaxation kinetic will be discussed. As the two processes are not coupled a possible explanation could be that two species are involved during the incorporation or release of oxygen. This species might be e.g. background impurities solving/dissolving at the grain boundaries, or protons or water vapor.

Influence of impurities and water vapor

The thin films contain acceptor type impurities due to contamination during the deposition process. Furthermore, some contaminations on the substrate might lead to acceptor type doping of the film. For impurity controlled mechanism it was reported that oxygen vacancies are introduced by the following reaction [247]



Arita et al. [248] reported that impurities have a catalytic effect on the diffusion and surface exchange coefficient, which leads to an increase of both coefficients (cf. figure 6.24). But a double fold relaxation kinetics was not observed in the studied doped single crystals. So it might be that there are two processes running in parallel. One involves the background impurities by creating oxygen vacancies (cf. equation 6.18) and the other one might be correlated to the defect (oxygen vacancies or titanium interstitials), which are also formed under dry and hydrogen free conditions. But the surface exchange coefficient observed here, is about one to two orders of magnitude lower in comparison to the single crystal values. So this is not the most plausible explanation for the additional kinetic process, because it does not explain the difference between thin film and single crystal. So a second possibility will be discussed. The surrounding atmosphere was created by the following exothermic reaction



At lower temperatures more water vapor is present in the atmosphere than at higher temperatures. It has been reported that at intermediate temperatures water is dissolved into the rutile lattice and substitutional hydroxyl defects are formed on

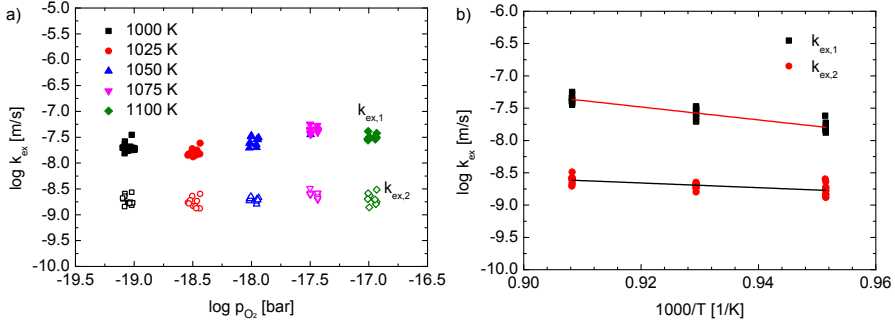
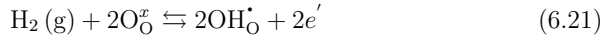


Figure 6.23: a) Oxygen partial pressure dependence of the surface exchange coefficients. b) Arrhenius plot for the determination of activation energy.

oxygen lattice sites. Furthermore also the protons can dissolved into the rutile lattice and also forms an hydroxyl defect [249]. The simplest possible reactions of this two dissolution processes can be described by [250,251]



Several reports study the influence of water vapor on oxygen diffusion in rutile [247, 251–254]. Most of them only observe single bulk diffusion. The reported oxygen diffusion coefficients are lower in comparison to those reported for dry measurement conditions (cf. figure 6.24). Only Moore et al. [253] reported for oxygen rich conditions with water vapor two bulk diffusion processes. One is a fast and the other a slow diffusion process. Under dry measurement conditions they determined only one diffusion coefficient, which has a similar diffusion coefficient as determined for the fast process detected during the measurement with water vapor. The fast process was assigned to an oxygen vacancy related diffusion process and the slower one was correlated to a titanium-interstitial-induced defect mechanism. In all these reports bulk diffusion is assumed to be the rate-determining step during the relaxation process. Only Haul et al. [251] report values for bulk diffusion as well as a surface exchange process. They demonstrate that the bulk diffusion coefficient is decreased due to the presence of water vapor whereas the surface exchange coefficient is increased. But they did not observe a double surface exchange processes or two bulk diffusion processes as it was shown for the thin films in this work. Note, that such a scenario of a combined effect of surface exchange and bulk diffusion did not result in a reasonable fit of the relaxation data (cf. figure 6.20 a)).

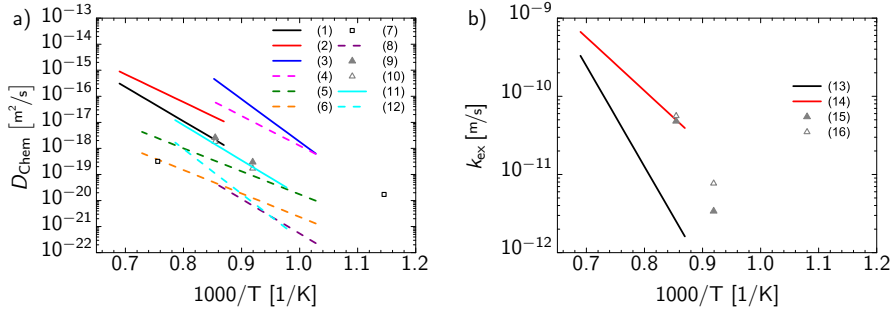


Figure 6.24: a) Diffusion coefficients and b) surface coefficients for rutile reported in literature for under dry and wet measurement conditions. The solid lines and filled symbols indicate values determined under dry conditions and dashed lines and open symbols represents values, measured with water vapor. (Arita et al. [248] undoped (1) and 0.08 mol% Cr_2O_3 doped (2) rutile single crystal, Zhang et al. [255] (3) and (4), Dennis et al. [247] (5) and (6), Freer et al. [252] (7), Morishita et al. [254] (8) and (9), Haul et al. [251] (10) and (11), Moore et al. [253] (12) and (13), Arita et al. [248] undoped (13) and 0.08 mol% Cr_2O_3 doped (14) rutile single crystal, Haul et al. [251] (15) and (16))

It has been shown by Erdal et al. [256] that at lower temperatures water plays an important role for the defect formation in rutile and it has also a significant contribution to conductivity. Above a temperature of 973 K and under reducing conditions, however, the defect chemistry is mostly influenced by titanium interstitials and oxygen vacancies as it was also reported elsewhere [257–260]. For the temperature area examined here (1000–1100 K) the presence of water vapor and protons should play a minor role. However, it has been demonstrated by von Hippel et al. [261] that hydroxyl defects are removed above a temperature of 1023 K, which shows that in the lower temperature range some hydroxyl defects could be present in the lattice of the here studied thin films. However, one should expect that some changes up to higher temperature arise due to the release of hydroxyl defects. But there is no change of activation energy for the studied thin films and the two surface exchange processes (cf. figure 6.25). At higher temperatures due to the exothermic reaction (cf. equation 6.19) there should be more protons present in the surrounding atmosphere than water vapor. Therefore, it might be possible that due to the release or incorporation of protons a second surface exchange process occurs during the equilibration process. For the temperature range investigated here a diffusion coefficient of $(1.91\text{--}3.57) \cdot 10^{-10} \text{ m}^2/\text{s}$ and $(1.35\text{--}5.19) \cdot 10^{-11} \text{ m}^2/\text{s}$ has been observed for protons along and perpendicular to the c -axis of the rutile phase [262]. This

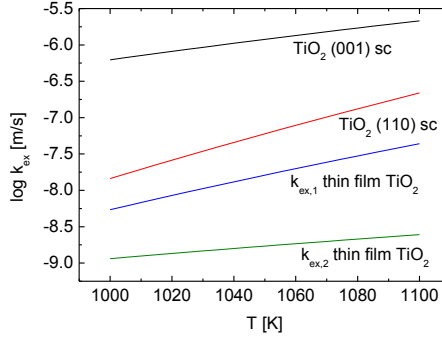


Figure 6.25: Temperature dependence of surface exchange coefficients determined in a reducing atmosphere for (001) and (110) rutile single crystals and a 300 nm TiO_{2-x} film for 1000–1100 K.

diffusion coefficients are orders of magnitudes higher in comparison to the oxygen diffusion coefficients in rutile (cf. figure 6.24). Up to a temperature of approximately 690 K no surface exchange process has been observed. Therefore, it seems to be unlikely that release or incorporation of protons determines the relaxation kinetics in the rutile film and might be the origin of the second process. Nevertheless, it has been reported that the presence of water vapor has an influence on the equilibration process.

Another open question is why a double exchange process is observed in the thin films and not in the single crystals, although the surrounding atmosphere was created under the same conditions. Norby et al. [250, 263] report that hydroxyl related defects preferentially forms at defects or grain boundaries in oxides. Since the grain boundary and defect concentration in the thin films should be higher in comparison to the single crystals this might explain the appearance of two processes in the thin film whereas in the single crystals only one process has been observed in this thesis. However, as previously, mentioned Haul et al. [251] observed an enhancement of the surface exchange coefficient under the presence of water. Furthermore, the diffusion of protons in rutile is much faster in comparison to oxygen diffusion. There must be an additional reason for the two surface exchange reactions, which might be also responsible for the slow down of the surface exchange process. Therefore, additionally also the influence of grain boundaries on the relaxation kinetics will be discussed.

Exclusion of bulk diffusion in thin titania film

The surface exchange coefficients are one to two orders of magnitude lower than the surface exchange coefficients of the single crystals (cf. figure 6.25). This may be attributed to additional space charge zones caused by the grain boundaries in the polycrystalline film, which might have a retarding effect on the surface exchange processes due to an additional energy barrier. Nowotny et al. [232] report previously that the chemical diffusion in polycrystalline TiO_{2-x} is slower in comparison to a rutile single crystal. They proposed that a retarding field due to a segregation-induced concentration gradient of extrinsic and/or intrinsic defects affects the chemical diffusion. Furthermore, they suggest that the potential barrier of grain shell and core may be different due to segregation of intrinsic and/or extrinsic effects which also has a retarding effect on the chemical diffusion. Höfler et al. [264] reported for nanocrystalline titania that the diffusion is five orders of magnitudes faster in contrast to polycrystalline or single crystalline material. So although the grain sizes are smaller, which means that the amount of space charge zones is significantly increased an enhancement of the diffusion is observed, which is contradictory to the results of Nowotny et al. [232].

The equilibration kinetics in the studied thin film should be mostly dominated by the surface exchange coefficient as the bulk diffusion coefficient can be estimated by $D_{\text{Chem}} = \frac{d^2\pi}{16t}$ [265] with a film thickness of $d = 300$ nm and a relaxation time of $t = 300$ s. In that case, the diffusion coefficient would be approximately $6 \cdot 10^{-17} \text{ m}^2/\text{s}$, which is not a realistic value for the chemical diffusion. This statement is supported by the obtained lower limits of chemical diffusion coefficients for (001) and (110) rutile single crystals. They were estimated to be $3 \cdot 10^{-10} \text{ m}^2/\text{s}$ for (001) TiO_2 and $6 \cdot 10^{-11} \text{ m}^2/\text{s}$ for (110) TiO_2 at 1100 K. With the obtained values of D_{Chem} for (001) and (110) rutile single crystals the relaxation time can be calculated by $t = \frac{d^2\pi}{16D_{\text{Chem}}}$ to 59 μs and 295 μs . Therefore, it can be concluded that the chemical diffusion within the TiO_{2-x} thin film plays a minor role. However, the additional energy barriers at the grain boundaries can also affect the exchange process. Another possible explanation might be that an oxygen partial pressure induced space charge potential at the surface influences the surface exchange process [266]. Most of the recently published works focus on the bulk diffusion in titania. Gruenwald et al. [93] demonstrate for polycrystalline material that the diffusion coefficient is only slightly different in comparison to rutile single crystals. The surface exchange coefficients for the polycrystalline material was about one order of magnitude higher in comparison to the rutile single crystal values, which is also in contrast to the results of the thin films studied here. However, they also reported on a single surface exchange process and not on a double one.

Equilibration kinetics in thin perovskite films

Since only one publication [103] reports about the equilibration in titania thin films also the relaxation kinetics of other thin oxides films will be discussed. In the following the equilibration kinetics of several perovskite oxides that showed different relaxation kinetics for bulk and thin film will be discussed. It has been reported for several perovskite thin films that the surface exchange coefficient is reduced by up to two orders of magnitude in contrast to polycrystalline bulk material [267–269]. This phenomenon was explained by different grain sizes of the different studied materials [269, 270]. This observations supports the results of the thin titania films studied here for which also a reduction of one to two order of magnitude in comparison to the values determined for the rutile single crystal has been observed.

Another interesting result in these studies was that in highly orientated films only a single relaxation kinetics has been reported [269, 271–273], whereas in thin films with different orientations a double relaxation kinetics can be identified [267, 270, 274, 275]. The thin films where two processes occur, are polycrystalline after deposition or in the case of initially highly orientated films additional orientations arise after high temperature treatment. In these reports the origin of the two equilibration processes was assigned to inhomogeneities [103, 267] or different diffusion coefficients for the mobile defects in the anion and cation sub-lattice [69, 246], which results in space charge formation [276]. The latter explanation should be valid only for bulk diffusion and not for the exchange process on the surface. However, the authors clearly demonstrate that two processes determine the equilibration kinetics, even if a conclusive explanation is missing.

An important point to be stressed out here is the fact that the double relaxation is only observed for polycrystalline thin films, but not for bulk ceramic samples for which up to now no double exchange has been reported [268, 277–280]. This is a surprising observation, if one considers that the bulk diffusion in the thin films is a negligible process in comparison to the surface exchange. The conclusion would be that there should be only one single process in the thin metal oxide films, which determines the relaxation kinetics. Because once the oxygen is incorporated from the surface into the thin film, the oxygen should distribute very fast in the whole thin film due to the fast diffusion in comparison to the exchange process. Regardless of the orientation of the grains, which can have a different exchange coefficient, only the fastest process should be visible, since the exchange within the grains should be fast due to bulk diffusion. Nevertheless, the films with different orientations seem to possess a property, which might originate from texturing of these thin films, that neither the ceramics nor the highly oriented films have.

Furthermore, the substrate might have a significant influence on the relaxation kinetic. Kubicek et al. [271] show that due to substrate induced tensile or compressive strain in thin $\text{La}_{1-x}\text{Sr}_x\text{CoO}_{3-\delta}$ films the surface exchange coefficient can be influenced. Furthermore, Garcia et al. [270] suggested for the double surface relaxation of a $\text{La}_2\text{NiO}_{4+\delta}$ thin film that the fast reaction constant is correlated to the film surface exchange process whereas the slower process is limited by the oxygen diffusion at the film substrate interface or a material chemical degradation. However, the sapphire used in this studies shows no significant change in conductivity under various temperatures and oxygen partial pressure so therefore it seems to be unlikely that there should be any kind of oxygen exchange between film and substrate. Finally, it should be mentioned here that in all these reports the perovskite thin films and the bulk materials were measured under oxygen rich conditions. The gases were not saturated with water vapor, so there should not be significant amount of water or protons in the surrounding atmosphere. Therefore, it may be concluded that the orientation of the thin film in combination with the substrate generates some conditions, which leads to the appearance of the double fold kinetics.

In contrast to the published works on thin perovskite films and ceramics, Kerman et al. [245] reported a double relaxation under highly reducing conditions with water vapor for different orientations of SrTiO_3 single crystals. The heterogeneous relaxation process was attributed to independent anionic and cationic sub-lattice relaxation. Since a surface exchange process is considered, only the interface between the atmosphere and the sample surface should be involved in the reaction and not the crystal lattice. Moreover, in oxygen rich conditions this behavior has not been reported [281–283]. The surface and the crystal structure were not investigated after the high temperature treatment by Kerman et al. [245] and therefore, it is not possible to judge whether a change of the sample surface or some changes in the crystallographic orientation leads to an heterogeneous equilibration process.

Lastly, the temperature dependence of the pre-exponential factors of the two surface exchange processes A_1 and A_2 will be discussed. They seem to be constant over the entire analyzed temperature range as displayed in figure 6.26 c). The fast diffusion process has the major contribution in the relaxation process. The scattering of the data points for lower temperatures might be caused by some inaccuracy due to non-stable gas changes in reducing oxygen atmosphere, since this process is highly temperature dependent. For higher temperatures the gas changes are more defined and therefore the resulting diffusion coefficient can be determined more accurately. Ko et al. [103] also observed temperature independent pre-exponential factors and that the fast relaxation process is the domination process during equilibration.

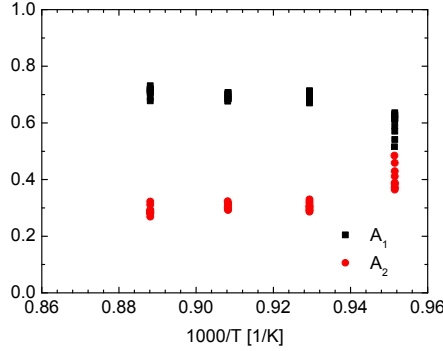


Figure 6.26: Temperature dependence on the pre-exponential factors A_1 and A_2 .

6.3 Summary

The defect chemistry in rutile single crystals in (001) and (110) orientation and TiO_{2-x} thin films was investigated in this study. All types of samples show n -type conductivity over the whole investigated oxygen partial pressure range. The point defect chemistry of the rutile single crystals was determined by ionic charge compensation at intermediate oxygen partial pressure and dominated by electronic charge compensation at reducing conditions. In contrast the thin films only show ionic charge compensation for the entire studied oxygen partial pressure range, due to a higher acceptor dopant concentration as compared to the single crystals. Moreover, the grain boundaries of the nano-crystals in the thin film increase the total area of grain boundaries and also the space charge zones adjacent to the grains. This leads to an enhanced ionic conduction in the high oxygen partial pressure regime. The change of conductivity from electronic to ionic can be interpreted in terms of an increased titanium vacancy concentration in the grain boundary and adjacent space charge accumulation. The determined activation energy for oxygen vacancy formation of bulk and thin film are identical and comparable to those published in literature. At higher oxygen partial pressure ionic conduction is present in the thin film. The thermal activation energy for oxygen vacancy diffusion is in good agreement with the reported values for polycrystalline TiO_{2-x} at high oxygen partial pressures.

The equilibration kinetics of single crystalline rutile with (001) and (110) orientations and of a polycrystalline rutile film on sapphire were studied for a temperature range of 1000–1100 K under reducing oxygen partial pressure conditions. The relaxation in the studied single crystalline rutile was mainly controlled by a surface exchange process. The velocity of surface exchange strongly depends on the sur-

face orientation. The surface exchange process of the (001) orientation is orders of magnitude faster in comparison to the (110) orientation, which can be correlated to the lower formation energy of oxygen vacancies, which may be presumably involved at the surface exchange reaction, on the rutile surface. In contrast to previously published works, the relaxation kinetics were not dominated by bulk diffusion, although the studied temperatures are in a similar range. The differences may be explained by different sample geometries or due to some inaccuracies caused by the use of approximation formulas. Furthermore, differences in surface properties might lead to different relaxation characteristics.

The equilibration kinetics of the thin film are controlled by a heterogeneous relaxation process. Two surface exchange coefficients for a slow and a fast process can be determined. Several possibilities have been discussed as origin for the occurrence of a heterogeneous process. The incorporation or release of a second species such as water was discussed as well as the influence of the texturing of the thin film and the interaction between substrate and thin film. However it was not possible within this thesis to conclusively clarify the origin of the two kinetic processes. Further studies are necessary in order to get a detailed understanding of the complex interplay of grain boundaries, substrate and thin films, background impurities and/or water vapor in the surrounding atmosphere.

7 High temperature conductivity of $\text{Ta}_2\text{O}_{5-x}$

In this chapter the results of high temperature equilibrium conductivity measurements in dependence on the oxygen partial pressure of a $\text{Ta}_2\text{O}_{5-x}$ ceramic and a $\text{Ta}_2\text{O}_{5-x}$ thin film will be presented. At first, the preparation and structure of the ceramic sample will be described. Then the high temperature equilibrium characteristic of the ceramic within the defect chemistry model of $\text{Ta}_2\text{O}_{5-x}$ published in literature will be discussed. These results will be compared to the electrical conductivity characteristic of a $\text{Ta}_2\text{O}_{5-x}$ thin film which is prepared by reactive sputtering.

7.1 Sample preparation of polycrystalline $\text{Ta}_2\text{O}_{5-x}$

The $\text{Ta}_2\text{O}_{5-x}$ ceramic samples were prepared from $\text{Ta}_2\text{O}_{5-x}$ powder (Tantalum (V) Oxide, Purity 99.9%), which were supplied by Mateck GmbH, Jülich, Germany. After the powder was mixed with a binder (Optapix PAF 35, Zschimmer & Schwarz GmbH&Co), it was first uniaxially and then isostatically (8250 bar) compressed into a pellet. In order to remove the binder, the pellet was annealed at 600 °C for 12 hours. Afterwards the pellet was sintered in dry oxygen with a flow of 50 sccm at 1300 °C for 24 hours. The heating rate was set to 1 K/min and the cooling rate to 0.5 K/min.¹ The density of the ceramic was determined with Archimedes' principle to be 99.68% of the $\text{Ta}_2\text{O}_{5-x}$ bulk density [285]. The sintered ceramic has grains with a size of approximately 1–5 μm , as can be seen in the SEM picture presented in figure 7.1 a), which shows a cross-section of the prepared ceramic. The sample has a relatively high porosity due to inter-granular pores, which can be caused by the phase transformation from the orthorhombic low temperature phase to the tetragonal high temperature phase and the rapid expansion of the grains caused by the volume increase during the phase transformation [286]. The XRD scan in figure 7.1 b) endorses the presence of both phases in the prepared material.

¹The $\text{Ta}_2\text{O}_{5-x}$ ceramics were prepared by Dr. Paul Meuffels and Cerstin Makovicka, Peter Grünberg Institute, Forschungszentrum Jülich GmbH, Jülich, Germany.

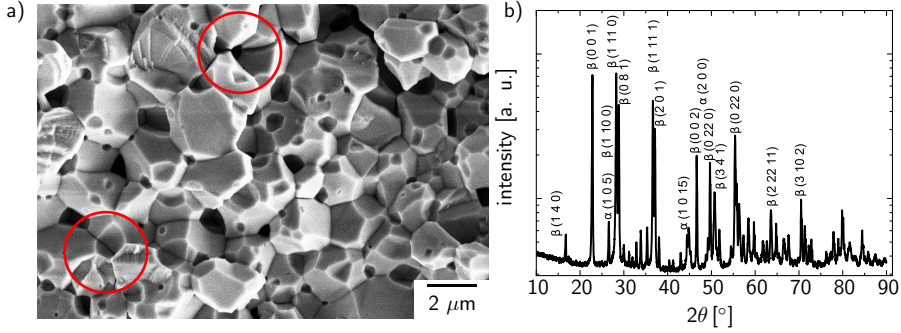


Figure 7.1: a) SEM image of a sintered $\text{Ta}_2\text{O}_{5-x}$ pellet with a grain size of $1\text{--}5\ \mu\text{m}$ and pores. Two representative regions, where micro-cracks occur, are marked with red circles. b) XRD measurements from $\text{Ta}_2\text{O}_{5-x}$ ceramics. The visible signals are corresponding to a mixture of α - and β -phase [61, 284]. For clarity, only some of the signals have been assigned in the graph to low and high temperature phase.

Although the calcination temperature is lower than the reported transition temperature of $1360^\circ\text{C} \pm 10^\circ\text{C}$ [60, 61] a coexistence of the two different phases has been observed below this temperature by Wu et al. [287]. In contrast, a reversible phase change process was reported previously [52, 61]. For the chemical homogenization and densification of the grains in $\text{Ta}_2\text{O}_{5-x}$ it is necessary to work with sinter temperatures around 1300°C [288]. Therefore, it is not feasible to work with lower sinter temperatures.

In addition some micro-cracks are visible in the sintered $\text{Ta}_2\text{O}_{5-x}$ ceramic, which can be caused by the highly anisotropic linear expansion coefficients leading to thermal stress during cooling [289, 290]. It has been demonstrated that the stress is clearly increased at triple grain boundaries [291], and as can be seen in figure 7.1 a) most of the micro-cracks occur at these triple points. Although micro-cracks and pores can not be prevented in the ceramic it is possible to study the high temperature equilibrium conductivity behavior of these samples. Therefore a $480\ \mu\text{m}$ thick slice of the pellet was cut off. From this piece a sample with the dimension $2.88 \times 10\ \text{mm}^2$ was prepared. The samples were contacted with $250\ \text{nm}$ thick sputtered platinum contacts with the geometry described in 3.5.

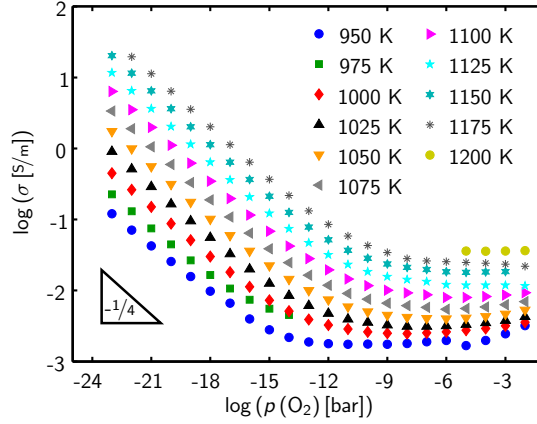


Figure 7.2: HTEC characteristic of a $\text{Ta}_2\text{O}_{5-x}$ ceramic for temperatures of 950–1200 K.

7.2 High temperature conductivity measurements of polycrystalline $\text{Ta}_2\text{O}_{5-x}$

The high temperature equilibrium conductivity of the $\text{Ta}_2\text{O}_{5-x}$ ceramic was studied in a temperature range of 950–1200 K at oxygen partial pressures of 10^{-2} – 10^{-23} bar. The results of the conductivity measurements are presented in figure 7.2. At higher oxygen partial pressure and a temperature above approximately 1075 K the conductivity is dominated by ionic conductivity, which is indicated by oxygen partial pressure independence on the conductivity, resulting from

$$[\text{V}_{\text{O}}^{\bullet\bullet}] = [\text{M}_{\text{Ta}}^{\prime\prime}].$$

Below this temperature a slight slope is visible, which indicates p -type conductivity. However, the conductivity is mainly determined by the ionic conductivity. At more reducing conditions n -type conductivity can be observed with a characteristic slope of $-\frac{1}{4}$. This slope can be correlated to an extrinsic defect dominated mechanism (cf. chapter 2.3.2), where the electron concentration, and thus the conductivity, has the same dependence on the oxygen partial pressure as the data shown here.

$$n = K_2^{\frac{1}{2}} [\text{M}_{\text{Ta}}^{\prime\prime}]^{-\frac{1}{2}} p(\text{O}_2)^{-\frac{1}{4}}.$$

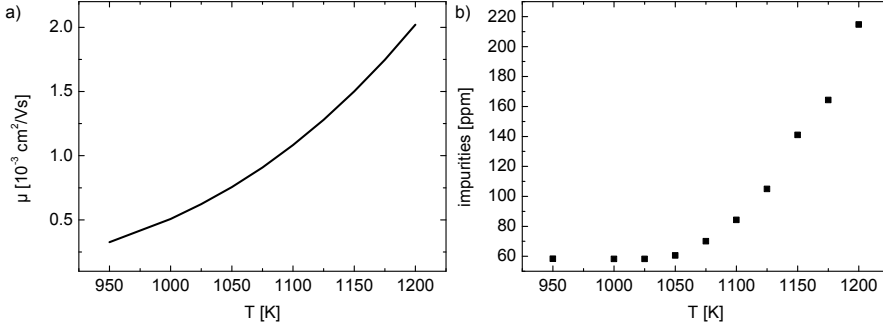


Figure 7.3: a) Temperature dependence of oxygen vacancy mobility after [80] in the measured temperature range. b) Calculated impurity concentration.

The slope in the reducing region does not change with decreasing oxygen partial pressure in contrast to the report of Johannesen et al. [292], which observe also intrinsic n -type conductivity (slope $-\frac{1}{6}$). The ionic conductivity in the extrinsic region can be described as

$$\sigma = 2e\mu_{V_O^{\bullet\bullet}} [V_O^{\bullet\bullet}] = 2e\mu_{V_O^{\bullet\bullet}} [M''_{Ta}]. \quad (7.1)$$

Using the known value for the oxygen vacancy mobility reported for an oxygen partial pressure of 1 bar [80] in Ta_2O_{5-x} the concentration of the background impurities can be determined

$$\mu_{V_O^{\bullet\bullet}}(T) = \frac{6030}{T} \exp\left(-\frac{0.85\text{eV}}{k_B T}\right) \text{ cm}^2/\text{Vs}. \quad (7.2)$$

The calculated values for the oxygen vacancy mobility are displayed in figure 7.3 a) and the resulting impurity concentrations are shown in figure 7.3 b) for an oxygen partial pressure of 10^{-4} bar. At temperatures below 1075 K the impurity concentration is constant and in the range of 55–70 ppm and above this temperature the impurity concentration starts to increase up to 200 ppm. This indicates a temperature dependent process within the Ta_2O_{5-x} ceramic. More details will be discussed after the determination of the activation energy. Similar to TiO_{2-x} the temperature dependence on the conductivity can be described by the Arrhenius equation (cf. equation (6.1)). The activation energies were determined for an oxygen partial pressure of 10^{-4} bar and 10^{-21} bar. The corresponding data are presented in figure 7.4 a) and b), respectively. For the more oxidizing conditions a change in the slope over the investigated temperatures can be observed. For temperatures between 950 K and 1050 K the activation energy can be determined to 0.66 eV and for the temper-

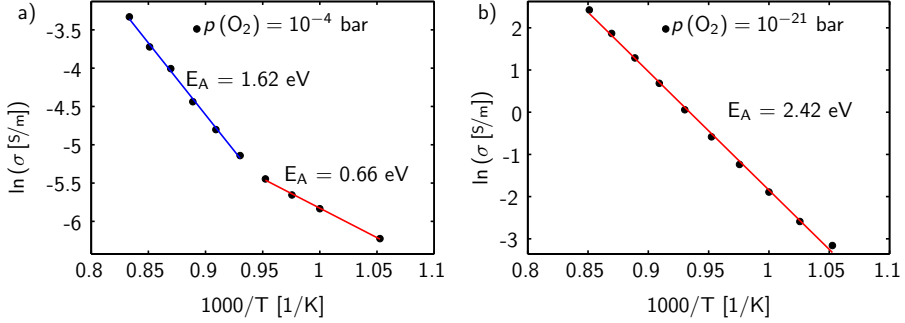
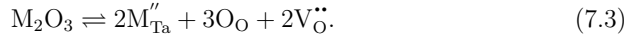


Figure 7.4: Arrhenius plots at a) $p(\text{O}_2) = 10^{-4} \text{ bar}$ and b) 10^{-21} bar for a $\text{Ta}_2\text{O}_{5-x}$ ceramic.

ature range 1075 K to 1200 K to 1.62 eV. The activation energy is thereby increased by almost 1 eV, which indicates a change in the point defect mechanism. McHale et al. [80] and Dellis et al. [81] reported a similar behavior. They interpreted the change in activation energy in terms of a precipitation-dissolution reaction, which is below a certain temperature T_c frozen in and the impurity concentration remains constant. Above T_c the concentration of the impurities is temperature dependent at the grain boundaries. The precipitation dissolution reaction is described by [80]



It has been demonstrated [51] that the solubility of cationic species from other oxides in $\text{Ta}_2\text{O}_{5-x}$ is very limited. The reaction is strongly temperature dependent. Below a certain temperature the impurity concentration is nearly constant and above this it is highly temperature activated, which is in good agreement with the observed impurity concentration in this work.

However, as already was shown in the last chapter (cf. chapter 6) for TiO_{2-x} the thermal activation energy for oxygen vacancy diffusion may depend on the oxygen partial pressure. The formation of space charge zones at grain boundaries can also influence the activation energy. Therefore, the reported values may not be representative for all prepared $\text{Ta}_2\text{O}_{5-x}$ samples. In accordance to the thin TiO_{2-x} film (cf. chapter 6.1.2) the thermal activation energy of oxygen vacancy diffusion is determined by an Arrhenius plot (cf. equations 6.7 and 7.1). It is assumed that in the case of ionic conduction at an oxygen partial pressure of 10^{-4} bar the acceptor dopant concentration is constant and thus also the oxygen vacancy concentration. The resulting Arrhenius plot is shown in figure 7.5. In the analyzed temperature range a change in the slope can be observed. For temperatures between 950 K

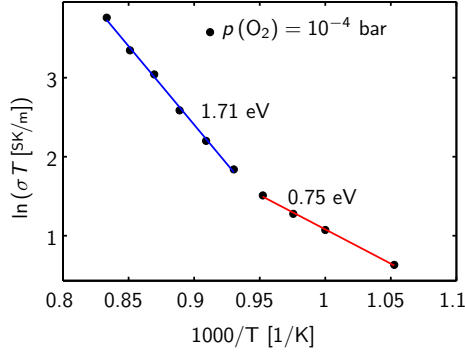


Figure 7.5: Arrhenius plot for the determination of thermal activation energy of oxygen vacancy diffusion at an oxygen partial pressure of $p(\text{O}_2) = 10^{-4} \text{ bar}$.

to 1050 K the activation energy for oxygen vacancy diffusion can be determined to 0.75 eV and for the temperature range 1075 K to 1200 K to 1.71 eV. The value for lower temperatures is in good agreement with the work of Mc Hale et al. [80]. However, for higher temperatures a change in the activation energy is visible. This was not considered in previous reports. There it is assumed that the activation energy of ionic conduction is stable over the entire temperature range. The change in activation energy might be caused by a transition from a mixture of p -type and ionic conductivity to pure ionic conduction at higher temperatures. At low temperatures, a slightly positive slope is observed, which can be correlated to p -type conductivity. As it is not sure that there is only ionic conduction present at high oxygen activities, it cannot clearly concluded what is the origin for the change in activation energy.

At very reducing conditions only one activation energy can be determined (2.42 eV) and there is no change in dependence on the temperature visible, which is in good agreement with literature values [78, 292, 293]. The energy is correlated to the formation of oxygen vacancies.

7.3 High temperature conductivity of polycrystalline $\text{Ta}_2\text{O}_{5-x}$ thin films

In this section the preparation of $\text{Ta}_2\text{O}_{5-x}$ thin films for high temperature equilibrium conductivity will be described first. Afterwards the oxygen partial pres-

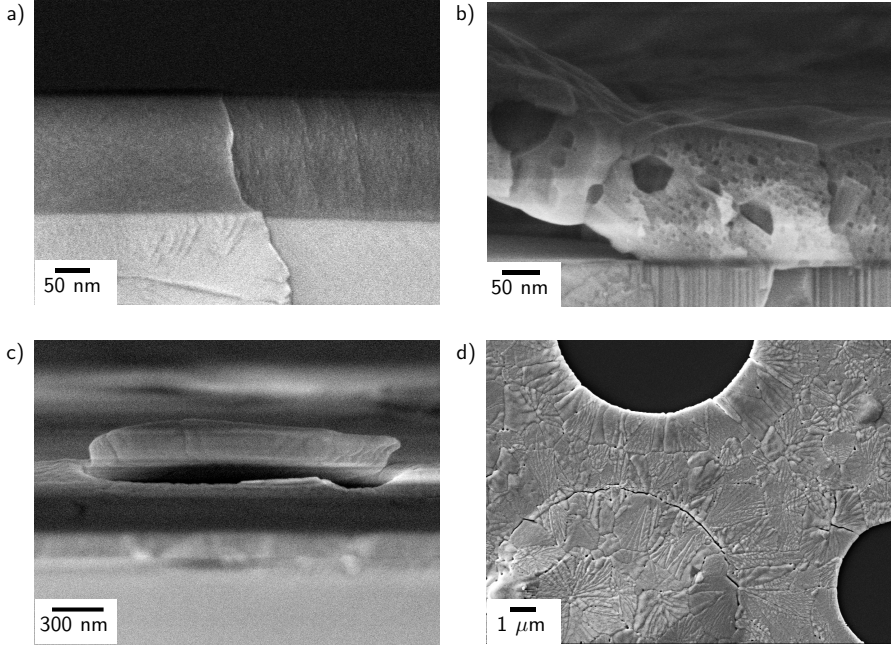


Figure 7.6: a) SEM cross-section of an as deposited amorphous $\text{Ta}_2\text{O}_{5-x}$ film. b) Cross-section after annealing in air at 1000 °C for four hours showing nanopores on the right side and delamination from the substrate due to mechanical stress caused by strain. c) Partial cracked circular buckle on a $\text{Ta}_2\text{O}_{5-x}$ thin film. d) Top view of a buckled thin film showing partial delamination from the substrate taken from [294].

sure dependent conductivity of a $\text{Ta}_2\text{O}_{5-x}$ thin film will be investigated. Differences and similarities to the polycrystalline $\text{Ta}_2\text{O}_{5-x}$ ceramic will be discussed.

7.3.1 Sample preparation of $\text{Ta}_2\text{O}_{5-x}$ thin films

All films for the HTEC measurements were sputtered on r-plane orientated sapphire single crystals. First a 300 nm thin film was deposited at room temperature. For the deposition with a sputtering power density of 1.20 W/cm² the same parameters as for the resistive switching cells were used (cf. section 4.3). The films have a smooth surface and in the SEM cross-section (cf. figure 7.6 a)) no textured structures are visible, which should be expected for an amorphous film. In order to prevent

crystallization during the high temperature conductance measurements the thin film was annealed in air for four hours at 1000 °C. Afterwards the roughness of the $\text{Ta}_2\text{O}_{5-x}$ film is strongly increased. In figure 7.6 b) a SEM cross-section image of the thin film is shown. In the right part of this picture the formation of nanopores can be seen, which was already reported in literature [134,295]. The formation of nanopores was correlated to the anisotropic crystal structure of the orthorhombic $\beta\text{-Ta}_2\text{O}_{5-x}$.

In the left part of figure 7.6 b) it can be seen that in addition to nanopores also micropores are present in the film, which might arise from the fusion of several nanopores. It should also be noted that in this part of the picture the thin film was lifted from the substrate. Usually surface buckling was caused by tensions within the material and/or between surface and substrate. In figure 7.6 c) it can be seen that the mechanical stress is at some points so strong that parts of the films were lifted from the substrate. The lifted part has a circular shape. The top view (cf. figure 7.6 d)) also shows that circular parts are completely removed from the substrate and there is also a circular buckle visible, where at the edges the films starts to crack due to the high tension. Additionally a rosette-like structure originates from the crystallization was visible at the samples surface, which was also observed for low temperature and high pressure crystallization in $\text{Ta}_2\text{O}_{5-x}$ films [296].

In order to minimize the stress during the crystallization process and to improve the film's adhesion to the substrate, the deposition temperature of the thin films for HTEC measurements was increased to 700 °C. The aim is to create a thin film, which is already crystalline after deposition and has a higher density than an amorphous film to prevent the formation of pores during the post-annealing process. A cross-section image of the as-deposited film is displayed in figure 7.7 a). The interface between sapphire single crystal and $\text{Ta}_2\text{O}_{5-x}$ film is smooth and the surface roughness is low. The as-deposited film already shows crystalline signals in the XRD pattern (cf. figure 7.7 c)), which can be assigned to the low temperature $\text{Ta}_2\text{O}_{5-x}$ phase. For the HTEC measurements a post-annealing step is necessary to ensure that the whole film is crystalline. After the film was annealed for four hours in air at 1000 °C, the cross-section was analyzed with SEM (cf. figure 7.7 b)). Although the as-deposited film was already crystalline, the post deposition annealing also leads to the formation of nanopores. However, in comparison to the room temperature films the adhesion between film and sapphire single crystal was improved. There is no buckling visible on the samples surface.

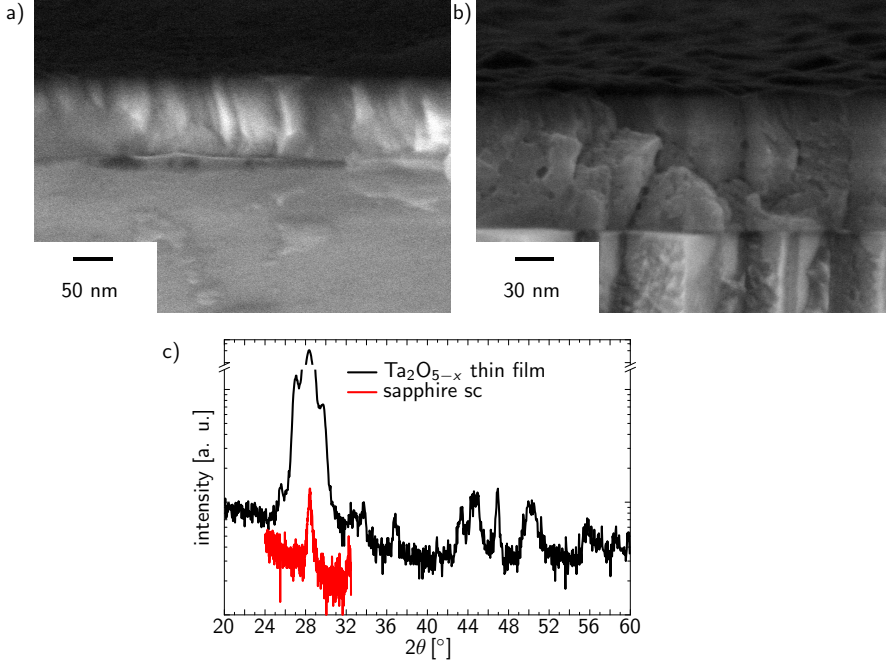


Figure 7.7: Cross-section of a $\text{Ta}_2\text{O}_{5-x}$ film a) after deposition at 700 °C and b) after annealing in air at 1000 °C for four hours. c) XRD scan of the as-deposited film with signals of the $\beta\text{-Ta}_2\text{O}_{5-x}$ phase and some reflexes from the sapphire single crystal (sc), the signals are also visible after deposition.

7.3.2 High temperature conductivity measurements of $\text{Ta}_2\text{O}_{5-x}$ thin films

In this section the high temperature equilibrium conductivity behavior of a thin $\text{Ta}_2\text{O}_{5-x}$ film on an r-plane sapphire single crystal will be discussed. The resistance of the thin film was measured parallel to the substrate. At high oxygen activity the resistance of substrate and $\text{Ta}_2\text{O}_{5-x}$ film is similar, therefore the measured conductance can be expressed by

$$G = G_{\text{Ta}_2\text{O}_5} + G_{\text{sapphire}}. \quad (7.4)$$

The conductivity values of a sapphire single crystal are already presented in 6.1.2. The resulting HTEC characteristic is shown in figure 7.8. At high oxygen activities

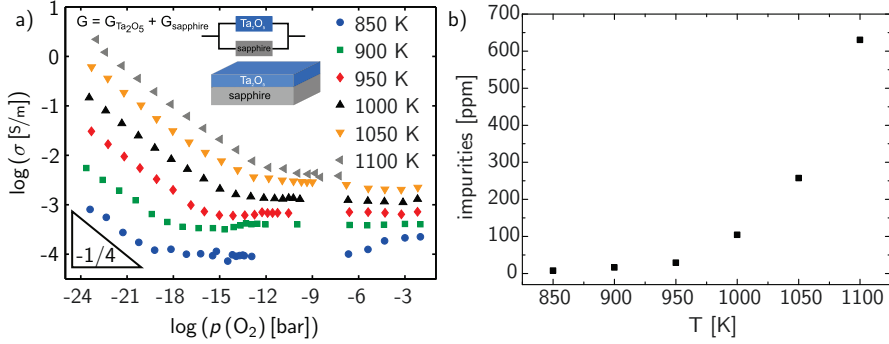


Figure 7.8: a) HTEC characteristic of a 300 nm thin $\text{Ta}_2\text{O}_{5-x}$ film on a r-plane oriented sapphire substrate. b) Temperature dependent impurity concentration for $p(\text{O}_2) = 10^{-17}$ bar.

the conductivity is nearly constant in the logarithmic plot, which indicates that in this regime the ionic conductivity is the dominating charge carrier due to background impurities. For an oxygen partial pressure range of 10^{-3} bar to 10^{-11} bar no significant slope can be observed. The conductivity in this range might be dominated by ionic conduction. At reducing oxygen conditions the film becomes n -conducting and the slope can be determined to $-\frac{1}{4}$, which corresponds to the following charge neutrality condition.

$$[\text{V}_{\text{O}}^{\bullet\bullet}] = [\text{M}_{\text{Ta}}'']$$

Based on the previous calculation for the ceramic $\text{Ta}_2\text{O}_{5-x}$ the impurity concentration for the thin film was calculated in ionic conduction regime. At low temperatures the impurity concentration is nearly constant, comparable to the ceramic case. Only a few ppm are solved in the ceramic thin film. At a temperature of 1000 °C the impurity concentration significantly starts to increase. The critical temperature point T_C is a little bit lower than for the bulk material, but the solution of aliovalent impurities seems to be an exothermic process also in thin films. The temperature dependence of the impurities is shown in figure 7.8 b). The precipitation dissolution reaction, which induces the change in the dopant concentration, is expected to be localized at the grain boundaries. Since the grains in the thin films are significantly smaller, the total number of the grain boundary area increases. This induces an enhanced ionic conduction over a wide range of oxygen partial pressures, which is comparable to the results for TiO_{2-x} thin films (cf. section 6.1.2). However, in contrast to the rutile single crystals also ionic conduction for the ceramic is visible,

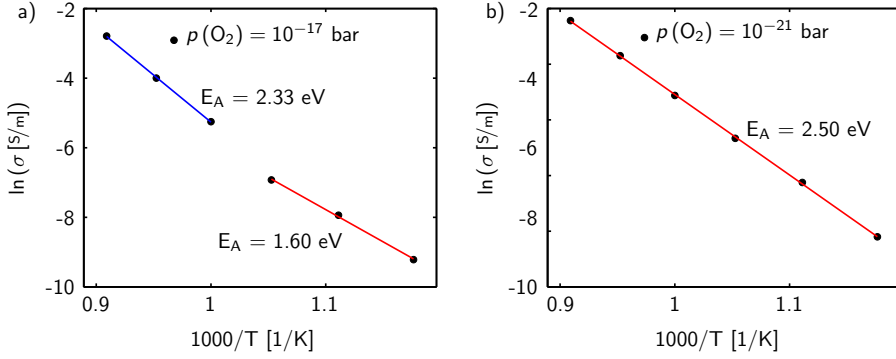


Figure 7.9: Arrhenius plots for oxygen partial pressures of a) $p(\text{O}_2) = 10^{-17} \text{ bar}$ and b) $p(\text{O}_2) = 10^{-21} \text{ bar}$.

but the oxygen partial pressure region is smaller in comparison to the thin $\text{Ta}_2\text{O}_{5-x}$ film.

If the conductivity at higher oxygen activities is strongly influenced by the dissolution of impurities, this should also be visible in a change of activation energy. Therefore, the temperature dependence of conductivity was investigated at partial pressures of $p(\text{O}_2) = 10^{-17} \text{ bar}$ and 10^{-21} bar . With the Arrhenius equation the activation energy is calculated to 1.60 eV ($T < T_C$) / 2.33 eV ($T > T_C$) and 2.50 eV . In the low oxygen activity region the activation energy is comparable to the determined ceramic value, which is assigned to the formation of oxygen vacancies. Similar to the activation energy of TiO_{2-x} the formation energy for oxygen vacancies does not depend on grain size for reducing oxygen conditions. Whereas for higher oxygen activities the activation energy is significantly increased, which can be caused by additional grain boundaries and the interfacial layer between sapphire substrate and $\text{Ta}_2\text{O}_{5-x}$ film. In the reducing oxygen partial pressure regime the ceramic as well as the thin film show n -type conductivity and no significant difference is visible.

However, as already discussed for the ceramic sample it is not clear if the activation energy for oxygen vacancy diffusion is valid for the entire temperature and oxygen partial pressure range. Therefore, the thermal activation energy of oxygen vacancy diffusion in the thin film was determined by an Arrhenius plot (cf. figure 7.10). For temperature ranges of $850\text{--}950 \text{ K}$ and $1000\text{--}1100 \text{ K}$ different slopes can be determined. The corresponding activation energies are 1.67 eV and 2.42 eV , respectively. In contrast to the reports of Dellis et al. [81] and McHale et al. [80] it is assumed that the impurity concentration is constant over the entire investigated temperature range. Since it cannot be ruled out that the conduction mechanism in the thin

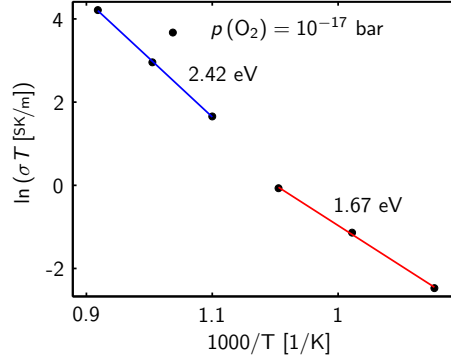


Figure 7.10: Arrhenius plot for the determination of thermal activation energy of oxygen vacancy diffusion at an oxygen partial pressure of $p(\text{O}_2) = 10^{-17}$ bar.

film changes with increasing temperatures, no clear statement about the origin of the changing activation energy can be made. At the investigated oxygen partial pressure $p(\text{O}_2) = 10^{-17}$ bar at higher temperatures a slight n -type conduction is visible.

7.4 Summary

The point defect chemistry in $\text{Ta}_2\text{O}_{5-x}$ ceramics and thin films was investigated in this section. During the preparation the ceramic as well as the film have mechanical stability problems due to pore formation and cracks, which are caused by the highly anisotropic cell parameters and linear expansion coefficients. The HTEC characteristic shows for ceramic and thin films sample for oxidizing conditions an oxygen partial pressure independent conductivity. However, the thin $\text{Ta}_2\text{O}_{5-x}$ film was ionic conductive over a larger oxygen partial pressure range than the ceramic. This may be correlated with an increased dopant concentration and an increase of the grain boundary density leading to increased space charge layer adjacent to the grains. At reducing oxygen partial pressure conditions the ceramic as well as the thin film show n -type conductivity. For low temperatures a slight slope for high oxygen activities is visible, which might indicate p -type conductivity. For oxidizing conditions two different activation energies were observed. A temperature dependent impurity concentration and a change in the conduction mechanism from ionic to n -type conduction were discussed as origin for this observation. Finally, it cannot be clarified which of these two explanations is more likely. At reducing oxygen

activity $\text{Ta}_2\text{O}_{5-x}$ is n -conducting and the defects are dominated by the extrinsic defects of the impurity concentration compensated by oxygen vacancies. The activation energy for oxygen vacancy formation is similar for the ceramic and the thin film. An intrinsic regime cannot be observed for the material in the investigated temperature range.

8 Summary and Conclusion

Within this thesis the microscopic processes in memristive devices are investigated in order to understand the defect configuration and defect motion in metal oxide thin films. Furthermore, the local redox processes localized in nanoscale filaments induced by field-driven defect motion have been elucidated.

It has been demonstrated by detailed XPS analysis that the oxygen content in binary metal oxides can be influenced by sputtering power density and by the oxygen to argon flow ratio. With increasing sputtering power density or decreasing oxygen content the films are increasingly oxygen deficient. This is consistent with the shift of the VBM towards higher binding energies and correlated to an increased electron concentration in the thin metal oxide films. A clear correlation between charge carrier concentration in pristine films and forming voltage has been demonstrated, namely a decrease of forming voltage with increasing charge carrier concentration. The other parameters such as reset current and set voltage show the same trend as the forming voltage. Moreover, it has been shown that the forming voltage is lowered in the $\text{Nb}_2\text{O}_{5-x}/\text{Ta}_2\text{O}_{5-x}$ heterosystem due to an increased charge carrier concentration in Nb_2O_5 . Also the reset current and the set voltage is lowered. After the electroforming process of $\text{Ta}_2\text{O}_{5-x}$ based MIM cells as well as $\text{Nb}_2\text{O}_{5-x}/\text{Ta}_2\text{O}_{5-x}$ heterosystems dendrite-like structures are visible at the platinum top electrode. The starting point of the dendrite-like structure is randomly distributed and might be correlated to impurities or imperfections in the pristine film. The extent of the propagation is correlated to the forming voltage. The metal oxide/metal interface plays a dominant role for the dendrite-like structure formation. The formation of the dendrite-like structure is attributed to an avalanche discharge within the adsorbate layer, which originates from *ex-situ* preparation.

The former $\text{Pt}/\text{Ta}_2\text{O}_{5-x}$ interface of dendrite-like structures of $\text{Ta}_2\text{O}_{5-x}$ based MIM structures has been studied by spectromicroscopy. The measurements show that the entire dendrite-like structure of the cell in LRS consists of a reduced phase, which is assigned to conductive TaO_2 . This is also supported by LC-AFM and work function measurements, which show an increased donor dopant concentration in the entire structure. It has been demonstrated by STEM that the dendrite-like structure remains amorphous despite the thermal impact during electroforming. Nevertheless,

changes in the tantalum oxygen bonds are possible, which might be assigned to an amorphous conductive phase. An explicit proof of the valence change from Ta^{4+} to Ta^{5+} for the subsequent switching is shown within the entire dendrite-like structure, since the concentration of the conductive TaO_{2-x} drops significantly for the HRS. The heat, which is transferred to the $\text{Ta}_2\text{O}_{5-x}$ by the avalanche discharge, leads to a local redox reaction in the entire dendrite-like structures. In contrast to the electroforming models based on ionic and electronic processes the dendrite-like structures induced by an avalanche discharge are propagated perpendicular to the electric field. The soft breakdown process induced by an avalanche discharge is localized in the interfacial adsorbate layer.

Additionally, dendrite-like structures of $\text{Nb}_2\text{O}_{5-x}/\text{Ta}_2\text{O}_{5-x}$ heterosystems with varying thicknesses of $\text{Nb}_2\text{O}_{5-x}$ have been investigated by spectromicroscopy. The dendrite-like structures in the heterosystems are smaller due to a lower forming voltage. The dendrite-like structure of the heterosystems are also correlated to an n -type doped region. An oxygen deficient component $\text{Nb}_2\text{O}_{5-\delta}$ can be identified within the dendrite-like structure. The oxygen deficient $\text{Nb}_2\text{O}_{5-\delta}$ cannot be assigned to pure NbO_2 or Nb_2O_5 .

The non linear switching kinetics of memristive devices are attributed to the non linear ionic motion of mobile donor dopants, which is a thermally activated process. The formation energy of the predominant defects as well as the equilibration processes during relaxation in TiO_{2-x} and $\text{Ta}_2\text{O}_{5-x}$ are studied in order to verify the processes during incorporation and release of oxygen to the solid. In this thesis bulk samples as well as thin films of TiO_{2-x} and $\text{Ta}_2\text{O}_{5-x}$ were studied.

The rutile single crystals with (001) and (110) orientation show n -type conductivity over the entire investigated oxygen partial pressure range. The equilibrium conductivity of the single crystals is assigned to ionic charge compensation at intermediate oxygen partial pressure and dominated by electronic charge compensation at reducing conditions. In contrast the thin films only show ionic charge compensation for the entire studied oxygen partial pressure range. The formation energy of oxygen vacancies is independent from crystal orientation and the presence of grain boundaries, since the determined values for single crystals and thin films are similar. For high oxygen activities in contrast to the single crystals the ionic conduction is predominant in the thin films. The presence of the ionic conduction at high oxygen partial pressure can be explained in terms of an increased titanium vacancy concentration and adjacent space accumulation at grain boundaries. The activation energy for oxygen vacancy diffusion in the thin films determined in the ionic conduction region fits well to the previously published values for polycrystalline TiO_2 . The formation energy of oxygen vacancies is not significantly influenced by grain boundaries.

Additionally, the equilibration kinetics of rutile single crystals and TiO_{2-x} thin film are investigated under reducing oxygen partial pressure conditions. For that purpose an equilibrium conductivity relaxation measurement setup was implemented in this thesis. For the rutile single crystals it has been shown that the relaxation process is dominated by a surface exchange process. The velocity of the surface exchange process depends also on the crystal orientation. The (001) rutile single crystals equilibrate faster than the (110) rutile single crystals, which can be correlated to the different formation energy of oxygen vacancies at the rutile surface, which may be involved at the surface exchange reaction. The relaxation process in TiO_{2-x} thin films is controlled by a heterogeneous relaxation process. Two surface exchange coefficients for a slow and fast process can be determined. As origin for the heterogeneous relaxation kinetic the incorporation or release of a second species such as water was discussed as well as the influence of the texturing of the thin film and the interaction between substrate and thin film. However it was not possible within this thesis to conclusively clarify the origin of the two kinetic processes. Further studies are necessary in order to get an detailed understanding of the complex interplay of grain boundaries, substrate and thin films, background impurities and/or water vapor in the surrounding atmosphere. In contrast to the surface exchange coefficients of the single crystals, the surface exchange coefficients for the thin films are one to two order of magnitude lower. This may be induced by a retarding field due to an additional energy barrier at the grain boundaries. Furthermore, an oxygen partial pressure induced space charge potential at the surface might also influence the surface exchange process.

The point defect chemistry in $\text{Ta}_2\text{O}_{5-x}$ ceramics and thin films was also investigated. Due to the highly anisotropic cell parameters and linear expansion coefficients pores and cracks occur during the preparation of $\text{Ta}_2\text{O}_{5-x}$ ceramics and thin films. The high temperature conductance in $\text{Ta}_2\text{O}_{5-x}$ shows for both, ceramic as well as thin film samples, no oxygen partial pressure dependence for oxidizing conditions. For low temperatures, a slight slope for high oxygen activities is visible, which might indicate p -type conductivity. For oxidizing conditions two different defect formation energies were observed. A temperature dependent impurity concentration and a change in the conduction mechanism from ionic to n -type conduction were discussed as origin for this observation. Finally, it cannot be clarified which of these two explanations is more likely. At reducing oxygen activity, $\text{Ta}_2\text{O}_{5-x}$ is n -conducting and the defects are dominated by the extrinsic defects of the impurity concentration compensated by oxygen vacancies. The activation energy for oxygen vacancy formation is similar for the ceramic and the thin film.

The ionic defect formation as well as their transport properties has been investigated. The formation energy of ionic defects in the reducing oxygen partial pressure is not influenced by additional grain boundaries. However, at higher oxygen partial pressures the thin films show an enhanced ionic conduction, which can be inter-

preted in terms of a stronger contribution of the space charge zones due to smaller grains. The equilibration process is controlled by the surface exchange process for single crystals and thin films. The velocity of the surface exchange process is influenced by the crystal orientation. The equilibration kinetics in the thin films are slower due to an additional energy barrier, which might be induced by space charge zones at the grain boundaries or an oxygen partial pressure induced space charge potential at the surface.

A Appendix

A.1 Sputterdeposition parameters

In section 3.1 the reactive sputtering process has been described. The sputtering parameters used in this thesis are listed in table A.1.

material	DC Power [W]	pressure [mbar]	Ar/O ₂ flow ratio	temperature [K]
Ta ₂ O _{5-x}	5	$3.50 \cdot 10^{-2}$	3 / 1	300
Ta ₂ O _{5-x}	20	$3.50 \cdot 10^{-2}$	3 / 1	300
Ta ₂ O _{5-x}	20	$3.50 \cdot 10^{-2}$	6 / 1	300
Ta ₂ O _{5-x}	20	$3.50 \cdot 10^{-2}$	9 / 1	300
Ta ₂ O _{5-x}	50	$3.50 \cdot 10^{-2}$	3 / 1	300
Ta ₂ O _{5-x}	80	$3.50 \cdot 10^{-2}$	3 / 1	300
Ta	30	$7.00 \cdot 10^{-3}$	1 / 0	300
Nb ₂ O _{5-x}	20	$3.50 \cdot 10^{-2}$	3 / 1	300
TiO _{2-x}	75	$3.50 \cdot 10^{-2}$	3 / 1	300
TiO _{2-x}	75	$3.50 \cdot 10^{-2}$	6 / 1	300
TiO _{2-x}	75	$3.50 \cdot 10^{-2}$	9 / 1	300
TiO _{2-x}	75	$3.50 \cdot 10^{-2}$	11 / 1	300
TiO _{2-x}	75	$3.50 \cdot 10^{-2}$	3 / 1	420

Table A.1: Overview of used sputter parameters.

List of abbreviations

AFM	atomic force microscopy
ECR	electronic conductivity relaxation
HRS	high resistance state
HTEC	high temperature equilibrium conductivity
LRS	low resistance state
MIM	metal insulator metal
PCA	principal component analysis
PEEM	photoemission electron microscopy
ReRAM	Resistive Random Access Memory
ROI	regions of interest
SEM	scanning electron microscope
STEM	scanning transmission electron microscopy
VBM	valence band maximum
VCM	valence change mechanism
XPS	X-ray photoelectron spectroscopy
XRD	X-ray diffraction
XRR	X-ray reflectometry

Bibliography

- [1] R. Waser, R. Dittmann, G. Staikov, and K. Szot, *Redox-Based Resistive Switching Memories - Nanoionic Mechanisms, Prospects, and Challenges*, Advanced Materials **21**, 2632 (2009).
- [2] R. Waser and M. Aono, *Nanoionics-based resistive switching memories*, Nature Materials **6**, 833 (2007).
- [3] A. Sawa, *Resistive switching in transition metal oxides*, Materials Today **11**, 28 (2008).
- [4] J. J. Yang, M. D. Pickett, X. Li, D. A. A. Ohlberg, D. R. Stewart, and R. S. Williams, *Memristive switching mechanism for metal/oxide/metal nanodevices*, Nature Nanotechnology **3**, 429 (2008).
- [5] J. J. Yang, F. Miao, M. D. Pickett, D. A. A. Ohlberg, D. R. Stewart, C. N. Lau, and R. S. Williams, *The mechanism of electroforming of metal oxide memristive switches*, Nanotechnology **20**, 215201 (2009).
- [6] Y. B. Nian, J. Strozier, N. J. Wu, X. Chen, and A. Ignatiev, *Evidence for an Oxygen Diffusion Model for the Electric Pulse Induced Resistance Change Effect in Transition-Metal Oxides*, Physical Review Letters **98**, 146403 (2007).
- [7] K. Szot, W. Speier, G. Bihlmayer, and R. Waser, *Switching the electrical resistance of individual dislocations in single-crystalline SrTiO₃*, Nature Materials **5**, 312 (2006).
- [8] A. A. Sharma, M. Noman, M. Abdelmoula, M. Skowronski, and J. A. Bain, *Electronic Instabilities Leading to Electroformation of Binary Metal Oxide-based Resistive Switches*, Advanced Functional Materials **24**, 5522 (2014).
- [9] C. Lenser, M. Patt, S. Menzel, A. Köhl, C. Wiemann, C. M. Schneider, R. Waser, and R. Dittmann, *Insights into Nanoscale Electrochemical Reduction in a Memristive Oxide: the Role of Three-Phase Boundaries*, Advanced Functional Materials **24**, 4466 (2014).

- [10] R. Münstermann, J. J. Yang, J. P. Strachan, G. Medeiros-Ribeiro, R. Dittmann, and R. Waser, *Morphological and electrical changes in TiO_2 memristive devices induced by electroforming and switching*, physica status solidi (RRL) -Rapid Research Letters **4**, 16 (2010).
- [11] Z. Wei, Y. Kanzawa, K. Arita, Y. Katoh, K. Kawai, S. Muraoka, S. Mitani, S. Fujii, K. Katayama, M. Iijima, T. Mikawa, T. Ninomiya, R. Miyanaga, Y. Kawashima, K. Tsuji, A. Himeno, T. Okada, R. Azuma, K. Shimakawa, H. Sugaya, T. Takagi, R. Yasuhara, K. Horiba, H. Kumigashira, and M. Oshima, *Highly reliable TaO_x ReRAM and direct evidence of redox reaction mechanism*, in 2008 IEEE International Electron Devices Meeting, pp. 1–4, 2008.
- [12] J. P. Strachan, G. Medeiros-Ribeiro, J. J. Yang, M. Zhang, F. Miao, I. Goldfarb, M. Holt, V. Rose, and R. S. Williams, *Spectromicroscopy of tantalum oxide memristors*, Applied Physics Letters **98**, 242114 (2011).
- [13] F. Miao, J. P. Strachan, J. J. Yang, M.-X. Zhang, I. Goldfarb, A. C. Torrezan, P. Eschbach, R. D. Kelley, G. Medeiros-Ribeiro, and R. S. Williams, *Anatomy of a Nanoscale Conduction Channel Reveals the Mechanism of a High-Performance Memristor*, Advanced Materials **23**, 5633 (2011).
- [14] Y. Yang, S. Choi, and W. Lu, *Oxide Heterostructure Resistive Memory*, Nano Letters **13**, 2908 (2013).
- [15] S. Menzel, M. Waters, A. Marchewka, U. Böttger, R. Dittmann, and R. Waser, *Origin of the Ultra-nonlinear Switching Kinetics in Oxide-Based Resistive Switches*, Advanced Functional Materials **21**, 4487 (2011).
- [16] S. Kim, S. Choi, and W. Lu, *Comprehensive Physical Model of Dynamic Resistive Switching in an Oxide Memristor*, ACS Nano **8**, 2369 (2014).
- [17] F. Miao, W. Yi, I. Goldfarb, J. J. Yang, M.-X. Zhang, M. D. Pickett, J. P. Strachan, G. Medeiros-Ribeiro, and R. S. Williams, *Continuous Electrical Tuning of the Chemical Composition of TaO_x -Based Memristors*, ACS Nano **6**, 2312 (2012).
- [18] G.-S. Park, Y. B. Kim, S. Y. Park, X. S. Li, S. Heo, M.-J. Lee, M. Chang, J. H. Kwon, M. Kim, U.-I. Chung, R. Dittmann, R. Waser, and K. Kim, *In situ observation of filamentary conducting channels in an asymmetric $\text{Ta}_2\text{O}_{5-x}/\text{TaO}_{2-x}$ bilayer structure*, Nature Communications **4**, 2382 (2013).
- [19] M. Fujimoto, H. Koyama, M. Konagai, Y. Hosoi, K. Ishihara, S. Ohnishi, and N. Awaya, *TiO_2 anatase nanolayer on TiN thin film exhibiting high-speed bipolar resistive switching*, Applied Physics Letters **89**, 223509 (2006).

-
- [20] C. Hermes, M. Wimmer, S. Menzel, K. Fleck, G. Bruns, M. Salinga, U. Böttger, R. Bruchhaus, T. Schmitz-Kempen, M. Wuttig, and R. Waser, *Analysis of Transient Currents During Ultrafast Switching of TiO_2 Nanocrossbar Devices*, IEEE Electron Device Letters **32**, 1116 (2011).
- [21] P. Gonon, M. Mougenot, C. Vallée, C. Jorel, V. Jousseau, H. Grampeix, and F. El Kamel, *Resistance switching in HfO_2 metal-insulator-metal devices*, Journal of Applied Physics **107**, 074507 (2010).
- [22] J. P. Strachan, J. J. Yang, L. A. Montoro, C. A. Ospina, A. J. Ramirez, A. L. D. Kilcoyne, G. Medeiros-Ribeiro, and R. S. Williams, *Characterization of electroforming-free titanium dioxide memristors*, Beilstein Journal of Nanotechnology **4**, 467 (2013).
- [23] S. Kim, S. Choi, J. Lee, and W. D. Lu, *Tuning Resistive Switching Characteristics of Tantalum Oxide Memristors through Si Doping*, ACS Nano **8**, 10262 (2014).
- [24] R. Muenstermann, T. Menke, R. Dittmann, S. Mi, C.-L. Jia, D. Park, and J. Mayer, *Correlation between growth kinetics and nanoscale resistive switching properties of SrTiO_3 thin films*, Journal of Applied Physics **108**, 124504 (2010).
- [25] M. Janousch, G. I. Meijer, U. Staub, B. Delley, S. F. Karg, and B. P. Andreasson, *Role of Oxygen Vacancies in Cr-Doped SrTiO_3 for Resistance-Change Memory*, Advanced Materials **19**, 2232 (2007).
- [26] C. Moreno, C. Munuera, S. Valencia, F. Kronast, X. Obradors, and C. Ocal, *Reversible Resistive Switching and Multilevel Recording in $\text{La}_{0.7}\text{Sr}_{0.3}\text{MnO}_3$ Thin Films for Low Cost Nonvolatile Memories*, Nano Letters **10**, 3828 (2010).
- [27] J. P. Strachan, M. D. Pickett, J. J. Yang, S. Aloni, A. L. David Kilcoyne, G. Medeiros-Ribeiro, and R. Stanley Williams, *Direct Identification of the Conducting Channels in a Functioning Memristive Device*, Advanced Materials **22**, 3573 (2010).
- [28] J. P. Strachan, J. J. Yang, R. Münstermann, A. Scholl, G. Medeiros-Ribeiro, D. R. Stewart, and R. S. Williams, *Structural and chemical characterization of TiO_2 memristive devices by spatially-resolved NEXAFS*, Nanotechnology **20**, 485701 (2009).
- [29] D.-H. Kwon, K. M. Kim, J. H. Jang, J. M. Jeon, M. H. Lee, G. H. Kim, X.-S. Li, G.-S. Park, B. Lee, S. Han, M. Kim, and C. S. Hwang, *Atomic structure of conducting nanofilaments in TiO_2 resistive switching memory*, Nature Nanotechnology **5**, 148 (2010).

- [30] C. Lenser, Z. Connell, A. Kovács, R. Dunin-Borkowski, A. Köhl, R. Waser, and R. Dittmann, *Identification of screw dislocations as fast-forming sites in Fe-doped SrTiO₃*, Applied Physics Letters **102**, 183504 (2013).
- [31] A. Marchewka, B. Roesgen, K. Skaja, H. Du, C.-L. Jia, J. Mayer, V. Rana, R. Waser, and S. Menzel, *Nanoionic Resistive Switching Memories: On the Physical Nature of the Dynamic Reset Process*, Advanced Electronic Materials **2** (2016).
- [32] S. Kumar, C. E. Graves, J. P. Strachan, A. L. D. Kilcoyne, T. Tylliszczak, Y. Nishi, and R. S. Williams, *In-operando synchronous time-multiplexed O K-edge x-ray absorption spectromicroscopy of functioning tantalum oxide memristors*, Journal of Applied Physics **118**, 034502 (2015).
- [33] S. Kumar, C. E. Graves, J. P. Strachan, E. M. Grafals, A. L. D. Kilcoyne, T. Tylliszczak, J. N. Weker, Y. Nishi, and R. S. Williams, *Direct Observation of Localized Radial Oxygen Migration in Functioning Tantalum Oxide Memristors*, Advanced Materials **28**, 2772 (2016).
- [34] J. Nowotny, T. Bak, M. K. Nowotny, and L. R. Sheppard, *TiO₂ Surface Active Sites for Water Splitting*, The Journal of Physical Chemistry B **110**, 18492 (2006).
- [35] D. A. H. Hanaor and C. C. Sorrell, *Review of the anatase to rutile phase transformation*, Journal of Materials Science **46**, 855 (2011).
- [36] D. T. Cromer and K. Herrington, *The Structures of Anatase and Rutile*, Journal of the American Chemical Society **77**, 4708 (1955).
- [37] Q. Wu, D. Li, Y. Hou, L. Wu, X. Fu, and X. Wang, *Study of relationship between surface transient photoconductivity and liquid-phase photocatalytic activity of titanium dioxide*, Materials Chemistry and Physics **102**, 53 (2007).
- [38] M. Horn, C. F. Schwerdtfeger, and E. P. Meagher, *Refinement of the structure of anatase at several remperatures*, Zeitschrift für Kristallographie **136**, 273 (1972).
- [39] O. Byl and J. John T. Yates, *Anisotropy in the Electrical Conductivity of Rutile TiO₂ in the (110) Plane*, The Journal of Physical Chemistry B **110**, 22966 (2006), PMID: 17107127.
- [40] K. Momma and F. Izumi, *VESTA3 for three-dimensional visualization of crystal, volumetric and morphology data*, Journal of Applied Crystallography **44**, 1272 (2011).

-
- [41] A. Belsky, M. Hellenbrandt, V. L. Karen, and P. Luksch, *New developments in the Inorganic Crystal Structure Database (ICSD): accessibility in support of materials research and design*, Acta Crystallographica Section B **58**, 364 (2002).
- [42] A. Magnéli, *Non-stoichiometry and structural disorder in some families of inorganic compounds*, Pure and Applied Chemistry **50**, 1261 (1978).
- [43] L. A. Bursill and B. G. Hyde, *On the aggregation of wadsley defects in slightly reduced rutile*, Philosophical Magazine **23**, 3 (1971).
- [44] L. A. Bursill and B. G. Hyde, *Crystallographic shear in the higher titanium oxides: Structure, texture, mechanisms and thermodynamics*, Progress in Solid State Chemistry **7**, 177 (1972).
- [45] R. F. Bartholomew and D. R. Frankl, *Electrical Properties of Some Titanium Oxides*, Physical Review **187**, 828833 (1969).
- [46] G. A. Acket and J. Volger, *Measurements of the bulk-conductivity of slightly reduced rutile (TiO_2) parallel and perpendicular to the c-axis*, Physica **29**, 225 (1963).
- [47] V. A. Shvets, V. S. Aliev, D. V. Gritsenko, S. S. Shaimeev, E. V. Fedosenko, S. V. Rykhliiski, V. V. Atuchin, V. A. Gritsenko, V. M. Tapilin, and H. Wong, *Electronic structure and charge transport properties of amorphous Ta_2O_5 films*, Journal of Non-Crystalline Solids **354**, 3025 (2008).
- [48] V. Rico, A. Borrás, F. Yubero, J. P. Espinós, F. Frutos, and A. R. González-Elipe, *Wetting Angles on Illuminated Ta_2O_5 Thin Films with Controlled Nanostructure*, The Journal of Physical Chemistry C **113**, 3775 (2009).
- [49] K. Kukli, J. Aarik, A. Aidla, O. Kohan, T. Uustare, and V. Sammelselg, *Properties of tantalum oxide thin films grown by atomic layer deposition*, Thin Solid Films **260**, 135 (1995).
- [50] J. Robertson, *High dielectric constant gate oxides for metal oxide Si transistors*, Reports on Progress in Physics **69**, 327 (2006).
- [51] R. S. Roth and J. L. Waring, *Effect of Oxide Additions on the Polymorphism of Tantalum Pentoxide III. "Stabilization" of the Low Temperature structure Type*, Journal of Research of the National Bureau of Standards - A. Physics and Chemistry **74 A**, 485 (1970).
- [52] R. S. Roth, J. L. Waring, and W. S. Brower, *Effect of Oxide Additions on the Polymorphism of Tantalum Pentoxide II. 'Stabilization' of the High Temperature Structure Type*, Journal of Research of the National Bureau of Standards - A. Physics and Chemistry **74A**, 477 (1970).

- [53] S. P. Garg, N. Krishnamurthy, A. Awasthi, and M. Venkatraman, *The O-Ta (Oxygen-Tantalum) system*, Journal of Phase Equilibria **17**, 63 (1996).
- [54] N. Schönberg, *An X-Ray Investigation of the Tantalum-Oxygen System*, Acta Chemica Scandinavica **8**, 240 (1954).
- [55] J. Niebuhr, *Die Niederen Oxide Des Tantals*, Journal of the Less Common Metals **10**, 312 (1966).
- [56] A. Wedig, M. Luebben, D.-Y. Cho, M. Moors, K. Skaja, V. Rana, T. Hasegawa, K. K. Adepalli, B. Yildiz, R. Waser, and I. Valov, *Nanoscale cation motion in TaO_x , HfO_x and TiO_x memristive systems*, Nature Nanotechnology **11**, 67 (2016).
- [57] B. R. Sahu and L. Kleinman, *Theoretical study of structural and electronic properties of β - Ta_2O_5 and δ - Ta_2O_5* , Physical Review B **69**, 165202 (2004).
- [58] N. Terao, *Structure des Oxydes de Tantale*, Japanese Journal of Applied Physics **6**, 21 (1967).
- [59] J. Harvey and H. Wilman, *The crystallisation of thin amorphous tantalum oxide films heated in air or vacuo, and the structure of the crystalline oxide*, Acta Crystallographica **14**, 1278 (1961).
- [60] M. B. A. Reisman, F. Holzberg and M. Berry, *Reactions of the Group VB Pentoxides with Alkali Oxides and Carbonates. III. Thermal and X-Ray Phase Diagrams of the System K_2O or K_2CO_3 with Ta_2O_5* , Journal of the American Chemical Society **78**, 4514 (1956).
- [61] J. L. Waring and R. S. Roth, *Effect of Oxide Additions on the Polymorphism of Tantalum Pentoxide (System Ta_2O_5 - TiO_2)*, Journal of Research of the National Bureau of Standards- A. Physics and Chemistry **72A**, 175 (1968).
- [62] K. K. Adepalli, M. Kelsch, R. Merkle, and J. Maier, *Influence of Line Defects on the Electrical Properties of Single Crystal TiO_2* , Advanced Functional Materials **23**, 1798 (2013).
- [63] A. Fujishima, T. N. Rao, and D. A. Tryk, *Titanium dioxide photocatalysis*, Journal of Photochemistry and Photobiology C: Photochemistry Reviews **1**, 1 (2000).
- [64] P. Pichat, *Heterogeneous Photocatalysis: From Fundamentals to Green Applications*, chapter Fundamentals of TiO_2 Photocatalysis. Consequences for Some Environmental Applications, pp. 321–359, Springer Berlin Heidelberg, Berlin, Heidelberg, 2016.
- [65] P. Kofstad, *Nonstoichiometry, diffusion, and electrical conductivity in binary metal oxides*, Wiley-Interscience, 1972.

-
- [66] J. Nowotny, *Oxide Semiconductors for Solar Energy Conversion Titanium Dioxide*, CRC Press Taylor & Francis Group, 2012.
- [67] J. F. Baumard, D. Panis, and A. M. Anthony, *A study of Ti-O system between Ti_3O_5 and TiO_2 at high temperature by means of electrical resistivity*, Journal of Solid State Chemistry **20**, 43 (1977).
- [68] U. Balachandran and N. G. Eror, *Electrical conductivity in non-stoichiometric titanium dioxide at elevated temperatures*, Journal of Materials Science **23**, 2676 (1988).
- [69] D.-K. Lee and H.-I. Yoo, *Unusual oxygen re-equilibration kinetics of $TiO_{2-\delta}$* , Solid State Ionics **177**, 1 (2006).
- [70] P. Kofstad, *Thermogravimetric studies of the defect structure of rutile (TiO_2)*, Journal of Physics and Chemistry of Solids **23**, 1579 (1962).
- [71] J. Nowotny, T. Bak, and T. Burg, *Electrical properties of polycrystalline TiO_2 at elevated temperatures. Electrical conductivity*, physica status solidi (b) **244**, 2037 (2007).
- [72] L. R. Sheppard, T. Bak, and J. Nowotny, *Electrical Properties of Niobium-Doped Titanium Dioxide. 1. Defect Disorder*, The Journal of Physical Chemistry B **110**, 22447 (2006).
- [73] J. A. S. Ikeda and Y. Chiang, *Space Charge Segregation at Grain Boundaries in Titanium Dioxide: I, Relationship between Lattice Defect Chemistry and Space Charge Potential*, Journal of the American Cer **76**, 2437 (1933).
- [74] K. Seip Førlund, *The Defect Structure of Rutile Containing Small Additions of Aluminum Oxide*, Acta Chemica Scandinavica **20**, 2573 (1966).
- [75] J. Carpentier, A. Lebrun, and F. Perdu, *Point Defects And Charge Transport in Pure And Chromium-Doped Rutile At 1273 K*, Journal of Physics and Chemistry of Solids **50**, 145 (1989).
- [76] D. Lee and H. Yoo, *Electrical conductivity and oxygen nonstoichiometry of acceptor (Ga)-doped titania*, Physical Chemistry Chemical Physics **10**, 6890 (2008).
- [77] R. Bredesen and P. Kofstad, *A reinterpretation of the defect structure of $L-Ta_2O_5$* , Solid State Ionics **27**, 11 (1988).
- [78] J. E. Stroud, W. C. Tripp, and J. M. Wimmer, *Defect Structure of Ta_2O_5* , Journal of the American Ceramic Society **57**, 172 (1974).

- [79] J. L. Carpentier, J. L. Dellis, A. Lebrun, P. Tellier, and J. C. Picot, *Détermination du nombre de transport ionique dans β -Ta₂O₅ à haute température par spectroscopie d'impédance électrique*, Journal of the Less Common Metals **168**, 295 (1991).
- [80] A. E. McHale and H. L. Tuller, *Defects and Charge Transport in β -Ta₂O₅: I. Analysis of the Conductivity Observed in Nominally Pure β -Ta₂O₅*, Journal of the American Ceramic Society **68**, 646 (1985).
- [81] J. L. Dellis, J. L. Carpentier, J. C. Picot, P. Tellier, and M. Filal, *Défauts de structure et transport de charges dans β -Ta₂O₅ en équilibre thermodynamique à haute température*, Journal of Alloys and Compounds **189**, 157 (1992).
- [82] J. Crank, *The mathematics of diffusion*, Oxford, 2nd edition, 1975.
- [83] I. Yasuda and T. Hikita, *Precise Determination of the Chemical Diffusion Coefficient of Calcium-Doped Lanthanum Chromites by Means of Electrical Conductivity Relaxation*, Journal of the Electrochemical Society **141**, 1268 (1994).
- [84] M. W. den Otter, H. J. M. Bouwmeester, B. A. Boukamp, and H. Verweij, *Reactor flush time correction in relaxation experiments*, Journal of The Electrochemical Society **148**, J1 (2001).
- [85] J. Maier, *Festkörper - Fehler und Funktion Prinzipien der Physikalischen Festkörperchemie*, Teubner Studienbücher, 2000.
- [86] T. Bak and J. Nowotny, *Reactivity of rutile with oxygen and hydrogen and related charge transfer*, Journal of Physical Chemistry C **115**, 15345 (2011).
- [87] W. S. Epling, C. H. F. Peden, M. A. Henderson, and U. Diebold, *Evidence for oxygen adatoms on TiO₂(110) resulting from O₂ dissociation at vacancy sites*, Surface Science **412413**, 333 (1998).
- [88] U. Diebold, J. Lehman, T. Mahmoud, M. Kuhn, G. Leonardelli, W. Hebenstreit, M. Schmid, and P. Varga, *Intrinsic defects on a TiO₂(110)(1×1) surface and their reaction with oxygen: a scanning tunneling microscopy study*, Surface Science **411**, 137 (1998).
- [89] M. A. Henderson, W. S. Epling, C. L. Perkins, C. H. F. Peden, and U. Diebold, *Interaction of Molecular Oxygen with the Vacuum-Annealed TiO₂(110) Surface: Molecular and Dissociative Channels*, The Journal of Physical Chemistry B **103**, 5328 (1999).
- [90] P. Stone, R. A. Bennett, and M. Bowker, *Reactive re-oxidation of reduced TiO₂ (110) surfaces demonstrated by high temperature STM movies*, New Journal of Physics **1**, 8 (1999).

-
- [91] R. D. Smith, R. A. Bennett, and M. Bowker, *Measurement of the surface-growth kinetics of reduced $\text{TiO}_2(110)$ during reoxidation using time-resolved scanning tunneling microscopy*, Physical Review B **66**, 035409 (2002).
- [92] M. Bowker and R. A. Bennett, *The role of Ti^{3+} interstitials in TiO_2 (110) reduction and oxidation*, Journal of Physics: Condensed Matter **21**, 474224 (2009).
- [93] T. B. Gruenwald and G. Gordon, *Oxygen diffusion in single crystals of titanium dioxide*, Journal of Inorganic and Nuclear Chemistry **33**, 1151 (1971).
- [94] A. N. Bagshaw and B. G. Hyde, *Oxygen tracer diffusion in the magnéli phases $\text{Ti}_n\text{O}_{2n-1}$* , Journal of Physics and Chemistry of Solids **37**, 835 (1976).
- [95] D. J. Derry, D. G. Lees, and J. M. Calvert, *A study of oxygen self-diffusion in the C-direction of rutile using a nuclear technique*, Journal of Physics and Chemistry of Solids **42**, 57 (1981).
- [96] F. Millot and C. Picard, *Oxygen self-diffusion in non-stoichiometric rutile TiO_{2-x} at high temperature*, Solid State Ionics **2830**, Part 2, 1344 (1988).
- [97] K. Hoshino, N. L. Peterson, and C. L. Wiley, *Diffusion and point defects in TiO_{2-x}* , Journal of Physics and Chemistry of Solids **46**, 1397 (1985).
- [98] E. Iguchi and K. Yajima, *Diffusion of Oxygen Vacancies in Reduced Rutile (TiO_2)*, Journal of the Physical Society of Japan **32**, 1415 (1972).
- [99] J. F. Baumard, *The chemical diffusivity of oxygen in oxygen deficient rutile for compositions close to TiO_2* , Solid State Communications **20**, 859 (1976).
- [100] N. Ait-Younes, F. Millot, and P. Gerdanian, *Isothermal transport in TiO_{2-x} . Part II. Chemical diffusion in TiO_{2-x}* , Solid State Ionics **12**, 437 (1984).
- [101] Z. Grzesik, T. Bak, J. Nowotny, and B. Henry, *Chemical diffusion in amphoteric oxide semiconductors*, Advances in Applied Ceramics **106**, 77 (2007).
- [102] M. K. Nowotny, T. Bak, and J. Nowotny, *Electrical Properties and Defect Chemistry of TiO_2 Single Crystal. III. Equilibration Kinetics and Chemical Diffusion*, The Journal of Physical Chemistry B **110**, 16292 (2006).
- [103] C. Ko, A. Karthikeyan, and S. Ramanathan, *Studies on oxygen chemical surface exchange and electrical conduction in thin film nanostructured titania at high temperatures and varying oxygen pressure*, The Journal of Chemical Physics **134**, 014704 (2011).
- [104] V. I. Barbanel and V. N. Bogomolov, *Diffusion of defects in rutile during its partial reduction in a vacuum*, Soviet Physics-Solid State **11**, 2160 (1970).

- [105] J. Moser, P. E. Childs, and J. J. B. Wagner, *Chemical diffusion in nonstoichiometric compounds*, Proceedings of the British Ceramic Society **19**, 29 (1971).
- [106] G. M. Crosbie, *Chemical diffusivity and electrical conductivity in TiO_2 containing a submicron dispersion of SiO_2* , Journal of Solid State Chemistry **25**, 367 (1978).
- [107] F. Morin, *A reassessment of chemical diffusivity in TiO_{2-x}* , Solid State Communications **58**, 161 (1986).
- [108] F. Millot, *Anisotropy of ionic transport properties of nonstoichiometric single crystals of rutile TiO_{2-x} at high temperature*, Journal of Materials Science Letters **4**, 902 (1984).
- [109] M. Radecka, P. Sobaś, and M. Rekas, *Ambipolar Diffusion in TiO_2* , Solid State Ionics **119**, 55 (1999).
- [110] J. Nowotny, T. Bak, and T. Burg, *Electrical properties of polycrystalline TiO_2 : Equilibration kinetics*, Ionics **13**, 71 (2007).
- [111] S. Hüfner, *Photoelectron spectroscopy: principles and applications*, Springer Science & Business Media, third edition edition, 2013.
- [112] K. Siegbahn, *Electron spectroscopy for atoms, molecules, and condensed matter*, Reviews of Modern Physics **54**, 709 (1982).
- [113] J. F. Watts and J. Wolstenholme, *An Introduction to Surface Analysis by XPS and AES*, John Wiley & Sons, Ltd, 2005.
- [114] S. Tanuma, C. J. Powell, and D. R. Penn, *Calculations of electron inelastic mean free paths. IX. Data for 41 elemental solids over the 50 eV to 30 keV range*, Surface and Interface Analysis **43**, 689 (2011).
- [115] J. F. Moulder and J. Chastain, *Handbook of X-ray Photoelectron Spectroscopy: A Reference Book of Standard Spectra for Identification and Interpretation of XPS Data*, Physical Electronics, 1995.
- [116] M. Henzler and W. Göpel, *Oberflächenphysik des Festkörpers*, Teubner, Stuttgart, 1. edition, 1991.
- [117] A. Köhl, *Micro-spectroscopic investigation of valence change processes in resistive switching SrTiO_3 thin films*, PhD thesis, RWTH Aachen, 2014.
- [118] M. Escher, N. Weber, M. Merkel, C. Ziethen, P. Bernhard, G. Schönhense, S. Schmidt, F. Forster, F. Reinert, B. Krömker, and D. Funnemann, *NanoESCA: a novel energy filter for imaging x-ray photoemission spectroscopy*, Journal of Physics: Condensed Matter **17**, S1329 (2005).

-
- [119] O. Renault, N. Barrett, A. Bailly, L. F. Zagonel, D. Mariolle, J. C. Cezar, N. B. Brookes, K. Winkler, B. Krömker, and D. Funnemann, *Energy-filtered {XPEEM} with NanoESCA using synchrotron and laboratory X-ray sources: Principles and first demonstrated results*, Surface Science **601**, 4727 (2007), Proceedings of the Fifth International Conference on LEEM/PEEMLEEM/PEEM 5 Proceedings of the Fifth International Conference on LEEM/PEEM.
- [120] J. Stöhr and S. Anders, *X-ray spectro-microscopy of complex materials and surfaces*, IBM Journal of Research and Development **44**, 535 (2000).
- [121] C. M. Schneider and G. Schönhense, *Investigating surface magnetism by means of photoexcitation electron emission microscopy*, Reports on Progress in Physics **65**, 1785 (2002).
- [122] C. A. Ohly, *Nanocrystalline alkaline Earth Titanates and their electrical conductivity characteristics under changing Oxygen ambients*, PhD thesis, RWTH Aachen, 2003.
- [123] F. M. B. Marques and G. P. Wirtz, *Oxygen Fugacity Control in Nonflowing Atmospheres: I, Experimental Observations in CO/CO₂ and O₂/N₂ Mixtures*, Journal of the American Ceramic Society **75**, 369 (1992).
- [124] F. Gunkel, *The influence of defects on the conductivity of the LAO/STO interface*, Master's thesis, RWTH Aachen, 2009.
- [125] I. Barin, *Thermochemical Data of Pure Substances*, volume I, VCH Publishers, third edition, 1995.
- [126] I. Goldfarb, F. Miao, J. J. Yang, W. Yi, J. P. Strachan, M. Zhang, M. D. Pickett, G. Medeiros-Ribeiro, and R. S. Williams, *Electronic structure and transport measurements of amorphous transition-metal oxides: observation of Fermi glass behavior*, Applied Physics A **107**, 1 (2012).
- [127] T. Tachikawa, M. Minohara, Y. Nakanishi, Y. Hikita, M. Yoshita, H. Akiyama, C. Bell, and H. Y. Hwang, *Metal-to-insulator transition in anatase TiO₂ thin films induced by growth rate modulation*, Applied Physics Letters **101**, 022104 (2012).
- [128] M. Björck and G. Andersson, *GenX: an extensible X-ray reflectivity refinement program utilizing differential evolution*, Journal of Applied Crystallography **40**, 1174 (2007).
- [129] Z. Y. Yin and B. K. Garside, *Low-loss GeO₂ optical waveguide fabrication using low deposition rate rf sputtering*, Applied Optics **21**, 4324 (1982).

- [130] S. J. Keun, K. Ki-han, C. H. Jun, C. W. Seok, P. Mungi, S. Kyung-han, P. Young, and L. Dong-Gun, *Synthesis and Characterization of Al-Doped Zinc Oxide Films by an Radio Frequency Magnetron Sputtering Method for Transparent Electrode Applications*, Transactions on Electrical and Electronic Materials **11**, 29 (2010).
- [131] D. Depla and S. Mahieu, *Reactive sputter deposition*, Springer, 2008.
- [132] G. S. Oehrlein, F. M. d’Heurle, and A. Reisman, *Some properties of crystallized tantalum pentoxide thin films on silicon*, Journal of Applied Physics **55**, 3715 (1984).
- [133] E. Atanassova, N. Novkovski, A. Paskaleva, and M. Pecovska-Gjorgjevich, *Oxygen annealing modification of conduction mechanism in thin rf sputtered Ta₂O₅ on Si*, Solid-State Electronics **46**, 1887 (2002).
- [134] R. Nakamura, M. Ishimaru, K. Sato, K. Tanaka, H. Nakajima, and T. J. Konno, *Formation of highly oriented nanopores via crystallization of amorphous Nb₂O₅ and Ta₂O₅*, Journal of Applied Physics **114**, 124308 (2013).
- [135] M. H. Suhail, G. M. Rao, and S. Mohan, *dc reactive magnetron sputtering of titanium-structural and optical characterization of TiO₂ films*, Journal of Applied Physics **71**, 1421 (1992).
- [136] M. Yamagishi, S. Kuriki, P. K. Song, and Y. Shigesato, *Thin film TiO₂ photocatalyst deposited by reactive magnetron sputtering*, Thin Solid Films **442**, 227 (2003), Selected papers from the 4th International Conference on Coatings on Glass.
- [137] Y. Syono, M. Kikuchi, T. Goto, and K. Fukuoka, *Formation of rutile-type Ta(IV)O₂ by shock reduction and cation-deficient Ta_{0.8}O₂ by subsequent oxidation*, Journal of Solid State Chemistry **50**, 133 (1983).
- [138] J. M. Sanz and S. Hofmann, *Auger electron spectroscopy and X-ray photoelectron spectroscopy studies of the oxidation of polycrystalline tantalum and niobium at room temperature and low oxygen pressures*, Journal of the Less Common Metals **92**, 317 (1983).
- [139] O. Kerrec, D. Devilliers, H. Groult, and P. Marcus, *Study of dry and electrogenerated Ta₂O₅ and Ta/Ta₂O₅/Pt structures by XPS*, Materials Science and Engineering: B **55**, 134 (1998).
- [140] B. Díaz, J. Światowska, V. Maurice, M. Pisarek, A. Seyeux, S. Zanna, S. Tervakangas, J. Kolehmainen, and P. Marcus, *Chromium and tantalum oxide nanocoatings prepared by filtered cathodic arc deposition for corrosion protection of carbon steel*, Surface and Coatings Technology **206**, 3903 (2012).

-
- [141] B. Díaz, J. Światowska, V. Maurice, A. Seyeux, E. Härkönen, M. Ritala, S. Tervakangas, J. Kolehmainen, and P. Marcus, *Tantalum oxide nanocoatings prepared by atomic layer and filtered cathodic arc deposition for corrosion protection of steel: Comparative surface and electrochemical analysis*, *Electrochimica Acta* **90**, 232 (2013).
- [142] S. D. Khanin and A. L. Ivanovskii, *The influence of structural defects on the electronic properties of amorphous Ta_2O_5* , *physica status solidi (b)* **174**, 449 (1992).
- [143] A. Arranz, V. Pérez-Dieste, and C. Palacio, *Electronic structure of stoichiometric and reduced Ta_2O_5 surfaces determined by resonant photoemission*, *Physical Review B* **66**, 075420 (2002).
- [144] H. Sawada and K. Kawakami, *Electronic structure of oxygen vacancy in Ta_2O_5* , *Journal of Applied Physics* **86**, 956 (1999).
- [145] B. Xiao and S. Watanabe, *Oxygen vacancy effects on an amorphous- TaO_x -based resistance switch: a first principles study*, *Nanoscale* **6**, 10169 (2014).
- [146] R. J. Bondi, M. P. Desjarlais, A. P. Thompson, G. L. Brennecke, and M. J. Marinella, *Electrical conductivity in oxygen-deficient phases of tantalum pentoxide from first-principles calculations*, *Journal of Applied Physics* **114**, 203701 (2013).
- [147] S. A. Chambers, T. Droubay, T. C. Kaspar, and M. Gutowski, *Experimental determination of valence band maxima for $SrTiO_3$, TiO_2 , and SrO and the associated valence band offsets with $Si(001)$* , *Journal of Vacuum Science & Technology B* **22**, 2205 (2004).
- [148] S. M. Sze and K. K. Ng, *Physics of semiconductor devices*, John Wiley & sons, 2006.
- [149] M. Houssa, M. Tuominen, M. Naili, V. Afanasev, A. Stesmans, S. Haukka, and M. M. Heyns, *Trap-assisted tunneling in high permittivity gate dielectric stacks*, *Journal of Applied Physics* **87**, 8615 (2000).
- [150] P. M. Kumar, S. Badrinarayanan, and M. Sastry, *Nanocrystalline TiO_2 studied by optical, {FTIR} and X-ray photoelectron spectroscopy: correlation to presence of surface states*, *Thin Solid Films* **358**, 122 (2000).
- [151] M. C. Biesinger, L. W. M. Lau, A. R. Gerson, and R. S. C. Smart, *Resolving surface chemical states in {XPS} analysis of first row transition metals, oxides and hydroxides: Sc, Ti, V, Cu and Zn*, *Applied Surface Science* **257**, 887 (2010).

- [152] T. B. Reed, *Free Energy of Formation of Binary Compounds: An Atlas of Charts for High-Temperature Chemical Calculations*, The MIT Press, Cambridge, Mass, 1971.
- [153] B. Enright and D. Fitzmaurice, *Spectroscopic Determination of Electron and Hole Effective Masses in a Nanocrystalline Semiconductor Film*, The Journal of Physical Chemistry **100**, 1027 (1996).
- [154] S. Furukawa, Y. Ohno, T. Shishido, K. Teramura, and T. Tanaka, *Reaction Mechanism and the Role of Copper in the Photooxidation of Alcohol over Cu/Nb₂O₅*, Chemical Physics and Physical Chemistry **12**, 2823 (2011).
- [155] M. R. N. Soares, S. Leite, C. Nico, M. Peres, A. J. S. Fernandes, M. P. F. Graça, M. Matos, R. Monteiro, T. Monteiro, and F. M. Costa, *Effect of processing method on physical properties of Nb₂O₅*, Journal of the European Ceramic Society **31**, 501 (2011).
- [156] A. T. Fromhold and E. L. Cook, *Kinetics of Oxide Film Growth on Metal Crystals: Electron Tunneling and Ionic Diffusion*, Physical Review **158**, 600 (1967).
- [157] R. Landrock, *Spatially resolved analysis of resistive switching in transition metal oxide thin films*, PhD thesis, RWTH Aachen, 2011.
- [158] S. Schmelzer, E. Linn, U. Böttger, and R. Waser, *Uniform Complementary Resistive Switching in Tantalum Oxide Using Current Sweeps*, IEEE Electron Device Letters **34**, 114 (2013).
- [159] S.-C. Na, J.-J. Kim, M. Chul Chun, D. Hee Jin, S.-E. Ahn, and B. Soo Kang, *Mechanism of the reset process in bipolar-resistance-switching Ta/TaO_x/Pt capacitors based on observation of the capacitance and resistance*, Applied Physics Letters **104**, 123503 (2014).
- [160] S. U. Sharath, T. Bertaud, J. Kurian, E. Hildebrandt, C. Walczyk, P. Calka, P. Zaumseil, M. Sowinska, D. Walczyk, A. Gloskovskii, T. Schroeder, and L. Alff, *Towards forming-free resistive switching in oxygen engineered HfO_{2-x}*, Applied Physics Letters **104**, 063502 (2014).
- [161] S. U. Sharath, J. Kurian, P. Komissinskiy, E. Hildebrandt, T. Bertaud, C. Walczyk, P. Calka, T. Schroeder, and L. Alff, *Thickness independent reduced forming voltage in oxygen engineered HfO₂ based resistive switching memories*, Applied Physics Letters **105**, 073505 (2014).
- [162] N. Raghavan, A. Fantini, R. Degraeve, P. J. Roussel, L. Goux, B. Goveoreanu, D. J. Wouters, G. Groeseneken, and M. Jurczak, *Statistical insight*

- into controlled forming and forming free stacks for HfO_x {RRAM}, Microelectronic Engineering **109**, 177 (2013), Insulating Films on Semiconductors 2013.
- [163] B. Govoreanu, G. S. Kar, Y. Y. Chen, V. Paraschiv, S. Kubicek, A. Fantini, I. P. Radu, L. Goux, S. Clima, R. Degraeve, N. Jossart, O. Richard, T. Vandeweyer, K. Seo, P. Hendrickx, G. Pourtois, H. Bender, L. Altimime, D. J. Wouters, J. A. Kittl, and M. Jurczak, $10 \times 10 \text{ nm}^2$ Hf/HfO_x crossbar resistive RAM with excellent performance, reliability and low-energy operation, in Electron Devices Meeting (IEDM), 2011 IEEE International, pp. 31.6.1–31.6.4, 2011.
- [164] K. Skaja, C. Bäumer, O. Peters, S. Menzel, M. Moors, H. Du, M. Bornhöft, C. Schmitz, V. Feyer, C.-L. Jia, C. M. Schneider, J. Mayer, R. Waser, and R. Dittmann, *Avalanche-Discharge-Induced Electrical Forming in Tantalum Oxide-Based Metal-Insulator-Metal Structures*, Advanced Functional Materials **25**, 7154 (2015).
- [165] E. Mikheev, B. D. Hoskins, D. B. Strukov, and S. Stemmer, *Resistive switching and its suppression in $\text{Pt}/\text{Nb}:\text{SrTiO}_3$ junctions*, Nature Communications **5**, 3990 (2015).
- [166] H. Schäfer and G. Breil, *Über Das System Nb_2O_5 - Ta_2O_5 - NbO_2 - TaO_2 - H_2O - H_2* , Zeitschrift für anorganische und allgemeine Chemie **267**, 265 (1952).
- [167] T. Nagata, M. Haemori, and T. Chikyow, *Combinatorial Synthesis of $\text{Cu}/(\text{Ta}_x\text{Nb}_{1-x})_2\text{O}_5$ Stack Structure for Nanoionics-Type ReRAM Device*, ACS Combinatorial Science **15**, 435 (2013).
- [168] O. Peters, *Spectroscopic Investigations of Resistively Switching Ta_2O_5 Thin Films*, Master's thesis, RWTH Aachen, 2014.
- [169] A. Prakash, S. Maikap, C. S. Lai, T. C. Tien, W. S. Chen, H. Y. Lee, F. T. Chen, M. Kao, and M. Tsai, *Bipolar resistive switching memory using bilayer TaO_x/WO_x films*, Solid-State Electronics **77**, 35 (2012).
- [170] M.-J. Lee, C. B. Lee, D. Lee, S. R. Lee, M. Chang, J. H. Hur, Y.-B. Kim, C.-J. Kim, D. H. Seo, S. Seo, U.-I. Chung, I.-K. Yoo, and K. Kim, *A fast, high-endurance and scalable non-volatile memory device made from asymmetric $\text{Ta}_2\text{O}_{5-x}/\text{TaO}_{2-x}$ bilayer structures*, Nature Materials **10**, 625 (2011).
- [171] H. Schroeder and D. S. Jeong, *Resistive switching in a $\text{Pt}/\text{TiO}_2/\text{Pt}$ thin film stack - a candidate for a non-volatile ReRAM*, Microelectronic Engineering **84**, 1982 (2007).

- [172] V. I. Gibalov and G. J. Pietsch, *Dynamics of dielectric barrier discharges in different arrangements*, Plasma Sources Science and Technology **21**, 024010 (2012).
- [173] N. Klein, *The mechanism of self-healing electrical breakdown in MOS structures*, IEEE Transactions on Electron Devices **ED-13**, 788 (1966).
- [174] J. Cazaux, *Material contrast in SEM: Fermi energy and work function effects*, Ultramicroscopy **110**, 242 (2010).
- [175] O. Renault, R. Brochier, A. Roule, P. Haumesser, B. Krömker, and D. Funemann, *Work-function imaging of oriented copper grains by photoemission*, Surface and Interface Analysis **38**, 375 (2006).
- [176] K. Tsukada, H. Inoue, F. Katayama, K. Sakai, and T. Kiwa, *Changes in Work Function and Electrical Resistance of Pt Thin Films in the Presence of Hydrogen Gas*, Japanese Journal of Applied Physics **51**, 015701 (2012).
- [177] K. Wandelt, *The local work function: Concept and implications*, Applied Surface Science **111**, 1 (1997), Proceedings of the International Vacuum Electron Sources Conference 1996.
- [178] N. D. Lang and W. Kohn, *Theory of Metal Surfaces: Charge Density and Surface Energy*, Physical Review B **1**, 4555 (1970).
- [179] L. Diederich, O. M. Küttel, P. Aebi, and L. Schlapbach, *Electron affinity and work function of differently oriented and doped diamond surfaces determined by photoelectron spectroscopy*, Surface Science **418**, 219 (1998).
- [180] W. Li and D. Y. Li, *On the correlation between surface roughness and work function in copper*, The Journal of Chemical Physics **122**, 064708 (2005).
- [181] G. Rietveld, M. Glastra, and D. van der Marel, *Doping dependence of the chemical potential in cuprate high- T_c superconductors I. $\text{La}_{2-x}\text{Sr}_x\text{CuO}_4$* , Physica C: Superconductivity **241**, 257 (1995).
- [182] M. T. Greiner, L. Chai, M. G. Helander, W.-M. Tang, and Z.-H. Lu, *Transition Metal Oxide Work Functions: The Influence of Cation Oxidation State and Oxygen Vacancies*, Advanced Functional Materials **22**, 4557 (2012).
- [183] H. Kim, O. Renault, A. Tyurnina, J.-P. Simonato, D. Rouchon, D. Marriolle, N. Chevalier, and J. Dijon, *Doping efficiency of single and randomly stacked bilayer graphene by iodine adsorption*, Applied Physics Letters **105**, 011605 (2014).
- [184] J. Walton and N. Fairley, *Noise reduction in X-ray photoelectron spectro-microscopy by a singular value decomposition sorting procedure*, Journal of Electron Spectroscopy and Related Phenomena **148**, 29 (2005).

-
- [185] C. J. Powell and A. Jablonski, *NIST Electron Inelastic-Mean-Free-Path Database-Version 1.2*, National Institute of Standards and Technology, Gaithersburg, MD, 2010.
- [186] H. Ono and K.-i. Koyanagi, *Infrared absorption peak due to Ta=O bonds in Ta₂O₅ thin films*, Applied Physics Letters **77**, 1431 (2000).
- [187] I. Montero, M. Fernández, and J. Albella, *Pore formation during the breakdown process in anodic Ta₂O₅ films*, Electrochimica Acta **32**, 171 (1987).
- [188] J. M. Albella, I. Montero, J. M. Martínez-Duart, and V. Parkhutik, *Dielectric breakdown processes in anodic Ta₂O₅ and related oxides*, Journal of Materials Science **26**, 3422 (1991).
- [189] K. Ueno, S. Abe, R. Onoki, and K. Saiki, *Anodization of electrolytically polished Ta surfaces for enhancement of carrier injection into organic field-effect transistors*, Journal of Applied Physics **98**, 114503 (2005).
- [190] J. M. Albella, I. Montero, M. Fernández, and J. M. Martínez-Duart, *Post-breakdown reanodization of tantalum*, Journal of Applied Electrochemistry **11**, 525 (1981).
- [191] L. Vázquez, I. Montero, and J. M. Albella, *AFM Study of the Dielectric Breakdown in Ta₂O₅ Films*, Chemistry of Materials **7**, 1680 (1995).
- [192] V. Kadary and N. Klein, *Electrical Breakdown: I. During the Anodic Growth of Tantalum Pentoxide*, Journal of The Electrochemical Society **127**, 139 (1980).
- [193] K. C. Kalra, P. Katyal, and K. C. Singh, *Anodic oxidation of tantalum in aqueous electrolytes*, Thin Solid Films **177**, 35 (1989).
- [194] H. J. Wan, P. Zhou, L. Ye, Y. Y. Lin, T. A. Tang, H. M. Wu, and M. H. Chi, *In Situ Observation of Compliance-Current Overshoot and Its Effect on Resistive Switching*, IEEE Electron Device Letters **31**, 246 (2010).
- [195] S. Tirano, L. Perniola, J. Buckley, J. Cluzel, V. Jousseau, C. Muller, D. Deleruyelle, B. D. Salvo, and G. Reimbold, *Accurate analysis of parasitic current overshoot during forming operation in RRAMs*, Microelectronic Engineering **88**, 1129 (2011), Proceedings of the 17th Biennial International Insulating Films on Semiconductor Conference 17th Biennial International Insulating Films on Semiconductor Conference.
- [196] C. Wiemann, M. Patt, I. P. Krug, N. B. Weber, M. Escher, M. Merkel, and C. M. Schneider, *A New Nanospectroscopy Tool with Synchrotron Radiation: NanoESCA@Elettra*, e-Journal of Surface Science and Nanotechnology **9**, 395 (2011).

- [197] G. R. Gruzalski and D. M. Zehner, *Defect states in substoichiometric tantalum carbide*, Physical Review B **34**, 3841 (1986).
- [198] B. C. Bayer, C. Castellarin-Cudia, R. Blume, S. A. Steiner, C. Ducati, D. Chu, A. Goldoni, A. Knop-Gericke, R. Schlogl, C. Cepek, J. Robertson, and S. Hofmann, *Tantalum-oxide catalysed chemical vapour deposition of single- and multi-walled carbon nanotubes*, RSC Advances **3**, 4086 (2013).
- [199] B. S. Itchkawitz, P. F. Lyman, G. W. Ownby, and D. M. Zehner, *Monolayer graphite on TaC(111): electronic band structure*, Surface Science **318**, 395 (1994).
- [200] T. Morikawa, S. Saeki, T. Suzuki, T. Kajino, and T. Motohiro, *Dual functional modification by N doping of Ta₂O₅: p-type conduction in visible-light-activated N-doped Ta₂O₅*, Applied Physics Letters **96**, 142111 (2010).
- [201] K. Chu, J. P. Chang, M. L. Steigerwald, R. M. Fleming, R. L. Opila, D. V. Lang, R. B. Van Dover, and C. D. W. Jones, *Material and electrical characterization of carbon-doped Ta₂O₅ films for embedded dynamic random access memory applications*, Journal of Applied Physics **91**, 308 (2002).
- [202] A. Nowak, J. Persson, B. Schmelzer, J. Szade, and K. Szot, *Low temperature reduction in Ta-O and Nb-O thin films*, Journal of Physics D: Applied Physics **47**, 135301 (2014).
- [203] Q. Ma and R. A. Rosenberg, *Angle-resolved X-ray photoelectron spectroscopy study of the oxides on Nb surfaces for superconducting r.f. cavity applications*, Applied Surface Science **206**, 209 (2003).
- [204] M. V. Kuznetsov, A. S. Razinkin, and E. V. Shalaeva, *Photoelectron spectroscopy and diffraction of surface nanoscale NbO/Nb(110) structures*, Journal of Structural Chemistry **50**, 514 (2009).
- [205] A. Darlinski and J. Halbritter, *Angle-resolved XPS studies of oxides at NbN, NbC, and Nb surfaces*, Surface and Interface Analysis **10**, 223 (1987).
- [206] S. Hofmann, *Auger- and X-Ray Photoelectron Spectroscopy in Materials Science: A User-Oriented Guide*, Springer Series in Surface Sciences, Springer Berlin Heidelberg, 2012.
- [207] M. F. Hochella and A. H. Carim, *A reassessment of electron escape depths in silicon and thermally grown silicon dioxide thin films*, Surface Science **197**, L260 (1988).
- [208] K. T. Jacob, C. Shekhar, and Y. Waseda, *An update on the thermodynamics of Ta₂O₅*, The Journal of Chemical Thermodynamics **41**, 748 (2009).

-
- [209] K. T. Jacob, C. Shekhar, M. Vinay, and Y. Waseda, *Thermodynamic Properties of Niobium Oxides*, Journal of Chemical & Engineering Data **55**, 4854 (2010).
- [210] S. Kim, S.-J. Kim, K. M. Kim, S. R. Lee, M. Chang, E. Cho, Y.-B. Kim, C. J. Kim, U.-I. Chung, and I.-K. Yoo, *Physical electro-thermal model of resistive switching in bi-layered resistance-change memory*, Scientific reports **3**, 1680 (2013).
- [211] T. Bak, J. Nowotny, and J. Stranger, *Electrical properties of TiO_2 : equilibrium vs dynamic electrical conductivity*, Ionics **16**, 673 (2010).
- [212] M. K. Nowotny, T. Bak, and J. Nowotny, *Electrical Properties and Defect Chemistry of TiO_2 Single Crystal. I. Electrical Conductivity*, The Journal of Physical Chemistry B **110**, 16270 (2006).
- [213] J. Nowotny, M. Radecka, and M. Rekas, *Semiconducting properties of undoped TiO_2* , Journal of Physics and Chemistry of Solids **58**, 927 (1997).
- [214] J.-F. Marucco, J. Gautron, and P. Lemasson, *Thermogravimetric and electrical study of non-stoichiometric titanium dioxide TiO_{2-x} , between 800 and 1100 °C*, Journal of Physics and Chemistry of Solids **42**, 363 (1981).
- [215] P. Odier, J. F. Baumard, D. Panis, and A. M. Anthony, *Thermal emission, electrical conductivity, and hall effect for defects study at high temperature ($T \geq 1250\text{K}$) in refractory oxides (Y_2O_3 , TiO_2)*, Journal of Solid State Chemistry **12**, 324 (1975).
- [216] R. N. Blumenthal, J. Coburn, J. Baukus, and W. M. Hirthe, *Electrical conductivity of nonstoichiometric rutile single crystals from 1000 ° to 1500 °C*, Journal of Physics and Chemistry of Solids **27**, 643 (1966).
- [217] D. S. Tannhauser, *Experimental evidence from conductivity measurements for interstitial titanium in reduced TiO_2* , Solid State Communications **1**, 223 (1963).
- [218] J. Pappis and W. D. Kingery, *Electrical Properties of Single-Crystal and Polycrystalline Alumina at High Temperatures*, Journal of the American Ceramic Society **44**, 459 (1961).
- [219] K. Kitazawa and R. L. Coble, *Electrical Conduction in Single-Crystal and Polycrystalline Al_2O_3 at High Temperatures*, Journal of the American Ceramic Society **57**, 245 (1974).

- [220] H. G. Bernd Huber and C. Ziegler, *Electrical properties of nanocrystalline anatase TiO_2 thin films with different crystallite size*, Surface Science **566568**, Part 1, 419 (2004), Proceedings of the 22nd European Conference on Surface Science.
- [221] T. Dittrich, J. Weidmann, F. Koch, I. Uhlendorf, and I. Lauermann, *Temperature- and oxygen partial pressure-dependent electrical conductivity in nanoporous rutile and anatase*, Applied Physics Letters **75**, 3980 (1999).
- [222] A. Weibel, R. Bouchet, and P. Knauth, *Electrical properties and defect chemistry of anatase (TiO_2)*, Solid State Ionics **177**, 229 (2006).
- [223] R. A. De Souza, *The formation of equilibrium space-charge zones at grain boundaries in the perovskite oxide SrTiO_3* , Physical Chemistry Chemical Physics **11**, 9939 (2009).
- [224] R. A. De Souza, V. Metlenko, D. Park, and T. E. Weirich, *Behavior of oxygen vacancies in single-crystal SrTiO_3 : Equilibrium distribution and diffusion kinetics*, Physical Review B **85**, 174109 (2012).
- [225] J. Maier, *Physical Chemistry of Ionic Materials: Ions and Electrons in Solids*, Wiley, 2004.
- [226] T. Burg, *Semiconducting properties of polycrystalline titanium dioxide*, PhD thesis, Centre for Materials Research in Energy Conversion School of Materials Science and Engineering Faculty of Science and Technology The University of New South Wales, 2008.
- [227] K. K. Adepalli, M. Kelsch, R. Merkle, and J. Maier, *Enhanced ionic conductivity in polycrystalline TiO_2 by "one-dimensional doping"*, Physical Chemistry Chemical Physics **16**, 4942 (2014).
- [228] P. Knauth and H. L. Tuller, *Electrical and defect thermodynamic properties of nanocrystalline titanium dioxide*, Journal of Applied Physics **85**, 897 (1999).
- [229] C. Demetry and X. Shi, *Grain size-dependent electrical properties of rutile (TiO_2)*, Solid State Ionics **118**, 271 (1999).
- [230] P. Knauth and H. L. Tuller, *Solute segregation, electrical properties and defect thermodynamics of nanocrystalline TiO_2 and CeO_2* , Solid State Ionics **136137**, 1215 (2000), Proceedings of the 12th International Conference on Solid State Ionics.
- [231] S. Bhowmik, K. P. Constant, J. C. Parker, and M. Ali, *Electrical characterization of nanocrystalline titaniaI: (Impedance spectroscopy studies between 300 K and 473 K)*, Materials Science and Engineering: A **204**, 258 (1995), Proceedings of the Symposium on Engineering of Nanostructured Materials.

-
- [232] J. Nowotny, T. Bak, T. Burg, M. K. Nowotny, and L. R. Sheppard, *Effect of Grain Boundaries on Semiconducting Properties of TiO_2 at Elevated Temperatures*, The Journal of Physical Chemistry C **111**, 9769 (2007).
- [233] M. D. Earle, *The Electrical Conductivity of Titanium Dioxide*, Physical Review **61**, 56 (1942).
- [234] T. Bak, M. K. Nowotny, L. R. Sheppard, and J. Nowotny, *Charge Transport in Cr-Doped Titanium Dioxide*, The Journal of Physical Chemistry C **112**, 7255 (2008).
- [235] J. Nowotny, T. Bak, M. K. Nowotny, and L. R. Sheppard, *Defect Chemistry and Electrical Properties of Titanium Dioxide. 2. Effect of Aliovalent Ions*, The Journal of Physical Chemistry C **112**, 602 (2008).
- [236] W. Wagner and A. Pruss, *International Equations for the Saturation Properties of Ordinary Water Substance. Revised According to the International Temperature Scale of 1990. Addendum to J. Phys. Chem. Ref. Data 16, 893 (1987)*, Journal of Physical and Chemical Reference Data **22**, 783 (1993).
- [237] Y. Li, K. Gerdes, H. Diamond, and X. Liu, *An improved method to increase the predictive accuracy of the ECR technique*, Solid State Ionics **204205**, 104 (2011).
- [238] P. A. M. Hotsenpiller, J. D. Bolt, W. E. Farneth, J. B. Lowekamp, and G. S. Rohrer, *Orientation Dependence of Photochemical Reactions on TiO_2 Surfaces*, The Journal of Physical Chemistry B **102**, 3216 (1998).
- [239] T. Ohno, K. Sarukawa, and M. Matsumura, *Crystal faces of rutile and anatase TiO_2 particles and their roles in photocatalytic reactions*, New Journal of Chemistry **26**, 1167 (2002).
- [240] F. Labat, P. Baranek, and C. Adamo, *Structural and Electronic Properties of selected Rutile and Anatase TiO_2 Surfaces: An ab Initio Investigation*, Journal of Chemical Theory and Computation **4**, 341 (2008).
- [241] H. Perron, C. Domain, J. Roques, R. Drot, E. Simoni, and H. Catalette, *Optimisation of accurate rutile TiO_2 (110), (100), (101) and (001) surface models from periodic DFT calculations*, Theoretical Chemistry Accounts **117**, 565 (2007).
- [242] B. J. Morgan and G. W. Watson, *A Density Functional Theory + U Study of Oxygen Vacancy Formation at the (110), (100), (101), and (001) Surfaces of Rutile TiO_2* , The Journal of Physical Chemistry C **113**, 7322 (2009).

- [243] M. K. Nowotny, T. Bak, and J. Nowotny, *Electrical Properties and Defect Chemistry of TiO₂ Single Crystal. IV. Prolonged Oxidation Kinetics and Chemical Diffusion*, The Journal of Physical Chemistry B **110**, 16302 (2006).
- [244] R. Merkle and J. Maier, *How Is Oxygen Incorporated into Oxides? A Comprehensive Kinetic Study of a Simple Solid-State Reaction with SrTiO₃ as a Model Material*, Angewandte Chemie International Edition **47**, 3874 (2008).
- [245] K. Kerman, C. Ko, and S. Ramanathan, *Orientation dependent oxygen exchange kinetics on single crystal SrTiO₃ surfaces*, Physical Chemistry Chemical Physics **14**, 11953 (2012).
- [246] H.-I. Yoo and C.-E. Lee, *Two-Fold Diffusion Kinetics of Oxygen Re-Equilibration in Donor-Doped BaTiO₃*, Journal of the American Ceramic Society **88**, 617 (2005).
- [247] P. F. Dennis and R. Freer, *Oxygen self-diffusion in rutile under hydrothermal conditions*, Journal of Materials Science **28**, 4804 (1993).
- [248] M. Arita, M. Hosoya, M. Kobayashi, and M. Someno, *Depth Profile Measurement by Secondary Ion Mass Spectrometry for Determining the Tracer Diffusivity of Oxygen in Rutile*, Journal of the American Ceramic Society **62**, 443 (1979).
- [249] L.-B. Mo, Y. Wang, Y. Bai, Q.-Y. Xiang, Q. Li, W.-Q. Yao, J.-O. Wang, K. Ibrahim, H.-H. Wang, C.-H. Wan, and J.-L. Cao, *Hydrogen Impurity Defects in Rutile TiO₂*, Scientific Reports **5**, 17634 (2015).
- [250] T. Norby, M. Widerøe, R. Glockner, and Y. Larring, *Hydrogen in oxides*, Dalton Transaction , 3012 (2004).
- [251] R. Haul and G. Dümmbgen, *Sauerstoff-selbstdiffusion in Rutilkristallen*, Journal of Physics and Chemistry of Solids **26**, 1 (1965).
- [252] R. Freer and P. F. Dennis, *Oxygen Diffusion Studies. I. A Preliminary Ion Microprobe Investigation of Oxygen Diffusion in Some Rock-Forming Minerals*, Mineralogical Magazine **45**, 179 (1982).
- [253] D. K. Moore, D. J. Cherniak, and E. B. Watson, *Oxygen diffusion in rutile from 750 to 1000 °C and 0.1 to 1000 MPa*, American Mineralogist **83**, 700 (1998).
- [254] Y. Morishita, B. J. Giletti, and J. R. Farver, *Volume self-diffusion of oxygen in titanite*, Geochemical Journal **30**, 71 (1996).

-
- [255] X. Y. Zhang, E. B. Watson, and D. J. Cherniak, *Oxygen self-diffusion fast-paths in titanite single crystals and a general method for deconvolving self-diffusion profiles with tails*, *Geochimica et Cosmochimica Acta* **71**, 1563 (2007).
- [256] S. Erdal, C. Kongschaug, T. S. Bjørheim, N. Jalarvo, R. Haugsrud, and T. Norby, *Hydration of Rutile TiO_2 : Thermodynamics and Effects on n- and p-Type Electronic Conduction*, *The Journal of Physical Chemistry C* **114**, 9139 (2010).
- [257] J. He, R. K. Behera, M. W. Finnis, X. Li, E. C. Dickey, S. R. Phillpot, and S. B. Sinnott, *Prediction of high-temperature point defect formation in TiO_2 from combined ab initio and thermodynamic calculations*, *Acta Materialia* **55**, 4325 (2007).
- [258] J. He and S. B. Sinnott, *Ab Initio Calculations of Intrinsic Defects in Rutile TiO_2* , *Journal of the American Ceramic Society* **88**, 737 (2005).
- [259] A. Moballegh and E. C. Dickey, *Electric-field-induced point defect redistribution in single-crystal TiO_{2-x} and effects on electrical transport*, *Acta Materialia* **86**, 352 (2015).
- [260] X. Li, M. W. Finnis, J. He, R. K. Behera, S. R. Phillpot, S. B. Sinnott, and E. C. Dickey, *Energetics of charged point defects in rutile TiO_2 by density functional theory*, *Acta Materialia* **57**, 5882 (2009).
- [261] A. V. Hippel, J. Kalnajs, and W. B. Westphal, *Protons, dipoles, and charge carriers in rutile*, *Journal of Physics and Chemistry of Solids* **23**, 779 (1962).
- [262] O. W. Johnson, S. Paek, and J. W. DeFord, *Diffusion of H and D in TiO_2 : Suppression of internal fields by isotope exchange*, *Journal of Applied Physics* **46**, 1026 (1975).
- [263] T. Norby and P. Kofstad, *Proton and native-ion conductivities in Y_2O_3 at high temperatures*, *Solid State Ionics* **20**, 169 (1986).
- [264] H. J. Höfler, H. Thomas, and R. S. Averback, *Diffusion in Nanocrystalline Materials*, in *Atomic Migration and Defects in Materials*, volume 75 of *Defect and Diffusion Forum*, pp. 195–210, Trans Tech Publications, 1991.
- [265] T. Bieger, J. Maier, and R. Waser, *Kinetics of oxygen incorporation in SrTiO_3 (Fe-doped): an optical investigation*, *Sensors and Actuators B: Chemical* **7**, 763 (1992).
- [266] R. Merkle and J. Maier, *Oxygen incorporation into Fe-doped SrTiO_3 : Mechanistic interpretation of the surface reaction*, *Physical Chemistry Chemical Physics* **4**, 4140 (2002).

- [267] G. Kim, S. Wang, A. J. Jacobson, and C. L. Chen, *Measurement of oxygen transport kinetics in epitaxial $\text{La}_2\text{NiO}_{4+\delta}$ thin films by electrical conductivity relaxation*, Solid State Ionics **177**, 1461 (2006).
- [268] S. Wang, A. Verma, Y. L. Yang, A. J. Jacobson, and B. Abeles, *The effect of the magnitude of the oxygen partial pressure change in electrical conductivity relaxation measurements: oxygen transport kinetics in $\text{La}_{0.5}\text{Sr}_{0.5}\text{CoO}_{3-\delta}$* , Solid State Ionics **140**, 125 (2001).
- [269] X. Chen, S. Wang, Y. L. Yang, L. Smith, N. J. Wu, B. Kim, S. S. Perry, A. J. Jacobson, and A. Ignatiev, *Electrical conductivity relaxation studies of an epitaxial $\text{La}_{0.5}\text{Sr}_{0.5}\text{CoO}_{3-\delta}$ thin film*, Solid State Ionics **146**, 405 (2002).
- [270] G. Garcia, M. Burriel, N. Bonanos, and J. Santiso, *Electrical Conductivity and Oxygen Exchange Kinetics of $\text{La}_2\text{NiO}_{4+\delta}$ Thin Films Grown by Chemical Vapor Deposition*, Journal of The Electrochemical Society **155**, P28 (2008).
- [271] M. Kubicek, Z. Cai, W. Ma, B. Yildiz, H. Hutter, and J. Fleig, *Tensile Lattice Strain Accelerates Oxygen Surface Exchange and Diffusion in $\text{La}_{1-x}\text{Sr}_x\text{CoO}_{3-\delta}$ Thin Films*, ACS Nano **7**, 3276 (2013), PMID: 23527691.
- [272] A. Zomorrodian, H. Salamati, Z. Lu, X. Chen, N. Wu, and A. Ignatiev, *Electrical conductivity of epitaxial $\text{La}_{0.6}\text{Sr}_{0.4}\text{Co}_{0.2}\text{Fe}_{0.8}\text{O}_{3-\delta}$ thin films grown by pulsed laser deposition*, International Journal of Hydrogen Energy **35**, 12443 (2010), Bio-Ethanol and Other Renewable Sources and Reforming Process for Sustainable Hydrogen Production.
- [273] Y. L. Yang, A. J. Jacobson, C. L. Chen, G. P. Luo, K. D. Ross, and C. W. Chu, *Oxygen exchange kinetics on a highly oriented $\text{La}_{0.5}\text{Sr}_{0.5}\text{CoO}_{3-\delta}$ thin film prepared by pulsed-laser deposition*, Applied Physics Letters **79**, 776 (2001).
- [274] M. Sogaard, A. Bieberle-Hütter, P. V. Hendriksen, M. Mogensen, and H. L. Tuller, *Oxygen incorporation in porous thin films of strontium doped lanthanum ferrite*, Journal of Electroceramics **27**, 134 (2011).
- [275] G. Kim, S. Wang, A. J. Jacobson, Z. Yuan, W. Donner, C. L. Chen, L. Reimus, P. Brodersen, and C. A. Mims, *Oxygen exchange kinetics of epitaxial $\text{PrBaCo}_2\text{O}_{2+\delta}$ thin films*, Applied Physics Letters **88**, 024103 (2006).
- [276] R. Meyer, A. F. Zurhelle, R. A. De Souza, R. Waser, and F. Gunkel, *Dynamics of the metal-insulator transition of donor-doped SrTiO_3* , Physical Review B **94**, 115408 (2016).
- [277] J. A. Lane and J. A. Kilner, *Measuring oxygen diffusion and oxygen surface exchange by conductivity relaxation*, Solid State Ionics **136****137**, 997 (2000), Proceedings of the 12th International Conference on Solid State Ionics.

- [278] D. Chen and Z. Shao, *Surface exchange and bulk diffusion properties of $Ba_{0.5}Sr_{0.5}Co_{0.8}Fe_{0.2}O_{3-\delta}$ mixed conductor*, International Journal of Hydrogen Energy **36**, 6948 (2011).
- [279] Z. Li and R. Haugsrud, *Effects of surface coatings on the determination of D_{chem} and k_{chem} in $La_2NiO_{4+\delta}$ by conductivity relaxation*, Solid State Ionics **206**, 67 (2012).
- [280] S. Kim, S. Wang, X. Chen, Y. L. Yang, N. Wu, A. Ignatiev, A. J. Jacobson, and B. Abeles, *Oxygen Surface Exchange in Mixed Ionic Electronic Conductors: Application to $La_{0.5}Sr_{0.5}Fe_{0.8}Ga_{0.2}O_{3-\delta}$* , Journal of The Electrochemical Society **147**, 2398 (2000).
- [281] D. B. Schwarz and H. U. Anderson, *Determination of Oxygen Chemical Diffusion Coefficients in Single Crystal $SrTiO_3$ by Capacitance Manometry*, Journal of The Electrochemical Society **122**, 707 (1975).
- [282] P. Pasierb, S. Komornicki, and M. Rekas, *Comparison of the chemical diffusion of undoped and Nb-doped $SrTiO_3$* , Journal of Physics and Chemistry of Solids **60**, 1835 (1999).
- [283] V. Metlenko, W. Jung, S. R. Bishop, H. L. Tuller, and R. A. De Souza, *Oxygen diffusion and surface exchange in the mixed conducting oxides $SrTi_{1-y}Fe_yO_{3-\delta}$* , Phys. Chem. Chem. Phys. **18**, 29495 (2016).
- [284] R. S. Roth, J. L. Waring, and H. S. Parker, *Effect of oxide additions on the polymorphism of tantalum pentoxide. IV. The system Ta_2O_5 - Ta_2WO_8* , Journal of Solid State Chemistry **2**, 445 (1970).
- [285] N. C. Stephenson and R. S. Roth, *Structural systematics in the binary system Ta_2O_5 - WO_3 . V. The structure of the low-temperature form of tantalum oxide L - Ta_2O_5* , Acta Crystallographica B **27**, 1037 (1971).
- [286] G. L. Brennecka and D. A. Payne, *Densification and grain growth for powder-derived Ta_2O_5 - TiO_2 ceramics*, Journal of the Ceramic Society of Japan **115**, 678 (2007).
- [287] S. Wu, H. M. Chan, and M. P. Harmer, *Effect of Alumina Additions on Microstructural Aspects of the β to α Transformation in Tantalum (V) Oxide*, Journal of the American Ceramic Society **88**, 2369 (2005).
- [288] J. M. Heintz, J. J. M. Besson, L. Rabardel, and J. P. Bonnet, *Grain growth and densification study of β - Ta_2O_5* , Ceramics International **18**, 263 (1992).
- [289] Y. W. Bae, W. Y. Lee, and D. P. Stinton, *Effects of Temperature and Reagent Concentration on the Morphology of Chemically Vapor Deposited β - Ta_2O_5* , Journal of the American Ceramic Society **78**, 1297 (1995).

- [290] C. M. Weyant, K. T. Faber, J. D. Almer, and J. V. Guiheen, *Residual Stress and Microstructural Evolution in Tantalum Oxide Coatings on Silicon Nitride*, Journal of the American Ceramic Society **88**, 2169 (2005).
- [291] A. G. Evans, *Microfracture from thermal expansion anisotropy-I. Single phase systems*, Acta Metallurgica **26**, 1845 (1978).
- [292] O. Johannesen and P. Kofstad, *The electrical conductivity of sintered specimens of Ta_2O_5 with additions of foreign oxides*, Solid State Ionics **12**, 235 (1984).
- [293] U. Balachandran and N. G. Eror, *Electrical conductivity in Ta_2O_5* , Materials Research Bulletin **17**, 151 (1982).
- [294] U. N. Lederer, *Sauerstoffdiffusion in Tantaloxid*, Master's thesis, RWTH Aachen, 2014.
- [295] R. Nakamura, K. Tanaka, M. Ishimaru, K. Sato, T. J. Konno, and H. Nakajima, *Self-elongated growth of nanopores in annealed amorphous Ta_2O_5 films*, Scripta Materialia **66**, 182 (2012).
- [296] C.-H. Lu, Y.-C. Chen, and Y.-C. Sun, *Low-temperature crystallization of electroceramic thin films at elevated pressure*, Journal of Materials Chemistry **12**, 1628 (2002).

Acknowledgment

This work would not have been possible without the help and support of many other people. I would like to thank everyone, who supported me during my thesis.

I would like to thank Prof. Dr. Rainer Waser for giving me the opportunity to work at his institute. In this highly fascinating research topic he gave me the freedom to follow my interests. His ongoing interest in my work and fruitful discussions were very helpful. Furthermore, I thank Dr. Roger De Souza for agreeing to act as second reviewer for this thesis.

I would like to thank Prof. Dr. Regina Dittmann for the support during the spectroscopic measurements. Her guidance and stimulating ideas for experiments and interpretations helped to guide this work into the right direction.

Thanks to Maria Garcia, Luise Snyders and Martina Heins for the help in administrative questions during my time at the institute.

I would like to thank Dr. Felix Gunkel for the introduction into the field of defect chemistry and high temperature equilibrium conductivity measurements. Furthermore, I would like to thank him for his helpful advice and ideas for the chemical diffusion experiment.

I would like to thank Christoph Bäumer for the spectromicroscopy measurements and discussions about photoelectron spectroscopy. Many thanks also go to Dr. Annemarie Köhl for many discussions on photoelectron spectroscopy. Furthermore I want to thank my Master student Oliver Peters for his valuable contribution to the spectromicroscopy project on tantalum oxide based cells. I would also like to thank Michael Andrä, who has measured a part of the XPS data. For the simulations and discussion about resistive switching I am very grateful to Dr. Stephan Menzel. Furthermore, I would like to thank Dr. Sebastian Schmelzer for his helpful advice at the beginning of my work on developing reactive sputtering processes. Thanks go also to Dr. Marco Moors for LC-AFM measurements.

I would like to thank Mirka Grates, Georg Pickartz and Stephan Masberg for the technical support in the cluster lab. Special thanks go to René Borowski

for deposition and structuring of top electrodes and for fast and reliable technical support. Moreover, I would like to thank Marcel Gerst and Jochen Friedrich for the technical support in implementing the electronic conductivity relaxation set-up.

I would like to thank Dr. Paul Meuffels and Cerstin Makovicka for the preparation of the tantalum oxide ceramic. Furthermore, I would like to thank Dr. Paul Meuffels for his helpful advice and ideas for the chemical diffusion experiment.

Finally, I thank Benedikt Arndt, Ronja Heinen, Dr. Anja Herpers, Dr. Sebastian Wicklein, Dr. Christoph Hermes, Nabeel Aslam, Michael Andrä, Nicolas Raab, Felix Hensling, Bernd Rösigen, Chencheng Xu and all other present and former colleagues at the PGI 7 for fruitful discussions and contributions to a nice atmosphere at the institute. My special thanks to Dr. Felix Gunkel, Christoph Bäumer and Johannes Schmalstieg for proofreading this thesis.

I would like to thank Dr. Roger De Souza, Ute Lederer and Dr. Susanne Hoffmann-Eifert for discussions about defect chemistry and diffusion in tantalum oxide. Moreover, I want to thank Manuel Bornhöft and Hongchu Du for performing the STEM measurements. I would also like to thank Maximilian Kruth for the preparation of the TEM lamella of the dendrite-like structures. Furthermore, I would like to thank Vitaliy Feyer, Christoph Schmitz and Giovanni Zamborlini for support during the synchrotron measurements.

I thank my family and Barbara and Gerhard Schmalstieg for supporting and encouraging me during my studies. A big thanks goes to Johannes Schmalstieg for his patience, encouragement, support and simply being there whenever it was needed.

Lebenslauf

Persönliche Angaben

Name: Katharina Skaja
Geburtsort: Datteln

Schulbildung

08/1997 - 06/2006: St. Antonius Gymnasium, Lüdinghausen
Abschluss Abitur

Studium

10/2006 - 07/2011: Physikstudium an der TU Dortmund
Abschluss Diplom

Berufliche Tätigkeit

seit 10/2011: wissenschaftliche Mitarbeiterin am Peter Grünberg Institut 7
Forschungszentrum Jülich

Aachen, den 14.02.2017

Band / Volume 35

Defect Engineering of SrTiO₃ thin films for resistive switching applications

S. Wicklein (2014), xi, 144 pp

ISBN: 978-3-89336-963-8

Band / Volume 36

Integration and Characterization of Atomic Layer Deposited TiO₂ Thin Films

for Resistive Switching Applications

M. Reiners (2014), xiv, 166 pp

ISBN: 978-3-89336-970-6

Band / Volume 37

Resistive switching in ZrO₂ based metal-oxide-metal structures

I. Kärkkäinen (2014), xviii, 125 pp

ISBN: 978-3-89336-971-3

Band / Volume 38

Resistive switching phenomena of extended defects in Nb-doped SrTiO₃ under influence of external gradients

C. Rodenbücher (2014), xiii, 200 pp

ISBN: 978-3-89336-980-5

Band / Volume 39

Micro-spectroscopic investigation of valence change processes in resistive switching SrTiO₃ thin films

A. Köhl (2014), viii, 166 pp

ISBN: 978-3-89336-988-1

Band / Volume 40

Strained Silicon and Silicon-Germanium Nanowire Tunnel FETs and Inverters

S. Richter (2014), iii, 117 pp

ISBN: 978-3-95806-002-9

Band / Volume 41

Integration of Redox-Based Resistive Switching Memory Devices

F. Lentz (2014), i, 166 pp

ISBN: 978-3-95806-019-7

Band / Volume 42

Ladungstransportuntersuchungen an nanofunktionalen Bauelementen mit Diodencharakteristik basierend auf funktionalisierten Nanopartikeln

N. Babajani (2015), iv, 138, XLVII

ISBN: 978-3-95806-026-5

Band / Volume 43

**Transport and Noise Properties of Nanostructure Transistors
for Biosensor Applications**

J. Li (2015), vii, 175 pp

ISBN: 978-3-95806-034-0

Band / Volume 44

**Quantitative scanning tunneling spectroscopy
of non-polar III-V compound semiconductor surfaces**

M. Schnedler (2015), 122 pp

ISBN: 978-3-95806-075-3

Band / Volume 45

Model-based Algorithm Development with Focus on Biosignal Processing

Y. Yao (2015), x, 169 pp

ISBN: 978-3-95806-080-7

Band / Volume 46

**Growth and characterization of crystalline rare-earth based thin oxide films
for the application as gate dielectric in nanotechnology**

A. B. Schäfer (2015), xiii, 157 pp

ISBN: 978-3-95806-111-8

Band / Volume 47

**TEM/STEM Investigations of Phase Change Materials for Non-volatile
Memory Applications**

M. Bornhöft (2017), viii, 135 pp

ISBN: 978-3-95806-221-4

Band / Volume 48

**Investigation of ternary nitride semiconductor alloys
by scanning tunneling microscopy**

V. Portz (2017), 140 pp

ISBN: 978-3-95806-232-0

Band / Volume 49

**Redox processes and ionic transport in resistive switching
binary metal oxides**

K. Skaja (2017), VII, 203 pp

ISBN: 978-3-95806-236-8

Information
Band / Volume 49
ISBN 978-3-95806-236-8

